Radar Data Assimilation and Forecasts of Evolving Nonlinear Wave Fields

by

Sina Hassanaliaragh

A dissertation submitted in partial fulfillment
of the requirements for the degree of
Doctor of Philosophy
(Naval Architecture and Marine Engineering and Scientific Computing)
in The University of Michigan
2009

Doctoral Committee:

Research Scientist Okey G. Nwogu, Co-Chair
Professor Robert F. Beck, Co-Chair
Professor Nikolaos D. Katopodes
Professor Robert L. Smith
Research Scientist David R. Lyzenga

To my parents Manijeh and Reza Aragh,
and my lovely sisters, Golbon and Leila

ACKNOWLEDGEMENTS

I owe a debt of gratitude to many people whose support has been crucial to my success in completing this dissertation. First of all, I have been privileged to have the direction and guidance of Dr. Okey G. Nwogu, my academic advisor. From the inception of this project, Okey has been generous with his time and has provided eminently helpful advice on every thing from the methodology to the writing process. My other committee members, Robert Beck, Robert Smith, Nick Katopodes, and David Lyzenga, have also contributed insightful and critical comments and suggestions. I thank Dave Lyzenga as well as Joel Johnson of Ohio State University for providing field data and synthetic radar data.

I am also grateful to the Office of Naval Research (ONR) for providing me with financial support as part of the MURI project on "Optimal Vessel Performance in Evolving Nonlinear Wave Fields", during the last three years of my Doctoral studies.

I would like to thank my special lovely friend, Ms. Nazanin Zarinkamar, who kept my hands through tough years of my Ph.D. studies.

Finally I owe much to my parents for always believing in me and encouraging me to achieve my goals. Their compassion, generosity, and steadfast emotional support have been invaluable in helping me to focus on my academic pursuits. They forever inspire me with their infinite capacity for love, joy, and faith.

TABLE OF CONTENTS

LIST OF FIGURES

Figure

LIST OF TABLES

Table

LIST OF APPENDICES

APPENDIX

NOMENCLATURE

a_n: Fourier coefficients of the surface elevation in two-dimensional flows
a_n^*: Fourier coefficients of the adjoint variable η^* in 2D flows
a_{nm}: Fourier coefficients of the free surface elevation in three-dimensional flows
a_{nm}^*: Fourier coefficients of the adjoint variable η^* in 3D flows
b_n: Fourier coefficients of the free surface tangential velocity in two-dimensional flows
b_n^*: Fourier coefficients for the adjoint variable u_s in 2D flows
b_{nm}: Fourier coefficients of u_s
b_{nm}^*: Fourier coefficients for the adjoint variable u_s in 3D flows
c_n: Fourier coefficients of the velocity potential in two-dimensional flows
c_{nm}: Fourier coefficients of v_s
c_{nm}^*: Fourier coefficients for the adjoint variable v_s in 3D flows
c: Wave speed
c_E: Eulerian time-mean current velocity
c_S: Mean mass-transport velocity
$\mathbf{d}_k$: Newton search direction at iteration k
D_η: Dissipative term in the mass equation
D_u: Dissipative term in the momentum equation
E: Total energy of the fluid
$G(\theta)$: Directional spreading function
h_0: Fluid depth
g: Acceleration of gravity
$\mathbf{g}_k$: Gradient vector at iteration k
H: Wave height
H_k: Hessian matrix at iteration k
$\mathcal{H}$: Hilbert transform
I: Total momentum of the fluid, and the identity matrix
J: Cost function
k_1: Wavenumber in x-direction
k_2: Wavenumber in y-direction
$\mathbf{k}$: Wavenumber vector, $\mathbf{k} = (k_1, k_2)$,
$\mathcal{L}$: Linear integral operator relating the velocity potential and vertical velocity on $z = 0$

M: Total mass of the fluid

p: Pressure

$\mathcal{P}$: Principal value integral

p_G: Pressure generation term in the momentum equation

q: Volume flux of the flow due to waves

$\mathbf{q}$: Vector of the free surface variables, $(\eta, \mathbf{u}_s)$ or (η, Φ)

Q: Volume flux of the flow per unit span

R: Bernoulli's constant

$S(f)$: Frequency spectrum

$S(k)$: Wave number spectrum

T: Wave period

$\mathcal{T}$: Linear integral operator relating the tangential velocity and vertical velocity on $z = 0$

$\mathbf{u}_0$: Tangential velocity on the mean free surface $z = 0$

$\mathbf{u}_s$: Tangential velocity on the free surface; $\mathbf{u}_s = (u_s, v_s)$,

$\mathbf{u}'_s$: Tangent linear tangential velocity

$\mathbf{u}^*_s$: Adjoint tangential velocity

$\bar{u}$: Mean fluid velocity

U, V, W: Horizontal and vertical fluid velocities on the free surface

W_j: Weighting function

x, y, z: Cartesian coordinates

w_0: Vertical fluid velocity on the mean free surface $z = 0$

α, γ: Constant parameters in the JONSWAP spectrum

α_k: Step size in the minimization algorithm

β: Side-band growth rate

$\hat{\delta}$: Side-band frequency parameter

ϵ: Wave steepness parameter $= ka$

η: Free surface elevation

η': Tangent linear free surface elevation

η^*: Adjoint free surface elevation

η_{obs}: Observed surface elevation

λ: Wave length

ω: Angular frequency

ω_c: Angular frequency of the carrier wave

$\delta\omega$: Angular frequency of the side-bands

ϕ: Velocity potential of the flow

ϕ_0: Velocity potential on the mean free surface $z = 0$

Φ: Velocity potential on the free surface

Φ': Tangent linear velocity potential

Φ^*: Adjoint velocity potential

φ: Phase angle

ψ: Stream function of the flow

ρ: Density of the fluid

ABBREVIATION

ADJ: Adjoint
ANA: Adjoint Newton Algorithm
ATN: Adjoint Truncated Newton
FD: Finite Difference
FFT: Fast Fourier Transform
FNL: Fully Nonlinear
HOS: High-Order Spectral
KE: Kinetic Energy
MTF: Modulation Transfer Function
NLS: Nonlinear Schrodinger
NRCS: Normalized Radar Cross Section
NWP: Numerical Weather Prediction
PE: Potential Energy
RK4: Forth-order Runge-Kutta integration
SA: Simulated Annealing
TLM: Tangent Linear Model

CHAPTER 1

Introduction

1.1 Motivation

Recent advances in remote sensing technology are beginning to allow for measurement of the ocean wave fields in near-real time. Assimilation of real-time measured data into short-term wave forecast models could greatly enhance the safety and effectiveness of offshore and marine operations. Real-time wave field forecasts could, for instance, be used to predict the potential occurrence of large amplitude 'rogue'waves that can appear without warning and potentially cause significant damages to vessels and/or lead to capsizing. Wave field forecasts could also be used to predict periods of calm seas for launch/recovery operations and at-sea cargo transfer operations. During such sensitive operations, decisions need to be made shortly before or during the task about suspension of work based on expected risk of damage or loss of life. These decisions must be based upon accurate short and medium-term wave forecasts.

Wave forecasting can be viewed as an initial/boundary value problem. Given an estimate of the present state of the sea surface (initial condition), wave forecast models simulate (forecast) the short-term evolution of the sea surface subject to conditions imposed at the boundaries of the computational domain. The quality of the wave forecast is strongly dependent on the accuracy of both the initial and boundary conditions. The problem of determination of initial/boundary conditions for a numerical model is a very important, complicated, and challenging task, and has become a science in itself, which is often referred

to as "Data Assimilation" [38].

Data assimilation attempts to combine physics-based models with observational data to provide an improved estimate of the state of a system that is better than what could be obtained by just using either observations or numerical models alone. Assimilation is used extensively in meteorology and increasingly in oceanography. It provides a mechanism for extracting and filtering the useful information from noisy and potentially inaccurate data and combining it with the numerical model, while the model provides the mechanism for carrying the information forward from earlier observations to the desired time in future.

Data assimilation is, therefore, a useful technique whenever there is insufficient or inaccurate data to define the sea state. Even if a site is data-rich such that one can obtain an excellent picture of the sea state at any time from direct observations, there is still interest in forecasting the future state of the sea surface using an efficient numerical model. Numerical wave prediction models, however, are far from perfect. In addition to errors associated with numerical discretization and imperfect initial/boundary conditions, the energy input terms due to wind forcing and dissipation terms due to wave breaking and/or bottom friction are not perfectly known. Given the mentioned imperfections in numerical models as well as inherent noise present in radar observations and the complexity of the nonlinear imaging mechanisms, data assimilation is considered as an extremely important tool to improve estimates of the sea state. An illustration of the problem whose solution is sought in this thesis is presented in Figure 1.1.

Developing an efficient strategy to assimilate radar measurements into the numerical wave model needs a deep understanding of marine radar imaging mechanisms, numerical wave models, and different assimilation techniques. In the following section, a broad literature review of the above-mentioned topics is given.

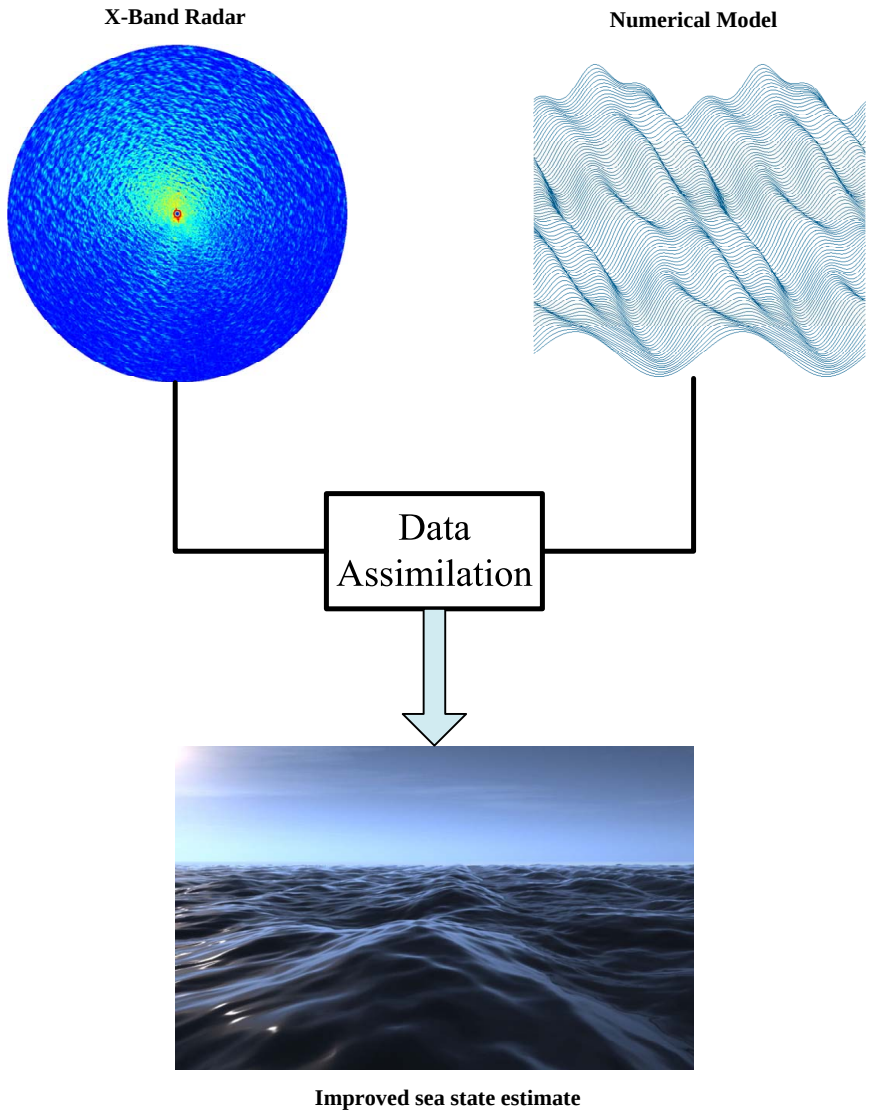

Figure 1.1: Illustration of the research problem.

1.2 Literature Review

1.2.1 Marine Radars

Over the last 40 years, routine sea state measurements have been carried out mainly using moored wave rider buoys. Buoys provide high-resolution measurements in time at a single spatial location with low angular (directional) resolution, and may become inoperational during large storm events such as hurricanes. Considerable interest has been

also shown in the application of remote sensing techniques to the measurement of ocean surface waves and currents. These studies have largely dealt with the use of three forms of radars: SAR (Synthetic Aperture Radar) which is capable of providing high resolution at spacecraft altitude for stationary surfaces, but resolution is degraded for (moving) ocean surfaces. On the other hand, surface velocity effects provide an additional imaging mechanism (velocity bunching) for SAR, although this mechanism is useful over a limited range of conditions; Real-aperture SLAR (Side-Looking Aperture Radar) which is only useful at aircraft altitudes, because of low azimuthal resolution (governed by antenna beamwidth); and HF (High-Frequency) radar. Because of the size of the antennas required, HF radar has only been deployed as a land-based system.

The shortcomings of point sensors can be overcome by utilizing marine radars which map the sea surface with reasonable resolutions in both the temporal and spatial domains. The marine radars used for wind and wave retrievals usually operate at the X-Band (9.5 GHz) with horizontal polarization (HH). The marine radar scans the ocean surface at grazing incidence by rotating its antenna. With each antenna revolution, it collects an intensity image of the backscatter of the ocean surface, producing a temporal radar-image-sequence. The radar's instantaneously received power is proportional to the product of the illuminated area on the sea surface by antenna, and the local scattering cross section per unit area. Radar's temporal resolution depends on the antenna revolution period, while its spatial resolution is a function of the antenna length and pulse length.

The interaction of electromagnetic waves and water waves has been extensively investigated by numerous authors. The fundamental interaction between radar and sea surface is assumed to be Bragg scattering, though at small angles of incidence, specular reflections are also important. For microwave radars, the small wavelength of electromagnetic waves (1-10cm) imply that small ripples on the sea surface in resonance with the incident electromagnetic waves are responsible for the radar backscatter (return) at intermediate incidence angles. Longer surface gravity waves become visible in radar images by four different mechanisms: hydrodynamic modulation of the shorter waves by the long waves, shadowing effect, tilting modulation, and wind modulation effect. Tilting and shadowing are purely geometric effects. Since shorter waves are riding on longer waves, they are tilted with respect to

the horizontal plane. Shadowing is important at low grazing angles when larger amplitude waves block the radar signals. Wind modulation becomes important when the wind-induced roughness on the sea surface changes with time and this will affect the backscattered signal. Some of the radar imaging mechanisms will be discussed in more detail in Chapter 2.

Ijima et al. [34] and F. Wright [82] were among the first to report the use of marine navigation radars for imaging ocean waves. Wright(1965) was able to recognize long swells of lengths 30 to over 400 meters when a local wind roughened the surface of the swells. Oudshoorn [59], Willis and Beaumont [81], Evmenov et al. [23], and Mattie and Harris [53] have also reported wave field images obtained by such radars. These researchers mostly investigated the use of radar images to obtain estimates of the mean wave direction, wavelength, and period.

Hoogeboom and Rosenthal [33] and Ziemer et al. [87] were able to obtain quantitative information from marine radars by digitizing the radar images and finding their two-dimensional Fourier transforms. They showed that two-dimensional spectrum of the digitized radar image was similar to the spectrum obtained from conventional buoy measurements. Hence, it appeared that such radar systems could be successfully used to determine the directional properties of waves and even the full directional spectrum. However, a major problem existed in the interpretation of two-dimensional wave number spectra, whether they be obtained from a ship-board radar or any other imaging mechanism, since a 180 degree directional ambiguity existed in the resulting spectra. Atanassov et al. [3] have shown that this directional ambiguity can be removed by the use of two radar images, separated by a short time interval, together with knowledge of dispersion relation for gravity waves.

Young and Rosenthal [85] developed an analysis technique for a full time series of radar images, each taken at a successive revolution of the radar antenna and using these series of images, found a three-dimensional energy density spectrum through a three-dimensional Fourier transform. In three-dimensional wavenumber-frequency space, the linear dispersion relation in the absence of surface currents can be represented by a shell which is invariant to rotations about the frequency axis. This linear dispersion shell is distorted in presence of a surface current. Young and Rosenthal found the mean currents through a least-squares fit. An advantageous side-effect of these authors' analysis was the very high signal-to-noise

ratio obtained. Signal-to-noise ratio is the ratio of the energy at the spectral peak to the background energy levels well away from the dispersion shell.

Most of the preceding analysis of marine radar images provided information on the non-dimensional directional wave spectrum, i.e. the fraction of the overall wave energy in each frequency and direction band. Estimates of the significant wave height and instantaneous water surface elevation require knowledge of the transfer function between the sea surface elevation and radar backscatter. Alpers and Hasselmann [1] tried to relate the backscattered microwave signals to the surface elevation through a modulation transfer function (MTF) by including the shadowing and tilting effects. Using signal processing in the frequency domain, they were able to improve the signal-to-noise ratios. They used a somewhat simplified representation of the hydrodynamic interaction starting from the action balance equation for short waves. Ziemer and Rosenthal [87] proposed a modulation transfer function from the radar wave spectrum to surface wave spectrum in Fourier space, based on tilting, shadowing, and hydrodynamic effects. They simulated radar images first with all three modulation types, and then with only shadowing influence and found out that nonlinear effects in the imaging process are mainly caused by shadowing effects.

Nieto Borge [9] used X-Band marine radars to find the characteristics of the sea state such as directional spectrum and significant wave height. Due to the nonlinearity of the imaging mechanism of ocean waves, the significant wave height could not be determined directly, so a short calibration phase was needed with an additional elevation sensor (Ziemer and Gunther [**?**]). Basic idea was that the significant wave height was assumed to be linearly correlated to the root square of the signal-to-noise ratio of the radar images. Nieto Borge found a correlation factor of 0.89 between the buoy measurements and the derived significant wave height from a commercial radar (WaMos).

WaMoS (Wave Monitoring System) is one of the most internationally accepted operational marine radar-based wave monitoring systems which is installed on an offshore platform operating in Ekofisk oil field in central North Sea. Initially developed by the German Research Center (GKSS), the system analyzes the sea clutter (changes in the backscattered images) within a range of 3 miles from the platform, and determines the two-dimensional wave spectrum from which the statistical sea state parameters can be derived in real-time.

Nieto Borge et al. [10] later proposed an empirical scheme for the inversion of radar images based on shadowing effect only, which he thought would be dominant for low angles of incidence. He observed a difference between the image spectra from the radar and the corresponding one from buoy, which was due to wave imaging mechanisms discussed before. By using an empirical modulation transfer function which was a power function of the wave number, and using the numerical simulations, this difference was minimized. Nieto Borge's approach consisted of: 3-D Fourier decomposition of the sea clutter time series in order to estimate the image amplitude and phase spectra; High-pass filtering of the spectra to eliminate long-range dependence modulation effects as the radar intensity power decay law with the range; Band-pass filtering of the spectra to extract wave-related components of amplitude and phase spectra. The wave amplitudes are determined by applying the inverse modulation transfer function to the filtered amplitude spectrum. Finally, the sea surface elevation is reconstructed and re-scaled (using the significant wave height) by inverse discrete Fourier transform using the filtered wave amplitude and phase spectra.

Dankert and Rosenthal [18] proposed another empirical inversion scheme. In general, for moderate incidence angles, tilt and hydrodynamic modulations will be dominant, and at grazing angles, shadowing will play a role as well. The above-mentioned modulation mechanisms contribute to the imaging of surface waves whose wavelengths are greater than two times the radar resolution. In this method, no in-situ measurement is needed and no external calibration is necessary. Hydrodynamic modulation is neglected and it is based on the determination of the surface tilt angle in antenna look direction at each pixel of the radar image. Radar cross section(RCS) depends on the mean local depression angle. Deviation of RCS from its mean value represents a local and temporal change of depression angle, which is assumed to be equal to the local ocean surface tilt. The resulting tilt modulation of 'Bragg'waves is described by a two-scale [1] or an improved three-scale model [70].

Dankert et al. [19] described an algorithm for the retrieval of high-resolution wind and wave fields from radar-image sequences. They extracted wind directions from wind-induced streaks, which were approximately in-line with the mean surface wind direction. Their methodology was based on the retrieval of local gradients from the mean radar backscatter image and assumed the mean surface wind direction to be oriented normal to the local

gradient. Wind speeds were then derived from the mean radar cross section. Using neural networks, these authors then established a relation between the radar backscatter and the wind vector. For the verification of their algorithm, they compared wind directions and speeds from nearly 3300 radar-image sequences to in-situ data from a co-located wind sensor. Their inversion algorithm did not need a prior calibration of the acquisition system, and was validated by comparing the resulting radar-derived significant wave heights with those acquired from three colocated in-situ sensors.

Johnson et al. of Ohio State University carried out one-dimensional direct numerical simulations of the radar backscatter from synthetic sea surfaces. Based on the correlation of the radar cross section with large-scale surface height/slope statistics, he was able to improve the incoherent retrievals which were based on linear fit to height/slope. He also examined the RCS-to-surface height correlation as a function of the modulation transfer function phase and found a 45 degree shift to be the best and suggested the combined influence of tilt modulation and shadowing. Johnson applied a filter based on the linear dispersion relation (Dankert/Rosenthal filter) and was able to improve the initially retrieved surface elevation. They also tried a retrieval technique based on the phase difference between scattering measurements in two vertically-separated antennas 'vertical interferometry'. These authors later used a technique to retrieve the surface height profiles from variations in the apparent Doppler frequency (coherent measurements) versus range which required time-stepped simulations to be performed. The latter approach was found to yield reasonable performance both in visible and shadowed portions of the surface.

Due to the complexity of the modulation mechanisms and nonlinearity of the sea state, it is believed that including a data assimilation module using a physics-based numerical wave model could potentially improve the estimates of the ocean wave field from marine radars.

1.2.2 Numerical Wave Models

The study of nonlinear gravity waves has been the subject of numerous theoretical, and experimental investigations. These have classical origins in the work last century of

Boussinesq (1872), Korteweg and de Vries (1895), and Stokes (1880). Today, work on the subject can be divided roughly into two categories, the analysis of steady waves, which progress by translation at constant velocity without change of form, and the time-dependent nonlinear evolution of surface waves. The latter topic is being investigated in this research work.

Most of the early work on the nonlinear problem of a train of waves of constant form propagating steadily over fluid on a horizontal bed were based on asymptotic expansions of flow velocity potential in terms of a small parameter. In Stokes' method, the expansion is performed in terms of the wave steepness parameter. For Stokes expansions to be rapidly convergent, water depth should be large enough. Complementary to Stokes' expansions were techniques based on series expansion in terms of shallowness parameter that give rise to cnoidal wave solutions. Cnoidal wave solutions are applicable to waves which are not too high in water which is not too deep. Neither of the above approaches is uniformly valid in all water depths.

Chappelear [12], and Dean [20] developed numerical methods for fully nonlinear waves. These methods, which may be categorized as "Fourier approximation methods", are based on the use of truncated Fourier expansions of the stream function or velocity potential. The nonlinear wave problem then reduces to solving a number of nonlinear equations for each of the Fourier coefficients, for equi-spaced values of the surface elevation and for quantities characterizing the wave train as a whole, such as wave speed. In the approach of Chappelear and Dean, solutions of these quantities proceeded by a method of successive corrections to an initial estimate in such a way that error in the surface boundary conditions were minimized.

For unsteady waves, Longuet-Higgins and Cokelet [47] pioneered in the application of boundary integral methods for fully nonlinear water waves. However, boundary integral methods are computationally expensive for three-dimensional flow problems. If N is assumed to be the total number of grid points in the domain, the computational cost of these methods is of order $O(N^3)$, since they demand the inversion of full matrices. Multer [56] used Fourier methods in an attempt to solve the fully nonlinear equations, but his results were of finite accuracy and he experienced some trouble with growing high-frequency oscillations. Pseudo-spectral methods for free surface problems were initiated by Fenton and

Rienecker [25], where instead of using a boundary integral formulation, the solution of the three dimensional Laplace equation was written in terms of Fourier series. All horizontal variations were approximated by truncated Fourier series and finite difference is used to evolve the equations in time. The series truncation is the only approximation in Fenton and Rienecker's method and no additional analytical approximation is imposed in this method.

Instead of solving the Laplace equation numerically as in previous methods, there have been efforts to find a formal solution of the Laplace equation analytically so that the velocity potential can be written in terms of two free surface variables: the free surface elevation and the free surface velocity potential. Then using the formal solution of the Laplace equation, it has been shown that the kinematic and dynamic free surface boundary conditions can be reduced to a pair of coupled evolution equations for the two free surface variables. This closed set of equations is written in two horizontal coordinates. Efforts to use the latter approach have been originally made by West et al. [80], and later continued by Matsuno [52], Craig and Sulem [15], Choi [13], Kent [39], and Clamond and Grue [14] among other researchers.

There are two slightly-different classes of Higher Order Spectral Methods (HOSM) by West et al. [80] and Dommermuth and Yue [21]. West et al. expanded the velocity potential at the free surface in Taylor series in terms of the potential at mean sea level, and introduced a vertical derivative operator which multiplies one or two dimensional Fourier coefficients of the velocity potential by the magnitude of the wave number (similar to Choi and Craig and Sulem's operator for deep water condition). Then by directly inverting the expansions, and applying the above- mentioned operator, West et al. were able to find vertical velocity at the free surface in terms of free surface velocity potential and surface elevation, and therefore were able to close the system of equations. They retained terms in vertical velocity up to certain order to ensure that the evolution equations were consistent with the desired order of approximation. Products of the surface variables and their derivatives were calculated in physical space and by taking the (FFT) of the evolution equations, the transformed equations were time-incremented in Fourier space and then using the inverse Fourier transform, the updated surface variables were transformed back to physical space.

Dommermuth and Yue [21] used a slightly different expansion for the vertical velocity. Instead of truncating the expansion to keep the consistency of ordering of evolution equations they kept more nonlinear terms in the expansion which led to some difficulties in the long-time evolution of the waves.

Craig and Sulem [15] presented a spectral method to model time dependent spatially periodic surface waves in water of arbitrary depth. This method was later extended by Smith [73] and Guyenne and Nicholls [29] to variable depths and moving bottoms. In order to close the system of equations, Craig and Sulem expanded the so-called Dirichlet-to-Neumann operator in homogeneous powers of surface elevation, giving a result which is valid uniformly in wave number. Dirichlet-to-Neumann operator relates the boundary values of the velocity potential on the free surface, to its normal derivative on the free surface. This expansion differs from the spectral methods of both West et al. and Dommermuth and Yue, were both velocity potential and surface elevation are assumed to be $O(\epsilon)$ quantities, and the expansion is not uniform in wave number.

The expansion-based wave model used in this thesis, were originally developed by West et al. [80] in Fourier space and deep water condition. This model will be solved very efficiently using a pseudo-spectral method based on the FFT. This will significantly reduce the computational cost from $O(N^2)$ for iterative methods, to $O(N \log N)$.

1.2.3 Data Assimilation

Data Assimilation (DA) is an analysis technique in which all the available information such as intial/boundary conditions and model parameters are incorporated into the model in order to estimate as accurately as possible the state of the oceanic/atmospheric flow. Available information include the observations (radars, satellites, buoys, ...), and physical laws which govern the evolution of the flow (evolution of the free surface). These physical laws are solved using numerical models by discretizing the problem domain. During the last 20 years data assimilation has gradually reached a mature center stage position at both Numerical Weather Prediction centers as well as being at the center of activities at many federal research institutes and universities.

Data assimilation, in the context of the present thesis, is defined as finding the optimal initial/boundary conditions that minimize the difference between the radar measurements and wave model predictions. Data assimilation methods combine the model with observational data to obtain a better estimate of the sea state and predict its short term evolution. Ocean wave field is highly sensitive to the initial conditions. An ideal data assimilation system should produce not only an improved estimate of the wave field, but also an estimate of the associated uncertainty. The challenge is that the number of control variables is large, for example, for a typical three-dimensional numerical wave prediction model the number of variables are of the order $10^5 - 10^6$. Solving the generalized least-squares minimization problem with this large number of variables would be exhaustive.

Data assimilation techniques can, in a broad sense, be divided into sequential and variational methods.

- sequential assimilation, that only takes into account the observations in the past until the time of analysis, which is the case of real-time assimilation systems.
- non-sequential or variational assimilation, where observation from the future can be used, for instance in a re-analysis exercise.

Another distinction can be made between methods that are intermittent or continuous in time. In an intermittent method, observations can be processed in small batches, which is technically convenient. In a continuous method, observation batches over longer periods are considered, and the correction to the analyzed state is smooth in time, which is physically more realistic and consistent. The four basic types of assimilation are illustrated in Figure 1.2.

In sequential methods whenever the model time reaches an instant at which observations are available, the model-predicted state is used as a background which is corrected with the new observations. The integration of the model is then restarted from the updated state, and this process is repeated until all the available measurements are incorporated. In operational NWP systems, the state obtained at the end of the assimilation period, is taken as the initial condition for the following forecast. One of the drawbacks of this method is

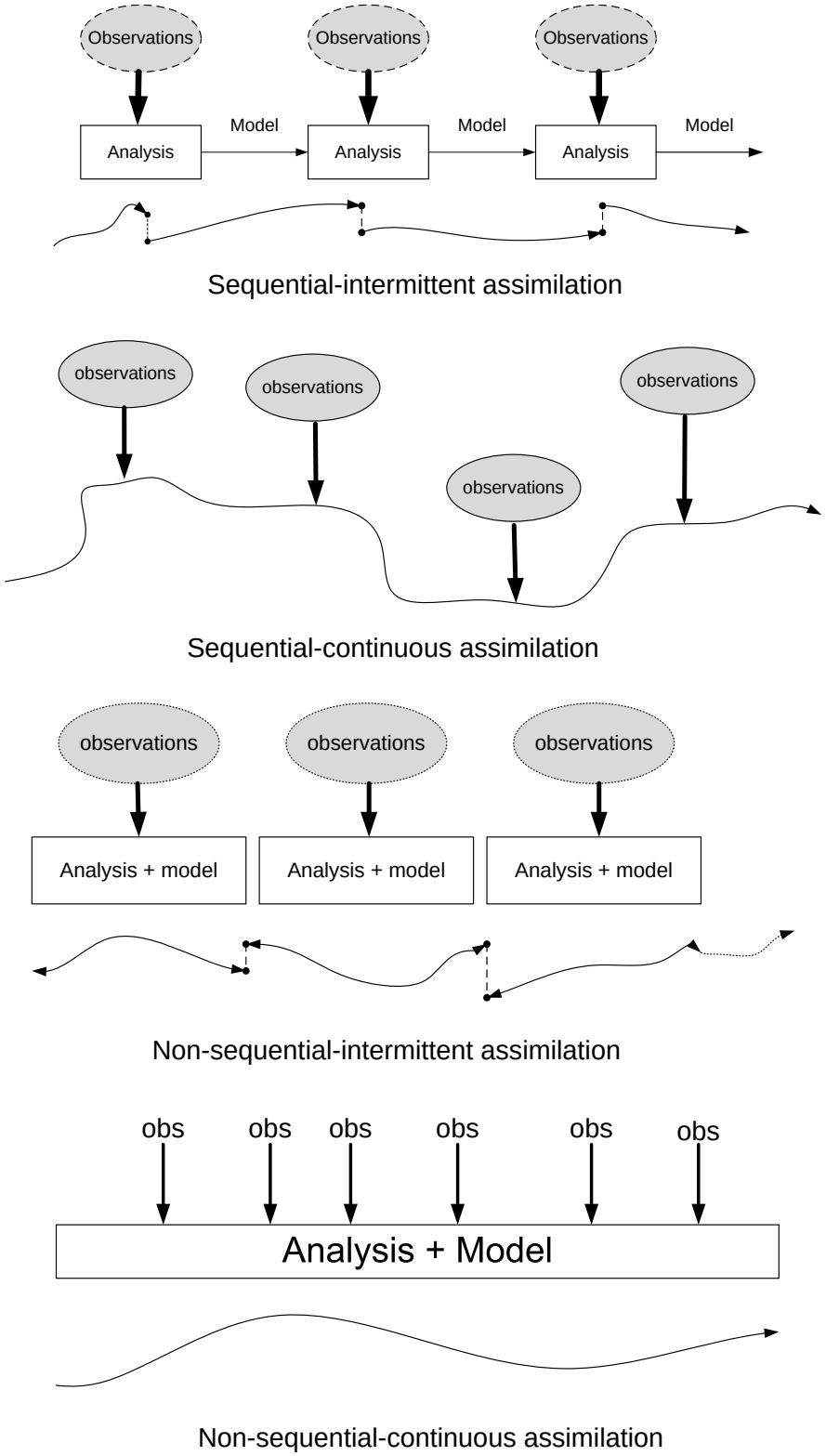

Figure 1.2: Different types of data assimilation.

that each piece of observation influences the estimated states only at later times, and not at previous times (see Figure 1.2).

Sequential methods put the model in a state which is, in general, not consistent with its true dynamics. The model is disturbed and will need some time to reach dynamic consistency. To keep the disturbance as small as possible, only a correction of the model state in the direction of the data takes place (see Figure 1.2). Several sequential methods differ in the degree of consistency of the correction with model dynamics, e.g., Nudging, Successive Correction, Optimal Interpolation, Kalman Filter, and Kalman Smoother ([28]).

The Kalman filter(Gelb [27]) is an optimal method for linear problems and all the others are essentially approximations to it. The assimilation may be carried out continuously or intermittently depending on whether data are available at every model time step or at some specific time intervals. The process includes two steps: analysis and forecast. In the forecast step, the most recent assimilated state is used as initial condition to advance the model forward in time up to the next time observations are available, and then a new analysis is performed. In the analysis step, forecast and new observations are combined to obtain a better estimate of the field. The simplest sequential assimilation method is direct insertion. In this method one directly substitutes the model variables for their corresponding observed values, when available. If the data and model are not sufficiently compatible, problems may arise in the form of spurious oscillations that may contaminate the forecast quality (Daley [17] and Maanotte-Rizzioli et al. [50]).

Another empirical and fairly widely used method for sequential data assimilation is Newtonian relaxation or "nudging" (Hoke and Anthes [32]), which consists of adding to the evolution equations a term that nudges the solution towards the observations. The relaxation time scale is chosen based on empirical considerations and may depend on the model variables. If it is very small, the solution converges towards observations too fast, and the dynamics do not have enough time to adjust. On the other hand, if the nudging time scale is too large, the errors in the model can grow too much before the nudging becomes effective. Zou et al. [89] made optimal parameter estimations of the nudging time scale. Although this method is not generally used for large-scale assimilation, some groups use it for assimilating small-scale observations.

The next simplest sequential method is referred to as "successive corrections", which is usually less intrusive on the model dynamics. In this method, a weighting function that decays monotonically with the spatial/temporal distance between model variable and observation position, is used. Several observations will influence the analyzed value depending on the decay scales of the weighting function. The weighting function may be kept constant through the iterations (Bergthorsson and Doos [7]), or changed (by modifying its decay scale or radius of influence), to get a better representation of the smaller scales in the analysis.

In the Kalman filter, there is an extra step which involves an evolution equation for the forecast error covariance matrix, besides the forecast and assimilation steps. The perfect model assumption usually made in variational methods as discussed below, can be relaxed in this case. A time evolving forecast error covariance is very useful, considering that in both sequential and variational methods, a problem arises of how to weight previous, present, and future information to obtain the best estimate. The Kalman filter (or its extensions such as the extended Kalman filter or Kalman smoother [27] automatically provides those weights via the evolving forecast error covariance, however the computational demands of the Kalman filter are so high that its application to large and even medium-scale models is impractical. The search for better approximations to the Kalman filter that can simulate better the time evolution of forecast errors, has led to a current research area of great interest (Fukumori and Malanotte-Rizzioli [26]).

In variational methods, all observations over the assimilation period will be used. In these methods a cost function is usually defined as the difference between radar measurements and model predicted values over a finite time interval, with appropriate weighting factors. One looks for the model solution that leads to a minimum cost function. Since the model solution is uniquely defined by the corresponding initial conditions at the beginning of the assimilation period, these initial conditions are taken as the control variables, i.e., as the variables with respect to which the minimization is effectively performed.

The introduction of conjugate gradient method by Fletcher-Reeves in the 1960's, marked the beginning of the field of large-scale nonlinear optimization, since it requires storage of only a few vectors, and could do so much more rapidly than the simpler steepest descent method. Conjugate gradient methods are still one of the best choices for solving very large

problems with relatively inexpensive objective functions (Liu and Nocedal [45]). They can also be more suitable than limited memory methods on several types of multi-processor computers. Within a given iteration of the conjugate gradient method, an estimate is made of the best way to change each component of the control vector, so as to produce the maximum reduction of the cost function, by finding the gradients of the function with respect to the control variables and combining this gradient with information from the previous iterations to produce a search direction. The search direction is an estimate of the relative change in each component of the control vector to produce the maximum reduction in the cost function(Navon and Legler [57]).

Newton and quasi-Newton methods have quadratic rate of convergence, and super-linear rate of convergence, respectively, but require storage of the Hessian matrices (matrix of second derivatives) of size N×N at each iteration. Quasi-Newton methods are based on the idea that an approximation to the curvature of a nonlinear function can be made without explicitly forming the Hessian matrix. The major advantages of the quasi-Newton method over the traditional Newton method are that the quasi-Newton method requires only first derivatives, whereas for the Newton method the user must supply second derivatives, and that it has a better computational and storage efficiency for large-scale systems.

Method of Broyden-Fletcher-Goldfarb-Shanno (BFGS) is very efficient but is not a good candidate for large-scale optimizations required in variational data assimilation due to the fact that it requires the storage of the approximation to the Hessian matrix. The recent developments of limited memory Newton-based methods have narrowed the class of problems for which the conjugate gradient methods are recommended. Limited memory BFGS (or L-BFGS) is one of the most efficient methods currently employed operationally for large-scale unconstrained minimization problems [45]. It uses an economic number of vectors (between 5 and 7) and does not require any matrix storage.

Truncated Newton methods are also very suitable for large-scale problems and require only the storage of functions and gradients. There have been efforts to modify these algorithms by using the first- and second-order adjoint techniques. Wang et. al [77] calculated the gradients using the first-order adjoint technique and calculated the Hessian-vector products using the second-order adjoint method which was computationally comparable to using

direct finite difference approximation. However, the former gives the exact Hessian-vector product, while the latter provides only an approximation to the Hessian-vector product if the difference parameter is taken to be the square root of the machine accuracy. Wang et. al [77] concluded that their so-called method of Adjoint Truncated Newton (ATN) performed better than truncated Newton or the L-BFGS algorithms both in terms of CPU time and number of iterations, and could be easily embedded in variational assimilation algorithms.

Wang and Droegemeier [78] later proposed to use the so-called Tangent Linear Model (TLM) to find the Newton search direction, instead of using the gradient as previously discussed. This method is referred to as Adjoint Newton Algorithm (ANA). Well-posedness of the TLM equation is a necessary condition in order for this method to have a quadratic rate of convergence. Hybrid methods have been also tested with ceratin amount of success combining the L-BFGS with truncated Newton method (see [54] and [55]).

Above-mentioned minimization methods belong to the larger class of local minimization algorithms which find the local minima of a function assuming the convexity of the function in a neighborhood of the local minimum point. Global methods such as Simulated Annealing (SA) and Hit and Run (HR) were also used by numerous authors. SA is a stochastic algorithm that simulates the physical annealing process in which a substance is melted and then slowly cooled down in search of a lower energy configuration. Instead of performing a gradient descent, a line search method is used to locate the next configuration. In large-scale minimization problems the global methods are however out-performed by local methods because of their high computational cost. However, there should be a mechanism to investigate the uniqueness of the solution in such algorithms.

In variational algorithms the optimal initial condition is obtained through an iterative procedure, each step of which requires the explicit knowledge of the gradient of the cost function with respect to the initial condition. This iterative procedure repeats until the magnitude of the gradient becomes less than a pre-defined criterion. The variational formulation is suitable for large-scale problems and is one of the most advanced algorithms that has been used operationally.

The most efficient minimization algorithms such as conjugate gradients or quasi-Newton require gradient information. One way to calculate the gradient is the direct method based

on finite difference approximation in which each control variable (initial condition in our case) has to be perturbed and the basic evolution model needs to be integrated N times, once for each of the discrete values of the initial condition. For a problem with only a few control parameters, finding these gradients is not usually too difficult, but for the problem considered in this thesis with a large number of control variables and high-resolution measurements, and considering the fact that the forecast needs to be made in near-real time, finding a more efficient approach to calculate the gradient would be a crucial task.

The advance by Le Dimet and Talagrand [43] was to show that the gradient of the cost function with respect to all control variables could be obtained from one single integration of the adjoint of the evolution equations backward in time, and that it was not necessary to perturb each of the components of the initial conditions, one at a time. The most straightforward application of the adjoint technique requires three model integrations per iteration. First, the equations are integrated over the assimilation period. Then the adjoint equations are integrated backwards in time to $t = 0$, forced with the difference between the observations and the forward model values. This gives the gradient of the cost function with respect to all the control variables, but does not indicate how to adjust the parameters in a descent algorithm, so a third integration is normally needed, using the forward equations in order to gauge a step length. The control parameters are then updated and the process is repeated. Whether the variational method is of practical value or not depends on how rapidly the convergence can be achieved.

The use of adjoint equations in mathematics and engineering has become increasingly widespread. However the theory of such equations remains relatively new. Marchuk [51] describes the early history of adjoint equations. He credits the conception of adjoint operators to Lagrange, but notes that the utility of adjoint equations was not realized until 1920s when physicists were developing quantum mechanics. Then, in the late 1950s, adjoint operator theory was further developed when it was applied to nuclear reactor theory.

Since the 1950s, adjoint equations theory has developed in conjunction with functional analysis, calculus of variations, and sensitivity analysis and applied to a wide range of physical problems such as parameter estimation in groundwater and tidal flows, turbulence control [8], and shallow water flow control [71], to data assimilation in meteorology [38].

These equations have proven to be a quick and reliable way to extract large amounts of information from a limited data set. After the seminal paper of Le Dimet and Talagrand [43] in 1986, these equations have been operationally used in NWP models worldwide.

The whole role of the adjoint model is simply to calculate the gradient of the cost function with respect to the control variables. This derivative exists except when there are discontinuous processes. Examples of such processes are rainout (in meteorology), and wave breaking (in oceanography). However if such discontinuities can be smoothed, then the adjoint model could still exist. In practice, it is necessary to simplify or smooth physical processes with threshold or on-off switches for the purpose of the adjoint calculation. The fully nonlinear processes are however modeled in the forward equations.

The adjoint method in contrast with sequential methods, always guarantees full consistency with the dynamics. For linear models, the Kalman Smoother ([6]) is equivalent to the adjoint method. Applying the adjoint method would bring the model trajectory as close as possible to the data by varying control variables (see Figure 1.3).

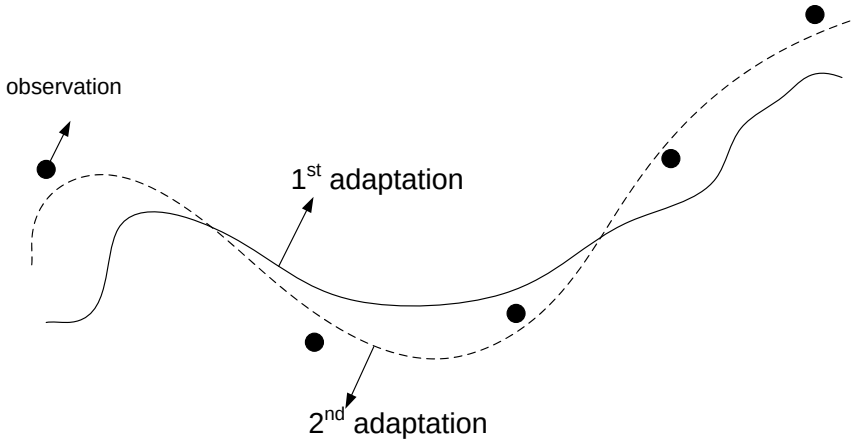

Figure 1.3: Schematic representation of variational methods. Two trajectories differing in the value of the cost function are displayed.

Adjoint methods can be useful whenever the sensitivity of a scalar cost function with respect to model inputs is required, and have application in fields outside of data assimilation, such as predictability or ensemble forecasting, or targeting observations (finding where to place observations for most impact on the forecast).

1.3 Dissertation Overview

This dissertation is composed of 6 chapters. Chapter 2 reviews some of the marine radar imaging mechanisms and discusses the limitations and complexities associated with radar retrieval process. In chapter 3, starting from original Euler equations and based on the Hamiltonian system of nonlinear surface waves, the forward wave evolution model is derived in constant depth for one-dimensional and two-dimensional surface gravity waves in absence of surface pressure and surface tension; Approximate evolution equations are then derived up to third-order in terms of surface elevation and tangential velocity/velocity potential at the free surface. The energy conservation will be also addressed.

In chapter 4, the pseudo-spectral approach to solve the one-dimensional and two-dimensional evolution equations is introduced; One-dimensional approximate evolution equations are validated with the exact fully nonlinear solutions for steady and progressive periodic waves; The ability of the derived model in predicting nonlinear wave-wave interactions such as Benjamin-Feir instability problem will also be discussed and model solutions are compared with three-dimensional laboratory experiments; Three-dimensional model is validated using the exact fully nonlinear solutions for steady short-crested waves.

In chapter 5, the proposed variational data assimilation scheme using the adjoint technique to find the gradients is introduced; Adjoint equations are derived for the evolution equations up to third-order. One-dimensional assimilation scheme is validated using numerous tests such as:

- A simple nonlinear model with exact analytical solution.
- A simple nonlinear wave model (KdV).
- One-dimensional synthetic sea surface generated form JONSWAP spectrum.
- One-dimensional synthetic radar data from combined electromagnetic-hydrodynamic simulations, provided by Ohio State University for different grazing angles and wind speeds.

Two-dimensional assimilation scheme is validated using the two-dimensional synthetically generated sea surface form JONSWAP spectrum and field data collected at the southern coast of Alaska in April 2006. Preliminary results of a new variational scheme to estimate the slowly varying surface currents are also presented at the end of Chapter 5. Chapter 6 will conclude this dissertation by outlining the research findings, contributions, and recommendations for improvements.

CHAPTER 2

Ocean Waves and Radar Imaging Mechanisms

2.1 Introduction

Ocean waves are typically measured at single points with one-dimensional or two-dimensional in situ sensors, e.g., wave rider buoys or laser sensors. These sensors typically provide the time series for surface elevation, velocities, and accelerations, with a high temporal resolution at a certain location. In situ sensors for wave measurements are adequate to measure areas with a somehow spatial homogeneous conditions, however in many cases such conditions don't exist. The sea state parameters, which are measured by the 1-D and 2-D sensors in such areas, are hardly representative of the wave situation in the neighborhood, and in the case of 1-D sensors, there is a lack of directional information on the sea state. In addition to these shortcomings, deployment of buoys is limited by a maximum current speed and water depth.

With the growing need for the sea state information for marine operations, different technologies have been developed with different applications. Special interest has been shown recently in the use of remote sensing techniques to measure ocean surface waves and currents. One technique to remotely measure the sea state is based on the use of conventional X-Band marine radars used generally for traffic control and navigation purposes. The shortcomings of the point sensors can be effectively overcome by utilizing such radars, which are able to map a large area on the ocean surface with a reasonable spatial and temporal resolution which specifically makes them suitable to collaborate with the numerical wave

models. These systems also have the capability of measuring the backscatter from the sea surface under most environmental conditions.

2.2 Ocean wave dynamics

Waves on the sea exist over a range of scales from swell to capillary waves, and they propagate over a range of directions determined not only by the local wind but also by propagation into the observing area from distant locations. The simplest specification of the sea surface is in terms of the wave spectrum $S(\mathbf{k}, \omega)$, a function of both wave number $\mathbf{k}$, and frequency ω, which is the Fourier transform of the covariance of the sea surface elevation η at two locations in space and time:

$$S(\mathbf{k}, \omega) = \frac{1}{(2\pi)^3} \int \int \langle \eta(\mathbf{x}, t), \eta(\mathbf{x}+\mathbf{r}, t+\tau) \rangle \exp\left[i\left(\mathbf{k}\cdot \mathbf{r} - \omega\tau\right)\right] \mathrm{d}\mathbf{r}\mathrm{d}\tau \tag{2.1}$$

where the angled braces denote an ensemble average. In reality, the covariance $\langle \eta, \eta \rangle$ and the spectrum S are functions of space and time, but the scales over which these variations occur, are generally much larger than the scales of variation with $\mathbf{r}$ and τ and the wave fields can be regarded as locally homogeneous but varying gradually form place to place. Mean square surface elevation can be obtained from (2.1):

$$\bar{\eta^2} = \int \int S(\mathbf{k}, \omega) \mathrm{d}\mathbf{k}\mathrm{d}\omega \tag{2.2}$$

The spectrum of the instantaneous sea surface is obtained by integrating (2.1) over all frequencies:

$$\Psi(\mathbf{k}) = \int S(\mathbf{k}, \omega) \mathrm{d}\omega = \frac{1}{(2\pi)^2} \int \langle \eta(\mathbf{x}, t), \eta(\mathbf{x}+\mathbf{r}, t) \rangle \exp\left[i\mathbf{k}\cdot \mathbf{r}\right] \mathrm{d}\mathbf{r}, \tag{2.3}$$

and also,

$$\bar{\eta^2} = \int \Psi(\mathbf{k}) \mathrm{d}\mathbf{k}, \tag{2.4}$$

The expressions stated so far do not reflect anything about the wave dynamics. The simplest dynamical statement about the gravity waves is that, when the wave slope is small, their intrinsic frequency in a frame of reference moving with the underlying deep water is given by:

$$\sigma = \sqrt{gk} \tag{2.5}$$

which is the so-called dispersion relation. The ocean waves are dispersive, with longer components traveling faster than shorter ones. The phase speed is given by $c = \sigma/k = \sqrt{g/k}$. When the wave slope $\epsilon = ka$ of a wavetrain of local amplitude a is not small, nonlinear wave-wave interaction effects modify the dispersion relation. There is the fractional increase in the wave speed of $1/2\epsilon^2$ noted by Stokes in nineteenth century, and harmonics of the basic wave appear that also propagate with its phase velocity. There are no good indications that the expression (2.5) is not an adequate approximation when the wavelength is less than approximately half the water depth.

It is important to recognize that σ in (2.5) is the intrinsic frequency and that if the water is moving relative to a fixed point, whether as a result of a current $\mathbf{U}$, or for short waves, as a result of the orbital velocity of long swells, the observed or apparent frequency ω, measured at a fixed point, will include a Doppler shift:

$$\omega = \sigma + \mathbf{k}\cdot\mathbf{U}, \tag{2.6}$$

Among the short wave components in a wind-generated wave field, the orbital velocities of the dominant waves maybe considerably larger than the intrinsic propagation velocity of the short waves so that these Doppler effects are large. A single short wave group with intrinsic frequency σ is spread over a considerable range of apparent frequencies ω, and this can make the identification of the spectral density $S(\mathbf{k},\omega)$ difficult, especially at high frequencies, with the dynamical characteristics of the short wave trains.

2.2.1 Wave Interactions

Ocean waves interact among themselves and with the environment in a variety of ways, but the interactions can be conveniently classified in two major categories:

- Weak resonant interactions explored by Phillips [63] and Hasselman [30] among others. In waves of small slope, the first nonlinear effects appear as a regular perturbation to the linear solutions, distributed over the whole wave field, and not localized in space or time. The response of waves to these perturbations is likewise slow and distributed, taking many wave periods to be significant, though the cumulative effect may be large. They lead to a considerable and interesting class of phenomena such as energy exchanges among different modes, Benjamin-Feir instability of a single wave train, and the existence of envelope solitons. In all such phenomena, the time scale of the evolution is much larger than the wave period, i.e., the waves are locally more like linear waves, but as a result of weak interactions, they change slowly in space/time.

- Wave breaking with the formation of whitecaps, deformation of short waves riding on swells, and the rapid response of waves to the changes in currents. In this class, changes occur rapidly, with the time scale of the reaction to the disturbance being in effect instantaneous. From the mathematical point of view, these effects cannot usefully be considered as small perturbations of a basically linear wave, and many of the common techniques such as Fourier analysis are not applicable.

Waves on the surface of the ocean receive their energy from the wind. The most useful characterization of the wind energy input is probably in terms of a time scale T_w over which the energy density increases by a factor e in the absence of dissipative processes such as breaking. It is a function of wind speed U_w (or more properly the friction velocity, $u_* = (\tau/\rho_a)^{1/2}$, where τ is the surface wind-induced shear stress and ρ_a the air density; $u_* = C_D^{1/2} U_w$, where C_D is the surface drag coefficient). It also depends on the wavelength of the components being considered. An approximate representation of T_w can be written as (Phillips [64]):

$$T_w \sim 3(c/u_*)^2(\text{wave periods}). \tag{2.7}$$

If the wind suddenly begins to blow, or if the wave components being observed are removed by blockage or deflection/reflection by a current, this gives an estimate of the time needed to re-establish the wave field. The corresponding spatial scale is obtained by multiplying the group velocity $c_g = 1/2c$ by equation (2.7).

2.2.2 Saturation

A given wave component does not continue to grow indefinitely. It may lose some energy due to weak wave-wave interactions, but ultimately its energy density is limited by wave breaking. With continuous wind input, waves will break sporadically, the local instabilities removing energy from the waves and restoring stability. Such waves in an active wind-generated sea are said to be saturated; Increased energy input from the wind does not appreciably increase the wave amplitude or energy density but will increase the rate of wave breaking. Under such conditions, the spectral density of components significantly shorter than the spectral peak is independent of u_* and can be a function only of the wave number k or frequency σ and g. Therefore, in the dimensional world (Phillips [64, 62]),

$$\Psi(k) \propto k^{-4}, \tag{2.8}$$

The frequency spectrum of the surface elevation at a fixed point (the integral of equation (2.1) over all k) is likewise expected to be:

$$\Phi(\omega) = \beta g^2 \omega^{-5}, \tag{2.9}$$

where $\beta \approx 10^{-2}$ under most oceanic conditions.

2.3 Radar Imaging Mechanisms

Most of the marine radars used for wind/wave retrieval operate at the X-Band (9.5 GHz) with horizontal (HH) polarization. They have the capability of measuring the backscatter from the ocean surface in most weather conditions, independent of lighting condition. The marine radar scans the sea surface at grazing incidence by rotating its antenna. During each rotation, the radar emits many short electromagnetic pulses (on the order of 2-5cm) and receives the backscattered electromagnetic energy from the ocean surface. With each antenna revolution, the radar collects an intensity image of the backscatter of the ocean surface (Radar Cross Section (RCS)), producing a temporal radar-image sequence.

It has been shown that the radar cross section (RCS) is strongly dependent on wind speed([44] and [31]) and wind direction([31] and [75]). At grazing incidence (Θ >70 degrees) and vertical (VV) polarization, the main backscatter mechanism at the ocean surface is Bragg scattering ([84]). At grazing incidence and HH polarization, the RCS predicted from Bragg theory is too low . Lyzenga et al. [49] added the effect of wedge scattering as an important additional backscatter mechanism at grazing incidence and HH polarization. The sea surface is imaged by the radar, because the RCS of the ocean surface is modulated by the long surface gravity waves, which are within the resolution of the radar. This modulation of the RCS is mathematically described for local amplitudes by the Modulation Transfer Function (MTF), which is defined as the expansion of the RCS for the spectral amplitudes of the wave field $\hat{\eta}(\mathbf{k})$ (Alpers et. al. [2]),

$$\sigma_0 = \bar{\sigma}_0 + \delta\sigma_0 = \bar{\sigma}_0 \cdot \left(1 + \int M(\mathbf{k}) \cdot e^{i(\mathbf{k}\cdot\mathbf{r} - \omega(\mathbf{k})t)} \mathrm{d}\hat{\eta}(\mathbf{k})\right). \tag{2.10}$$

with the mean RCS, $\bar{\sigma}_0$, the modulation part, $\delta\sigma_0$, the wave number vector, $\mathbf{k}$, and the angular frequency $\omega(\mathbf{k})$. For the present application, MTF is a sum of the following contributing processes:

- hydrodynamic modulation
- tilt modulation

- Shadowing effect
- Wind roughness effect

The wind effect is based on the variation of the wind friction velocity along the ocean surface, which generates the small-scale roughness of the sea surface and raises the variance of the mean RCS $\bar{\sigma}_0$. By integrating a radar-image sequence over time, signatures with higher variability in time (like surface waves) are averaged out. Only static patterns such as the shadows from the towers or other obstacles and the wind signatures remain visible. The mean RCS of a radar-image sequence consists mainly of the mean wind information.

Tilting modulation is a purely geometric effect which leads to a higher backscatter from a wave front which is directed toward the radar. The longer waves tilt the small facets from the horizontal plane toward or away from the radar. This leads to a change of local incidence angles and therefore to a change of radar backscatter, which increases with decreasing the incidence angle. The strongest modulation occurs for the tilt component of the ocean surface waves in antenna viewing direction or 180° to it. Therefore if the wave crests are parallel to the antenna viewing direction, there would be no modulation contribution.

At moderate incidence angles ($20< \Theta <70$), the modulation is mainly due to the tilting and hydrodynamic modulation ([2]), while at grazing incidence, the modulation stems in addition from shadowing of the radar beam due to the ocean surface waves. This phenomenon is also purely geometric and highly nonlinear, and prevents part of the imaged sea surface to be detected by the radar. In this case, besides the swell wave slope, the wave amplitude will also play an important role in detecting the sea surface by the radar. These modulation mechanisms of the small-scale surface roughness lead to the imaging of the waves that are greater than twice the radar resolution. An illustration of different mentioned imaging mechanisms is displayed in Figure 2.2.

Shadowing plays a very important role in the current application of ship-board radars with small incidence angles ($1 - 2°$).

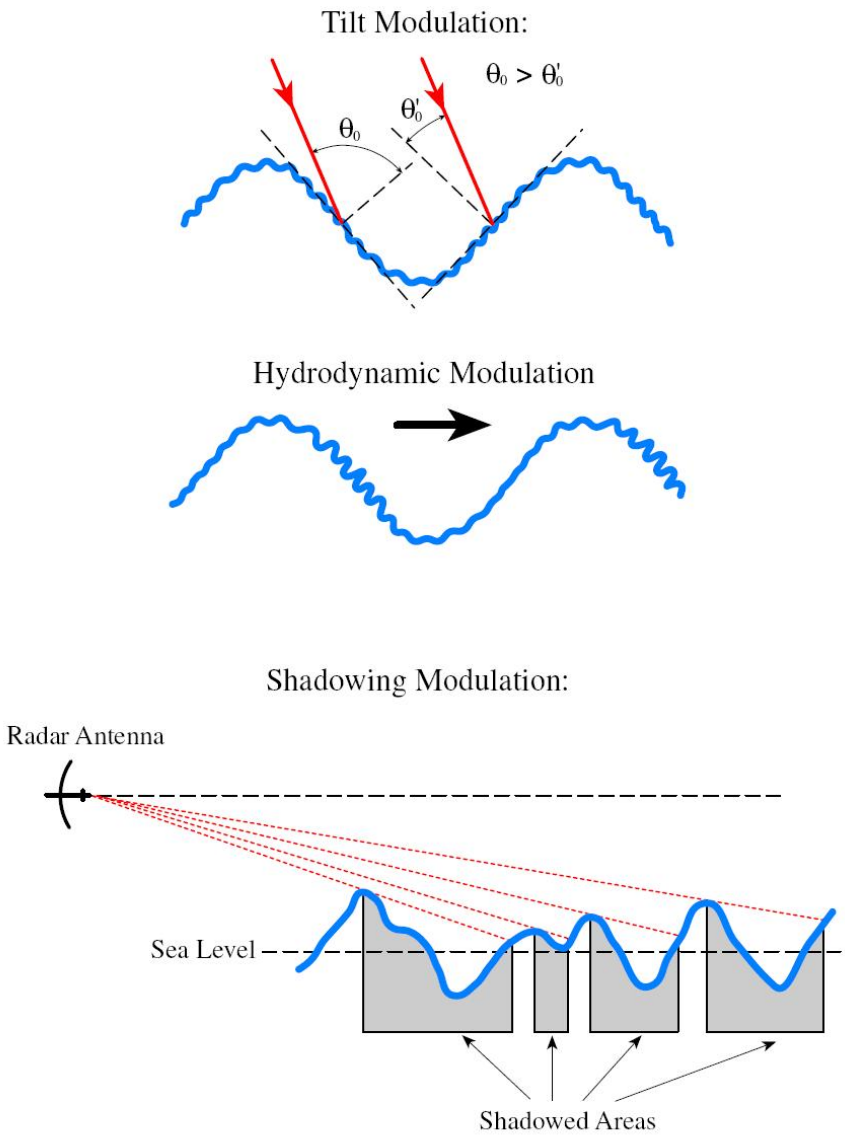

Figure 2.1: Radar Imaging Mechanisms.

2.3.1 Hydrodynamic modulation: The modification of short waves by longer waves

The short wave components are convected and distorted by longer waves or swell. Short wave energy density and amplitude are in fact concentrated near the crests of the long waves and somewhat depleted near the troughs. In a wind-wave field, the short waves may then be saturated only locally, near the long wave crests and somewhat under-saturated elsewhere. The long waves propagate faster than the short waves, so that a given group of short waves, being overtaken by a swell crest, may become saturated with local breaking events, then as the crest moves past, become unsaturated as it slips into the trough. It continues, however, to receive energy from the wind, and, if the input is sufficient, it is ready again for more occasional wave breaking just before and at the next crest of the swell.

This local saturation produces a modulation in the return signal of the microwaves sent by the radar, which in turn enables the long wave pattern to be discerned if its wavelength is greater than about twice the discrimination distance. The modification of short wave structure by long waves was first analyzed correctly by Longuett-Higgins and Stewart [46], but their analysis was limited to conditions in which the swell amplitude is less than the short wavelength. Numerical calculations that are free of this restriction were performed by Longuett-Higgins [48], and, if the ratio of long-to-short wavelength is large, simple asymptotic methods may be used.

A simple geometry of the short waves riding on a swell is shown in Figure 2.2. Axes x and y are chosen in the direction of swell propagation and along the crests, respectively. ϕ is the angle between the viewing direction and the direction of propagation of the swell, and θ, the direction of the local wind relative to the viewing direction. The short, locally generated short waves are assumed to be riding over the swell. The local wavelength of a wave train and its direction of propagation vary as a result of the variable orbital velocities and vertical accelerations produced by the swell.

The modulations are strongest when $\phi = 0$ and disappear when $\cos\phi << 1$, that is, when the short waves are running almost along the crests of the swell. It is interesting to note that short waves propagating exactly along the swell crests are deformed somewhat since the

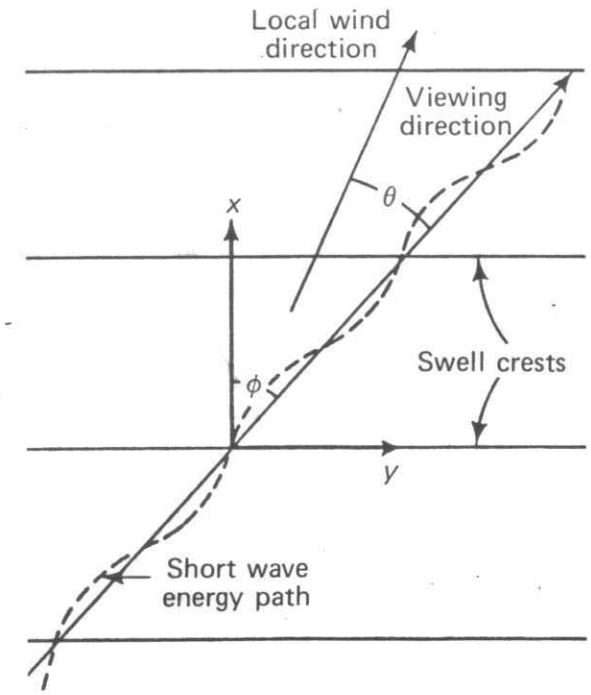

Figure 2.2: Short wave trajectories over the long waves.

effective gravitational acceleration experienced by these short waves is smaller there, and the propagation speed smaller than in troughs. Between long wave crests when the short waves are unsaturated, the dynamics of the interaction are expressed most simply by the conservation of action spectral density of the short waves. The amplitude of modulations $\delta\Psi$ in short wave spectral density at a fixed wave number referred to the mean is (see [64]):

$$\frac{\delta\Psi}{\Psi} = \left[\frac{9}{2}\cos(\phi-\theta) - \frac{1}{f(\theta)}\frac{\partial f}{\partial\theta}\sin(\phi-\theta)\right] \times \left(\frac{C\cos\phi - \frac{c}{2}}{C - \frac{c}{2}\cos\phi}\right)\epsilon. \tag{2.11}$$

The amplitude of the modulation in the short wave action spectral density at a fixed wave number is proportional to the swell slope ϵ, and according to Bragg scattering theory, the amplitude of the modulations in the return signal intensity relative to the mean is equal to $\delta\Psi/\Psi$. The angle ϕ between the direction of propagation of the swell and the viewing direction can be determined directly from radar imagery, but the direction of the wind needs extra information. The phase speed C of the swell can be deduced from the wavelength of the observed swell pattern, and the mean phase speed c of the scatterers by a knowledge of the Bragg wavelength.

The local wind must be sufficiently strong to generate locally short waves at the Bragg scattering wavelength but not so large that the dominant locally generated waves have orbital velocities comparable with those of the swell. In this latter case, the modulations of the short waves by the longer, locally generated waves may be dominant, but being on a scale smaller than the resolution of the radar. Beal [4] gives a range of $2m/s < U_{10} < 10m/s$, over which the swell-induced modulations have been detected. The swell can be imaged successfully when there is a substantial component of the swell traveling along the line of sight of the radar.

The first factor in (2.11) involves the spectral distribution of the locally generated short waves that provide the surface scatterers, the first term representing the consequences of variations in the wave number magnitude and the second in local short wave direction. The directional distribution of the short wave components $f(\theta)$ is not well established and different functions have been proposed and used by different authors.

Since the intensity of the modulation in the spectral density of the sampled waves is proportional to the swell slope and a function of the angle of observation relative to the swell, the modulations in return signal potentially provide a means for measuring the amplitude of the swell or long, dominant waves directly from the imagery. However, careful calibration by comparison with the ground truth data (for example from the buoys and pressure gauges) would be required before swell measurements could be interpreted with confidence.

Several other environmental phenomena would also affect the surface wave pattern, such as shear currents, spatially varying surface currents, internal waves, and currents associated with submarine topography in shallow regions, to name a few.

2.3.2 Tilt modulation

Tilting modulation becomes increasingly important for low grazing angles (high incidence angles). Previous numerical studies with ocean-like surfaces for incidence angles ranging from 0° to 70°, have generally demonstrated the success of the composite surface model in this angular region [36]. Studies for greater than 70° incidence have been more limited [68] due to the fact that use of a tapered wave incident field to avoid edge effects

in finite-size surface simulations results in a loss of angular resolution in scattered fields as grazing incidence is approached. Angular resolution can be regained by using longer surface profiles in the simulation so that tapered wave spot sizes become larger on the surface, but the computational costs increase as well.

Johnson [35] applied a numerical approach which enabled larger surface profiles to be considered so that backscattering for incidence angles greater than 85° could be calculated. The spectrum chosen for the ocean surface was a Pierson-Moskowitz spectrum. Simulations were performed using the impedance boundary condition (IBC) approximation to capture surface conductivity effects. Initial comparisons with small perturbation method (SPM), or Bragg model [66], and composite surface theory [83] showed an excellent agreement between the numerical results and the SPM predictions (within 1 dB at all angles less than 87° and within 1.6 dB at 89°) in the low rms height case. Figure 2.3 (left) compares computed horizontal (HH) and vertical (VV) backscattered cross sections for the wavenumber range 0.036 rad/m - 146.6 rad/m, with those predicted by SPM. The right plot compares numerical model results in the high rms height case with those of the composite surface model (with three different choices for the cutoff wavenumber parameter). This figure clearly shows that the use of composite surface model at near grazing angles requires an improved understanding of the cutoff wavenumber parameter in this angular region.

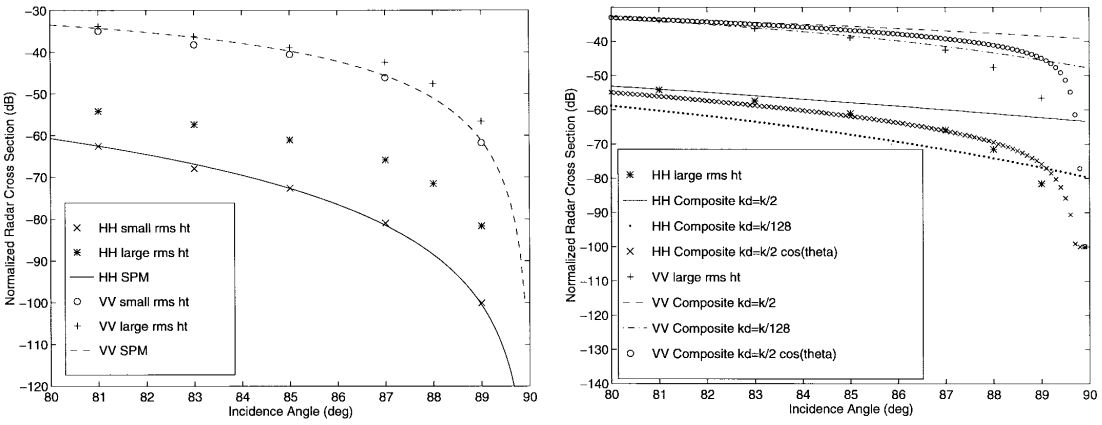

Figure 2.3: Left: Comparison of numerical and SPM backscattering predictions for small rms height case ($k_{dl} = 146.6 rad/m$, $k\sigma = 0.088$) and large rms height case ($k_{dl} = 0.036 rad/m$, $k\sigma = 14.25$); Right: Comparison of numerical and composite surface model backscattering predictions for large rms height case. From [35]

Comparisons with numerical simulations have shown that perturbation theory in the small rms height limit provides accurate predictions at up to 89° observation, while studies in larger rms height cases, show problems in the standard analytical models as grazing incidence is approached. However, using an appropriately scaled Bragg model was shown to provide reliable predictions for a broad range of incidence angles [35].

CHAPTER 3

Wave Evolution Model

3.1 Introduction

Pseudo-spectral methods for water wave problems were initially investigated using time-dependent Fourier-series method initiated by Fenton and Rienecker [25], where, instead of using a boundary integral formulation, the solution of the three dimensional Laplace equation was written in terms of Fourier series. This approach was then greatly improved by Dommermuth and Yue [21], who expanded the free surface boundary conditions about the mean surface and then found the solution of Laplace equation recursively to a desired order of approximation by using a pseudo-spectral method based on Fast Fourier Transform (FFT). This method is referred to as High-Order Spectral (HOS) method.

Instead of solving the Laplace equation numerically as in previous methods, there have been efforts to find a formal solution of the Laplace equation analytically so that the velocity potential can be written in terms of two free surface variables: the free surface elevation and free surface velocity potential. Then, using this formal solution, it has been shown that free surface boundary conditions can be reduced to a pair of coupled nonlinear equations for the evolution of the two free surface variables. Efforts to use the latter approach have been made by West et al. [80] (see Appendix B), Matsuno [52], Craig and Sulem [15](see Appendix A), Choi [13], and Clamond and Grue [14] among others.

Tanaka [74] pointed out differences between the two original versions of HOS, i.e., West's formulation and that of Dommermuth and Yue, concerning the series expansion for the ver-

tical velocity on the free surface, and its subsequent treatment in the free surface evolution equations. West et al. truncated the free surface equations at consistent nonlinear orders in order to conserve the Hamiltonian structure of waves. In contrast to the series used by Dommermuth and Yue, those used by West et al. are naturally ordered with respect to the steepness parameter ϵ. Thus the Dommermuth and Yue formulation is not consistent, after being truncated, with the underlying Hamiltonian structure of the canonical pair of free surface equations.

Craig and Sulem expanded in Fourier space the so-called Dirichlet-to-Neumann operator that determines the normal velocity on the free surface from the velocity potential at the free surface, while other works have focused on finding the evolution equations in physical space. Matsuno [52] and Choi [13] developed second and third order approximate equations respectively, while Clamond and Grue [14] formulated the higher order effects using a boundary integral representation.

In this chapter, the free surface evolution equations are first derived for surface elevation and free surface velocity potential, and are then extended to free surface elevation and free surface tangential velocity. It is believed that the latter is more stable. The final form of these evolution equations can be shown to be equivalent to Craig and Sulem's formulation (Appendix A) and will be also shown to reduce to West et al.'s formulation for deep water condition in Fourier space (Appendix B). These evolution equations can be efficiently solved with any order of approximation using a pseudo-spectral method as will be presented in the next chapter.

3.2 Governing Equations

For an ideal (inviscid, irrotational) fluid, one can define a velocity potential $\phi(\mathbf{x}, z, t)$ satisfying the Laplace equation:

$$\nabla^2\phi + \frac{\partial^2\phi}{\partial z^2} = 0, \quad \text{for } -\infty \leq z \leq \eta(\mathbf{x}, t) \tag{3.1}$$

where $\eta(\mathbf{x}, t)$ is the free surface elevation, $\mathbf{x} = (x, y)$, and the horizontal gradient, ∇, is

defined as:

$$\nabla = (\frac{\partial}{\partial x}, \frac{\partial}{\partial y}) \tag{3.2}$$

the boundary conditions to be imposed at $z = -\infty$ is given by:

$$\nabla\phi = \frac{\partial\phi}{\partial z} = 0, \quad \text{as } z \to -\infty \tag{3.3}$$

and the boundary condition at $|\mathbf{x}| = \infty$ is given by:

$$\nabla\phi = \frac{\partial}{\partial z} = 0, \quad \text{as } |\mathbf{x}| \to \infty \tag{3.4}$$

The current formulation is also valid for the boundary condition that ϕ is periodic in x and y directions, and this boundary condition will be used when solving the problem numerically, as explained in the next chapter. At the free surface, the velocity potential ϕ and surface elevation η satisfy the following kinematic and dynamic boundary conditions:

$$\eta_t + \nabla\phi\cdot\nabla\eta = \phi_z \quad \text{at } z = \eta(\mathbf{x}, t) \tag{3.5}$$

$$\phi_t + \frac{1}{2}\nabla\phi\cdot\nabla\phi + \frac{1}{2}\phi_z\cdot\phi_z + gz + \frac{p}{\rho} = 0 \quad \text{at } z = \eta(\mathbf{x}, t) \tag{3.6}$$

where p is the applied external pressure at the free surface, and the surface tension effects are neglected here.

By substituting $z = \eta$ into (3.5) and (3.6), and using the following chain rule for differentiation,

$$\left.\frac{\partial\phi}{\partial t}\right|_{z=\eta} = \frac{\partial\Phi}{\partial t} - \left.\frac{\partial\phi}{\partial z}\right|_{z=\eta}\left(\frac{\partial\eta}{\partial t}\right) \tag{3.7}$$

$$\left.\frac{\partial\phi}{\partial x_j}\right|_{z=\eta} = \frac{\partial\Phi}{\partial x_j} - \left.\frac{\partial\phi}{\partial z}\right|_{z=\eta}\left(\frac{\partial\eta}{\partial x_j}\right) \tag{3.8}$$

where $(x_1, x_2) = (x, y)$, one can express the free surface boundary conditions in terms of free surface elevation η and free surface velocity potential Φ:

$$\eta_t + \nabla\Phi\cdot\nabla\eta = (1 + \nabla\eta\cdot\nabla\eta)W \tag{3.9}$$

$$\Phi_t + \frac{1}{2}\nabla\Phi\cdot\nabla\Phi + g\eta = \frac{1}{2}(1+\nabla\eta\cdot\nabla\eta)W^2 \tag{3.10}$$

Where $\Phi(\mathbf{x},t)$ is defined as:

$$\Phi(\mathbf{x},t) = \phi(\mathbf{x},\eta,t) \tag{3.11}$$

And W is the vertical velocity evaluated at the free surface defined as:

$$W = \left.\frac{\partial\phi}{\partial z}\right|_{z=\eta} \tag{3.12}$$

Zakharov [86] formulated the surface wave problem as a Hamiltonian system that conserves mass, momentum, and energy with the Hamiltonian function defined as:

$$E = \frac{1}{2}\int_{\mathbf{x}}\int_{-h_0(x)}^{\eta}[|\nabla\phi|^2 + \phi_z^2]\mathrm{d}z\mathrm{d}\mathbf{x} \;+\; \frac{1}{2}\int_{\mathbf{x}} g\eta^2\mathrm{d}\mathbf{x} \tag{3.13}$$

which is the same as total energy of the surface waves, with the first term being the kinetic energy and the second term, the potential energy. Zakharov stated that the surface elevation η and free surface velocity potential Φ are the appropriate variables with which the surface waves can be written in the form of Hamilton's canonical equations:

$$\eta_t = \frac{\delta E}{\delta\Phi} \quad \text{and} \quad \Phi_t = -\frac{\delta E}{\delta\eta} \tag{3.14}$$

Applying these canonical equations to the Hamiltonian (3.13), one can derive the same set of evolution equations as (3.9) and (3.10).

Equations (3.9) and (3.10) can be considered as the evolution equations for η and Φ defined in the horizontal plane, although an additional unknown, W, has been introduced. If one can express W in terms of η and Φ, the system (3.9)- (3.10) will be a closed system for η and Φ. In order to write W in terms of η and Φ, one first expands Φ and W in Taylor series about the mean free surface $z = 0$:

$$\Phi = \phi_0 + \eta w_0 - \frac{\eta^2}{2}\nabla^2\phi_0 - \frac{\eta^3}{6}\nabla^2 w_0 + \frac{\eta^4}{24}\nabla^4\phi_0 + O(\epsilon^5) \tag{3.15}$$

$$W = w_0 - \eta\nabla^2\phi_0 - \frac{\eta^2}{2}\nabla^2 w_0 + \frac{\eta^3}{6}\nabla^4\phi_0 + \frac{\eta^4}{24}\nabla^4 w_0 + O(\epsilon^5) \tag{3.16}$$

Parameter ϵ is the the wave slope parameter which is defined as $\epsilon = k\eta$. The Laplace equation has been used to substitute $-\nabla^2\phi$ for $\frac{\partial^2\phi}{\partial z^2}$, and

$$\phi_0 = \phi(\mathbf{x}, 0, t) \quad \text{and} \quad w_0 = \frac{\partial\phi}{\partial z}(\mathbf{x}, 0, t) \tag{3.17}$$

The relationship between two physical variables at the mean free surface, ϕ_0 and w_0, can be found by formally solving the following linear Dirichlet boundary value problem for ϕ:

$$\left(\nabla^2 + \frac{\partial^2}{\partial z^2}\right)\phi = 0 \quad \text{for} \quad -h_0 < z < 0 \tag{3.18}$$

$$\phi = \phi_0(\mathbf{x}, t) \quad \text{at} \quad z = 0 \tag{3.19}$$

$$\phi_z \to 0 \quad \text{as} \quad z \to -h_0 \tag{3.20}$$

$$\nabla\phi \to 0 \quad \text{and} \quad \phi_z \to 0 \quad \text{as} \quad |\mathbf{x}| \to \infty \tag{3.21}$$

System of equations (3.18)- (3.21) can be solved using Fourier transform defined by:

$$\hat{f}(\mathbf{k}, z, t) = \mathcal{F}\left[f(\mathbf{x}, z, t)\right] = \int_{-\infty}^{\infty} f(\mathbf{x}, z, t)e^{-i\mathbf{k}\cdot\mathbf{x}}d\mathbf{x}, \tag{3.22}$$

$$f(\mathbf{x}, z, t) = \mathcal{F}^{-1}\left[\hat{f}(\mathbf{k}, z, t)\right] = \left(\frac{1}{2\pi}\right)^2 \int_{-\infty}^{\infty} \hat{f}(\mathbf{k}, z, t)e^{i\mathbf{k}\cdot\mathbf{x}}d\mathbf{k}, \tag{3.23}$$

The general solution of the Dirichlet problem (3.18)- (3.21) can be written as:

$$\hat{\phi} = A(\mathbf{k}, t)\cosh k(z + h_0), \tag{3.24}$$

Obtaining $A(\mathbf{k}, t)$ using (3.19) will result in:

$$\hat{\phi} = \frac{\cosh k(z + h_0)}{\cosh kh_0}\hat{\phi}_0, \tag{3.25}$$

Now, using the fact that $w_0(\mathbf{x}, t) = \phi_z(\mathbf{x}, 0, t)$, the Fourier transform of the vertical

velocity at the mean free surface, $\hat{w}_0$ can be found as:

$$\hat{w_0} = \hat{\phi_0} k \tanh(kh_0) = \frac{-\tanh(kh_0)}{|\mathbf{k}|} \nabla \cdot \hat{\mathbf{u}}_0, \tag{3.26}$$

where $\mathbf{u}_0$ is the velocity at the mean free surface $z = 0$. Taking the inverse Fourier transform of (3.26) yields the following relationships between physical variables at the mean free surface $z = 0$:

$$\begin{aligned} w_0 &= -\mathcal{L}[\phi_0], \\ w_0 &= \mathcal{T}[\mathbf{u}_0], \end{aligned} \tag{3.27}$$

Where $\mathcal{L}$ and $\mathcal{T}$ are linear integral operators. Since a pseudo-spectral method is used to solve the system of evolution equations, the linear integral operator $\mathcal{L}$ acting on a general Fourier component f is of particular interest, and is given by:

$$\mathcal{L}[f] = \mathcal{F}^{-1}[-k\mathcal{F}[f]], \tag{3.28}$$

Where $\mathbf{k} = (k_1, k_2)$, and $k = (k_1^2 + k_2^2)^{\frac{1}{2}}$, with k_1 and k_2 being the wave numbers in x and y directions, respectively.

In case of finite water depth, the integral operator $\mathcal{L}$ will change to:

$$\mathcal{L}[f] = \mathcal{F}^{-1}[-k \tanh kh_0 \mathcal{F}[f]], \tag{3.29}$$

Approximate evolution equations are first derived in terms of the velocity potential on the free surface, Φ and the equations are then derived in terms of tangential velocity on the free surface, $\mathbf{u}_s$.

Using the relation between ϕ_0 and w_0 given by (3.27) in expressions (3.15) and (3.16), one gets the following expressions for Φ and W:

$$\Phi = \phi_0 - \eta\mathcal{L}[\phi_0] - \frac{\eta^2}{2}\nabla^2\phi_0 + \frac{\eta^3}{6}\nabla^2(\mathcal{L}[\phi_0]) + \frac{\eta^4}{24}\nabla^4\phi_0 + O(\epsilon^5) \tag{3.30}$$

$$W = -\mathcal{L}[\phi_0] - \eta\nabla^2\phi_0 + \frac{\eta^2}{2}\nabla^2(\mathcal{L}[\phi_0]) + \frac{\eta^3}{6}\nabla^4\phi_0 - \frac{\eta^4}{24}\nabla^4(\mathcal{L}[\phi_0]) + O(\epsilon^5) \tag{3.31}$$

The series (3.30) can be directly inverted at different orders as follow:

$$\begin{aligned}
\phi_0 = \Phi \quad & : O(1) \\
& + \eta\mathcal{L}[\Phi] \quad : O(\epsilon) \\
& + \eta\mathcal{L}\left[\eta\mathcal{L}[\Phi]\right] + \frac{\eta^2}{2}\nabla^2\Phi \quad : O(\epsilon^2) \\
& + \eta\mathcal{L}\left[\eta\mathcal{L}\left[\eta\mathcal{L}[\Phi]\right]\right] + \frac{\eta}{2}\mathcal{L}\left[\eta^2\nabla^2\Phi\right] + \frac{\eta^2}{2}\nabla^2\left(\eta\mathcal{L}[\Phi]\right) - \frac{\eta^3}{6}\nabla^2\left(\mathcal{L}[\Phi]\right) \quad : O(\epsilon^3)
\end{aligned} \tag{3.32}$$

By substituting the inverted series (3.32) at different orders into the expression for the vertical velocity at the free surface, W, given by (3.31), one can express W in terms of Φ at different orders of ϵ:

$$\begin{aligned}
W = & -\mathcal{L}[\Phi] \\
& - \eta\nabla^2\Phi - \mathcal{L}\left[\eta\mathcal{L}[\Phi]\right] \\
& + \frac{\eta^2}{2}\nabla^2\left(\mathcal{L}[\Phi]\right) - \eta\nabla^2\left(\eta\mathcal{L}[\Phi]\right) - \mathcal{L}\left[\frac{\eta^2}{2}\nabla^2\Phi + \eta\mathcal{L}\left[\eta\mathcal{L}[\Phi]\right]\right] \\
& + \frac{\eta^3}{6}\nabla^4\Phi + \frac{1}{2}\eta^2\nabla^2\left(\mathcal{L}\left[\eta\mathcal{L}[\Phi]\right]\right) - \eta\nabla^2\left(\frac{\eta^2}{2}\nabla^2\Phi + \eta\mathcal{L}\left[\eta\mathcal{L}[\Phi]\right]\right) \\
& - \mathcal{L}\left[-\frac{1}{6}\eta^3\mathcal{L}\left[\nabla^2\Phi\right] + \frac{1}{2}\eta^2\nabla^2\left(\eta\mathcal{L}[\Phi]\right) + \eta\mathcal{L}\left[\frac{1}{2}\eta^2\nabla^2\Phi + \eta\mathcal{L}\left[\eta\mathcal{L}[\Phi]\right]\right]\right] + O(\epsilon^4)
\end{aligned} \tag{3.33}$$

By substituting the closure equation (3.33) into the free surface boundary conditions, given by (3.9)- (3.10), one can finally derive evolution equations at different orders. This system is closed and describes finite amplitude/weakly nonlinear surface waves of arbitrary wavelength. In the following section approximate evolution equations are derived up to third-order.

3.3 Approximate Evolution Equations

3.3.1 First-order Approximation

For $\epsilon \ll 1$, after neglecting all nonlinear terms, the first-order evolution equations can be written as:

$$\eta_t = -\mathcal{L}[\Phi] \quad , \quad \Phi_t = -g\eta \tag{3.34}$$

Which can be combined into a single equation for Φ:

$$\Phi_{tt} = g\mathcal{L}[\Phi] \tag{3.35}$$

By substituting into (3.35), $\eta = ae^{i(\mathbf{k}\cdot\mathbf{x}-\omega t)}$ and $\Phi = be^{i(\mathbf{k}\cdot\mathbf{x}-\omega t)}$, and using (3.28), one obtains the dispersion relation for surface gravity waves in deep water:

$$\omega^2 = gk \tag{3.36}$$

where $k = |\mathbf{k}|$.

3.3.2 Higher-order approximations

By substituting the expression for W into the exact evolution equations (3.9)- (3.10), and neglecting the terms higher than second order, one can get the following second-order evolution equations:

$$\eta_t = -\mathcal{L}[\Phi] - \nabla\cdot(\eta\nabla\Phi) - \mathcal{L}\left[\eta\mathcal{L}[\Phi]\right] \tag{3.37}$$

$$\Phi_t = -g\eta - \frac{1}{2}\nabla\Phi\cdot\nabla\Phi + \frac{1}{2}\left(\mathcal{L}[\Phi]\right)^2 \tag{3.38}$$

Similarly, neglecting the terms higher than third order, will give us the following third-

order evolution equations:

$$\begin{aligned}\eta_t = &-\mathcal{L}[\Phi] - \nabla\cdot(\eta\nabla\Phi) - \mathcal{L}\left[\eta\mathcal{L}[\Phi]\right] \\ &- \nabla^2\left(\frac{1}{2}\eta^2\mathcal{L}[\Phi]\right) - \mathcal{L}\left[\eta\mathcal{L}\left[\eta\mathcal{L}[\Phi]\right] + \frac{1}{2}\eta^2\nabla^2\Phi\right]\end{aligned} \tag{3.39}$$

$$\begin{aligned}\Phi_t = &-g\eta - \frac{1}{2}\nabla\Phi\cdot\nabla\Phi + \frac{1}{2}\left(\mathcal{L}[\Phi]\right)^2 \\ &+ \eta\mathcal{L}[\Phi]\nabla^2\Phi + \mathcal{L}[\Phi]\mathcal{L}\left[\eta\mathcal{L}[\Phi]\right]\end{aligned} \tag{3.40}$$

Deriving higher order systems is straightforward. The present formulation requires no assumption on the wavelength and therefore the system with any order of approximation retains the linear dispersion relation. It has been shown in appendix A that the third-order formulation is equivalent to Craig and Sulem's Dirichlet-to-Neumann operator formalism in Fourier space. In the next section evolution equations are derived in terms of surface elevation and tangential velocity at the free surface, $\mathbf{u}_s$.

3.4 Surface Elevation-Tangential Velocity Formulation

The tangential component of the velocity on the free surface, $\mathbf{u}_s$ is obtained by:

$$\mathbf{u}_s = \mathbf{U} + W\nabla\eta \tag{3.41}$$

where $\mathbf{u}_s = (u_s, v_s)$, with u_s and v_s being the tangential velocities on the free surface in x and y directions, respectively. $\mathbf{U} = (U, V)$, where, U and V are the horizontal velocities on the free surface in x and y directions, respectively, and W has been already defined. Noting that for irrotational flows, $\mathbf{u}_s = \nabla\Phi$, it would be straightforward to derive the evolution

equation for η and $\mathbf{u}_s$ by taking the gradient of (3.9)- (3.10):

$$\begin{aligned} \eta_t + \mathbf{u}_s \cdot \nabla\eta &= (1 + \nabla\eta \cdot \nabla\eta)W, \\ \mathbf{u}_{s,t} + \frac{1}{2}\nabla\left(\mathbf{u}_s \cdot \mathbf{u}_s\right) + g\nabla\eta &= \frac{1}{2}\nabla(1 + \nabla\eta \cdot \nabla\eta)W^2, \end{aligned} \tag{3.42}$$

The relationship between w_0 and $\mathbf{u}_0$ was found by solving the Dirichlet boundary value problem ((3.26)).

Linear integral operator $\mathcal{T}$ acting on a Fourier component for deep water is given by:

$$\mathcal{T}\left[f\right] = \mathcal{F}^{-1}\left[-i\mathcal{F}[f]\right], \tag{3.43}$$

While for finite water depth,

$$\mathcal{T}\left[f\right] = \mathcal{F}^{-1}\left[-i\tanh kh_0\mathcal{F}[f]\right], \tag{3.44}$$

note that for any function f:

$$\mathcal{L}[f] = -\mathcal{T}[\nabla f] \tag{3.45}$$

Using (3.45) approximate evolution equations for η and $\mathbf{u}_s$ up to third-order are obtained as:

First-order Approximation:

$$\eta_t = \mathcal{T}\left[\mathbf{u}_s\right] \tag{3.46}$$

$$\mathbf{u}_{s,t} = -g\nabla\eta \tag{3.47}$$

Second-order Approximation:

$$\eta_t = \mathcal{T}\left[\mathbf{u}_s\right] - \nabla\cdot\left(\eta\mathbf{u}_s\right) - \mathcal{T}\left[\nabla\left(\eta\mathcal{T}[\mathbf{u}_s]\right)\right] \tag{3.48}$$

$$\mathbf{u}_{s,t} = -g\nabla\eta - \frac{1}{2}\nabla\left(\mathbf{u}_s \cdot \mathbf{u}_s\right) + \frac{1}{2}\nabla\left(\mathcal{T}[\mathbf{u}_s]\mathcal{T}[\mathbf{u}_s]\right) \tag{3.49}$$

Third-order Approximation:

$$\begin{aligned}\eta_t = &\mathcal{T}\left[\mathbf{u}_s\right] - \nabla\cdot\left(\eta\mathbf{u}_s\right) - \mathcal{T}\left[\nabla\left(\eta\mathcal{T}[\mathbf{u}_s]\right)\right] \\ &+ \nabla^2\left(\frac{1}{2}\eta^2\mathcal{T}[\mathbf{u}_s]\right) + \mathcal{T}\left[\nabla\left(\eta\mathcal{T}\left[\nabla\left(\eta\mathcal{T}[\mathbf{u}_s]\right)\right]\right)\right] + \mathcal{T}\left[\nabla\left(\frac{1}{2}\eta^2\nabla\cdot\mathbf{u}_s\right)\right]\end{aligned} \tag{3.50}$$

$$\begin{aligned}\mathbf{u}_{s,t} = &-g\nabla\eta - \frac{1}{2}\nabla\left(\mathbf{u}_s\cdot\mathbf{u}_s\right) + \frac{1}{2}\nabla\left(\mathcal{T}[\mathbf{u}_s]\mathcal{T}[\mathbf{u}_s]\right) \\ &- \nabla\left(\eta\mathcal{T}[\mathbf{u}_s]\nabla\cdot\mathbf{u}_s\right) - \nabla\left(\mathcal{T}[\mathbf{u}_s]\mathcal{T}\left[\nabla\left(\eta\mathcal{T}[\mathbf{u}_s]\right)\right]\right)\end{aligned} \tag{3.51}$$

These equations can be easily extended to higher orders depending on the desired accuracy.

3.5 Conservation Issues

Accuracy of the numerical model may be checked by monitoring the change of Hamiltonian or total energy during simulations. Using expression (3.13) for the total energy of surface gravity waves, and using integration by parts, one obtains:

$$\begin{aligned}E &= \frac{1}{2}\int_{\mathbf{x}}\int_{-h_0}^{\eta}\left[|\nabla\phi|^2 + \phi_z^2\right]\mathrm{d}z\mathrm{d}\mathbf{x} + \frac{1}{2}\int_{\mathbf{x}} g\eta^2\mathrm{d}\mathbf{x} \\ &= \frac{1}{2}\int_{-h_0}^{\eta}\left[\phi\nabla\phi\right]_{\mathbf{x}}\mathrm{d}z - \frac{1}{2}\int_{-h_0}^{\eta}\int_{\mathbf{x}}\phi\nabla^2\phi\ \mathrm{d}z\mathrm{d}\mathbf{x} + \frac{1}{2}\int_{\mathbf{x}}\left[\phi\phi_z\right]_{z=\eta}\mathrm{d}\mathbf{x} \\ &- \frac{1}{2}\int_{\mathbf{x}}\int_{-h_0}^{\eta}\phi\phi_{zz}\mathrm{d}z\mathrm{d}\mathbf{x} + \frac{1}{2}\int_{\mathbf{x}} g\eta^2\mathrm{d}\mathbf{x} = \frac{1}{2}\int_{\mathbf{x}}\Phi\eta_t\mathrm{d}\mathbf{x} + \frac{1}{2}\int_{\mathbf{x}} g\eta^2\mathrm{d}\mathbf{x}\end{aligned} \tag{3.52}$$

Where $d\mathbf{x} = dxdy$. The Laplace equation was used to replace ϕ_{zz} by $-\nabla^2\phi$, and periodicity of ϕ has been used to remove the boundary terms. The linearized kinematic free surface boundary condition, $\eta_t = W$, and kinematic condition on the sea bed, $z = -h_0$, have been also used in deriving the final expression in (3.52).

In the absence of any external force, the total energy should be conserved. In numerical computations, this energy conservation will be carefully monitored. If the expression for η_t from third order system (3.39) is substituted into the expression for total energy, one

obtains:

$$E = \frac{1}{2}\int_{\mathbf{x}} \left[-\Phi\mathcal{L}[\Phi] + \eta\left|\nabla\Phi\right|^2 - \eta\left[\mathcal{L}[\Phi]\right]^2 - \eta^2\mathcal{L}[\Phi]\nabla^2\Phi - \eta\mathcal{L}[\Phi]\mathcal{L}\left[\eta\mathcal{L}[\Phi]\right] + g\eta^2 \right] \mathrm{d}\mathbf{x} \quad (3.53)$$

Where integration by parts has been used. Note that two formulations (velocity potential and tangential velocity) presented here are equivalent, and the former has been used in energy relations for simplicity. Following the variational approach of Zakharov [86], and using the symmetry of the linear operator $\mathcal{L}$, it can be shown that the system of equations given by (3.39)- (3.40), has a Hamiltonian structure satisfying the canonical relations (3.14). Then, the rate of change of total energy in absence of any external force, can be written as:

$$\frac{\mathrm{d}E}{\mathrm{d}t} = \int \left[\frac{\delta E}{\delta\eta}\frac{\partial\eta}{\partial t} - \frac{\delta E}{\delta\Phi}\frac{\partial\Phi}{\partial t} \right] \mathrm{d}\mathbf{x} = 0 \quad (3.54)$$

Where the canonical relations (3.14) have been used, and periodic boundary conditions have been imposed. In addition to conservation of the total energy, the system also conserves mass and momentum:

$$\begin{aligned} \frac{\mathrm{d}M}{\mathrm{d}t} = \frac{\mathrm{d}}{\mathrm{d}t}\int \eta \mathrm{d}\mathbf{x} = \int \left[\frac{\partial\eta}{\partial t} + \frac{\delta\eta}{\delta\Phi}\frac{\partial\Phi}{\partial t} \right] \mathrm{d}\mathbf{x} &= \int \left[\frac{\partial\eta}{\partial t} + \frac{\delta\eta}{\delta\Phi}\left(-\frac{\delta E}{\delta\eta} \right) \right] \mathrm{d}\mathbf{x} \\ &= \int \left[\frac{\partial\eta}{\partial t} - \frac{\delta E}{\delta\Phi} \right] \mathrm{d}\mathbf{x} = 0 \end{aligned} \quad (3.55)$$

where M is the water mass. For horizontal momentum I, using integration by parts, one can write:

$$I = \int \eta\nabla\Phi \mathrm{d}\mathbf{x} = -\int \Phi\nabla\eta \mathrm{d}\mathbf{x} \quad (3.56)$$

$$\frac{\mathrm{d}I}{\mathrm{d}t} = -\int \frac{\mathrm{d}\Phi}{\mathrm{d}t}\nabla\eta \mathrm{d}\mathbf{x} = 0 \quad (3.57)$$

3.6 Conclusion

A third-order formulation for non-overturning surface gravity waves in a fluid of arbitrary depth was presented in this chapter. The derivations show that the evolution of the free surface can be expressed in the form of two sets of closed nonlinear equations for two surface variables: The free surface elevation and the free surface velocity potential (or free surface tangential velocity). The presented formulation allows one to express the free surface variables in terms of the wave steepness parameter, ϵ, up to any arbitrary order. The equations have been given up to third-order, but can be easily extended to higher orders. The evolution equations can be solved using pseudo-spectral method which will be introduced in the next chapter.

CHAPTER 4

Numerical Method for Evolution Equations

4.1 Introduction

Evolution equations derived in Chapter 3 are solved using a pseudo-spectral method which was first introduced by Fornberg and Whitham [24] for solving Kortweg-de-Vries (KdV) equation to study solitary wave interactions, instability of finite amplitude wave trains, and wave breaking. The basic advantage of the pseudo-spectral method over other numerical methods stems from using an FFT which reduces the computational cost from $O(N^2)$, for iterative methods, to $O(N \log N)$.

The formulation and numerical method are first given for 1-D and 2-D flows and then validated by comparing the numerical solution for different forms of steady and traveling waves with exact solutions. Energy conservation will be monitored carefully during numerical simulations, and stability/accuracy issues associated with numerical integration and the pseudo-spectral method will be also discussed briefly. A pneumatic wave maker together with a damping layer is then incorporated in the model to generate one-dimensional waves and absorb them at the ends of the computational domain. The predictions of the third-order model for modulation instability are qualitatively compared with fully nonlinear solutions as well as experimental measurements.

4.2 Numerical method for the free surface evolution in two-dimensional flows

For two-dimensional flows the integral operators $\mathcal{L}$ and $\mathcal{T}$ for finite water depth in physical space are given by:

$$\mathcal{L}[\Phi] = \frac{1}{2h_0}\mathcal{P}\int_{-\infty}^{\infty} \frac{\Phi_x(x',t)}{\sinh\left(\frac{\pi}{2h_0}(x'-x)\right)}\mathrm{d}x' \tag{4.1}$$

$$\mathcal{T}[u_s] = \frac{1}{2h_0}\mathcal{P}\int_{-\infty}^{\infty} \frac{u_s(x',t)}{\sinh\left(\frac{\pi}{2h_0}(x'-x)\right)}\mathrm{d}x' \tag{4.2}$$

where $\mathcal{P}$ stands for a principal value integral. In deep water, $\mathcal{T}$ operator is reduced to the Hilbert transform $\mathcal{H}$ as:

$$\mathcal{T}\left[u_s\right] = \mathcal{H}\left[u_s\right] = \frac{1}{\pi}\mathcal{P}\int_{-\infty}^{\infty} \frac{u_s(x')}{x'-x}\mathrm{d}x' \tag{4.3}$$

For two-dimensional flows the third-order evolution equations for η and Φ are reduced to:

$$\begin{aligned}
\eta_t &= -\mathcal{L}[\Phi] - (\eta\Phi_x)_x - \mathcal{L}\left[\eta\mathcal{L}[\Phi]\right] - \frac{1}{2}\left(\eta^2\mathcal{L}[\Phi]\right)_{xx} - \mathcal{L}\left[\eta\mathcal{L}\left[\eta\mathcal{L}[\Phi]\right]\right] - \frac{1}{2}\mathcal{L}\left[\eta^2\Phi_{xx}\right], \\
\Phi_t &= -g\eta - \frac{1}{2}\Phi_x^2 + \frac{1}{2}\left(\mathcal{L}[\Phi]\right)^2 + \mathcal{L}[\Phi]\left(\eta\Phi_{xx} + \mathcal{L}\left[\eta\mathcal{L}[\Phi]\right]\right),
\end{aligned} \tag{4.4}$$

while the third-order evolution equations for η and u_s can be written as:

$$\begin{aligned}
\eta_t = {} & \mathcal{T}\left[u_s\right] - (\eta u_s)_x - \mathcal{T}\left[(\eta\mathcal{T}[u_s])_x\right] + \left(\frac{1}{2}\eta^2\mathcal{T}[u_s]\right)_{xx} \\
& + \mathcal{T}\left[(\eta\mathcal{T}\left[(\eta\mathcal{T}[u_s])_x\right])_x\right] + \mathcal{T}\left[\left(\frac{1}{2}\eta^2 u_s\right)_x\right],
\end{aligned} \tag{4.5}$$

$$u_{s,t} = -g\eta_x - u_s u_{sx} + \mathcal{T}[u_s]\mathcal{T}[u_{sx}] - (\eta\mathcal{T}[u_s]u_{sx})_x - (\mathcal{T}[u_s]\mathcal{T}\left[(\eta\mathcal{T}[u_s])_x\right])_x,$$

where the subscripts represent partial differentiations. To solve the system of equa-

tions (4.4) or (4.5) numerically, a pseudo-spectral method using a Fourier basis in space ([24]) is used. First, for two-dimensional flows, the surface elevation, η, and the free surface tangential velocity, u_s, are expanded in Fourier series as:

$$\eta(x,t) = \sum_{n=-\frac{N}{2}}^{\frac{N}{2}} a_n(t) e^{ik_n x}, \qquad u_s(x,t) = \sum_{n=-\frac{N}{2}}^{\frac{N}{2}} b_n(t) e^{ik_n x} \tag{4.6}$$

or if the velocity potential formulation is used,

$$\Phi(x,t) = \sum_{n=-\frac{N}{2}}^{\frac{N}{2}} c_n(t) e^{ik_n x} \tag{4.7}$$

where N is the total number of Fourier modes, or equivalently grid points, and $k_n = n\Delta k$, with $\Delta k = \frac{2\pi}{L}$, and L being the total length of the computational domain. In order to compute the Fourier coefficients, a_n and b_n (or c_n), the most efficient form of the FFT is used which is to choose the number of grid points as a power of two. All linear differential and integral operators are calculated in Fourier space as follows:

$$\frac{\partial}{\partial x}\left(a_n(t) e^{ik_n x}\right) = ik_n a_n(t) e^{ik_n x} \tag{4.8}$$

$$\mathcal{L}\left[a_n(t) e^{ik_n x}\right] = -k_n \tanh k_n h_0 a_n(t) e^{ik_n x} \tag{4.9}$$

$$\mathcal{T}\left[a_n(t) e^{ik_n x}\right] = -i \tanh k_n h_0 a_n(t) e^{ik_n x} \tag{4.10}$$

All nonlinear terms in the evolution equations are evaluated in physical space. The pseudo-spectral method has spectral accuracy in space, which means that the error in evaluating an operator decreases exponentially with increasing the number of grid points, however this is true for functions that are smooth enough.

The numerical method for a problem using N Fourier modes and retaining nonlinearities up to order M consists of the following two parts:

- Given the surface elevation $\eta(x,t)$ and tangential velocity $u_s(x,t)$ on that surface at some instant of time t, the right-hand sides of the evolution equations are evaluated using the pseudo-spectral method. As mentioned, for periodic boundary conditions where the eigen-function expansions are represented as Fourier series, grid points are equally spaced and FFT is used to project between the Fourier (wave number) and physical domains.

- The solution is then evolved in time to obtain the new values $\eta(x,t+\Delta t)$ and $u_s(x,t+\Delta t)$. For the computations in the present thesis, a fourth-order Runge-Kutta integrator (RK4) with fixed time step size Δt is used.

This two-step procedure is repeated starting from the initial conditions until reaching the desired time. The coupled nonlinear evolution equations can be written as:

$$\eta_t = f\left(\eta(t), u_s(t)\right), \quad u_{s,t} = g\left(\eta(t), u_s(t)\right) \tag{4.11}$$

where f and g are two general nonlinear functions. If the compact notation $q = \begin{pmatrix} \eta \\ u_s \end{pmatrix}$ and $F = \begin{pmatrix} f \\ g \end{pmatrix}$ is used, a step of the classical RK4 scheme from the time step n to $(n+1)$ can be demonstrated as:

$$K_1 = F\left(q^n, t_n\right) \tag{4.12}$$

$$K_2 = F\left(q^n + \frac{1}{2}\Delta t K_1, t_n + \frac{1}{2}\Delta t\right) \tag{4.13}$$

$$K_3 = F\left(q^n + \frac{1}{2}\Delta t K_2, t_n + \frac{1}{2}\Delta t\right) \tag{4.14}$$

$$K_4 = F\left(q^n + \Delta t K_3, t_n + \Delta t\right) \tag{4.15}$$

$$q^{n+1} = q^n + \frac{1}{6}\Delta t\left[K_1 + 2K_2 + 2K_3 + K_4\right] \tag{4.16}$$

The local truncation error of this scheme is $O\left(\Delta t^5\right)$. The global truncation error for $t = O(1)$ is fourth-order in Δt. RK4 requires twice as many evaluations as the commonly used fourth-order multi-step Adams-Bashforth-Moulton (ABM4) method, but has a somewhat

lower global truncation error and a larger stability region, however, equations (3.39)- (3.40) or (3.50)- (3.51) are to be evaluated 4 times per time step.

4.2.1 Treatment of Nonlinear Terms

It is well known that spectral methods applied to nonlinear systems suffer from aliasing errors. These aliasing errors can be usually seen in water wave systems as sawtooth instabilities with wavelengths of the order one or two grid spacings which correspond to the highest wave numbers in the spectrum. Consider a simple nonlinear term as:

$$w(x) = u(x)v(x) \tag{4.17}$$

In the case of an infinite series expansion, the typical convolution sum for (4.17) can be written as:

$$\hat{w}_k = \sum_{m+n=k} \hat{u}_m \hat{v}_n \tag{4.18}$$

where

$$u(x) = \sum_{m=-\infty}^{\infty} \hat{u}_m e^{imx}, \quad v(x) = \sum_{n=-\infty}^{\infty} \hat{v}_n e^{inx}, \quad \text{and,} \quad \hat{w}_k = \frac{1}{2\pi} \int_0^{2\pi} w(x) e^{-ikx} \mathrm{d}x \tag{4.19}$$

Where in the present method u and v are approximated by their respective truncated Fourier series of degree $N/2$, (4.18) becomes

$$\hat{w}_k = \sum_{m+n=k} \hat{u}_m \hat{v}_n, \quad (|m|, |n| \leq N/2) \tag{4.20}$$

where $|k| \leq N/2$. The direct summation implied by (4.18) takes $O(N^2)$ operations (Note that N is the total number of equi-spaced points on the free surface). This is prohibitively expensive, especially when one considers that for a large-scale nonlinear problem. However the use of FFT enables one to calculate (4.18) in $O(N \log N)$ operations which saves a significant time.

The approach taken in this dissertation for evaluating terms similar to (4.18) is to use

the inverse Fourier transform to transform $\hat{u}_m$ and $\hat{v}_n$ to physical space, to perform there a multiplication similar to (4.20), and then to use the Discrete Fourier Transform to determine $\hat{w}_k$.

$$\begin{aligned} U_j &= \sum_{k=-N/2}^{N/2-1} \hat{u}_k e^{ikx_j}, \\ V_j &= \sum_{k=-N/2}^{N/2-1} \hat{v}_k e^{ikx_j}, \text{ for } j = 0, 1, ..., N-1 \end{aligned} \tag{4.21}$$

and define

$$W_j = U_j V_j, \quad \text{for } j = 0, 1, ..., N-1 \tag{4.22}$$

and

$$\hat{W}_k = \frac{1}{N} \sum_{j=0}^{N-1} W_j e^{-ikx_j}, \quad k = -\frac{N}{2}, ..., \frac{N}{2} - 1, \tag{4.23}$$

where $x_j = \frac{2\pi j}{N}$. Use of the discrete transform orthogonality relation leads to:

$$\hat{W}_k = \sum_{m+n=k} \hat{u}_m \hat{v}_n + \sum_{m+n=k\pm N} \hat{u}_m \hat{v}_n = \hat{w}_k + \sum_{m+n=k\pm N} \hat{u}_m \hat{v}_n. \tag{4.24}$$

The convolution sum (4.18) in the pseudo-spectral method is evaluated at the cost of 3 FFTs and N multiplications. Therefore, the total operation count is $(15/2)N \log N = O(N \log N)$, compared to $O(N^2)$ operations in direct summation. Note that the complex FFT algorithm used in the present work, from FFTW library, takes $5N \log N$ operations for each FFT, which is halved using the complex conjugate property.

The second term on the right-hand side of (4.24) is the aliasing error. The strategy used in this thesis to remove aliasing errors, is truncation or so-called 2/3-rule (Orszag [58]). The key to this "de-aliasing technique" is the use of a discrete transform with M rather than N

points, where $M \geq 3N/2$. Let

$$\begin{aligned} y_j &= 2\pi j/M, \\ U_j &= \sum_{k=-M/2}^{M/2-1} \tilde{u}_k e^{iky_j}, \\ V_j &= \sum_{k=-M/2}^{M/2-1} \tilde{v}_k e^{iky_j}, \\ W_j &= U_j V_j, \end{aligned} \tag{4.25}$$

where

$$\tilde{u}_k = \begin{cases} \hat{u}_k \quad , & |k| \lesssim N/2 \\ 0 & \text{Otherwise} \end{cases} \tag{4.26}$$

Thus the $\tilde{u}_k$ coefficients are the $\hat{u}_k$ coefficients padded with zeros for the additional wave numbers. Likewise, let

$$\tilde{W}_k = \frac{1}{M} \sum_{j=0}^{M-1} W_j e^{-iky_j}, \quad k = -\frac{M}{2}, ..., \frac{M}{2} - 1. \tag{4.27}$$

Then

$$\tilde{W}_k = \sum_{m+n=k} \tilde{u}_m \tilde{v}_n + \sum_{m+n=k\pm N} \tilde{u}_m \tilde{v}_n. \tag{4.28}$$

One is only interested in $\tilde{W}_k$ for $|k| \leq N/2$, and choose M such that the second term on the right-hand side vanishes for these k. Since $\tilde{u}_m$ and $\tilde{v}_m$ are zero for $|m| > N/2$, the worst case scenario is

$$-\frac{N}{2} - \frac{N}{2} \leq \frac{N}{2} - 1 - M \tag{4.29}$$

Or

$$M \geq \frac{3N}{2} - 1 \tag{4.30}$$

The operation count for this transform method is $(\frac{45}{4})N \log(\frac{3}{2}N)$, which is roughly 50% larger than the simpler, but aliased method discussed earlier. This de-aliasing technique is also termed as truncation and is sometimes referred as the 2/3-rule. In most of the one-dimensional simulations in this thesis, an ideal low-pass filter is used to eliminate such

high-wavenumber instabilities. At every time step, the following function is multiplied by the Fourier coefficients $a_n(t)$ and $b_n(t)$:

$$\gamma_k = \begin{cases} 1 & \text{if } \frac{|k|}{k_{max}} \leq \theta,\ 0 < \theta \leq 1, \\ 0 & \text{if } \frac{|k|}{k_{max}} > \theta, \end{cases} \tag{4.31}$$

where k_{max} is the largest wavenumber in the spectrum. Care should be taken to specify a sufficiently high spatial resolution and a value of θ close to one so that only energy levels located in the high-wave number region of the spectrum get suppressed by filtering. A value of $\theta = 0.7$ was used in third-order simulations. The total energy is monitored carefully during the simulations to minimize non-physical dissipation of energy. It is worthwhile to point out that a useful alternative when modeling physical experiments may be to introduce wave number-dependent damping terms explicitly on the right-hand side of the evolution equations. These types of filters are discussed later in laboratory experiments.

4.2.2 Comparison with exact solutions for steady water waves

The Fourier approximation method of Rienecker and Fenton [67] was implemented in order to find the solution of the fully nonlinear equations governing irrotational flow with a free surface. In this method all horizontal variations are approximated by truncated Fourier series. Fourier approximation is the only assumption in this method. In the following paragraphs the Fourier approximation method is formulated.

Fourier approximation method

Consider steady periodic waves of length L and height H propagating over water of depth h. A coordinate system (x, z) is considered, located under the crest at the mean water level and propagating with the wave. In such a frame, the motion is steady; Throughout this section the wavenumber $k = \frac{2\pi}{L}$ and gravitational acceleration g are used to make the variables and governing equations dimensionless. An illustration of the problem to be solved

is shown in Figure 4.1.

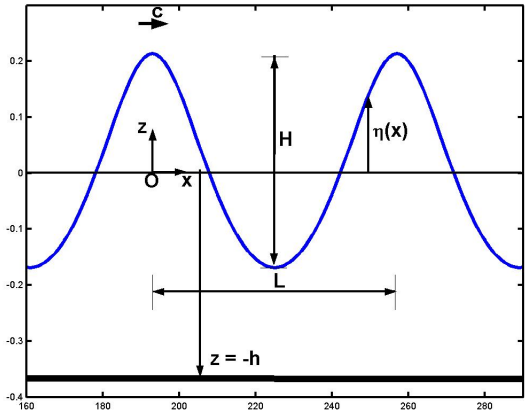

Figure 4.1: Illustration of a stationary wave with height H, length L, propagating on fluid of depth h with speed c

It is assumed that the wave height H and water depth h are given. The system of equations is presented here, each being written in the form $f_i(\mathbf{z}) = 0$, where i is the reference number of the equation and $\mathbf{z}$ is the vector of variables, $\mathbf{z} = (z_1, z_2, ...)$. All variables and their reference numbers are shown in Table 4.1

The first equation relates the dimensionless water depth kh and wave height kH through the specified value of wave height-to-depth ratio:

$$f_1(z_1, z_2) = kH - (H/h)\, kh = 0, \tag{4.32}$$

If the depth is infinite, this is replaced by:

$$f_1(z_1) = kh + 1 = 0, \tag{4.33}$$

Second equation relates the dimensionless wave height kH to the value of H/L, if that is specified

$$f_2 = kH - 2\pi\,(H/L) = 0, \tag{4.34}$$

Variable reference number j	Dimensionless variable z_j	Initial value from linear theory
1	kh	See text
2	kH	$kh(H/h)$
3	$T(gk)^{1/2}$	$2\pi/(\tanh kh)^{1/2}$
4	$c(k/g)^{1/2}$	$(\tanh kh)^{1/2}$
5	$c_E(k/g)^{1/2}$	0
6	$c_S(k/g)^{1/2}$	0
7	$\bar{u}(k/g)^{1/2}$	$(\tanh kh)^{1/2}$
8	$q(k^3/g)^{1/2}$	0
9	rk/g	$0.5\tanh kh$
10	$k\eta_0$	$0.5kH$
11	$k\eta_1$	$0.5kH\cos(\pi/N)$
12	$k\eta_2$	$0.5kH\cos(2\pi/N)$
...	...	...
$N+10$	$k\eta_N$	$-0.5kH$
$N+11$	B_1	$0.5kH(\tanh kh)^{-1/2}$
$N+12$	B_2	0
...	...	...
$2N+10$	B_N	0

Table 4.1: Dimensionless variables of steady wave problem and their initial values from linear theory.

or to the value of H/gT^2, where T is the apparent wave period.

$$f_2 = kH - \left(H/gT^2\right)\left(T(gk)^{1/2}\right)^2 = 0, \tag{4.35}$$

The next equation relates the wave speed c, relative to a frame in which the period is T, to wavelength and period by the definition $c = L/T$, which in dimensionless form becomes:

$$f_3 = c(k/g)^{1/2}T(gk)^{1/2} - 2\pi = 0, \tag{4.36}$$

In the next two equations, fluid velocities in the steady frame of calculation are related to those in the physical frame of interest, through which the waves travel at speed c in the positive x direction. In the frame of the waves, the apparent flow is in the negative x direction, under the steady waves. If the mean fluid speed in this frame is $\bar{u}$, the mean fluid

velocity would be $-\bar{u}$. The time-mean current in the physical frame is c_E, or equivalently:

$$f_4 = c_E(k/g)^{1/2} + \bar{u}(k/g)^{1/2} - c(k/g)^{1/2} = 0, \tag{4.37}$$

The mean mass-transport velocity c_S in the physical frame is given by $c_S h = ch - Q$, where Q is the volume flux per unit span in the computational frame. It is convenient to introduce q, the volume flux due to waves, given by $q = \bar{u}h - Q$, to give

$$f_5 = c_S(k/g)^{1/2} + \bar{u}(k/g)^{1/2} - c(k/g)^{1/2} - \frac{q(k^3/g)^{1/2}}{kh} = 0, \tag{4.38}$$

For infinite depth, the last term on the right-hand side is removed. The sixth equation incorporates the specified value of either $c_E/(gH)^{1/2}$, obtained from current-meter measurements or $c_S/(gH)^{1/2}$ if that is known (such as in a closed wave tank, when it is zero). That is,

$$f_6 = c_x(k/g)^{1/2} - \frac{c_x}{(gH)^{1/2}}(kH)^{1/2} = 0, \tag{4.39}$$

Where the c_x represents either c_E or c_S. The fully nonlinear free surface boundary conditions are to be satisfied at each of the $N+1$ equi-spaced points on the surface between the crest and the trough. The elevation $\eta(x)$ of the surface above the mean level at these points is denoted by $\eta_m = \eta(x_m)$, with m ranging from 0 to N. η_0 is the elevation at the crest, and η_N is that at the trough. The mean value of $\eta(x)$ is zero, and in terms of the point values this is satisfied if:

$$f_7 = k\eta_0 + k\eta_N + 2\sum_{m=1}^{N-1} k\eta_m = 0, \tag{4.40}$$

This trapezoidal type of sum is obtained from an $N-$term Fourier interpolation of the point values and subsequent integration. The requirement that the crest and trough elevations differ by H, is given by the next equation

$$f_8 = k\eta_0 - k\eta_N - kH = 0, \tag{4.41}$$

After stating the geometrical properties of steady waves though the preceding equations,

now the dynamic and kinematic boundary conditions on the free surface are stated in dimensionless form in terms of the stream function $\psi(x,z)$. Horizontal and vertical fluid velocities can be written as:

$$u = \frac{\partial \psi}{\partial z}, \quad v = -\frac{\partial \psi}{\partial x}, \tag{4.42}$$

A series representation for ψ satisfying the periodicity in x direction, on a flow of mean velocity $-\bar{u}$, with depth h can be written as:

$$\psi(x,z) = -\bar{u}(h+z) + \left(\frac{g}{k^3}\right)^{1/2} \sum_{j=1}^{N} B_j \frac{\sinh jk(h+z)}{\cosh jkh} \cos jkx, \tag{4.43}$$

where the B_j coefficients are dimensionless. The expression (4.43) also satisfies the bottom boundary condition at $z = -h$, i.e., $\psi = 0$. The free surface is a streamline on which $\psi = -Q = q - \bar{u}h$ is a constant. The kinematic free-surface boundary condition is to be satisfied at each of the $N+1$ points on the free surface, $kx_m = m\pi/N$ ($x_m = mL/2N$), that is:

$$f_{m+9} = -q(k^3/g)^{1/2} - k\eta_m \bar{u}(k/g)^{1/2} + \sum_{j=1}^{N} B_j \left[\frac{\sinh j(kh + k\eta_m)}{\cosh jkh}\right] \cos\frac{jm\pi}{N} = 0, \tag{4.44}$$

for m $= 0, 1, ..., N$.

For the case of infinitely deep water, the term in the bracket is replaced by $\left[e^{jk\eta_m}\right]$. The other boundary condition is that the pressure should be constant on the surface. It follows from Bernoulli's equation (3.6) that:

$$\frac{1}{2}\left[\left(\frac{\partial \psi}{\partial x}(x,\eta(x))\right)^2 + \left(\frac{\partial \psi}{\partial y}(x,\eta(x))\right)^2\right] + g(\eta(x)+h) = R. \tag{4.45}$$

where R is a constant. Introducing $r = R - gh$ so that deep water case can be treated,

and substituting the series for ψ from (4.43) gives:

$$\begin{aligned} f_{N+10+m} = \frac{1}{2}\left(-\bar{u}(k/g)^{1/2} + \sum_{j=1}^{N} jB_j \left[\frac{\cosh j(kh+k\eta_m)}{\cosh jkh}\right]\cos\frac{jm\pi}{N}\right)^2 \\ + \frac{1}{2}\left(\sum_{j=1}^{N} jB_j \left[\frac{\sinh j(kh+k\eta_m)}{\cosh jkh}\right]\sin\frac{jm\pi}{N}\right)^2 + k\eta_m - \frac{rk}{g} = 0. \end{aligned} \tag{4.46}$$

for m $= 0, 1, ..., N$.

This completes the set of $2N + 10$ nonlinear equations in $2N + 10$ variables, however in this thesis the case without the presence of currents is considered.

The system of equations can be written as:

$$\mathbf{f}(\mathbf{z}) = (f_i(\mathbf{z}),\ i = 1, 2, ..., 2N + 10) = 0, \tag{4.47}$$

This system is solved iteratively by Newton's method. If an approximate solution after n iterations is denoted by $\mathbf{z}^{(n)}$, to give a better approximation $\mathbf{z}^{(n+1)}$ the method requires solution of the following linear matrix equation at each iteration until the sequence of solution vectors is converged:

$$\left[\frac{\partial f_i}{\partial z_j}\right]^{(n)} \left(\mathbf{z}^{(n+1)} - \mathbf{z}^{(n)}\right) = -\mathbf{f}\left(\mathbf{z}^{(n)}\right) \tag{4.48}$$

This is the method applied by Rienecker and Fenton [67], and was determined to converge quickly to a solution. The Jacobian matrix is obtained by differentiating each of the equations with respect to each of the variables. The derivatives are calculated numerically. If the variable z_j is changed by an amount δj, then the derivative of equation i with respect to variable z_j is obtained by:

$$\frac{\partial f_i}{\partial z_j} \approx \frac{f_i\left(z_1, z_2, ..., z_j + \delta j, ..., z_{2N+10}\right) - F_i\left(z_1, z_2, ..., z_j, ..., z_{2N+10}\right)}{\delta j} \tag{4.49}$$

and the whole Jacobian matrix is determined by evaluation of each of the $2N + 10$ equations a total of $2N + 10$ times. A fixed value of δj equal to 10^{-8} was chosen for the present computations. The initial estimate for the wave number is obtained from the linear

dispersion relation and initial estimates for all other variables are given in Table 4.1. For very large waves it was found that the Stokes approximation was not a sufficiently accurate initial estimate of the solution and this method failed to converge. In such a situation it was necessary to extrapolate to the initial approximation from converged solutions for lower-amplitude waves. Convergence of the discussed Fourier approximation method is shown in Figure 4.2 for different values of H/h, in water depth of $2m$, and wave period $T = 4s$.

It is observed that the exact fully nonlinear solution is sharp-crested with a flatter trough, while the distance between crest and trough remains constant. For larger waves the number of iterations to converge increased.

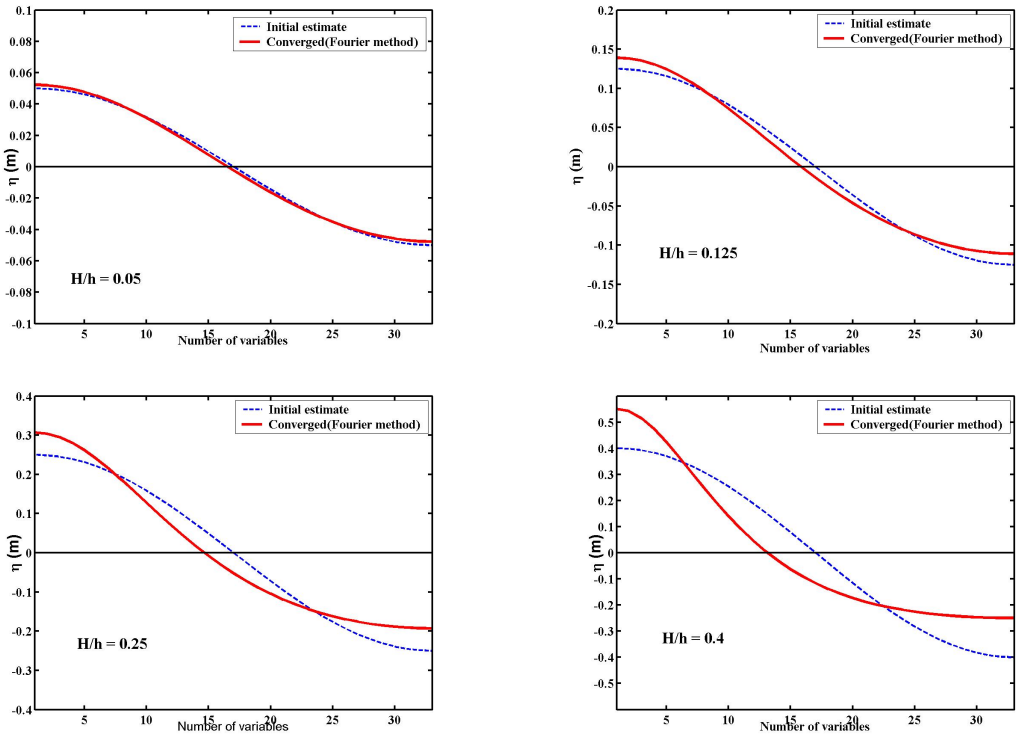

Figure 4.2: Initial linear estimates and computed wave profiles by Fourier approximation method for $L/h \approx 9$.

Verifying the pseudo-spectral formulation of normal velocity on the free surface

The outward normal derivative of the velocity potential on the free surface may be written as:

$$\frac{\partial \phi}{\partial n} = \nabla \phi \cdot \hat{n} = \frac{(\nabla \phi) \cdot (\nabla G)}{|\nabla G|}, \tag{4.50}$$

where $G = z - \eta(x,t)$, and

$$\frac{\partial \phi}{\partial n} = \frac{\phi_z - \phi_x \eta_x}{(1+\eta_x^2)^{\frac{1}{2}}} = \frac{\eta_t}{(1+\eta_x^2)^{\frac{1}{2}}} \tag{4.51}$$

The kinematic free surface boundary condition which relates the velocities at the free surface can now be re-written as:

$$\eta_t = \frac{\partial \phi}{\partial n} \left(1+\eta_x^2\right)^{\frac{1}{2}}. \tag{4.52}$$

The term on the right-hand side of (4.52) is the normal velocity on the free surface and is denoted by u_n. One can obtain u_n by calculating the value of $W - U\eta_x$. The steps taken to verify the pseudo-spectral formulation are as follow:

- Values of η, U, and W are first calculated for fully nonlinear system by a Fourier approximation method, and the corresponding u_n is calculated and used as a bench mark.
- Having obtained the free surface variables from fully nonlinear solution, tangential velocity on the free surface u_s is calculated from the relation $u_s = U + W\eta_x$.
- so-calculated values of η and u_s are substituted into the right-hand sides of the evolution equations (3.46), (3.48), and (3.50) to obtain η_t (which approximates the u_n), and the result is compared with the value of u_n from exact solution.

For the steep waves with $\epsilon = 0.3$ the linear theory did not provide a good initial estimate, and the iteration did not converge to a solution. For a wave height H this difficulty was overcome by taking the following steps:

- The problem is first solved for a smaller-amplitude wave H_1 using the initial estimate $\mathbf{z}_1$ from the linear theory which is given in Table 4.1. The converged accurate solution is stored as $\mathbf{Z}_1$.

- The initial wave height H_1 is increased by ΔH, giving a new wave height H_2. In the present work, $\Delta H = 0.05m$ was used. Again, the linear solution from Table 4.1 is used as an initial estimate $\mathbf{z}_2$ for the iterative solution. The converged solution vector is stored as $\mathbf{Z}_2$.

- The following linear extrapolation is used to obtain the initial estimate $\mathbf{z}_3$ for a higher wave height $H_1 + 2\Delta H$:

$$\mathbf{z}_3 = 2\mathbf{Z}_2 - \mathbf{Z}_1 \tag{4.53}$$

- The process repeats until the desired wave height H is achieved.

The first, second, and third-order closure expression in pseudo-spectral model are compared with the results of the Fourier method taken as a benchmark.

Figure 4.3 shows the comparison of u_n profiles calculated by pseudo-spectral method with those calculated by Fourier approximation. For small-amplitude waves with mild steepness ($\epsilon = 0.05$) the u_n profiles calculated by different orders of pseudo-spectral method are close, however for steeper and higher-amplitude waves ($\epsilon = 0.2, 0.3$), the difference becomes more significant, since the lower-order approximations are not able to capture the nonlinearity and asymmetry of wave profiles well.

Table 4.2 summarizes the maximum absolute errors in calculating u_n for different orders of approximation and a range of wave steepness ϵ. The order of approximation can be verified by looking at the rate at which the error decreases with higher-order approximations. In these calculations 64 points per wave length were used. For any order of approximation the results converge to a limit exponentially fast as the number of modes N (or grid points) is increased. In practice, an order of approximation is first selected so that a given accuracy can be achieved and then the number of modes N is optimally chosen to limit the round-off errors.

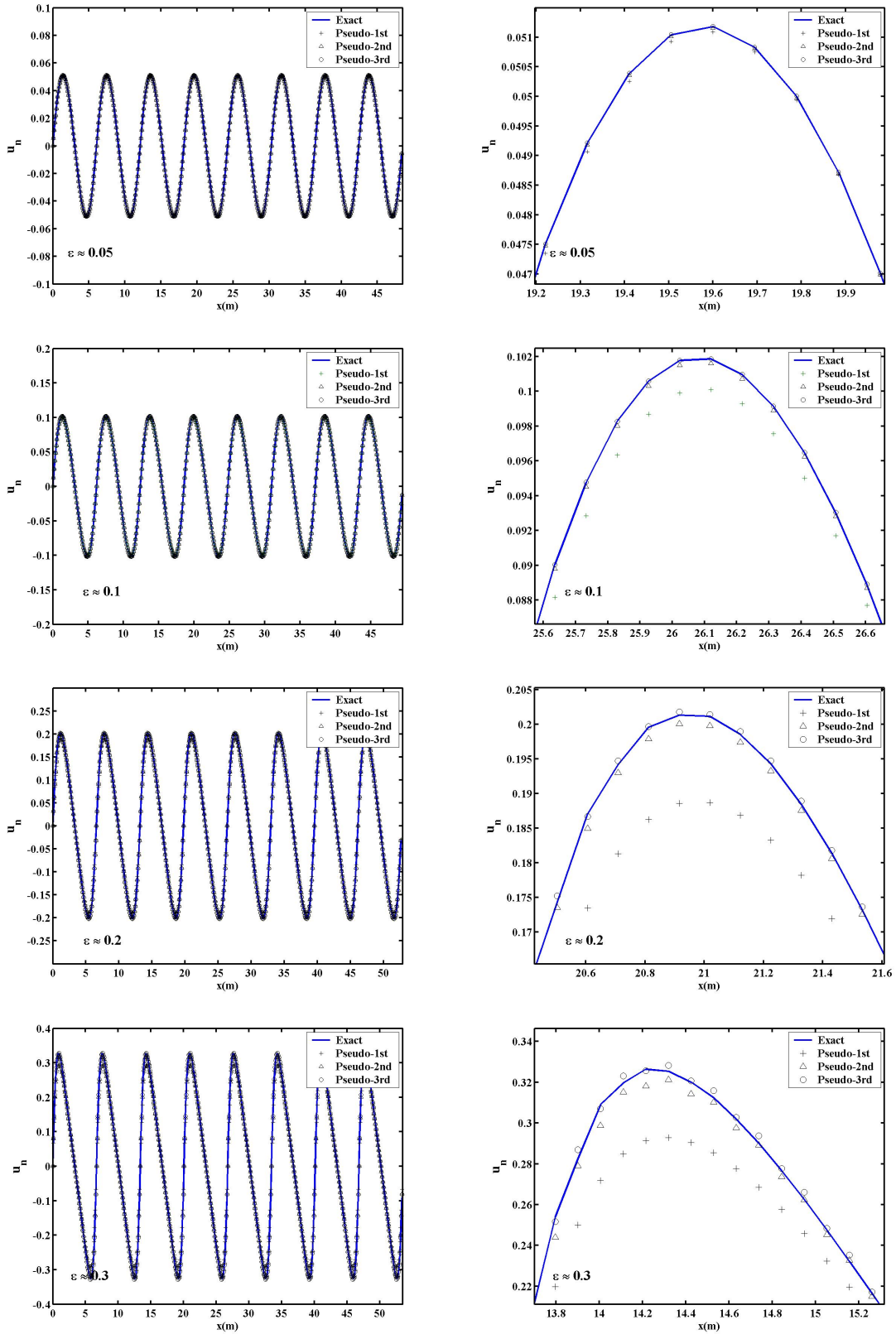

Figure 4.3: Comparison of dimensionless normal velocity profile u_n for 1st, 2nd, and 3rd-order pseudo-spectral method with exact solutions. $h = 2m, T = 2s$.

Steepness(ϵ)	first order	second order	third order
0.05	1.27×10^{-4}	2.85×10^{-5}	7.30×10^{-6}
0.1	9.74×10^{-4}	2.84×10^{-4}	2.13×10^{-5}
0.2	1.39×10^{-2}	4.77×10^{-3}	3.72×10^{-3}
0.3	3.73×10^{-2}	1.15×10^{-2}	8.80×10^{-3}

Table 4.2: Maximum absolute error in the free surface normal velocity u_n of a periodic wave of steepness ϵ for different pseudo-spectral approximations.

In order to check the accuracy of the pseudo-spectral method for shallow water applications a shallow water wave with shallowness parameter $kh = 0.2$ was calculated using the Fourier approximation method and its u_n profile was compared with that from pseudo-spectral method with different orders of approximation. Figure 4.4 shows the comparison.

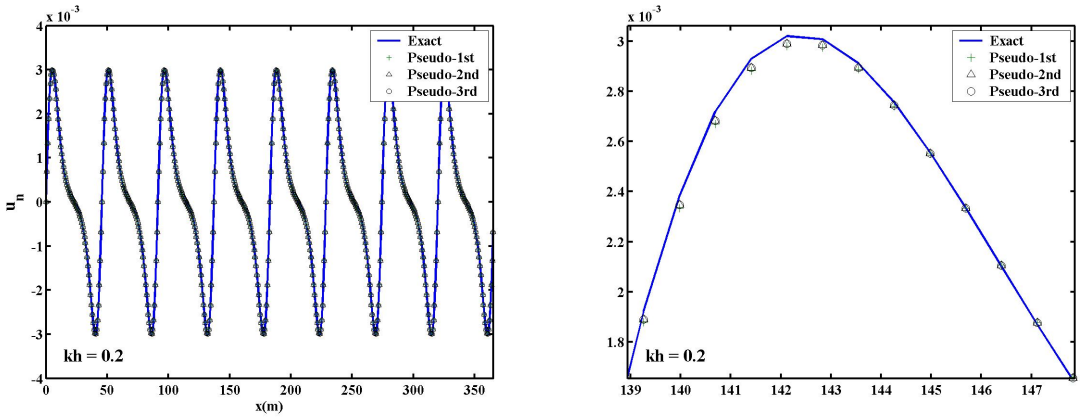

Figure 4.4: Comparison of dimensionless normal velocity profile u_n for 1st, 2nd, and 3rd-order pseudo-spectral method with exact solution. $h = 1.5m, T = 12s$.

Since the steepness parameter ϵ was used to derive the evolution equations, and for the shallow water, the parameter kh has a dominant effect, there is no significant difference among different pseudo-spectral approximations.

4.2.3 Test with progressive waves

Traveling of periodic waves is investigated in this section. In addition to the preservation of the wave profile, special attention is paid to the conservation of energy during the simulations. The initial conditions for η and u_s are prescribed from the fully nonlin-

ear solution using Fourier method for a specified steepness parameter ϵ, and the wave is allowed to propagate freely across the computational domain. Third-order evolution equations (3.50)- (3.51) are used to evolve the wave profile. Figure 4.5 shows a comparison of surface elevation and tangential velocity at three different times $t/T = 10, 20, 40$, for fundamental wave period T, for a wave of steepness $\epsilon = 0.1$, while Figures 4.6 and 4.7 show the comparison for $\epsilon = 0.2$ and $\epsilon = 0.3$, respectively.

Notice that the fully nonlinear solution obtained by the Fourier series truncation method differs from the traveling wave solution of the third-order system (3.50)- (3.51), and is expected to lose accuracy when the value of ϵ is increased. For the simulations with $\epsilon = 0.1$ and $\epsilon = 0.2$, 64 points per wavelength were used with a total of 512 Fourier modes (8 wavelengths), while for the case $\epsilon = 0.3$, 128 points per wavelength were used with a total number of 1024 Fourier modes. As shown in Figures 4.5 and 4.6, the initial shape and amplitudes of the free surface elevation and tangential velocity profiles are well preserved even after 40 wave periods. Even for $\epsilon = 0.3$ which is about 70% of the theoretical highest wave (with $\epsilon \approx 0.44$), the wave profile is preserved well after 20 wave periods. However for this case some short-wave length instabilities were observed after $t/T \approx 30$, which may be prevented by decreasing the cut-off wave number in the filtering process without affecting the energy conservation significantly. In all these computations the time step size was chosen as $\Delta t = T/40$.

A good estimate of the phase error between the numerical solution and the exact solution is to compare the numerical phase speed c_{num} with the exact phase speed c_{exact}. Table 4.3 summarizes the phase velocity errors for different values of wave steepness parameter ϵ.

ϵ	$\frac{(c_{num}-c_{exact})}{c_{exact}} \times 100$
0.1	0.1035
0.2	0.1215
0.3	0.293

Table 4.3: errors between numerical and exact phase velocities for three different values of wave steepness parameter $\epsilon = 0.1, 0.2, 0.3$.

In order to check the conservation of energy and momentum, these quantities were carefully monitored during the simulations. For one-dimensional flows, from (3.53), the

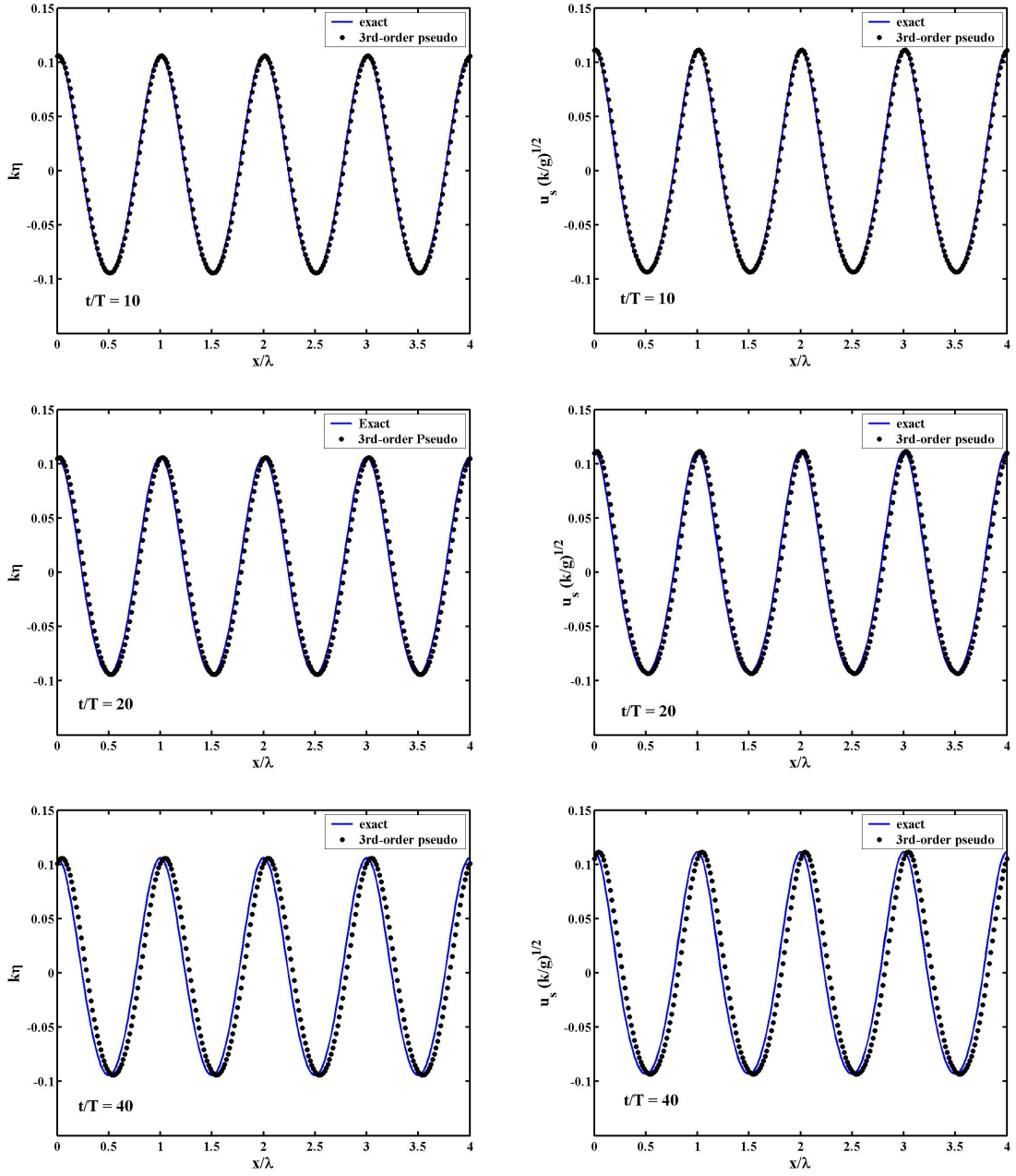

Figure 4.5: Comparison of numerical solution for η and u_s with exact solutions after a traveling time of $t/T = 10, 20,$ and 40. For this computation, the wave steepness, $\epsilon \approx 0.1$, and 64 points per wave length were used.

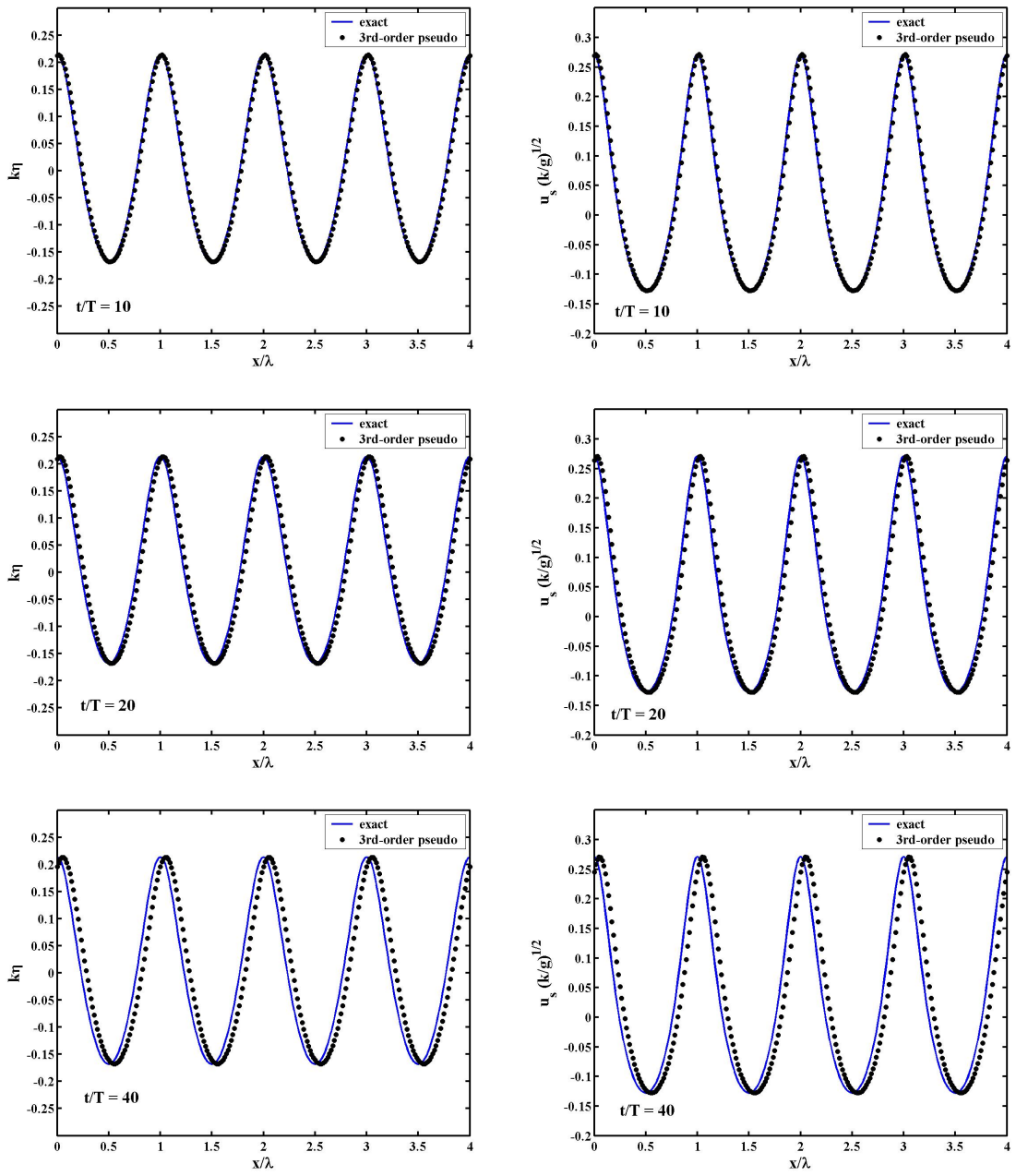

Figure 4.6: Comparison of numerical solution for η and u_s with exact solutions after a traveling time of $t/T = 10, 20,$ and 40. For this computation, the wave steepness, $\epsilon \approx 0.2$, and 64 points per wave length were used.

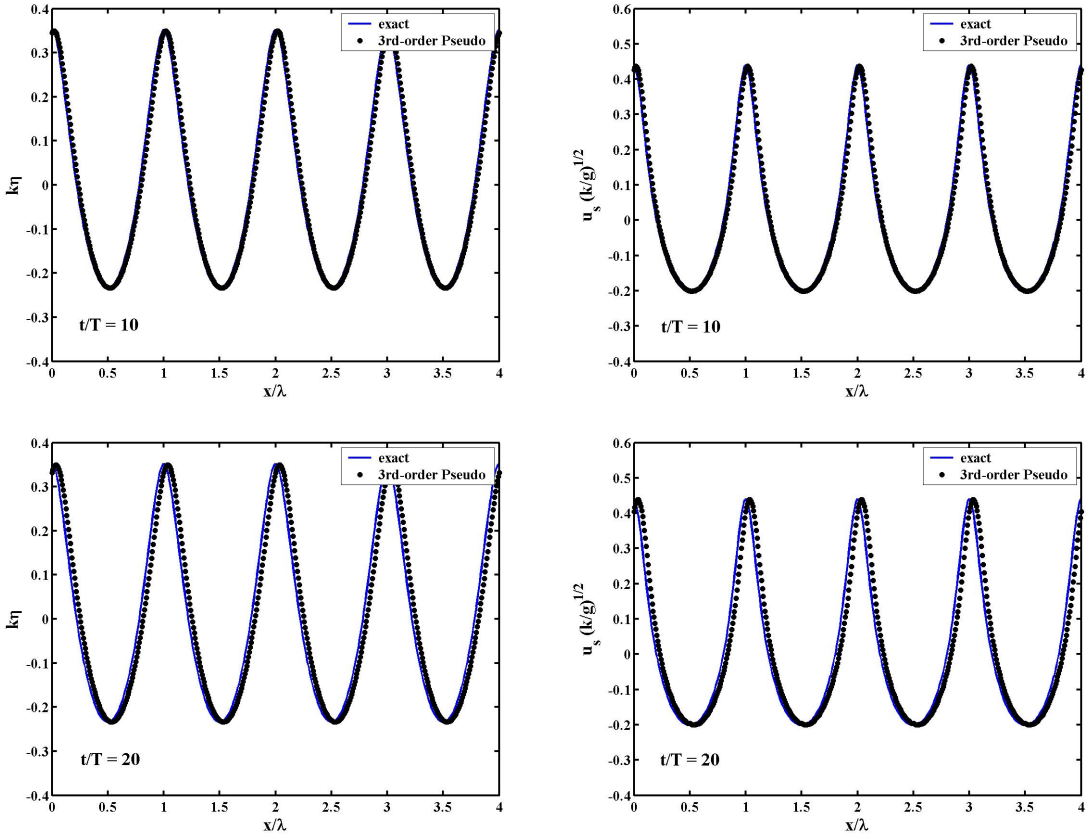

Figure 4.7: Comparison of numerical solution for η and u_s with exact solutions after a traveling time of $t/T = 10, 20$. For this computation, the wave steepness, $\epsilon \approx 0.3$.

kinetic energy E_k and potential energy E_p are given as:

$$\begin{aligned} E_k &= \frac{1}{2}\int_x \left[\eta\Phi_x^2 - \Phi\mathcal{L}[\Phi] - \eta\left(\mathcal{L}[\Phi]\right)^2 - \eta^2\Phi_{xx}\mathcal{L}[\Phi] - \left(\eta\mathcal{L}[\Phi]\right)\mathcal{L}\left[\eta\mathcal{L}[\Phi]\right]\right]\mathrm{d}x, \\ E_p &= \frac{1}{2}\int_x g\eta^2\mathrm{d}x \end{aligned} \tag{4.54}$$

From (3.56), the total momentum for one-dimensional waves can be obtained by:

$$I = \int_x \eta\Phi_x\mathrm{d}x. \tag{4.55}$$

Table 4.4 shows the variation of the potential energy E_p, kinetic energy E_k, total energy E_t, and total momentum I during the numerical simulations for two values of wave steepness $\epsilon = 0.05, 0.1$.

t/T	$\epsilon = 0.05$				$\epsilon = 0.1$			
	$\mathbf{E}_p$	$\mathbf{E}_k$	$\mathbf{E}_t$	**I**	$\mathbf{E}_p$	$\mathbf{E}_k$	$\mathbf{E}_t$	**I**
0	0.28618	0.28835	0.57453	0.18915	1.1065	1.11929	2.22580	0.72942
5	0.28617	0.28834	0.57451	0.18914	1.1063	1.11935	2.22570	0.72938
10	0.28616	0.28832	0.57448	0.18913	1.1061	1.11947	2.22557	0.72935
15	0.28615	0.28830	0.57446	0.18913	1.1058	1.11962	2.22546	0.72933
20	0.28616	0.28827	0.57443	0.18913	1.1056	1.11978	2.22536	0.72934
25	0.28616	0.28824	0.57441	0.18914	1.1053	1.11992	2.22526	0.72937
30	0.28618	0.28821	0.57439	0.18914	1.1051	1.12003	2.22516	0.72942
35	0.28620	0.28816	0.57436	0.18916	1.1050	1.12008	2.22508	0.72949
40	0.28622	0.28812	0.57434	0.18918	1.1049	1.12007	2.22501	0.72958

Table 4.4: Variation of the potential energy E_p, kinetic energy E_k, total energy E_t, and momentum I during the simulation of progressive waves for $\epsilon = 0.05$ and $\epsilon = 0.10$.

Table 4.5 shows the same quantities for $\epsilon = 0.2$.

Tables 4.4 and 4.5 apparently show that the applied third-order pseudo-spectral model conserves total energy to 0.033%, 0.035%, and 0.061% after 40 wave periods, for the cases $\epsilon = 0.05, 0.1$, and 0.2, respectively, while the momentum is conserved to 0.016%, 0.022%, and 0.056% for $\epsilon = 0.05, 0.1$, and 0.2, respectively.

t/T	$\epsilon = 0.2$			
	$\mathbf{E}_p$	$\mathbf{E}_k$	$\mathbf{E}_t$	**I**
0	4.97092	5.10672	10.07764	3.16909
5	4.96396	5.11261	10.07657	3.16867
10	4.97058	5.10495	10.07553	3.16849
15	4.96491	5.10953	10.07444	3.16837
20	4.96844	5.10522	10.07366	3.16858
25	4.96750	5.10537	10.07287	3.16889
30	4.96676	5.10555	10.07231	3.16938
35	4.97089	5.10100	10.07188	3.17010
40	4.96637	5.10504	10.07140	3.17084

Table 4.5: Same as Table 4.4 for $\epsilon = 0.2$.

4.2.4 Two-dimensional Modulation Instability(Initial Value Problem)

In order to evaluate the performance of the third-order pseudo-spectral model in predicting the Benjamin-Feir instability, the evolution of a progressive wave train subject to small side-band perturbations is investigated. A brief background on the problem is given first.

Theoretical Background

Benjamin and Feir [5] performed a perturbation analysis of the uniform wave train based on the Euler equations and showed that a wave train with initial amplitude a_c, wave number k_c and frequency ω_c is unstable to perturbations with frequency $\delta\omega$, when the following condition is satisfied:

$$0 < \hat{\delta} \leq \sqrt{2}, \tag{4.56}$$

where $\hat{\delta} \equiv \delta\omega/\epsilon\omega_c$, and $\epsilon = a_c k_c$, the steepness of the carrier wave. The modulation instability is considered as an interaction among three mono-chromatic wave trains: carrier

wave(ω_c), upper (ω_+), and lower (ω_-) side-bands, that satisfy the following conditions:

$$2\omega_c = \omega_+ + \omega_-,$$

$$\omega_\pm = \omega_c \pm \delta\omega, \tag{4.57}$$

$$2k_c = k_+ + k_- + \Delta k,$$

where Δk is a small mismatch of the wavenumber from Phillips [63] four-wave resonance conditions for infinitesimal waves. Due to the cancelation of this resonant de-tuning in the presence of amplitude dispersion, side-bands grow exponentially, and the growth rate $\mathrm{d}(\ln a)/\mathrm{d}(kx)$, as predicted by Benjamin and Feir [5] is given by:

$$\beta = \epsilon^2 \hat{\delta} \left(2 - \hat{\delta}^2\right)^{1/2}, \tag{4.58}$$

As pointed out by Phillips, the interaction between surface gravity waves is very weak in the sense that they exchange energy only through the four-wave resonant interaction. In order to detect the effect of such a weak interaction, one needs to trace the evolution of the wave field for a sufficiently long time. There are several numerical approaches that have been used to predict the long-term evolution of gravity waves:

- Nonlinear Schrodinger (NLS) equation.
- Modified NLS (Dysthe's model).
- Kinetic equations (Zakharov's equation).
- Higher Order Spectral (HOS) methods.
- Fully Nonlinear (FNL) computations.

Original NLS equation and its further modifications ([22]) are considered to be weakly nonlinear formulations which are based on the narrow-banded assumption. When the instability occurs in the wave train, the energy starts to be transferred to a broader band,

thus, these simplified models fail to describe the large-amplitude wave events that occur beyond their time range of validity.

In High-Order Spectral methods the velocity potential on the free surface is expanded about the mean surface in terms of the wave steepness parameter ϵ, and the free surface variables are represented as truncated Fourier series whose coefficients are calculated using Fast Fourier Transform with the assumption of periodicity. The free surface variables in these methods are evolved in physical space.

Kinetic equations which were originally introduced by Zakharov [86], are based on the Hamiltonian formalism of the water wave problem. These methods interpret a wave field as a superposition of component waves with different Fourier amplitudes. These amplitudes are evolved in Fourier space and the nonlinear terms are expressed as convolution integrals. It was shown that HOS formulation of West et al. with third-order nonlinearity is equivalent to the Zakharov's equation (Tanaka [74]).

Landrini et al. [42] investigated the above-mentioned models systematically and compared the results with experimental measurements in a large tank as well as a high-resolution fully nonlinear model (FNL) based on boundary integral equations. Figure 4.8 shows the comparisons of the evolution of a system beginning as a carrier wave with steepness $k_c a_c = 0.1$ and frequency ω_c, plus two closely-spaced side-bands with frequencies $\omega_c \pm \delta\omega$, using Krasitskii [40], NLS, and Dysthe method, with FNL used as a benchmark.

Figure 4.8 corresponds to a non-breaking condition. As shown in the figure, the lower side-band $\delta\omega_-$, grows more relative to the upper one, $\delta\omega_+$, in contrast to well-known results based on NLS, but as predicted by Krasitskii and Dysthe. Figure 4.9 displays the initial growth rates computed by Landrini et al. based on Krasitskii's model. This plot is very useful in setting up wave tank experiments and can be used as a benchmark to validate the third-order pseudo-spectral model.

Numerical Calculations

In order to validate the third-order pseudo-spectral model, the long-time evolution of a progressive wave train subject to side-band perturbations is studied numerically. The

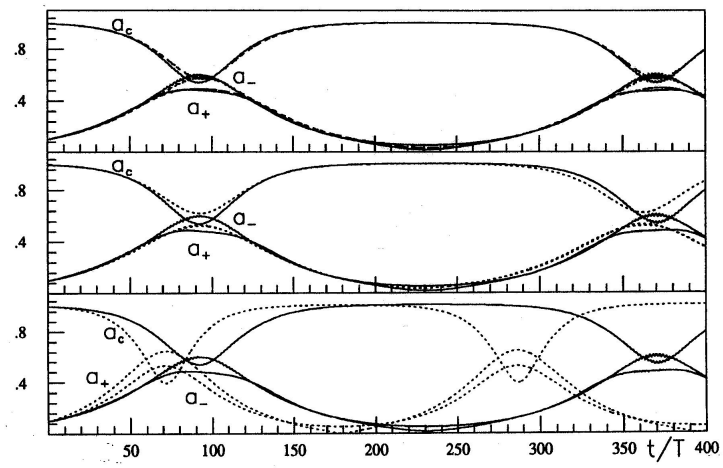

Figure 4.8: Time evolution of Fourier components normalized with the initial value a_c; from top down, the FNL solution (solid lines) versus weakly nonlinear solutions(dashed lines): Krasitskii-model(upper), Dysthe equation(middle), and NLS-equation. From Landrini et. al. [42].

following initial condition was used in the simulation:

$$\eta(x,0) = a_c \cos(k_c x) + a_+ \cos(k_1 x - \phi_1) + a_- \cos(k_2 x - \phi_1). \tag{4.59}$$

where the career wave steepness $k_c a_c = 0.10$, and for the side-bands, $k_1/k_c = 0.8$, and $k_2/k_c = 1.2$. Initial phase shift ϕ_1 was $\pi/4$, and the side-band amplitudes $a_+/a_c = a_-/a_c = 0.1$ were used. Total computational domain was $L_x = 50L$, where $L = 2\pi/k_c$. Initial condition for the free surface tangential velocity was calculated using the linear approximation:

$$b_n(0) = \sqrt{g|k|}a_n(0). \tag{4.60}$$

where $a_n(0)$ and $b_n(0)$ are the Fourier coefficients of the surface elevation $\eta(x,0)$, and tangential velocity $u_s(x,0)$, respectively, assuming the deep water condition. A total number of 2048 Fourier modes were used (more than 40 points per carrier-wave length). The time step $\Delta t = T_c/50$ was chosen in the simulation, where T_c is the carrier wave period which was $2s$ in this example. Evolution of the initial wave profile (4.59) is shown in Figure 4.10.

Notice that the highest wave amplitude at $t = 92.5T_c$ is almost three times the initial carrier wave amplitude. Wavenumber spectra clearly shows the spreading of energy from the main wave to the side-bands. An increase in the amplitude of the lower side-band relative to

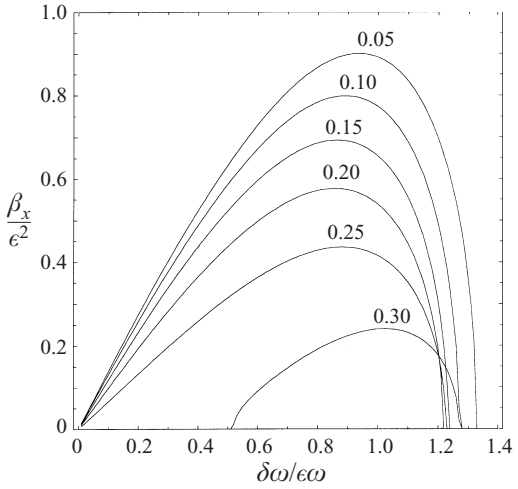

Figure 4.9: Initial growth rate, β_x, of the side-band, based on Krasitskii's reduced four-wave interaction equation (1994) for steepness values of $\epsilon = 0.05$, 0.01, 0.15, 0.2, 0.25, and 0.3, plotted against the normalized modulational frequency (From [76]).

the upper one as the peak modulation is approached (around $t = 92.5T_c$), is clearly observed in wavenumber spectra and Figure 4.11, as confirmed by experiments of Lake et al. [41] and the results of Landrini et al. (see Figure 4.8). As discussed before, Nonlinear Schrodinger model is based on narrow-bandedness assumption. The spectrum becomes wide-banded as time increases, therefore, the NLS model loses accuracy in predicting the fore-mentioned behavior.

The peak modulation point is very close to the one predicted by FNL and Dysthe models, however, beyond $t = 350T_c$ because of the filtering applied to higher harmonics to remove the aliasing, energy starts to decrease globally. This problem prevents the model from predicting the second cyclic recurrence of the modulation/de-modulation behavior as clearly as the one reported by Landrini et al. [42]. Dommermuth and Yue [21] reported a similar problem.

4.2.5 Two-dimensional Modulational Instability(Validation with Laboratory Experiments)

In January 2007, a set of three-dimensional laboratory experiments were conducted to study the evolution and interaction of nonlinear surface waves in a multi-directional wave

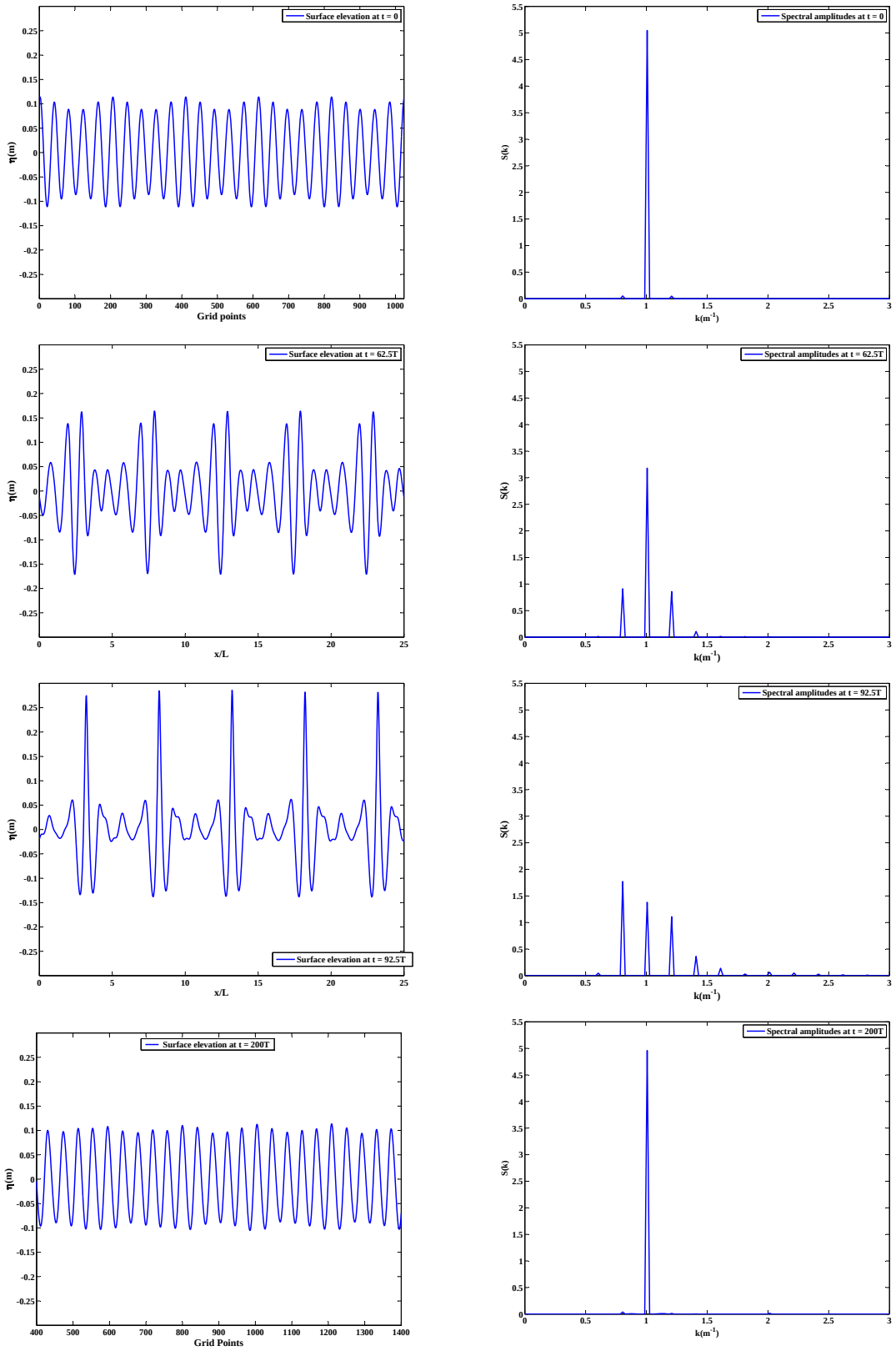

Figure 4.10: Benjamin-Feir instability: numerical solutions of the third-order model for surface elevation η and wavenumber spectra at times t = 0, $62.5T_c$, $92.5T_c$, $200T_c$. Initial wave profile is given by (4.59).

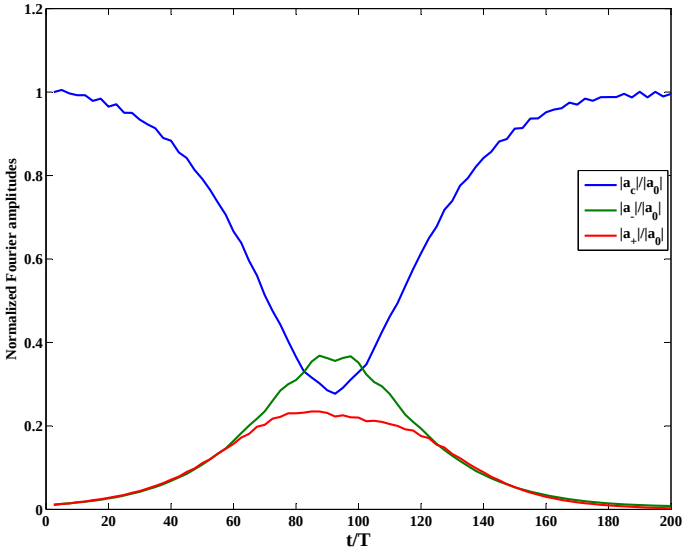

Figure 4.11: Time evolution of Fourier components of the main mode and side-bands, normalized with the initial value a_c calculated by the third-order pseudo-spectral model.

basin at the Institute of Ocean Technology (IOT) in Canada. The basin is a rectangular wave tank of 75m by 32m (including the wave generation and wave absorption areas) with water depth of 2.5m. The basin is equipped with a multi-segmented piston-type wavemaker in an "L" configuration. The wavemaker is able to generate both long-crested and short-crested waves. Twenty wave probes are installed on a 25m long boom (see Figures 4.12 and 4.13), with four extra wave probes at the four corners of the basin. A current-meter is also located at the center of the boom.

The numerical model was configured as a boundary-value problem with an internal (pneumatic) wavemaker used to generate waves inside the computational domain. Outgoing waves are absorbed in damping (sponge) layers placed at both ends of the computational domain. In the following section the implementation of the numerical wave tank in the model is discussed in details.

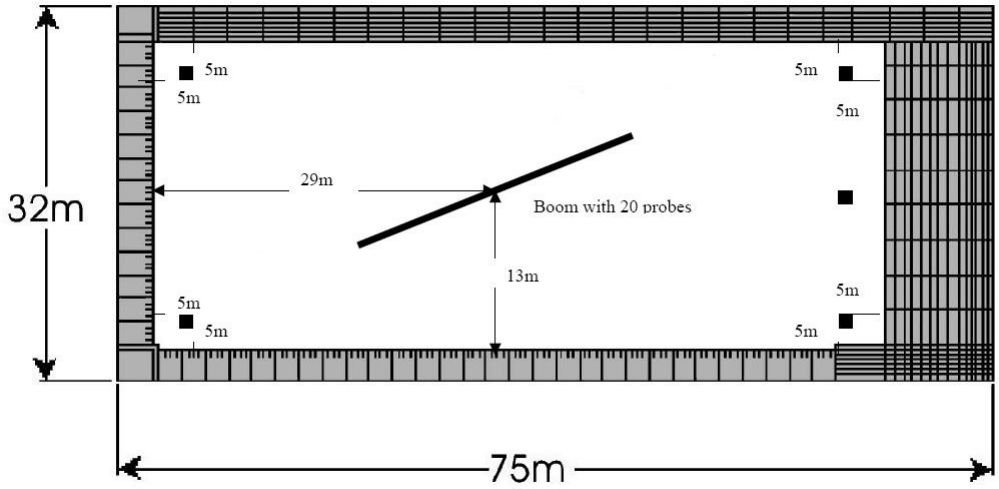

Figure 4.12: Layout of the experimental setup in the wave basin and wave probes.

Numerical Wave Tank

To generate waves from rest, a pneumatic wavemaker is used in which a pressure distribution is prescribed at the free surface which involves a generating term ∇p_G (with p_G being the pressure distribution on the surface), and a dissipative term D_u (wave absorber). A damping term D_η is also included in the kinematic free surface boundary condition. Therefore the free surface evolution equations (4.11) are modified as follows:

$$\begin{aligned} \eta_t &= f(\eta, u_s) + D_\eta, \\ u_{s,t} &= g(\eta, u_s) - \nabla p_G + D_u, \end{aligned} \tag{4.61}$$

Pneumatic wave makers are numerically more efficient that paddle wave makers. For example, the singularity at the intersection between the free surface and a partially submerged paddle wave maker is avoided by using the pneumatic wave maker. The linear theory of generating waves by pressure distribution on the surface is described by Wehausen and Laitone [79].

A multi-chromatic wave (with M components) of angular frequencies ω_j is generated

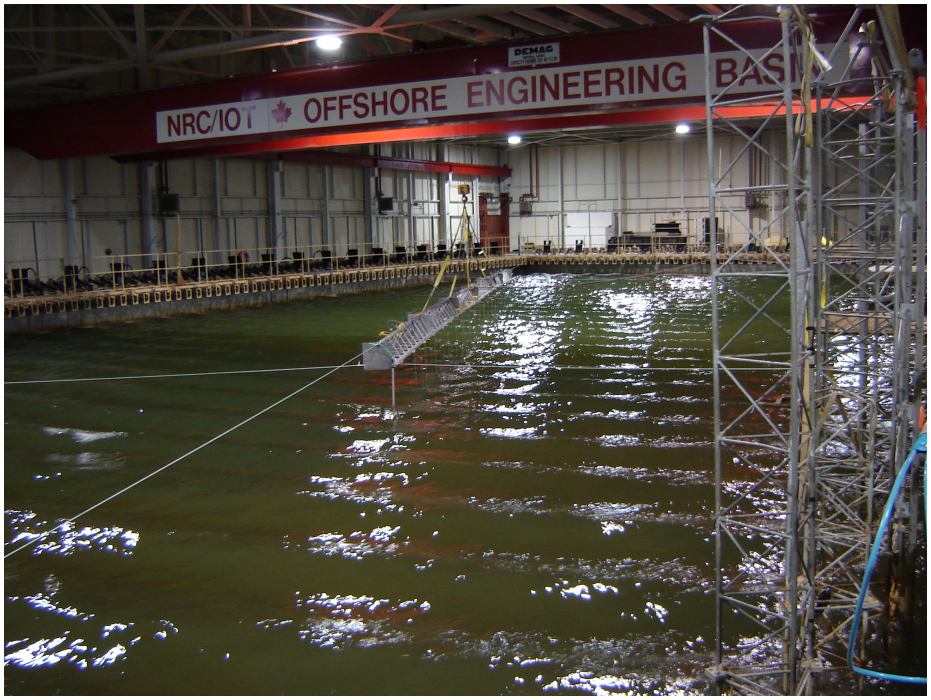

Figure 4.13: Generation of multi-directional waves and arrangement of wave probes.

from rest choosing a pressure distribution of the form:

$$p_G(\mathbf{x}, t) = \sum_{j=1}^{M} \sin(\omega_j t + \varphi_j) P_j(\mathbf{x}) H(t), \tag{4.62}$$

where φ_j are the constant phase shifts, P_j are localized functions in space, and H is a ramping function to impose the pressure on the surface gradually. The following expression was used for $H(t)$:

$$H(t) = \begin{cases} \frac{1}{2}\left[1 - \cos\left(\frac{\pi t}{t_s}\right)\right] & \text{for } t \leq t_s \\ 1 & \text{for } t > t_s \end{cases} \tag{4.63}$$

In order to generate two-dimensional waves that propagate along the $x-$axis, the functions P_j are chosen of the form:

$$P_j = A_j e^{-x^2/2\lambda_j^2}, \tag{4.64}$$

Since the pseudo-spectral method is used in this work, the analytical expression for

Fourier coefficients of P_j can be written as:

$$\hat{P}_j = \sqrt{2\pi} A_j \lambda_j e^{-k^2\lambda_j^2/2} \delta(k_1), \tag{4.65}$$

where A_j and λ_j are constants and δ is the Dirac function. This even function is localized, smooth, monotonic and rapidly decaying in both physical and Fourier space. To generate waves with amplitudes a_j and wavenumbers k_j (given by $\omega_j = \sqrt{gk_j \tanh k_j h}$) in the far-field, one must take([79]):

$$\lambda_j = \frac{1}{k_j}, \quad A_j = g a_j \sqrt{\frac{e}{2\pi}} \left(1 + \frac{2k_j h}{\sinh 2k_j h}\right). \tag{4.66}$$

the parameters a_j and φ_j can be tuned to model different sea states, for example a JONSWAP spectrum.

Waves propagating out of the domain are absorbed in damping regions at both ends of the computational domain. Dissipation of wave energy in these damping layers is achieved by introducing a term proportional to the surface elevation into the right-hand side of the mass equation:

$$D_\eta = -\mu(x)\eta, \tag{4.67}$$

and a term proportional to the free surface tangential velocity into the right-hand side of the momentum equation:

$$D_u = -\mu(x) u_s, \tag{4.68}$$

where the function $\mu(x)$ corresponds to the damping strength with unit of s^{-1}. Introduction of such damping terms leads to the non-conservation of mass and momentum inside the damping layers. However, extensive tests with different combinations of damping terms showed that the inclusion of damping terms in both the mass and momentum equations was more effective than just a damping term in the momentum equation.

Numerical simulations to evaluate the performance of the damping layer showed that waves could be effectively damped out in a layer of one-wave length wide by employing a

quadratic variation of $\mu(x)$ with a peak value of $\mu_0 = 30/T$, where T is the wave period. The following expression was used for $\mu(x)$ in the simulations:

$$\mu(x) = \begin{cases} \left[1 - \left(\frac{x}{x_d}\right)^2\right] \mu_0 & \text{for } 0 < x < x_d, \\ 0 & \text{for } x_d < x < L - x_d, \\ \left[1 - \left(\frac{L-x}{x_d}\right)^2\right] \mu_0 & \text{for } L - x_d < x < L, \end{cases} \tag{4.69}$$

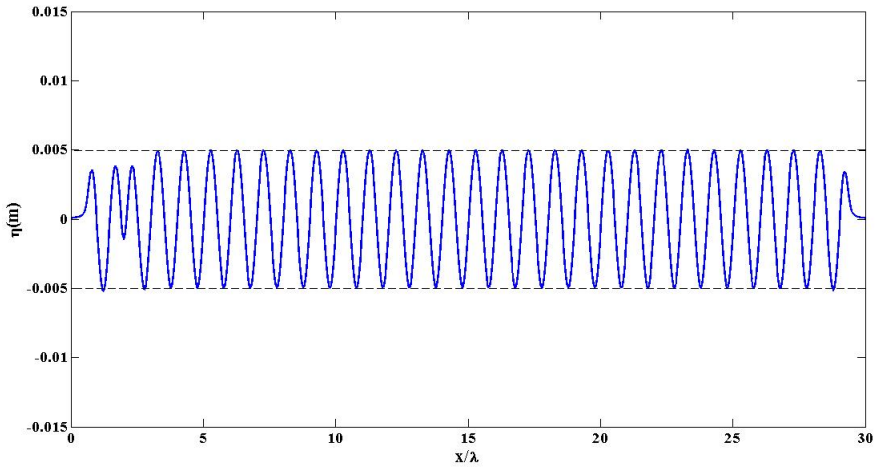

Figure 4.14: Wave generation and absorption using pneumatic wave maker and sponge layers. The incident wave is a small wave of amplitude $a = 0.005m$ and period $T = 1s$, moving from left to right on a constant depth, after propagating for 100 wave periods.

As illustrated in Figure 4.14, a regular wave of amplitude $a = 0.005m$, and period $T = 1s$ is generated, moving from left to right on constant depth (deep water condition). Simulation was continued up to time $t/T = 100$, with ramp-function parameter $t_s/T = 10$. The internal wave maker is located two-wave lengths away from the left boundary (one-wave length away from the damping zone).

The described numerical wave tank was set up and implemented with the prescribed properties in order to compare the numerical model predictions of the Benjamin-Feir-type instabilities with the experimental measurements. The incident wave train had a principal wave with a frequency of 1 Hz and height of 6 cm, and two side-bands with frequencies of 0.9 Hz and 1.1 Hz and heights of 1cm. Waves were measured in the basin (see Figure 4.12)

with 20 probes mounted on the 25-m long boom in the middle of the basin at a spacing of 1.2m. As illustrated in Figure 4.12, four additional probes were placed at the corners of the basin at distances of approximately 5m from the boundaries.

The measured time series at one of the corner probes (probe No. 26), 5 meters away from the wavemaker, was used to derive the pressure time history for the pneumatic wavemaker. As discussed in the numerical wave tank section, linear theory was used to convert the surface elevation time history to pressure time history required by the internal wavemaker. Numerical simulations were performed using totally 1024 points with $\Delta x = 0.04875m$ and $\Delta t = T/50 = 0.02s$.

At the beginning of the simulation the largest wave in the front of the group became too steep and started to break. In order to avoid such instabilities during the simulation, a viscous term of Smagorinsky type was added to the right-hand sides of the mass and momentum equations and the evolution equations (4.61) were modified as follows:

$$\begin{aligned} \eta_t &= f(\eta, u_s) + D_\eta + \nu\eta_{xx}, \\ u_{st} &= g(\eta, u_s) - \nabla p_G + D_u + \nu u_{s,xx}, \end{aligned} \tag{4.70}$$

where the eddy viscosity coefficient ν is given by the Smagorinsky's [72] formulation with the turbulent length scale proportional to the grid size Δx:

$$\nu = (C_s \Delta x)^2 \, |u_{s,x}|, \tag{4.71}$$

where C_s is an empirical coefficient which was taken to be equal to 0.3 in the present simulation. This viscous term was effective in locally suppressing the steep waves inside the computational domain. As a result of adding these viscous terms, the step filter which was previously used for nonlinear model was modified such that much fewer terms in the spectrum were set to zero. Figure 4.15 shows a comparison of the measured and predicted surface elevation time histories at probes No. 1 ($x = 17.8m$), probe No. 10 ($x = 28.6m$), and probe No. 20 ($x = 40.6m$).

Propagating away from the wavemaker, waves get highly modulated as a result of nonlinear wave-wave interactions. The initially symmetric wave envelope at the wavemaker

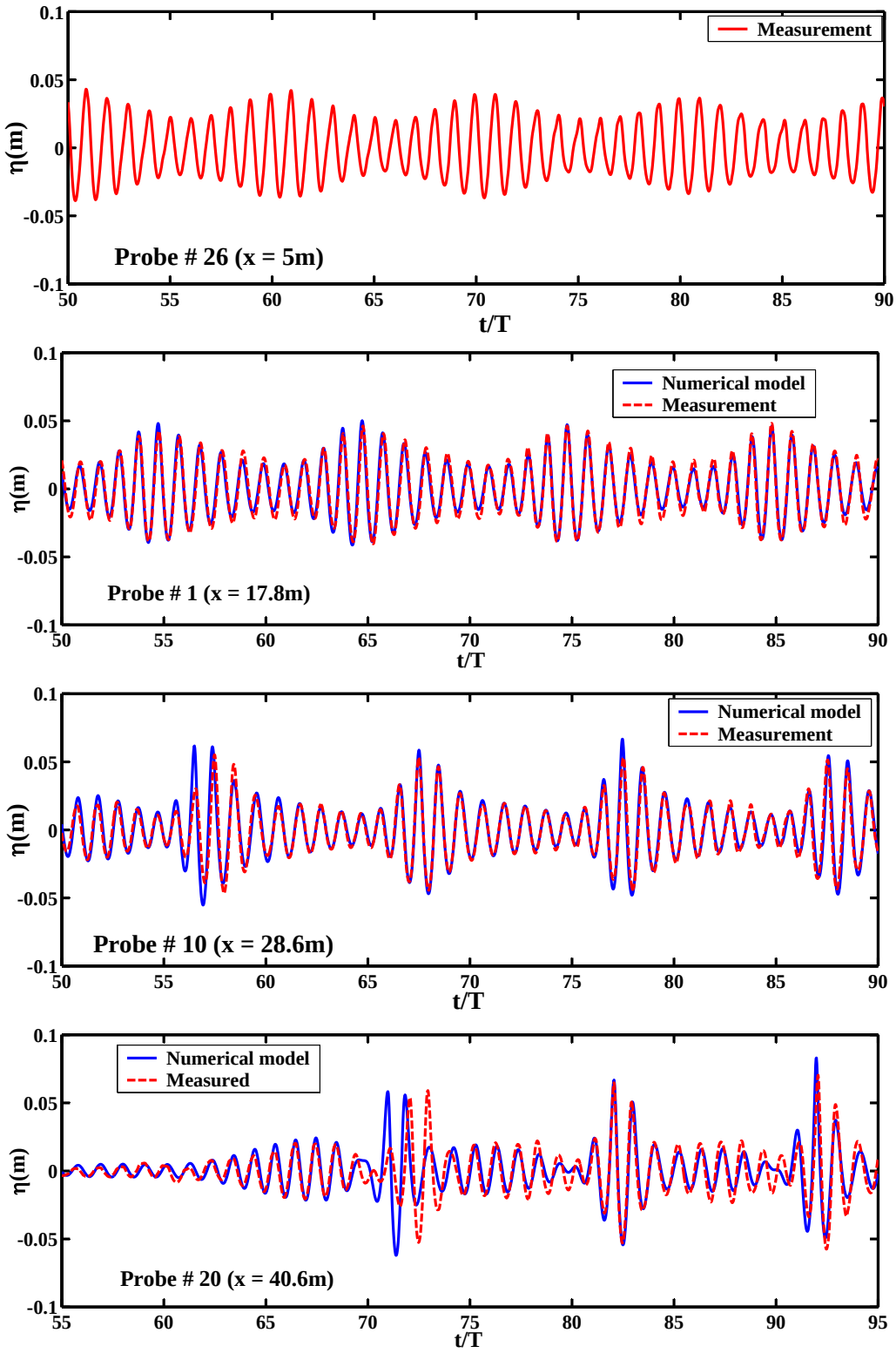

Figure 4.15: Comparison of measured and model-predicted surface elevation time histories at wave probes 1, 10, 20, 26. Initial signal comprised of a principal wave of amplitude $6cm$ and frequency $1Hz$, with two side-bands of amplitude $1cm$ and frequencies $(1 \pm 0.1$ Hz).

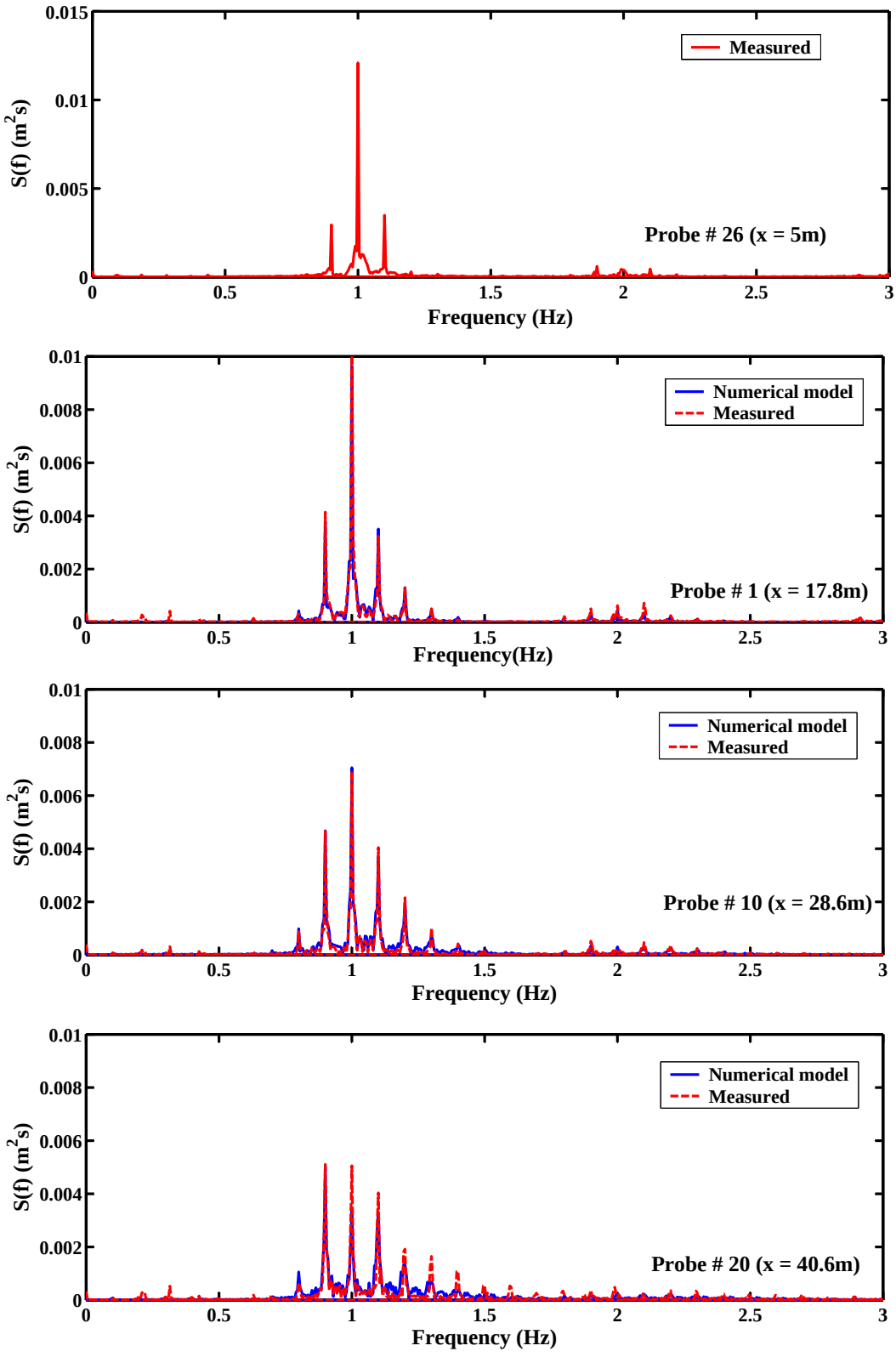

Figure 4.16: Comparison of measured and numerically predicted spectral amplitudes at probes 26, 1, 10, 20.

becomes highly asymmetric with larger and steeper waves located towards the front of the group. Fairly good agreement is obtained between the measured values and numerically-predicted values at probes 1 and 10. Results show a more pronounced difference at probe N0. 20, specially for the first packet in the group. However, the third-order model reasonably predicted the phases and amplitudes of largest waves in the group and exactly matched the amplitudes in the middle packet.

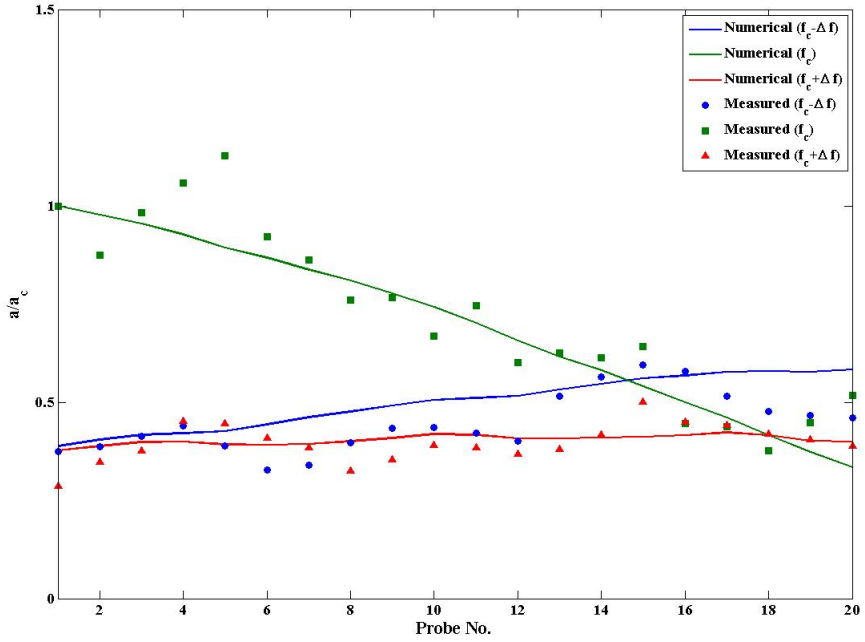

Figure 4.17: Comparison of measured and numerically predicted variation of fundamental component (f_c) and side-bands ($f_c \pm \Delta f$) along the boom.

Figure 4.16 shows a comparison of the spectral amplitudes at the same probes as Figure 4.15. The figure clearly shows the spreading of energy toward higher frequency modes. The third-order model is able to reasonably match the measured spectrum across a broad band of frequencies.

Evolution of the amplitudes of the fundamental frequency component and two side-bands are also compared along the boom (see Figure 4.17). The length of the time record used in these calculations was about 165s (totally 8192 points), giving a frequency resolution of $0.006Hz$. As expected, nonlinear interactions lead to the transfer of energy from the

fundamental wave component (f_c) to the side-bands ($f_c \pm \Delta f$). Numerical model predictions vary almost uniformly along the boom, while the measured amplitudes oscillate about some mean linear trend. This behavior may be attributed to three-dimensional effects and the growth of cross-modes as waves propagate along the boom and become steeper.

4.3 Numerical method for the free surface evolution in three-dimensional flows

For two-dimensional water waves the free surface elevation η, and free surface tangential velocities u_s and v_s are expanded in two-dimensional Fourier series instead of (4.6) as:

$$\begin{aligned}
\eta(\mathbf{x},t) &= \sum_{n=-\frac{Nx}{2}}^{\frac{Nx}{2}} \sum_{m=-\frac{Ny}{2}}^{\frac{Ny}{2}} a_{nm}(t) e^{ink_1 x + imk_2 y} \\
u_s(\mathbf{x},t) &= \sum_{n=-\frac{Nx}{2}}^{\frac{Nx}{2}} \sum_{m=-\frac{Ny}{2}}^{\frac{Ny}{2}} b_{nm}(t) e^{ink_1 x + imk_2 y} \\
v_s(\mathbf{x},t) &= \sum_{n=-\frac{Nx}{2}}^{\frac{Nx}{2}} \sum_{m=-\frac{Ny}{2}}^{\frac{Ny}{2}} c_{nm}(t) e^{ink_1 x + imk_2 y}.
\end{aligned} \tag{4.72}$$

where Nx and Ny are the number of Fourier modes in x and y directions, respectively, and $k_1 = 2\pi/L_1$, and $k_2 = 2\pi/L_2$ with L_1 and L_2 being the computational domain lengths in x and y directions, respectively. The Fourier coefficients $a_{nm}(t), b_{nm}(t)$, and $c_{nm}(t)$ are calculated using two-dimensional FFT for given values of η, u_s, and v_s. Differential and linear transform operators are evaluated in Fourier space as follows:

$$\begin{aligned}
\nabla \left(a_{nm}(t) e^{i\mathbf{k}\cdot\mathbf{x}} \right) &= i\mathbf{k} a_{nm}(t) e^{i\mathbf{k}\cdot\mathbf{x}}, \\
\mathcal{T} \left[\hat{\mathbf{u}}_s(t) e^{i\mathbf{k}\cdot\mathbf{x}} \right] &= \frac{-\tanh(|\mathbf{k}|h_0)}{|\mathbf{k}|} \left(ink_1 b_{nm}(t) + imk_2 c_{nm}(t) \right) e^{i\mathbf{k}\cdot\mathbf{x}}, \\
\mathcal{L} \left[a_{nm}(t) e^{i\mathbf{k}\cdot\mathbf{x}} \right] &= -|\mathbf{k}| \tanh(|\mathbf{k}|h_0) a_{nm}(t) e^{i\mathbf{k}\cdot\mathbf{x}},
\end{aligned} \tag{4.73}$$

where $\mathbf{k} = (nk_1, mk_2)$, and $|\mathbf{k}| = \left((nk_1)^2 + (mk_2)^2 \right)^{1/2}$.

4.3.1 Test with short-crested waves

A short-crested system of waves is defined as a propagating surface gravity wave pattern that is not only periodic in its direction of propagation but is also periodic in the perpendicular horizontal direction (see Figure 4.18). According to linear theory, this pattern is formed when two wave trains of equal wavelength and amplitude are propagating at an angle to one another. Periodic progressive waves occur when the wave trains are co-directional; in the contra-directional case, time and space-periodic standing wave patterns are formed.

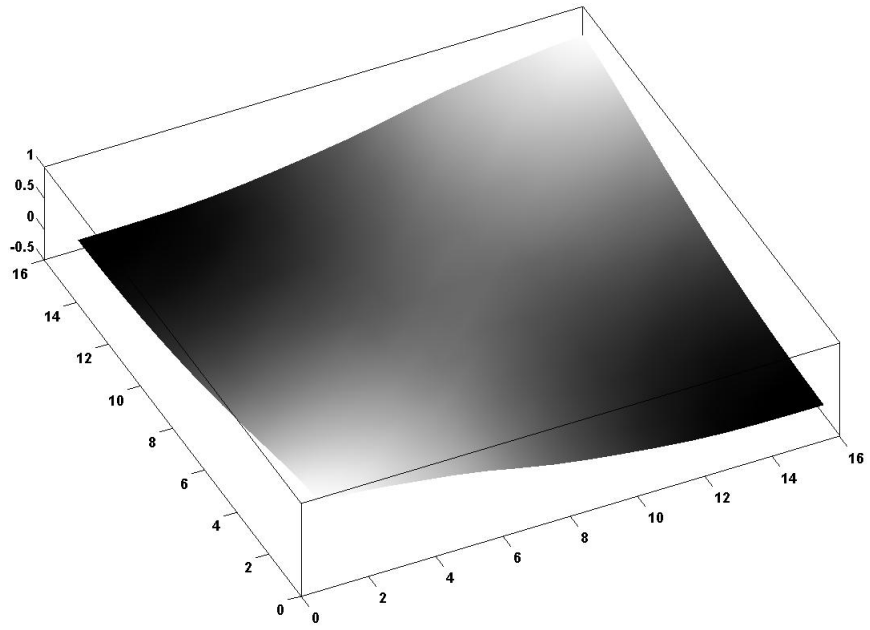

Figure 4.18: Perspective view of one wavelength of the surface of the short-crested wave with parameters $\theta = 60\,\mathrm{deg}, a = 0.45, and N = 16$. The wave is propagating to the upper left of the picture. The vertical scale has been exaggerated.

Short-crested waves may occur in a number of important maritime situations, such as the reflection of a swell off a vertical seawall or jetty which results in a short-crested wave pattern adjacent to the reflecting wall. These waves have a more complicated free surface shape than two-dimensional surface waves with more complex particle paths, that inspired the author to test the capability of the proposed pseudo-spectral method in capturing such wave patterns. To do so, first a fully nonlinear solution to the problem is sought using

Fourier series approach which is an extended version of the discussed method in section 4.1.1 to three dimensions.

Calculation of fully nonlinear short-crested waves

A coordinate system is chosen so that the wave is propagating without change of form in the x direction. The z axis is chosen vertically upward, and the y axis is horizontal, completing a right-handed system of coordinates. Let the surface shape of the wave be given by $z = \eta(x, y, t)$, and assume that the underlying fluid motion is incompressible, inviscid, and irrotational. Thus there exists a velocity potential $\phi(x, y, z, t)$ for this motion. For a wave of length L, the wavelengths in x and y directions are $L/\cos\theta$ and $L/\sin\theta$ respectively. In the case of an incident wave being fully reflected off the wall, L is the wavelength of the incident wave, and θ is angle between the direction of propagation of the incident wave and the normal to the wall. Hence the limit $\theta \to \pi/2$ should give the two-dimensional progressive wave, while the limit $\theta \to 0$ should give the two-dimensional standing wave.

All the equations are put into dimensionless form using the reference length $1/k$ and reference time $(gk)^{-1/2}$, with $k = 2\pi/L$. Because of the assumption that the wave is propagating without change of form, equations are solved for the functions $\phi(X, Y, z)$ and $\eta(X, Y)$ periodic in X and Y with period 2π, where

$$X = px - \omega t, \qquad Y = qy \tag{4.74}$$

where p and q are non-dimensional x and y direction wavenumbers, respectively, defined by

$$p = \sin\theta, \qquad q = \cos\theta, \tag{4.75}$$

and ω is the frequency.

It is convenient to define the three functions

$$\begin{aligned} U(X,Y) &= \phi_X\left[X,Y,\eta(X,Y)\right], \\ V(X,Y) &= \phi_Y\left[X,Y,\eta(X,Y)\right], \\ W(X,Y) &= \phi_z\left[X,Y,\eta(X,Y)\right], \end{aligned} \tag{4.76}$$

which are proportional to the components of the fluid velocities at the free surface; The actual x and y direction velocities are obtained by $pU(X,Y)$ and $qV(X,Y)$ respectively, while the vertical velocity is just $W(X,Y)$. Using (4.74) and (4.76), the governing Laplace equation can be written as

$$p^2\phi_{XX} + q^2\phi_{YY} + \phi_{zz} = 0, \tag{4.77}$$

for $z < \eta(X,Y)$.

The kinematic free surface boundary condition is

$$-\omega\eta_X + p^2U\eta_X + q^2V\eta_Y - W = 0, \quad \forall X,Y \tag{4.78}$$

while the dynamic free surface boundary condition or Bernoulli equation can be transformed into

$$-\omega U + \eta + \frac{1}{2}\left(p^2U^2 + q^2V^2 + W^2\right) = C, \quad \forall X,Y. \tag{4.79}$$

A necessary condition for no motion at infinitely deep in the fluid is

$$\phi_z \to 0 \ \text{ as } z \to -\infty. \tag{4.80}$$

In the case of finite depth, (4.80) is replaced by

$$\phi_z \to 0 \ \text{ as } z \to -h. \tag{4.81}$$

The semi-wave amplitude is defined as

$$a = \left[\eta(0,0) - \eta(\pi,0)\right]/2. \tag{4.82}$$

Since the wave peak is fixed at $(X, Y) = (0, 0)$.

An important derived quantity is the energy content of the wave system. Let KE and PE represent the dimensionless kinetic and potential energies per unit horizontal area. In terms of the velocity potential and surface elevation, they may be expressed as (Roberts and Schwartz [69]):

$$\begin{aligned} KE &= \frac{\omega}{8\pi^2} \int_0^{2\pi} \int_0^{2\pi} \eta \left(U + W\eta_X\right) \mathrm{d}X\mathrm{d}Y, \\ PE &= \frac{1}{8\pi^2} \int_0^{2\pi} \int_0^{2\pi} \eta^2 \mathrm{d}X\mathrm{d}Y, \end{aligned} \tag{4.83}$$

Expressions are sought for the surface elevation and the velocity potential that are doubly periodic in functions of transformed horizontal coordinates X and Y. A general representation is

$$\begin{aligned} \eta &= \sum_{m=0}^{\infty} \sum_{n=0}^{\infty} a_{mn} \cos mX \cos nY, \\ \phi &= \sum_{m=1}^{\infty} \sum_{n=0}^{\infty} b_{mn} f_{mn}(z) \sin mX \cos nY, \end{aligned} \tag{4.84}$$

The coefficient $a_{00} = 0$, since the mean surface level is fixed at $z = 0$. The functions f_{mn} are chosen so that each term in the summation satisfies the transformed Laplace equation (4.77) as well as the appropriate depth boundary condition. In the infinite-depth case

$$f_{mn}(z) = e^{\alpha_{mn} z}, \tag{4.85}$$

while in finite depth an appropriate choice is

$$f_{mn}(z) = \frac{\cosh[\alpha_{mn}(z + h)]}{\cosh(\alpha_{mn} h)}. \tag{4.86}$$

In either case the α_{mn} are given by

$$\alpha_{mn}^2 = (pm)^2 + (qn)^2. \tag{4.87}$$

Equations (4.78) and (4.79) are solved by a series truncation method similar to the

method which was discussed earlier in this chapter for one-dimensional stationary waves. N is chosen to be a fixed positive integer and the infinite series in (4.84) are replaced by

$$\begin{aligned} \eta &= \sum_{m=0}^{N-1} \sum_{n=0}^{N-1} a_{mn} \cos mX \cos nY, \\ \phi &= \sum_{m=1}^{N} \sum_{n=0}^{N-1} b_{mn} f_{mn}(z) \sin mX \cos nY, \end{aligned} \tag{4.88}$$

The resulting system of nonlinear algebraic equations are to be satisfied at the N^2 collocation points (X_i, Y_j) given by

$$\begin{aligned} X_i &= \pi(i - \frac{1}{2})/N, \\ Y_j &= \pi(j - \frac{1}{2})/N, \quad \text{for} i, j = 1, 2, ..., N. \end{aligned} \tag{4.89}$$

These points are distributed evenly throughout a basic rectangle of symmetry. This approach is similar to that used by Dean and Rienecker and Fenton to solve for two-dimensional progressive waves.

The amplitude equation (4.82), in terms of the unknowns in (4.88), becomes

$$a = \sum_{m=1}^{N-1} \sum_{n=0}^{N-1} a_{mn}, \quad m \text{ odd}. \tag{4.90}$$

The problem will be then to choose values for θ and a and solve the $2N^2 + 1$ equations (4.78) and (4.79), at the N^2 points (4.89), subject to equation (4.90), for the $2N^2 + 1$ unknowns, a_{mn}, b_{mn}, ω, and C. (Note that $a_{00} = 0$.) However the number of unknowns can be reduced by almost half to $N^2 + 1$, by observing that the basic element of symmetry of a short-crested wave is a right-angled triangle formed by dividing the rectangular domain along either diagonal. The consequence of this triangular symmetry is that:

$$a_{mn} = b_{mn} = 0, \quad \text{when } m + n \text{ is odd}. \tag{4.91}$$

These equations were programmed in MATLAB and solutions were obtained using the

Newton iterations starting from the linear solution

$$\begin{aligned} \omega = 1, \quad a_{11} = a, \quad b_{11} = a, \\ a_{mn} = b_{mn} = 0, \quad \forall (m,n) \neq (1,1) \end{aligned} \tag{4.92}$$

In case of steep waves, the initial estimate may be obtained for slightly different values of the parameters a and θ. The errors in the solution due to truncating the Fourier series can be roughly estimated. In infinite depth the constant C in (4.79) should be exactly zero, thus the departure of C from zero gives an estimate of the global error in the solution. Another indication of error due to the truncation can be estimated from the terms $b_{Nn}\sin(NX)\cos(nY)f_{Nn}(z), 0 < n < N-1$, which are the only Nth-order Fourier components retained in the truncation of (4.84). Since it is inconsistent to retain these terms (see governing equations (4.78)- (4.79)), the calculated values of b_{Nn} are virtually superfluous [69].

Numerical Results

In order to evaluate the pseudo-spectral model in capturing the characteristics of short-crested waves, two cases were studied. A mild short-crested wave with dimensionless wave steepness parameter $a = 0.3$ with an incidence angle $\theta = 60°$, and another with $a = 0.55$ and $\theta = 45°$ which is considered relatively steep. The convergence criterion for the iterative solution was that the sum of the residuals should be less than 10^{-8}. The convergence of the truncation method is shown in Table 4.6. Computed values of the dimensionless frequency ω_N, absolute value of the parameter C and two-norm of the vector b_{Nn} are given for both cases as a function of the truncation parameter N.

For $a = 0.3$, the frequency converged to at least five decimal places, while for the steeper case, $a = 0.55$, the convergence was achieved up to three decimal places. Figure 4.19 shows a perspective view of the two wave lengths of the discussed short-crested wave cases. As expected, it shares many physical features with both progressive and standing waves, namely the pronounced flattening of the troughs and the sharpening of the crests.

Figure 4.20 shows the contours of the surface elevation for these two cases. The asymmetrical pattern of the converged solution compared to the initial guess from linear theory

N	$a = 0.3, \theta = 60^\circ$			$a = 0.55, \theta = 45^\circ$		
	ω_N	$\lvert c\rvert$	$\lvert\lvert b_{Nn}\rvert\rvert_2$	ω_N	$\lvert c\rvert$	$\lvert\lvert b_{Nn}\rvert\rvert_2$
4	1.0041583	2.44×10^{-7}	3.38×10^{-4}	1.0389795	5.34×10^{-5}	7.32×10^{-4}
6	1.0041617	4.26×10^{-8}	1.39×10^{-5}	1.0400082	3.38×10^{-5}	2.61×10^{-4}
8	1.0041610	5.6×10^{-11}	4.41×10^{-7}	1.0394677	1.13×10^{-5}	3.61×10^{-5}
10	1.0041606	1.16×10^{-9}	2.87×10^{-8}	1.0394103	5.45×10^{-7}	3.62×10^{-6}
12	1.0041579	3.22×10^{-9}	6.49×10^{-9}	1.0392726	7.14×10^{-7}	4.76×10^{-7}

Table 4.6: Convergence of the truncation solution for dimensionless frequency for two cases: $a = 0.3, \theta = 60^\circ$ and $a = 0.55, \theta = 45^\circ$.

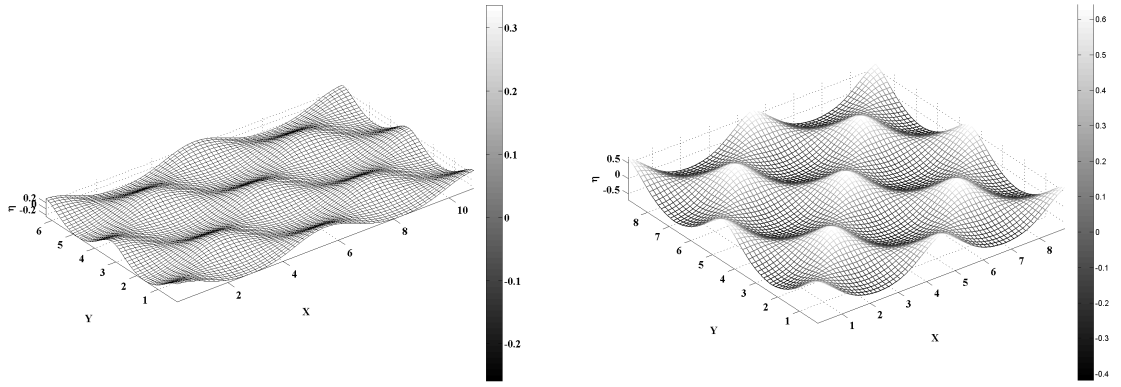

Figure 4.19: Perspective view of two wavelengths of the surface of the short-crested waves. Left: $\theta = 60^\circ, a = 0.30, N = 16$; Right: $\theta = 45^\circ, a = 0.55, N = 16$.

is clearly observed. This asymmetry is more pronounced for $a = 0.55, \theta = 45^\circ$.

Comparison of normal velocity profile u_n

The exact solution obtained by the Fourier truncation method is used as a benchmark to validate the pseudo-spectral model. The values of η_X, η_Y, U, V, and W are first extracted from the calculated Fourier coefficients a_{mn} and b_{mn} and are periodically extended to cover a 256×256 computational domain. Tangential and normal velocities on the free surface, $\mathbf{u}_s$ and u_n, are then calculated as follows:

$$\mathbf{u}_s = \mathbf{U} + W\nabla\eta, \quad \text{and} \quad u_n = W - \mathbf{U}\cdot\nabla\eta, \tag{4.93}$$

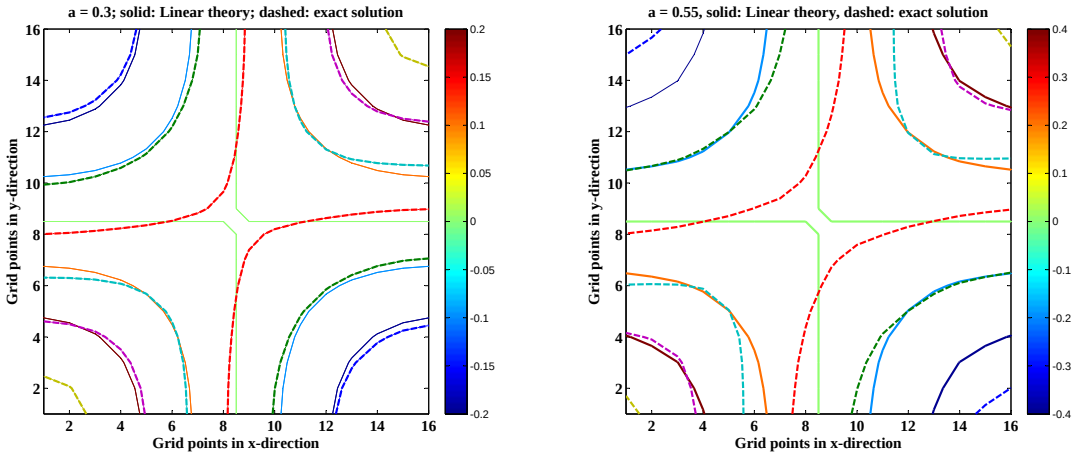

Figure 4.20: Contour lines of the surface elevation for $a = 0.3, \theta = 60^\circ$ and $a = 0.55, \theta = 45^\circ$. solid line: initial guess from linear theory; dashed line: exact solution.

Where $\mathbf{U} = (U, V)$. The exact values of η and $\mathbf{u}_s$ are then substituted into the right-hand sides of equations (3.46), (3.48), and (3.50) to obtain the first, second, and third-order approximations for u_n respectively. These approximations are finally compared with the exact u_n from (4.93). Figure 4.21 presents the comparison of free surface normal velocity profile calculated from pseudo-spectral model with the exact solution from Fourier truncation method. The results are presented for both cases $a = 0.3$ and $a = 0.55$. Figure 4.22 more clearly shows the same comparison along two perpendicular lines passing through the middle of the computational domain for the case $a = 0.3, \theta = 60^\circ$.

For the case $a = 0.3$, the maximum absolute error between the model and the exact solution ranged from 0.019 for first-order model to 0.018 and 0.016 in second and third-order models, respectively. For the steeper wave, these errors were almost three times higher.

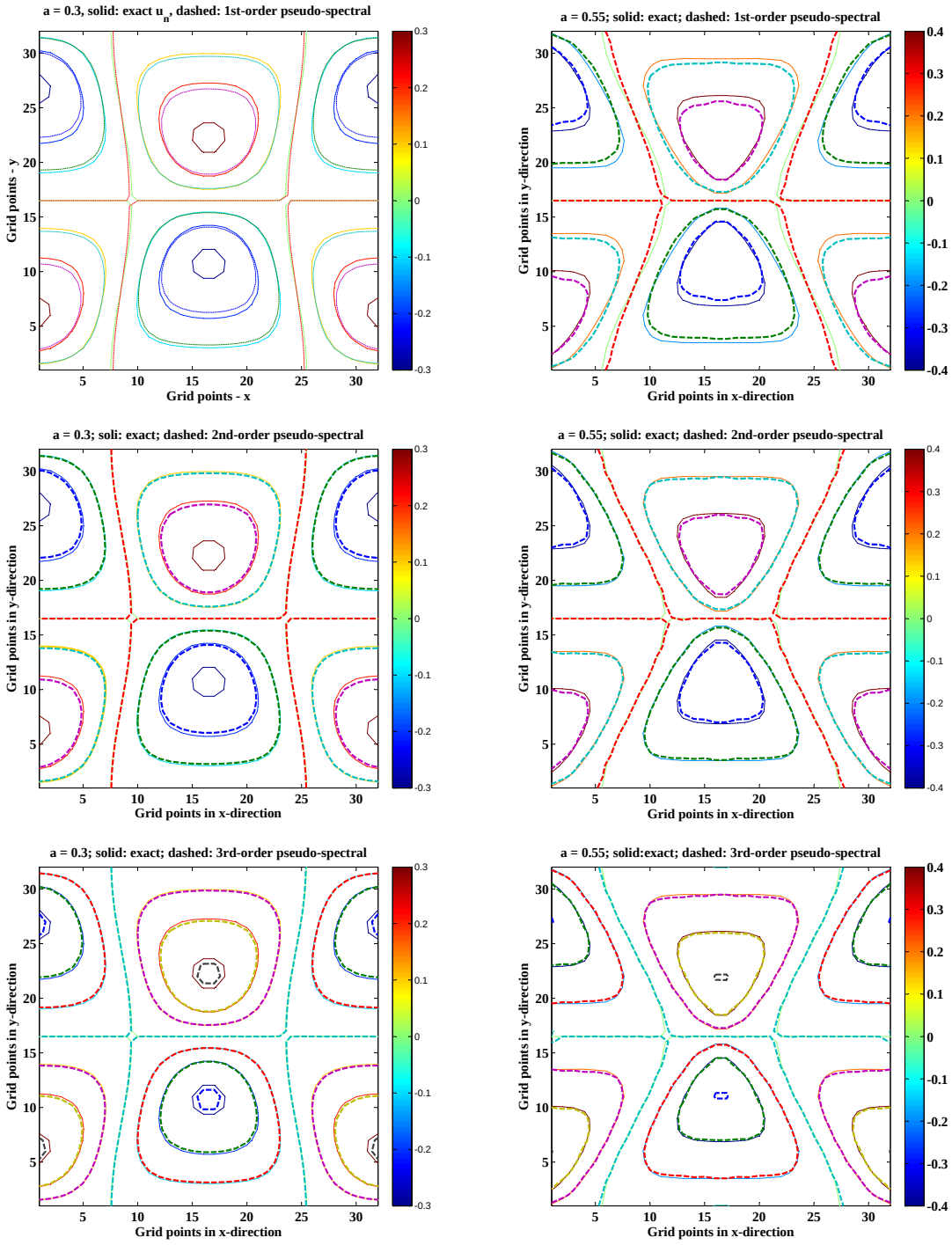

Figure 4.21: Comparison of the dimensionless u_n profiles approximated by the first, second, and third-order pseudo-spectral models, with exact solutions from Fourier truncation method. Left: $a = 0.3, \theta = 60°$; Right: $a = 0.55, \theta = 45°$.

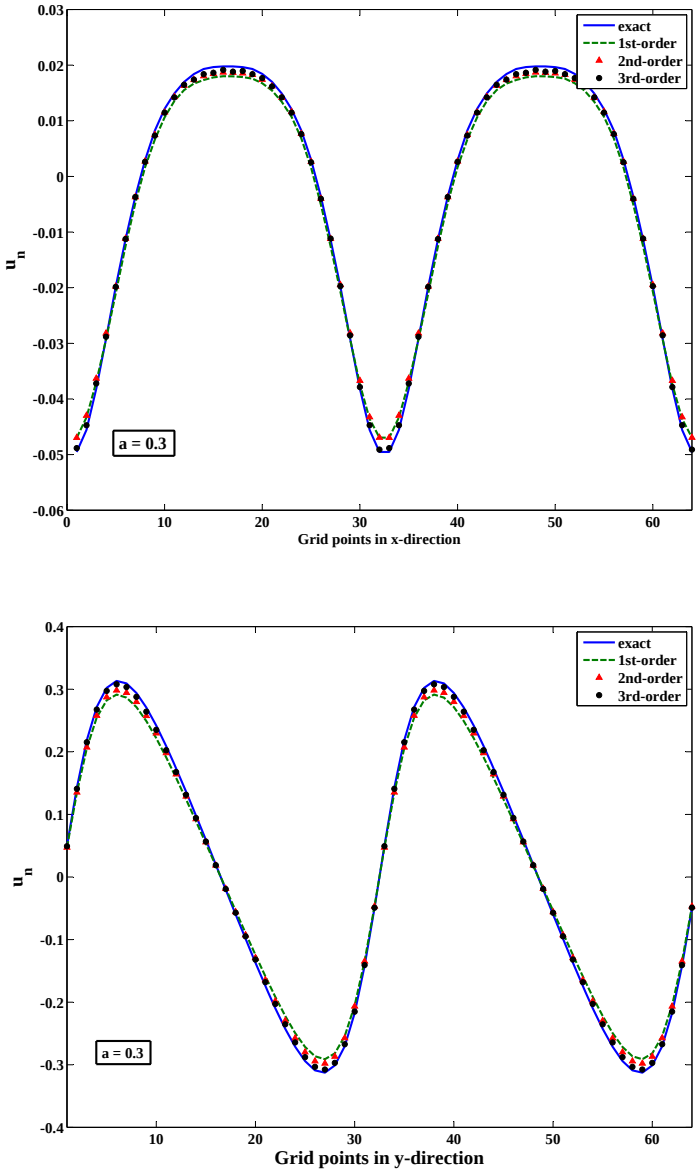

Figure 4.22: Comparison of the dimensionless u_n profiles calculated by first, second, and third-order pseudo-spectral models with exact solutions from Fourier truncation method along x and y directions for the case $a = 0.3, \theta = 60°$. Top: along x-direction; Bottom: along y-direction.

CHAPTER 5

Radar Data Assimilation

5.1 Introduction

Knowing the sea state shortly $(10 - 15$ minutes) ahead of time, will help operate marine vehicles more efficiently and avoid unpredicted damages to the seagoing vessels from rogue waves. This goal is achieved through a combination of real-time measurements from conventional marine radars and an efficient numerical wave evolution model. Radar returns are inherently mixed with noise. The noise originates from various sources such as measurement, inadequacy of the modulation transfer functions, and high nonlinearity of the sea state. Numerical models also suffer from discretization errors and lack of reliable estimates for the initial/boundary conditions, as well as model parameters. A variational data assimilation scheme is developed in this chapter that minimizes the differences between the measured and numerically predicted surface profiles. The corrected sea state is then allowed to evolve in order to forecast the sea state beyond.

5.2 Variational data assimilation

The objective of variational assimilation is to find an optimum solution to the numerical model that best fits a series of radar observations distributed in space and time. This algorithm is referred to as 4DVar in the data assimilation communities, since it includes three spatial dimensions and one temporal dimension. In this method a cost function,

measuring the difference between numerical solution and measurement, is usually defined as:

$$J(\eta(x,y,t)) = \sum_{i=1}^{NX}\sum_{j=1}^{NY}\sum_{k=1}^{NT} W_{ijk}\left[\eta(i,j,k) - \eta_{obs}(i,j,k)\right]^2. \tag{5.1}$$

where $\eta(i,j,k)$ are the discrete model-predicted values, $\eta_{obs}(i,j,k)$ are the observed values of sea surface elevation at the same grid points that the model is variables are defined, and W_{ijk} are the weighting factors that reflect the accuracy of the observations at different points and different times. NX and NY are the number of free surface variables in x and y-directions, respectively, and NT is the total number of available observations. One looks for the model solution that minimizes the cost function (5.1) over the assimilation interval. For our deterministic model, once the initial condition, boundary conditions, and model parameters are specified, the evolution of the sea surface can be determined. If it is assumed that the model parameters and boundary conditions are already known (in the present thesis, periodic boundary conditions are assumed in both directions), the cost function (5.1) would be a function of the initial state alone.

Since the model solution is uniquely defined by the corresponding initial condition at the beginning of the assimilation interval, these initial conditions are taken as control variables, i.e., as the variables with respect to which the minimization is performed. The optimal initial condition is found through an iterative process, each step of which requires the explicit knowledge of the gradient of the cost function with respect to the initial condition.

Gradient identification remains to be a challenging task, because the cost function is not directly related to the initial conditions and one cannot find the gradient of (5.1) with respect to the initial conditions analytically for such a nonlinear model. In general an arbitrary change in the initial state $\delta\eta_0$ will result in a change in J called the directional derivative of J at η_0 in the direction $\delta\eta_0$. The gradient of J is related to the directional derivative, δJ by:

$$\delta J = \langle \nabla_{\eta_0} J, \delta\eta_0 \rangle, \tag{5.2}$$

where

$$\nabla_{\eta_0} J = \begin{pmatrix} \left(\frac{\partial J}{\partial \eta_0}\right)_1 \\ \left(\frac{\partial J}{\partial \eta_0}\right)_2 \\ \vdots \\ \left(\frac{\partial J}{\partial \eta_0}\right)_N \end{pmatrix} \tag{5.3}$$

where N is the total number of points on the free surface (i.e. $NX \times NY$). One way to calculate the gradient numerically is the direct method based on finite difference approximations. In this approach each value of the initial condition η_0 would have to be perturbed and then the forward evolution equations need to be solved N times, once for each of the discrete values of η_0. The gradient array $\left(\frac{\partial J}{\partial \eta_0}\right)_i, \quad i = 1, 2, ..., N$ could then be evaluated as follows:

$$\left(\frac{\partial J}{\partial \eta_0}\right)_i = \frac{J(\eta_0 + \alpha e_i) - J(\eta_0)}{\alpha} \tag{5.4}$$

where e_i is a vector of zeros except for the ith component which is 1, and α is a small positive scalar. Care should be taken in choosing the value of perturbation parameter α to avoid round-off errors. For our application where N is $O(10^5 - 10^6)$, it is clear that the finite difference approach or any other direct method is impractical, especially when one considers that the gradient vector needs to be re-calculated at every iteration.

The beauty of the so-called adjoint method is that this same gradient can be obtained with a single integration of the adjoint model backward in time. As we shall see, the adjoint model is simply the adjoint of the so-called Tangent Linear Model (TLM), which is itself the linearized version of the evolution equations around the current state of the system. Derivation of the TLM and adjoint models will be explained in the next section.

5.3 Theory of adjoint equations and application to data assimilation

The most general form so far of the theory of adjoint equations seems to have been presented by Cacuci [11]. In this section the adjoint formalism is proved for general form

of cost functions and a general evolution model. Suppose that the free surface evolution equations, in its most general sense, can be written as:

$$\frac{\partial \mathbf{u}}{\partial t} = \mathbf{F(u)} \quad \text{where,} \quad \mathbf{u} = \begin{pmatrix} \eta \\ \Phi \end{pmatrix} \text{ or } \begin{pmatrix} \eta \\ \mathbf{u}_s \end{pmatrix} \tag{5.5}$$

$\mathbf{u}_0$ will denote the initial condition from which the numerical wave model is integrated and the operation $\mathbf{u} = \mathbf{F}(\mathbf{u}_0)$ will represent the integration of the model, and $\mathbf{u}$ will be the model predicted values obtained by this integration. $\mathbf{u}'(t)$ and $\mathbf{u}'_0$ will denote the first-order variation of the model solution at time t, and first order variation of the initial condition, respectively. The scalar function $\mathscr{J}\mathbf{(u)}$ measures the difference between model predicted values $\mathbf{u}$ and the available observations $\mathbf{u}_{obs}$, assumed to be distributed over a time interval $[t_0, t_1]$ which is referred to as assimilation interval. The cost function $\mathscr{J}$ is defined as:

$$\mathscr{J} = \int_{t_0}^{t_1} H[\mathbf{u}(t), t]\, \mathrm{d}t \tag{5.6}$$

Where, for a given $\mathbf{u}$, $H[\mathbf{u}, t]$ is a scalar measuring the difference between $\mathbf{u}$ and the observations available at time t (for example the squared norm of the difference between the observations at time t and the corresponding components of $\mathbf{u}$). In the present thesis, H is simply defined as:

$$H(\eta(t)) = \frac{1}{2} \int_{\mathbf{x}} [\eta(\mathbf{x}, t) - \eta_{obs}(\mathbf{x}, t)]^2 \, \mathrm{d}\mathbf{x} \tag{5.7}$$

Where the integration is carried our over the whole computational domain. For a given initial condition $\mathbf{u}_0$ and for the corresponding solution $\mathbf{u}$(t) of (5.5), the first-order variation $\delta\mathscr{J}$ resulting from a variation $\mathbf{u}'_0$ of $\mathbf{u}_0$ is equal to:

$$\delta\mathscr{J} = \int_{t_0}^{t_1} \langle \nabla_{\mathbf{u}} H(t), \mathbf{u}'(t) \rangle \, \mathrm{d}t \tag{5.8}$$

Where $\nabla_{\mathbf{u}} H(t)$ is the gradient of $H[\mathbf{u}, t]$ with respect to $\mathbf{u}$, taken at point ($\mathbf{u}$(t),t), which in this case will be the quantity $\eta(\mathbf{x}, t) - \eta_{obs}(\mathbf{x}, t)$, and $\mathbf{u}'(t)$ is the first-order variation of

$\mathbf{u}(t)$ resulting from the perturbation $\mathbf{u}'_0$ in the initial condition. By linearizing the evolution equations (5.5), we can get an equation that describes the linear evolution of small perturbations. This equation is referred to as "Tangent Linear Model"(TLM). The variation $\mathbf{u}'(t)$ is obtained from $\mathbf{u}'_0$ by integrating the tangent linear model:

$$d\mathbf{u}'/dt = \mathbf{F}'(t)\mathbf{u}' \tag{5.9}$$

Where $\mathbf{F}'(t)$ is the Jacobian operator obtained by differentiating $\mathbf{F}$ with respect to $\mathbf{u}$, and taken at the point $\mathbf{u}$(t). Equation (5.9) is linear and its solution at a given time t depends linearly on the initial condition at time t_0 which can be written in operator form as:

$$\mathbf{u}'(t) = \mathbf{R}(t, t_0)\mathbf{u}'_0$$

where $\mathbf{R}(t, t_0)$ is a well-defined linear operator, called the 'resolvent' of (5.9) between times t_0 and t. The resolvent $\mathbf{R}(t, t')$ is defined more generally for any two times t and t' lying between t_0 and t_1 and possesses the following two properties:

$$\mathbf{R}(t, t) = \mathbf{I} \ , \ \text{for any } t \tag{5.10}$$

where $\mathbf{I}$ is the identity operator and

$$\frac{\partial}{\partial t}\mathbf{R}(t, t') = \mathbf{F}'(t)\mathbf{R}(t, t') \tag{5.11}$$

for any t and t'.

To proceed with the proof, the inner product and adjoint operator will be first defined as follows:

Let $\mathscr{F}$ be a Hilbert space, with inner product denoted by $\langle \ , \ \rangle$. The inner product of two fields $\mathbf{v}$ and $\mathbf{w}$ in $\mathscr{F}$ can be written as:

$$\langle \mathbf{v}, \mathbf{w} \rangle = \int_0^T \int_{\mathbf{x}} \mathbf{v}.\mathbf{w} \mathrm{d}\mathbf{x} \mathrm{d}t \tag{5.12}$$

Let $\mathbf{v} \longrightarrow \mathbf{J}(\mathbf{v})$ be a differentiable scalar function defined on $\mathscr{F}$. At any point in $\mathscr{F}$, the

differential $\delta\mathbf{J}$ of $\mathbf{J}$ can be expressed in terms of the differential $\delta\mathbf{v}$ of $\mathbf{v}$ by the following inner product:

$$\delta\mathbf{J} = \langle \nabla_{\mathbf{v}}\mathbf{J}, \delta\mathbf{v} \rangle \tag{5.13}$$

where $\nabla_{\mathbf{v}}\mathbf{J}$ is the gradient of $\mathbf{J}$ with respect to $\mathbf{v}$ and is uniquely defined. Now Let $\mathbf{L}$ be a continuous linear operator in $\mathscr{F}$. There exists a unique continuous linear operator $\mathbf{L}^*$ in $\mathscr{F}$ such that the following equality between inner products holds for any $\mathbf{v}$ and $\mathbf{w}$ belonging to $\mathscr{F}$:

$$\langle \mathbf{w}, \mathbf{L}\mathbf{v} \rangle = \langle \mathbf{L}^*\mathbf{w}, \mathbf{v} \rangle \tag{5.14}$$

where $\mathbf{L}^*$ is called the 'adjoint operator' of $\mathbf{L}$.

Using the relations (5.13) and (5.14), Equation (5.8) can now be written as:

$$\begin{aligned} \delta\mathscr{J} &= \int_{t_0}^{t_1} \langle \nabla_{\mathbf{u}} H(t), \mathbf{R}(t, t_0)\mathbf{u}_0' \rangle \, \mathrm{d}t \\ &= \int_{t_0}^{t_1} \langle \mathbf{R}^*(t, t_0)\nabla_{\mathbf{u}} H(t), \mathbf{u}_0' \rangle \, \mathrm{d}t \\ &= \left\langle \int_{t_0}^{t_1} \mathbf{R}^*(t, t_0)\nabla_{\mathbf{u}} H(t)\mathrm{d}t, \mathbf{u}_0' \right\rangle \end{aligned} \tag{5.15}$$

where we have introduced, for all t, the adjoint $\mathbf{R}^*(t, t_0)$ of $\mathbf{R}(t, t_0)$. It is seen from the last line that the gradient of $\mathscr{J}$ with respect to $\mathbf{u}_0$ is equal to:

$$\nabla_{\mathbf{u}_0}\mathscr{J} = \int_{t_0}^{t_1} \mathbf{R}^*(t, t_0)\nabla_{\mathbf{u}} H(t)\mathrm{d}t \tag{5.16}$$

We now introduce the "adjoint equation" of the TLM (5.9) as:

$$-d\mathbf{u}^*/dt = \mathbf{F}^*(t)\mathbf{u}^* \tag{5.17}$$

The adjoint equation is derived from the tangent linear model (5.9) by taking its inner product with the adjoint variable $\mathbf{u}^*$ and then using integration by parts, to transfer derivatives from $\mathbf{u}'$ to $\mathbf{u}^*$.

$\mathbf{F}^*(t)$ is the adjoint of $\mathbf{F}'(t)$. Equation (5.17) is also linear, and we will denote by $\mathbf{S}(t', t)$ its resolvent between times t and t'.

For any two solutions $\mathbf{u}'(t)$ and $\mathbf{u}^*(t)$ of the tangent linear and adjoint equations (5.9) and (5.17), respectively, the inner product $\langle \mathbf{u}'(t), \mathbf{u}^*(t) \rangle$ is constant with time, since:

$$\begin{aligned}
\frac{d}{dt}\langle \mathbf{u}'(t), \mathbf{u}^*(t) \rangle &= \left\langle \frac{d\mathbf{u}'}{dt}(t), \mathbf{u}^*(t) \right\rangle + \left\langle \mathbf{u}'(t), \frac{d\mathbf{u}^*}{dt}(t) \right\rangle \\
&= \langle \mathbf{F}'(t)\mathbf{u}'(t), \mathbf{u}^*(t) \rangle - \langle \mathbf{u}'(t), \mathbf{F}^*(t)\mathbf{u}^*(t) \rangle \\
&= 0
\end{aligned}$$

Using the above argument, it can be shown that $\mathbf{S}(t, t')$ is the adjoint of $\mathbf{R}(t', t)$. Expression (5.16) then becomes:

$$\nabla_{\mathbf{u}_0} \mathscr{J} = \int_{t_0}^{t_1} \mathbf{S}(t_0, t) \nabla_{\mathbf{u}} H(t) \mathrm{d}t \tag{5.18}$$

If we write "inhomogeneous adjoint equation" as:

$$-d\mathbf{u}^*/dt = \mathbf{F}^*(t)\mathbf{u}^* + \nabla_{\mathbf{u}} H(t) \tag{5.19}$$

The solution of the above equation starting from the condition $\mathbf{u}^*(t_1) = 0$ is equal to:

$$\mathbf{u}^*(t) = \int_{t}^{t_1} \mathbf{S}(t, \tau) \nabla_{\mathbf{u}} H(\tau) \mathrm{d}\tau \tag{5.20}$$

as it can be verified by using the resolvent properties (5.10) and (5.11). Now from equations (5.18) and (5.19) one can conclude that:

$$\nabla_{\eta_0} \mathscr{J} = \eta^*(t_0) \tag{5.21}$$

In summery, the gradient of the cost function with respect to the initial condition, $\nabla_{\mathbf{u}_0} \mathscr{J}$, can be obtained, for given $\mathbf{u}_0$, by performing the following operations:

Starting from the initial condition $\mathbf{u}_0$ at time t_0, basic evolution equations (5.5) are integrated from t_0 to t_1, and the computed values of $\mathbf{u}(t)$ are stored for $t_0 \leq t \leq t_1$. Starting from $\mathbf{u}^*(t_1) = 0$, the inhomogeneous adjoint equation (5.19) is then integrated backwards in time from t_1 to t_0, the operator $\mathbf{F}^*(t)$ and the gradient $\nabla_{\mathbf{u}} H(t)$ being determined, at each

time t, from the values $\mathbf{u}(t)$ computed in the forward integration. The final value $\mathbf{u}^*(t_0)$ is the gradient of the cost function with respect to the initial condition.

Once the gradient of the cost function is obtained using adjoint method, an iterative descent algorithm is used to search for the optimal initial condition that minimizes the cost function over a finite time interval. Minimization algorithms will be presented for two-dimensional and three-dimensional flow problems separately. In the following sections the important result (5.21) will be verified using several linear and nonlinear models.

5.3.1 A nonlinear model with exact solutions

This section illustrates the adjoint process by using a quadratic model with exact solutions. It is emphasized that the adjoint model yields an exact gradient of the cost function with respect to the control variables. The following one-dimensional nonlinear model is assumed:

$$\frac{\partial \mathbf{x}}{\partial t} = -\mathbf{x}^2, \quad \text{with} \quad \mathbf{x}(0) = \mathbf{x}_0, \tag{5.22}$$

where $t \in [0, 1]$. The exact solution of the model is:

$$\mathbf{x}(t) = \frac{\mathbf{x}_0}{\mathbf{x}_0 t + 1}. \tag{5.23}$$

If the observations are model generated with the initial condition $\mathbf{x}(0) = 1$, then from equation (5.23) the observations may be written as:

$$\mathbf{x}_{obs}(t) = \frac{1}{t + 1}, \tag{5.24}$$

Let us define the cost function as:

$$J(\mathbf{x}_0) = \frac{1}{2} \int_0^1 [\mathbf{x}(t) - \mathbf{x}_{obs}(t)] \, \mathrm{d}t, \tag{5.25}$$

i.e.

$$\begin{aligned} J(\mathbf{x}_0) &= \frac{1}{2}\int_0^1 \left(\frac{\mathbf{x}_0}{\mathbf{x}_0 t+1}-\frac{1}{t+1}\right)^2 \mathrm{d}t \\ &= \frac{1}{2}\left[1+\mathbf{x}_0+\frac{2\mathbf{x}_0}{(1-\mathbf{x}_0)}\ln\frac{(\mathbf{x}_0+1)}{2}-\frac{1+3\mathbf{x}_0}{2(\mathbf{x}_0+1)}\right]. \end{aligned} \tag{5.26}$$

The Tangent Linear equation for the model (5.22) can be written as:

$$\frac{\partial \mathbf{x}'}{\partial t} = -2\mathbf{x}\mathbf{x}', \tag{5.27}$$

and the corresponding adjoint equation can be written as:

$$-\frac{\partial \mathbf{x}^*}{\partial t} = -2\mathbf{x}\mathbf{x}^* + (\mathbf{x}-\mathbf{x}_{obs}), \tag{5.28}$$

i.e.

$$-\frac{\partial \mathbf{x}^*}{\partial t} = -\frac{2\mathbf{x}_0}{\mathbf{x}_0 t+1}\mathbf{x}^* + \frac{\mathbf{x}_0}{\mathbf{x}_0 t+1} - \frac{1}{t+1}, \tag{5.29}$$

with the final condition $\mathbf{x}^*(1)=0$. where $\mathbf{x}^*$ is the adjoint variable. The gradient of the cost function with respect to the initial condition is given by:

$$\nabla_{\mathbf{x}_0} J = \mathbf{x}^*(0). \tag{5.30}$$

Equation (5.29) has an analytic solution of the form:

$$\begin{aligned} \mathbf{x}^*(t) &= (\mathbf{x}_0 t+1)^2\left[\int\left(\frac{1}{t+1}-\frac{\mathbf{x}_0}{\mathbf{x}_0 t+1}\right)\frac{1}{(\mathbf{x}_0+1)^2}\mathrm{d}t + c\right] \\ &= (\mathbf{x}_0 t+1)^2\left[\int\frac{\mathrm{d}t}{(t+1)(\mathbf{x}_0 t+1)^2}+\frac{1}{2(\mathbf{x}_0 t+1)^2}+c\right] \\ &= (\mathbf{x}_0 t+1)^2\left[\frac{1}{(1-\mathbf{x}_0)(\mathbf{x}_0+1)}+\frac{1}{(1-\mathbf{x}_0)^2}\ln\frac{t+1}{\mathbf{x}_0 t+1}+\frac{1}{2(\mathbf{x}_0 t+1)^2}+c\right], \end{aligned} \tag{5.31}$$

where c is an integration constant to be determined by the final condition of the adjoint variable. Therefore:

$$c = -\frac{1}{1-\mathbf{x}_0^2}-\frac{1}{(1-\mathbf{x}_0)^2}\ln\left(\frac{2}{\mathbf{x}_0+1}\right)-\frac{1}{2(\mathbf{x}_0+1)^2}, \tag{5.32}$$

and Equation (5.31) yields:

$$\mathbf{x}^*(0) = \frac{1}{2} + \frac{1}{1-\mathbf{x}_0} - \frac{1}{1-\mathbf{x}_0^2} - \frac{1}{(1-\mathbf{x}_0)^2}\ln\left(\frac{2}{\mathbf{x}_0+1}\right) - \frac{1}{2(\mathbf{x}_0+1)^2}. \tag{5.33}$$

Equation (5.33) is exactly the gradient of the cost function (5.26) with respect to the initial condition $\mathbf{x}_0$.

Once the gradient of the cost function with respect to control variables is identified using adjoint method, an iterative descent algorithm is used to search for the optimal value of the control variable that minimizes the cost function over a finite time interval. Minimization algorithms are discussed for two-dimensional and three-dimensional flow problems separately.

5.3.2 Deriving Adjoint of the 1st-order pseudo-spectral model

This section illustrates the process of deriving the adjoint equations for the simple case of linear one-dimensional evolution equations. The first-order model for the evolution of the free surface elevation and tangential velocity on the free surface is re-written as:

$$\begin{aligned} \eta_t - \mathcal{T}\left[u_s\right] &= 0, \\ u_{s,t} + g\eta_x &= 0, \end{aligned} \tag{5.34}$$

In order to derive the tangent linear equations corresponding to equation (5.34), variables η and u_s are perturbed as:

$$\begin{aligned} \eta &\rightarrow \eta + \eta', \\ u_s &\rightarrow u_s + u_s', \end{aligned} \tag{5.35}$$

after substituting (5.35) back into the basic equations (5.34) and canceling out terms

that constitute the basic equations:

$$\cancel{\eta_t} + \eta'_t - \cancel{\mathcal{T}\left[u_s\right]} - \mathcal{T}\left[u'_s\right] = 0,$$
$$\cancel{u_{s,t}} + u'_{s,t} + \cancel{g\eta_x} + g\eta'_x = 0, \tag{5.36}$$

Since this equation is linear, the tangent linear model is similar to the forward model. The inner product of the adjoint variables η^* and u^*_s with the tangent linear equation (5.36) is then calculated as follows (based on the definition of (5.12)):

$$\left\langle \eta^*, \eta'_t \right\rangle - \left\langle \eta^*, \mathcal{T}\left[u'_s\right] \right\rangle = 0,$$
$$\left\langle u^*_s, u'_{s,t} \right\rangle + \left\langle u^*_s, g\eta'_x \right\rangle = 0, \tag{5.37}$$

As it is seen in (5.12), the inner product is equivalent to integrating the product of two vectors over space and time. Now, using the integration by parts the spatial/temporal derivatives and linear operators are transferred from tangent linear variables η' and u'_s to the adjoint variables η^* and u^*_s:

$$\left\langle \eta', -\eta^*_t \right\rangle + \left\langle u'_s, \mathcal{T}\left[\eta^*\right] \right\rangle = 0,$$
$$\left\langle u'_s, -u^*_{s,t} \right\rangle - \left\langle \eta', g u^*_{s,x} \right\rangle = 0, \tag{5.38}$$

where the anti-symmetry of the linear operator $\mathcal{T}$ has been used, i.e. $\mathcal{T}^* = -\mathcal{T}$ (refer to (3.43), (4.2), and (4.3)). After adding up two sets of equation in (5.38) and pairing similar terms (terms that have η' or u'_s), the equality will hold if the following two sets of adjoint equations are satisfied at the same time, for all x and t:

$$\eta^*_t + g u^*_{s,x} = 0,$$
$$u^*_{s,t} - \mathcal{T}\left[\eta^*\right] = 0, \tag{5.39}$$

Adjoint equations (5.39) should be integrated backward in time to give the desired gradient of the cost function with respect to the initial conditions.

5.3.3 Gradient validation using a simple nonlinear model

In order to illustrate the reliability and efficiency of adjoint method, a simple nonlinear model of free surface evolution is considered. The Korteweg-de-Vries (KdV) equation was chosen for this purpose. For constant depth h_0, and uni-directional propagation, KdV equation that includes both nonlinearity and dispersion to the leading order, can be written as:

$$\eta_t + C_0\eta_x + C_1\eta\eta_x + C_2\eta_{xxx} = 0, \tag{5.40}$$

Where η is the surface elevation above the mean water line, and C_0, C_1, and C_2 are constants defined as:

$$C_0 = \sqrt{gh_0}, \quad C_1 = \frac{3}{2}\sqrt{g/h_0}, \quad C_2 = \frac{1}{6}h_0^2\sqrt{gh_0}, \tag{5.41}$$

Equation (5.40) takes an exact solitary wave solution of the form:

$$\eta(x,t) = H\sec h^2\left(\beta(x-ct)\right), \quad \text{with } \beta = \sqrt{\frac{3H}{4h_0^3}}. \tag{5.42}$$

With height H above the mean water level which propagates without change of form with speed c in one direction (see Figure 5.1). As the first step in deriving the adjoint model of (5.40), the control variable η is perturbed by a small amount η', substituted into the equation (5.40), and higher-order terms such as $\eta'\eta'$ are neglected:

$$\cancel{\eta_t} + \eta'_t + C_0\left(\cancel{\eta_x} + \eta'_x\right) + C_1\left(\cancel{\eta\eta_x} + \eta\eta'_x + \eta'\eta_x + \cancel{\eta'\eta'_x}\right) + C_2\left(\cancel{\eta_{xxx}} + \eta'_{xxx}\right) = 0, \tag{5.43}$$

Where terms that construct the basic model (5.40) were canceled out. The final form of the TLM can be written as:

$$\eta'_t + C_0\eta'_x + C_1(\eta\eta')_x + C_2\eta'_{xxx} = 0, \tag{5.44}$$

This model simulates the propagation of an initial perturbation η' in time. The next step is to write the inner product of the introduced adjoint variable η^* with the TLM (5.44):

$$\int_t\int_x \eta^*\eta'_t \mathrm{d}x\mathrm{d}t + C_0\int_t\int_x \eta^*\eta'_x \mathrm{d}x\mathrm{d}t + C_1\int_t\int_x \eta^*(\eta\eta')_x \mathrm{d}x\mathrm{d}t + C_2\int_t\int_x \eta^*\eta'_{xxx}\mathrm{d}x\mathrm{d}t = 0, \quad (5.45)$$

Where the integral form of the inner product $\langle , \rangle$ was used. Using the integration by parts all temporal and spatial derivatives are transferred from η' to η^* to give:

$$\begin{aligned} &-\int_t\int_x \eta'\eta^*_t \mathrm{d}x\mathrm{d}t - C_0\int_t\int_x \eta'\eta^*_x \mathrm{d}x\mathrm{d}t - C_1\int_t\int_x \eta\eta'\eta^*_x \mathrm{d}x\mathrm{d}t \\ &- C_2\int_t\int_x \eta'\eta^*_{xxx}\mathrm{d}x\mathrm{d}t + b.t. = 0, \end{aligned} \quad (5.46)$$

Where $b.t.$ represents all boundary terms that result from the integration by parts. If periodic boundary conditions are assumed for η, η', and η^*, and it is further assumed that $\eta'(0) = \eta^*(T) = 0$, all these boundary terms will vanish, and the final form of the adjoint model can be written as:

$$\eta^*_t + C_0\eta^*_x + C_1\eta\eta^*_x + C_2\eta^*_{xxx} = 0, \quad (5.47)$$

As can be seen, the solutions of the forward model, η contribute as the coefficients of the adjoint model. In this example, observations are generated by the model itself by adding 5% independent Gaussian noise to the model-generated solutions every 1 second, i.e., $\eta_{obs}(t_j) = \eta(t_j)\,(1+\epsilon_j)$, with ϵ_j being a random Gaussian noise with zero mean and standard deviation of 0.05. Totally 10 observations were generated, i.e., the assimilation interval was $10s$. The water depth $h_0 = 2m$ was used in the calculations.

Both forward and adjoint models were solved using a pseudo-spectral method with 256 Fourier modes (grid points), in a computational domain of length $L \sim 460m$ (about 10 times the effective width of the solitary wave profile, $2\pi/\beta$), which gives a spatial resolution of about $\Delta x = 1.8m$, and the solution was evolved in time using a fourth-order Runge-Kutta integrator with step size $\Delta t = 0.01s$. The propagation of the solitary wave is shown in Figure 5.1 while the model-generated observations are illustrated in Figure 5.2. The initial condition for the solitary wave was $\eta(x,0) = 0.2\,\mathrm{sec}\,h^2\,(\beta(x-200))$.

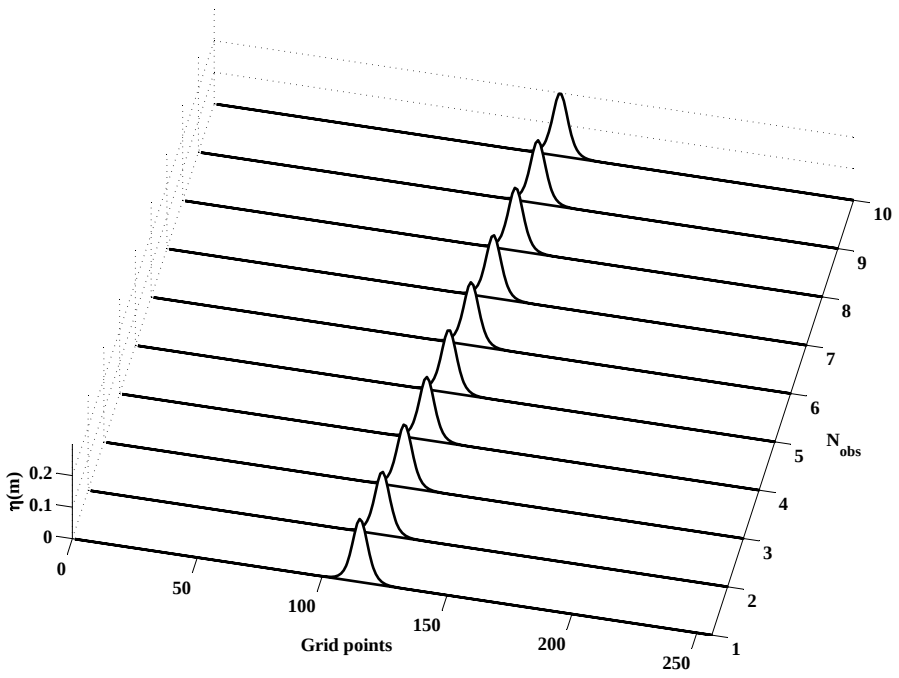

Figure 5.1: Evolution of the initial solitary wave $\eta(x,0) = 0.2\,\mathrm{sec}\,h^2\,(\beta(x-200))$; Solution plotted every 1 second.

The first step in identification of the gradient, would be to define the cost function. In this particular example, the cost function was simply defined as the discrepancy between the observations and model solutions over the assimilation interval $[t_1, t_{10}]$:

$$J = \frac{1}{2}\sum_{j=1}^{10}\sum_{i=1}^{256}\left(\eta(x_i,t_j) - \eta_{obs}(x_i,t_j)\right)^2. \tag{5.48}$$

To calculate the gradient of the cost function (5.48) with respect to the initial condition $\eta(x,0)$, the forward model (5.40) is first integrated from t_0 to $t_N (N = 10)$ with the model solutions $\eta(x,t_j),\ j = 1,2,\ldots,10$ being stored. The adjoint model (5.47) is then integrated backward in time, starting from $\eta^*(t_N) = \eta(t_N) - \eta_{obs}(t_N)$, and the adjoint variable η^* is modified by the data misfit $[\eta(t_j) - \eta_{obs}(t_j)]$ at times $t = t_j$ where observations are available (i.e. every 100 time steps). The value of gradient calculated from adjoint technique was compared with the one calculated from direct finite difference approximation. (see Figure 5.3).

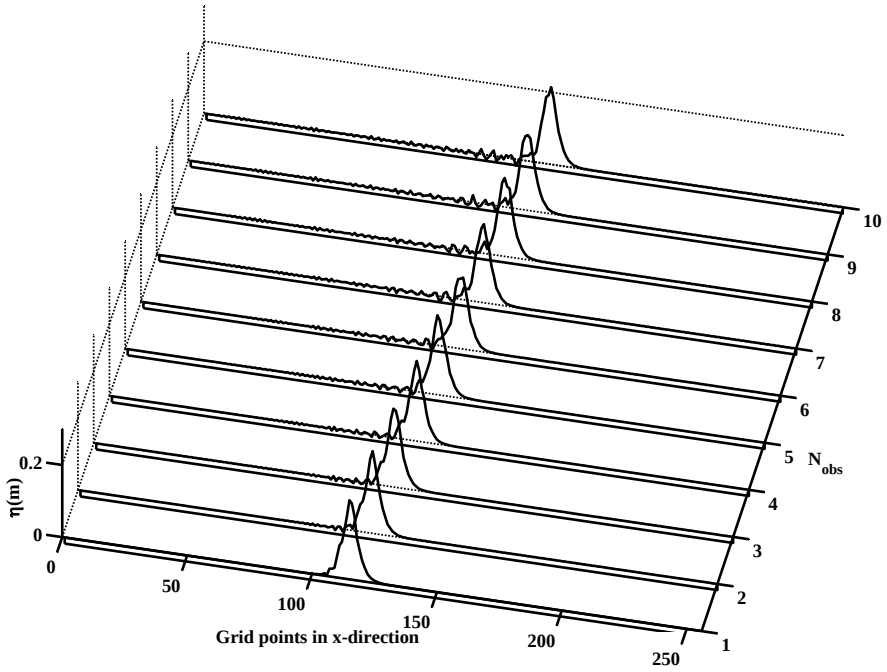

Figure 5.2: Observations generated by adding 5% uncorrelated Gaussian noise to the model solutions in 10 frames, $1s$ apart.

The adjoint method was about 200 ($\sim O(N)$) times faster than the finite difference method. The value of perturbation parameter α was 10^{-6}. The maximum absolute error between the adjoint and finite difference gradients was less than $0.025m$. This error will decrease if a smaller value of α is used, since the adjoint method is exact but the finite differencing is just a first-order approximation for the gradient which depends on the value of α.

5.4 Tangent linear/Adjoint of the pseudo-spectral wave model

Following the procedure explained in section 5.3, the tangent linear and adjoint equations of the original pseudo-spectral wave model presented in Chapter 3 (Equations (3.46)-(3.51)) are derived up to the third-order in wave steepness. Equations are first given for the three-dimensional flows, and their reduction to the two-dimensional flows would be

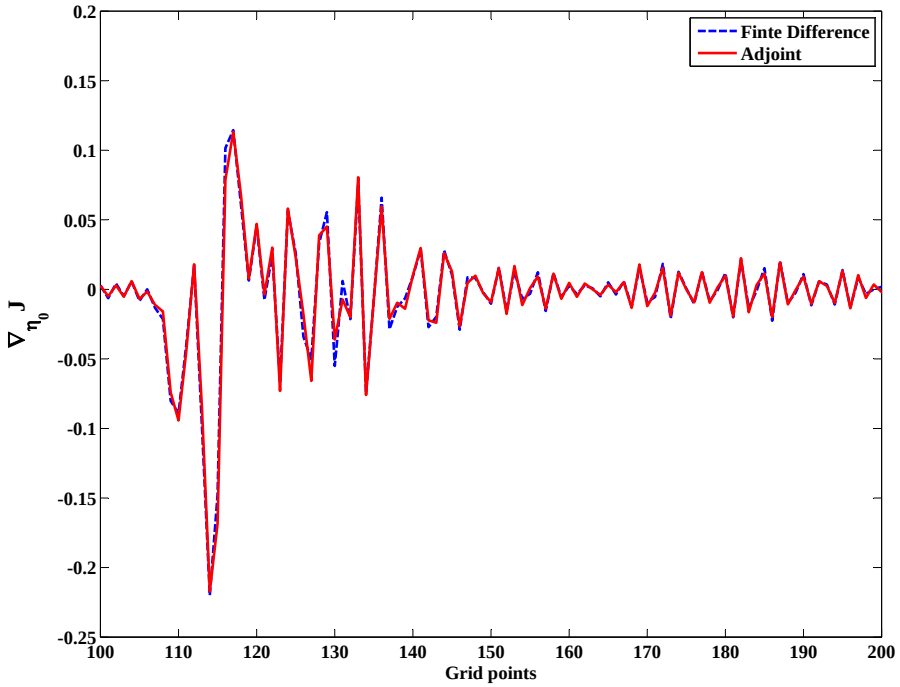

Figure 5.3: Comparison of adjoint-calculated gradient and finite difference-approximated gradient of the cost function with respect to initial condition, for the solitary wave problem.

straightforward.

5.4.1 Three-dimensional flows

First-order TLM

$$\eta'_t = \mathcal{T}[\mathbf{u}'_s],$$
$$\mathbf{u}'_{s,t} = -g\nabla\eta', \tag{5.49}$$

Second-order TLM

$$\begin{aligned}\eta'_t &= \mathcal{T}[\mathbf{u}'_s] - \nabla\cdot\left(\eta'\mathbf{u}_s + \eta\mathbf{u}'_s\right) - \mathcal{T}\left[\nabla\left(\eta'\mathcal{T}[\mathbf{u}_s] + \eta\mathcal{T}[\mathbf{u}'_s]\right)\right], \\ \mathbf{u}'_{s,t} &= -g\nabla\eta' - \nabla\left(\mathbf{u}_s\cdot\mathbf{u}'_s\right) + \nabla\left(\mathcal{T}[\mathbf{u}_s]\mathcal{T}[\mathbf{u}'_s]\right),\end{aligned} \tag{5.50}$$

Third-order TLM

$$\begin{aligned}\eta'_t = {} & \mathcal{T}[\mathbf{u}'_s] - \nabla\cdot\left(\eta'\mathbf{u}_s + \eta\mathbf{u}'_s\right) - \mathcal{T}\left[\nabla\left(\eta'\mathcal{T}[\mathbf{u}_s] + \eta\mathcal{T}[\mathbf{u}'_s]\right)\right] + \nabla^2\left(\frac{1}{2}\eta^2\mathcal{T}[\mathbf{u}_s] + \eta\eta'\mathcal{T}[\mathbf{u}'_s]\right) \\ & + \mathcal{T}\left[\nabla\left(\eta\mathcal{T}\left[\nabla\left(\eta\mathcal{T}[\mathbf{u}'_s]\right)\right]\right)\right] + \mathcal{T}\left[\nabla\left(\eta\mathcal{T}\left[\nabla\left(\eta'\mathcal{T}[\mathbf{u}_s]\right)\right]\right)\right] + \mathcal{T}\left[\nabla\left(\eta'\mathcal{T}\left[\nabla\left(\eta\mathcal{T}[\mathbf{u}_s]\right)\right]\right)\right] \\ & + \mathcal{T}\left[\nabla\left(\frac{1}{2}\eta^2\nabla\cdot\mathbf{u}'_s\right)\right] + \mathcal{T}\left[\nabla\left(\eta\eta'\nabla\cdot\mathbf{u}_s\right)\right],\end{aligned}$$

$$\begin{aligned}\mathbf{u}'_{s,t} = {} & -g\nabla\eta' - \nabla\left(\mathbf{u}_s\cdot\mathbf{u}'_s\right) + \nabla\left(\mathcal{T}[\mathbf{u}_s]\mathcal{T}[\mathbf{u}'_s]\right) - \nabla\left(\eta\mathcal{T}[\mathbf{u}_s]\nabla\cdot\mathbf{u}'_s\right) - \nabla\left(\eta\mathcal{T}[\mathbf{u}'_s]\nabla\cdot\mathbf{u}_s\right) \\ & - \nabla\left(\eta'\mathcal{T}[\mathbf{u}_s]\nabla\cdot\mathbf{u}_s\right) - \nabla\left(\mathcal{T}[\mathbf{u}_s]\mathcal{T}\left[\nabla\left(\eta\mathcal{T}[\mathbf{u}'_s]\right)\right]\right) - \nabla\left(\mathcal{T}[\mathbf{u}_s]\mathcal{T}\left[\nabla\left(\eta'\mathcal{T}[\mathbf{u}_s]\right)\right]\right) \\ & - \nabla\left(\mathcal{T}[\mathbf{u}'_s]\mathcal{T}\left[\nabla\left(\eta\mathcal{T}[\mathbf{u}_s]\right)\right]\right),\end{aligned} \tag{5.51}$$

First-order Adjoint

$$\begin{aligned}\eta^*_t &= -g\nabla\cdot\mathbf{u}^*_s, \\ \mathbf{u}^*_{s,t} &= \mathcal{T}[\eta^*],\end{aligned} \tag{5.52}$$

Second-order Adjoint

$$\eta_t^* = -g\nabla\cdot \mathbf{u}_s^* - \mathbf{u}_s^*\cdot \nabla\eta^* + \mathcal{T}[\mathbf{u}_s]\mathcal{T}[\nabla\eta^*],$$

$$\mathbf{u}_{s,t}^* = \mathcal{T}[\eta^*] - \eta\nabla\eta^* - \mathcal{T}\left[\eta\mathcal{T}\left[\nabla\eta^*\right]\right] - \mathbf{u}_s\nabla\mathbf{u}_s^* - \mathcal{T}\left[\nabla\mathbf{u}_s^*\mathcal{T}[\mathbf{u}_s]\right], \tag{5.53}$$

Third-order Adjoint

$$\begin{aligned}
\eta_t^* = & -g\nabla\cdot \mathbf{u}_s^* - \mathbf{u}_s\cdot \nabla\eta^* + \mathcal{T}[\mathbf{u}_s]\mathcal{T}[\nabla\eta^*] - \eta\mathcal{T}[\mathbf{u}_s]\nabla^2\eta^* - \mathcal{T}[\mathbf{u}_s]\mathcal{T}\left[\nabla\left(\eta\mathcal{T}\left[\nabla\eta^*\right]\right)\right] \\
& - \mathcal{T}\left[\nabla\eta^*\right]\mathcal{T}\left[\nabla\left(\eta\mathcal{T}[\mathbf{u}_s]\right)\right] - \eta\nabla\cdot\mathbf{u}_s\mathcal{T}\left[\nabla\eta^*\right] - \left(\nabla\cdot\mathbf{u}_s^*\right)\mathcal{T}[\mathbf{u}_s]\nabla\cdot\mathbf{u}_s \\
& - \mathcal{T}[\mathbf{u}_s]\mathcal{T}\left[\nabla\left(\mathcal{T}[\mathbf{u}_s]\nabla\cdot\mathbf{u}_s^*\right)\right],
\end{aligned}$$

$$\begin{aligned}
\mathbf{u}_{s,t}^* = & \mathcal{T}[\eta^*] - \eta\nabla\eta^* - \mathcal{T}\left[\eta\mathcal{T}\left[\nabla\eta^*\right]\right] - \mathbf{u}_s\nabla\cdot\mathbf{u}_s^* - \mathcal{T}\left[\nabla\cdot\mathbf{u}_s^*\mathcal{T}[\mathbf{u}_s]\right] + \mathcal{T}\left[\frac{1}{2}\eta^2\nabla^2\eta^*\right] \\
& + \mathcal{T}\left[\eta\mathcal{T}\left[\nabla\left(\eta\mathcal{T}\left[\nabla\eta^*\right]\right)\right]\right] + \nabla\left(\frac{1}{2}\eta^2\mathcal{T}\left[\nabla\eta^*\right]\right) + \nabla\left(\nabla\cdot\mathbf{u}_s^*\eta\mathcal{T}[\mathbf{u}_s]\right) + \mathcal{T}\left[\eta\nabla\cdot\mathbf{u}_s^*\nabla\cdot\mathbf{u}_s\right] \\
& + \mathcal{T}\left[\eta\mathcal{T}\left[\nabla\left(\mathcal{T}[\mathbf{u}_s]\nabla\cdot\mathbf{u}_s^*\right)\right]\right] + \mathcal{T}\left[\nabla\cdot\mathbf{u}_s^*\mathcal{T}\left[\nabla\left(\eta\mathcal{T}[\mathbf{u}_s]\right)\right]\right]
\end{aligned} \tag{5.54}$$

The anti-symmetry of the linear integral operator $\mathcal{T}$ was used in derivations, and periodicity in both directions was assumed for the free surface variables $(\eta, \mathbf{u}_s)$, tangent linear variables $(\eta', \mathbf{u}_s')$, and adjoint variables $(\eta^*, \mathbf{u}_s^*)$.

5.4.2 Two-dimensional flows

The tangent linear and adjoint equations given in (5.49)- (5.54) for three-dimensional flows can be reduced to the two-dimensional case in a straightforward manner.

First-order TLM

$$\begin{aligned} \eta'_t &= \mathcal{T}\left[u'_s\right], \\ u'_{s,t} &= -g\eta'_x, \end{aligned} \tag{5.55}$$

Second-order TLM

$$\begin{aligned} \eta'_t &= \mathcal{T}\left[u'_s\right] - \left(\eta' u_s + \eta u'_s\right)_x - \mathcal{T}\left[\left(\eta' \mathcal{T}\left[u_s\right] + \eta \mathcal{T}\left[u'_s\right]\right)_x\right], \\ u'_{s,t} &= -g\eta'_x - \left(u_s u'_s\right)_x + \left(\mathcal{T}\left[u_s\right] \mathcal{T}\left[u'_s\right]\right)_x, \end{aligned} \tag{5.56}$$

Third-order TLM

$$\begin{aligned} \eta'_t = {} & \mathcal{T}\left[u'_s\right] - \left(\eta' u_s + \eta u'_s\right)_x - \mathcal{T}\left[\left(\eta' \mathcal{T}\left[u_s\right] + \eta \mathcal{T}\left[u'_s\right]\right)_x\right] \\ & + \mathcal{T}\left[\left(\eta \mathcal{T}\left[\left(\eta \mathcal{T}\left[u'_s\right]\right)_x\right] + \eta \mathcal{T}\left[\left(\eta' \mathcal{T}\left[u_s\right]\right)_x\right] + \eta' \mathcal{T}\left[\left(\eta \mathcal{T}\left[u_s\right]\right)_x\right]\right)_x\right] \\ & + \mathcal{T}\left[\left(\frac{1}{2}\eta^2 u'_{s,x} + \eta\eta' u_{s,x}\right)_x\right] + \left(\frac{1}{2}\eta^2 \mathcal{T}\left[u'_s\right] + \eta\eta' \mathcal{T}\left[u_s\right]\right)_{xx}, \end{aligned}$$

$$\begin{aligned} u'_{s,t} = {} & -g\eta'_x - \left(u_s u'_s\right)_x + \left(\mathcal{T}\left[u_s\right] \mathcal{T}\left[u'_s\right]\right)_x \\ & - \left(\eta' \mathcal{T}\left[u_s\right] u_{s,x} + \eta \mathcal{T}\left[u'_s\right] u_{s,x} + \eta \mathcal{T}[u_s] u'_{s,x}\right)_x - \left(\mathcal{T}[u_s] \mathcal{T}\left[\left(\eta \mathcal{T}[u'_s] + \eta' \mathcal{T}[u_s]\right)_x\right]\right)_x \\ & - \left(\mathcal{T}[u'_s] \mathcal{T}\left[\left(\eta \mathcal{T}[u_s]\right)_x\right]\right)_x, \end{aligned} \tag{5.57}$$

First-order Adjoint

$$\begin{aligned} \eta_t^* &= -g u_{s,x}^*, \\ u_{s,t}^* &= \mathcal{T}[\eta^*], \end{aligned} \tag{5.58}$$

Second-order Adjoint

$$\begin{aligned} \eta_t^* &= -g u_{s,x}^* - u_s \eta_x^* + \mathcal{T}[u_s]\mathcal{T}[\eta_x^*], \\ u_{s,t}^* &= \mathcal{T}[\eta^*] - \eta\eta_x^* - \mathcal{T}\left[\eta\mathcal{T}\left[\eta_x^*\right]\right] - u_s u_{s,x}^* - \mathcal{T}\left[u_{s,x}^*\mathcal{T}[u_s]\right], \end{aligned} \tag{5.59}$$

Third-order Adjoint

$$\begin{aligned} \eta_t^* &= -g u_{s,x}^* - u_s \eta_x^* + \mathcal{T}[u_s]\mathcal{T}[\eta_x^*] - \eta\mathcal{T}[u_s]\eta_{xx}^* \\ &\quad - \mathcal{T}[u_s]\mathcal{T}\left[(\eta\mathcal{T}\left[\eta_x^*\right])_x\right] - \mathcal{T}\left[\eta_x^*\right]\mathcal{T}\left[(\eta\mathcal{T}[u_s])_x\right] - \eta u_{s,x}\mathcal{T}\left[\eta_x^*\right] \\ &\quad - u_{s,x}u_{s,x}^*\mathcal{T}[u_s] - \mathcal{T}[u_s]\mathcal{T}\left[\left(u_{s,x}^*\mathcal{T}[u_s]\right)_x\right], \\ u_{s,t}^* &= \mathcal{T}[\eta^*] - \eta\eta_x^* - \mathcal{T}\left[\eta\mathcal{T}\left[\eta_x^*\right]\right] - u_s u_{s,x}^* - \mathcal{T}\left[u_{s,x}^*\mathcal{T}[u_s]\right] + \mathcal{T}\left[\frac{1}{2}\eta^2\eta_{xx}^*\right] \\ &\quad + \mathcal{T}\left[\eta\mathcal{T}\left[(\eta\mathcal{T}\left[\eta_x^*\right])_x\right]\right] + \left(\frac{1}{2}\eta^2\mathcal{T}\left[\eta_x^*\right]\right)_x + \mathcal{T}\left[\eta u_{s,x}u_{s,x}^*\right] + \left(\eta u_{s,x}^*\mathcal{T}[u_s]\right)_x \\ &\quad + \mathcal{T}\left[\eta\mathcal{T}\left[\left(u_{s,x}^*\mathcal{T}[u_s]\right)_x\right]\right] + \mathcal{T}\left[u_{s,x}^*\mathcal{T}\left[(\eta\mathcal{T}[u_s])_x\right]\right], \end{aligned} \tag{5.60}$$

5.5 Data Assimilation for Two-dimensional Flows

Once the adjoint equations were derived and implemented, the gradient of the cost function with respect to initial conditions, which reflects the deviation of numerical predictions from radar measurements, can be efficiently found by integrating the adjoint model backward in time. The goal is to minimize this gradient. Since the number of free surface variables in two and three-dimensional problems differ significantly, two different minimization algorithms were adopted for these cases.

5.5.1 Minimization Algorithm for two-dimensional flows

The number of variables in two-dimensional problems is usually of the order 10^3, hence, using a minimization method that needs the storage of Hessian matrix (matrix of the second derivatives) at each iteration can be justified. A quasi-Newton method is used in the two-dimensional problems to minimize the cost function over the assimilation interval $[t_1, t_N]$, with the gradient information calculated using adjoint technique. By making a quadratic approximation of the cost function J at the point η_k, the value of the cost function at an adjacent point η can be calculated as:

$$J(\eta) = J(\eta_k) + \mathbf{g}_k^T + \frac{1}{2}\mathbf{d}_k^T \mathbf{H}_k \mathbf{d}_k \tag{5.61}$$

Point in this context is defined in N-dimensional space. $\mathbf{g}_k$ and $\mathbf{H}_k$ are the gradient vector and Hessian matrix of the cost function J at the point η_k, and the vector $\mathbf{d}_k$ is the step needed to be taken in order to get to the local minimum, and is referred to as the descent direction. In the neighborhood of η_k, the minimum of J occurs where the gradient becomes zeros, hence:

$$\mathbf{d}_k = \eta - \eta_k = -\mathbf{H}_k^{-1}\mathbf{g}_k, \tag{5.62}$$

gives the descent direction and subsequent points will follow as:

$$\eta_{k+1} = \eta_k + \alpha_k \mathbf{d}_k, \tag{5.63}$$

If the Hessian matrix was known, the expression (5.62) would have easily given the descent direction. However in quasi-Newton methods, an approximation to the Hessian is used instead. The approximation starts with the identity matrix, $\mathbf{H}_0 = \mathbf{I}$, and is updated at each iteration using the BFGS algorithm [57]:

$$\mathbf{H}_{k+1} = \left[\mathbf{I} - \frac{\mathbf{s}_k \mathbf{y}_k^T}{\mathbf{s}_k^T \mathbf{y}_k}\right] \mathbf{H}_k \left[\mathbf{I} - \frac{\mathbf{s}_k \mathbf{y}_k^T}{\mathbf{s}_k^T \mathbf{y}_k}\right]^T + \frac{\mathbf{s}_k \mathbf{s}_k^T}{\mathbf{s}_k^T \mathbf{y}_k}, \tag{5.64}$$

where,

$$\begin{aligned} \mathbf{s}_k &= \Delta\eta_k = \eta_{k+1} - \eta_k, \\ \mathbf{y}_k &= \Delta\mathbf{g}_k = \mathbf{g}_{k+1} - \mathbf{g}_k, \end{aligned} \tag{5.65}$$

This technique guarantees the movement towards the minimum with sufficiently small α_k since the Hessian $\mathbf{H}_k$ remains positive definite and symmetric for all k throughout the minimization process. The update formula for the inverse of the Hessian matrix has been also given in [57].

The step length α_k can be computed using an exact line search, however in this thesis an empirical method is used instead, to avoid additional computational effort. The initial step length is set to 1, a step is taken in the descent direction, and the cost function and its gradient are re-calculated. If the cost function was found to decrease, a new step is taken from the newly found point using the new gradient. Otherwise, a smaller step length equal to half of the previous one is taken using the previously computed gradient. A schematic illustration of the combination of the adjoint technique with a quasi-Newton minimization algorithm is displayed in Figure 5.4.

In the following sections the data assimilation scheme is implemented and tested with synthetically generated one-dimensional sea states, as well as with synthetic radar data from EM simulations.

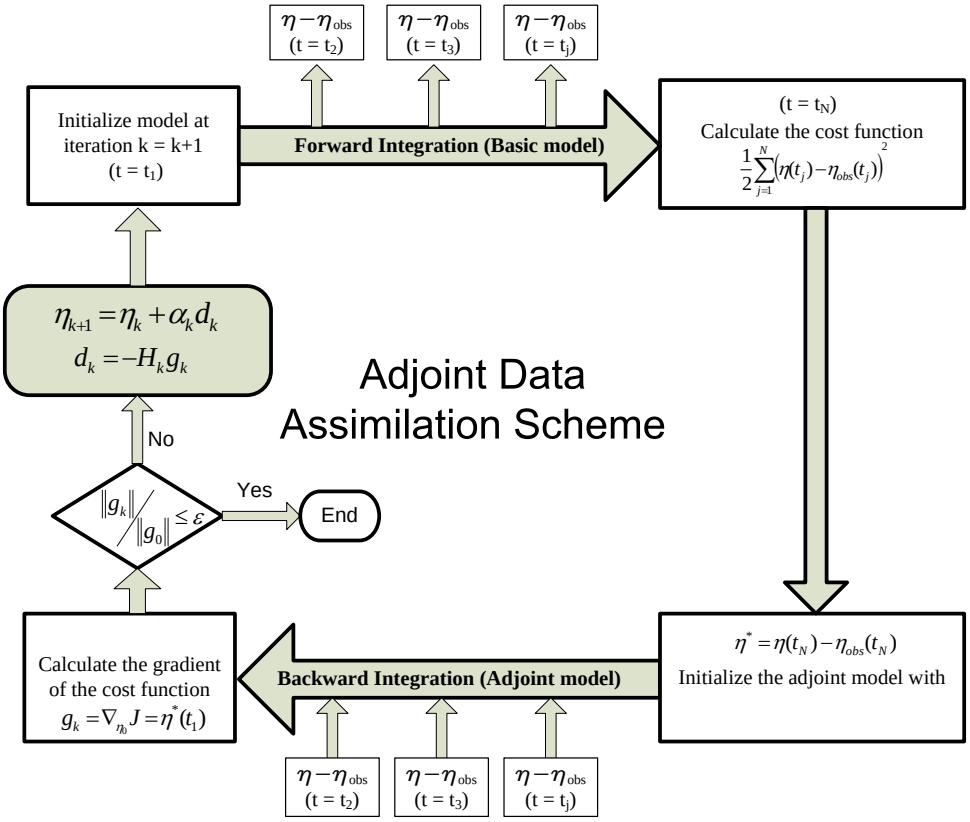

Figure 5.4: Schematic illustration of the adjoint data assimilation scheme used for two-dimensional flows.

5.5.2 Test with synthetically generated one-dimensional sea surface

Numerical tests were performed to examine the validity of the adjoint method for the 1-D pseudo-spectral wave model. A synthetic one-dimensional wave field was generated from a JONSWAP spectrum with significant wave height $H_s = 2m$, peak period $T_p = 10s$, and $\gamma = 3.3$. The simulations were carried out in a computational domain with length $L = 3066m$ at a spatial resolution of $\Delta x = 6m$ with totally 512 grid points (Fourier modes). The first-order forward model equations were integrated with time step size $\Delta t = 0.25s$. Uncorrelated Gaussian noise was added to 16 model-generated sea surfaces at intervals of $2.5s$ to be used as radar observations. The noise's standard deviation was 40% of the standard deviation of the sea surface elevation.

The adjoint-calculated gradient was first compared with the direct finite difference results to ensure the validity of the gradients. The converged optimal initial sea surface was

then used to forecast beyond the assimilation interval ($40s$) up to $t = 500s$. Figure 5.5 shows the comparison of the gradient of the cost function with respect to initial condition calculated from the two discussed methods: Adjoint method and direct FD.

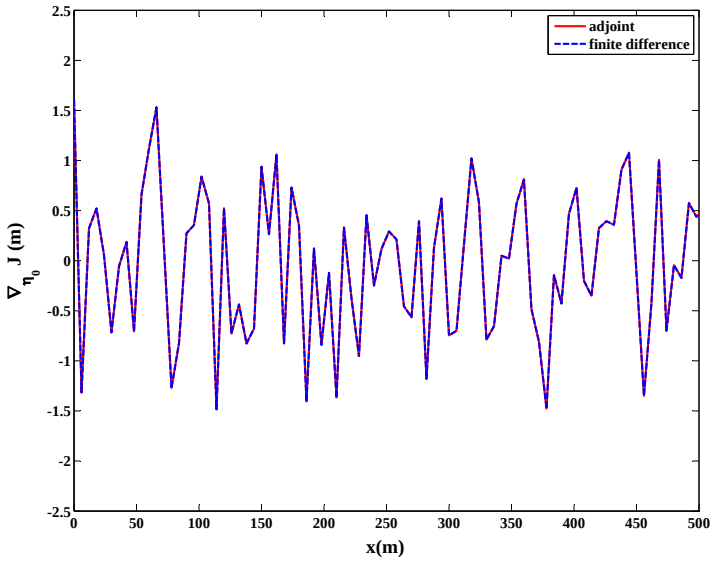

Figure 5.5: Comparison of the gradient of the cost function with respect to initial conditions calculated from adjoint and FD methods.The maximum absolute error = $O(\alpha)$.

The perturbation parameter α used in FD method was 10^{-6}, i.e. less than 0.001% of the standard deviation of the surface elevation, to ensure that the round-off errors don't corrupt the accuracy of the calculated gradient. The maximum absolute error between the two methods was about $7.5 \times 10^{-6} \approx O(\alpha)$ which confirms the first-order accuracy of the FD method, while the adjoint-calculated gradient is exact. The overall two-norm of the error was about $1.7 \times 10^{-4} \approx O(N\alpha)$.

The first-order evolution equations (3.46)- (3.47) were first integrated using noisy initial condition. However, the forecast was different from the known true sea surface because of the presence of noise in the initial condition. The simulation was then repeated with the adjoint assimilation scheme used to correct the initial condition. A quasi-Newton algorithm with BFGS update of the Hessian matrix was implemented to minimize the cost function, with the linear adjoint model (5.58) used to obtain the gradient of the cost function at each

iteration. The convergence criterion

$$||\mathbf{g}|| \leq 10^{-10}||\mathbf{g}_0||, \tag{5.66}$$

was used for this example which yielded a high quality of the retrieved surface profiles in terms of RMS errors relative to the clean reference solution. 20 iterations and about $15s$ of CPU time were required for this assimilation problem. The variation of the cost function scaled by its initial value (J/J_0) as well as those of the norm of the gradient also scaled by its initial value ($||\mathbf{g}||/||\mathbf{g}_0||$) as functions of the number of iterations are displayed in Figure 5.6. The Figure 5.6 indicates that the minimization algorithm could be stopped even after the second iteration by accepting a more reasonable criterion such as $||\mathbf{g}|| \leq 10^{-2}||\mathbf{g}_0||$, since the cost function has already reached its minimum by that time.

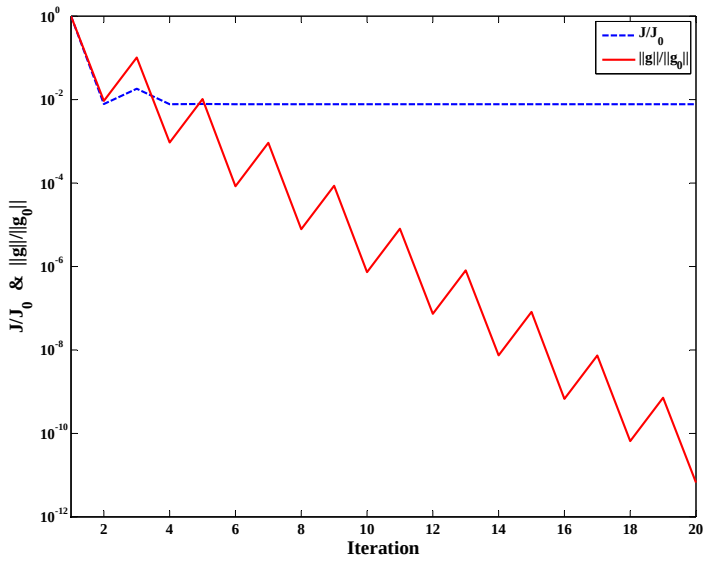

Figure 5.6: Variation of the log of the scaled cost function (J_k/J_0, dashed line) and scaled gradient norm ($||\mathbf{g}_k||/||\mathbf{g}_0||$, solid line) with the number of iterations using adjoint method with quasi-Newton minimization scheme.

Figure 5.7 shows that retrieved surface profiles obtained using the adjoint method are almost identical to the clean reference solution.

The optimal initial condition is then evolved to forecast up to $t = 500s$. The RMS errors between the retrieved profile at $t = 0$ and $t = 500s$, and their corresponding exact

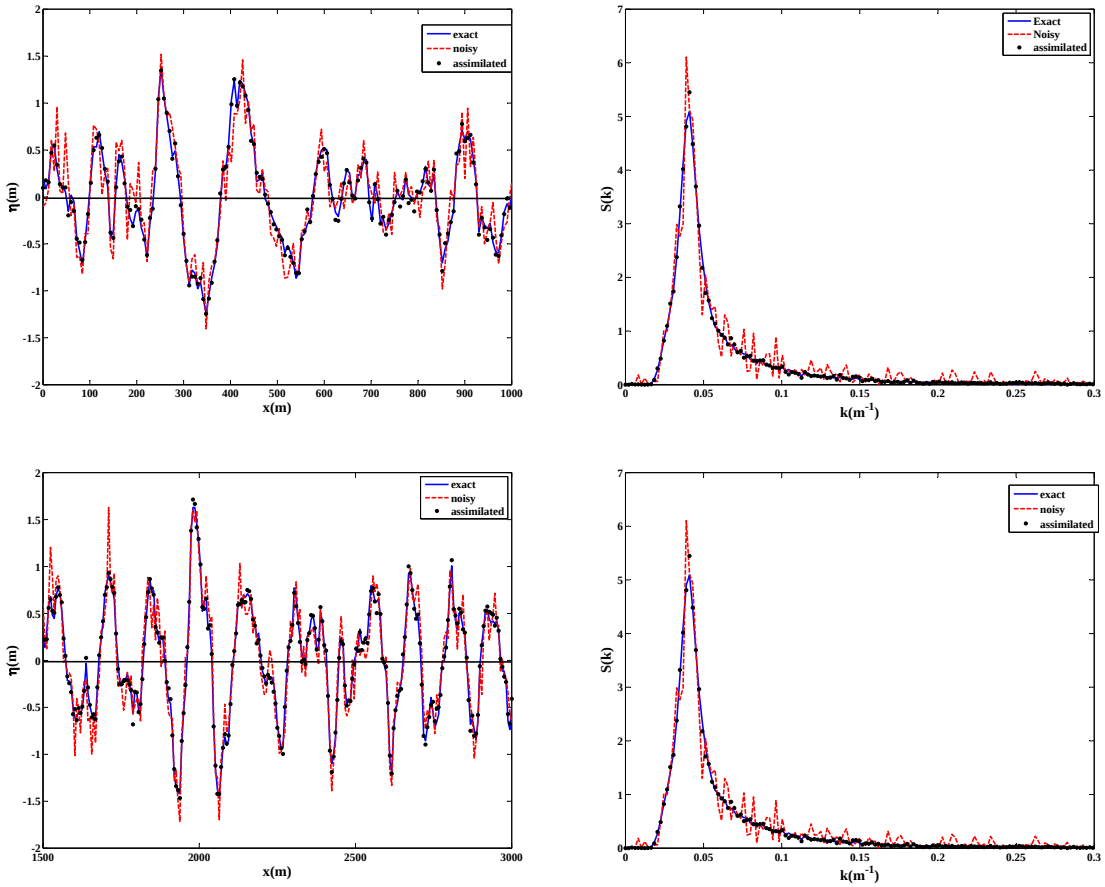

Figure 5.7: Left: Comparison of retrieved surface profiles (circles) at $t = 0$ (top left) and $t = 500s$ (bottom left) with the exact reference solution (solid) and noisy solution (dashed). Right: Comparison of wavenumber spectra at $t = 0$ (top right) and $t = 500s$ (bottom right).

reference profiles were $0.053m$ and $0.047m$, respectively, which are almost a quarter of the ones associated with the noisy profiles. The corresponding spectra also show that the assimilation scheme is able to filter-out the noise that was artificially added to the observations.

Figure 5.8 shows the comparison of surface elevation time history for the point in the middle of the computational domain ($x = 1533m$), obtained from optimal initial condition with the corresponding exact and noisy ones. The RMS error associated with the assimilated time history was $0.049m$ compared to $0.2m$ associated with the noisy one. In this numerical example, the data assimilation scheme was able to reduce the initially added 40% noise to about 10%, which can be reduced even further by including more observations within the

assimilation period or reducing the time interval between the observations.

Effect of nonlinearity

To investigate the effect of nonlinearity on the assimilation the same experiment is carried out with the third-order model equations this time. All model parameters were kept the same except that the third-order equations (3.50)- (3.51) were used to evolve the initial surface profile, and the third-order adjoint model (5.60) was used to calculate the gradient of the cost function with respect to the initial condition. In order to suppress the high-frequency oscillations of the adjoint variables η^* and u_s^*, a low-pass filter, similar to that implemented in the forward model, was used when integrating the adjoint equations backward. The cost function was scaled with the variance of the surface profile as follows:

$$J = \sum_{j=1}^{NT} \sum_{i=1}^{NX} \frac{1}{\sigma_{\eta_j}^2} \left[\eta\left(x_i, t_j\right) - \eta_{obs}\left(x_i, t_j\right)\right]^2, \tag{5.67}$$

where $\sigma_{\eta_j}^2$ denotes the variance of the surface profile at time $t = t_j$. This weighting function makes the cost function non-dimensional. The initial value for the Hessian matrix in the beginning of the minimization was also chosen as:

$$H_0 = \frac{\sigma_{x_0}}{||\mathbf{g}_0||} I \tag{5.68}$$

where σ_{x_0} is the standard deviation of the initial guess and $||\mathbf{g}_0||$ is the 2-norm of the initial gradient at the beginning of the assimilation. Adding the weighting factor was extremely helpful in improving the convexity of the cost function during the minimization process and guaranteed the stability of the adjoint model. Figure 5.9 shows the comparison of the calculated gradient using adjoint technique with that calculated by FD. The difference was $O(\alpha)$ which confirms the correctness of the adjoint model.

Data assimilation experiment was then carried out using the first 16 noisy observational

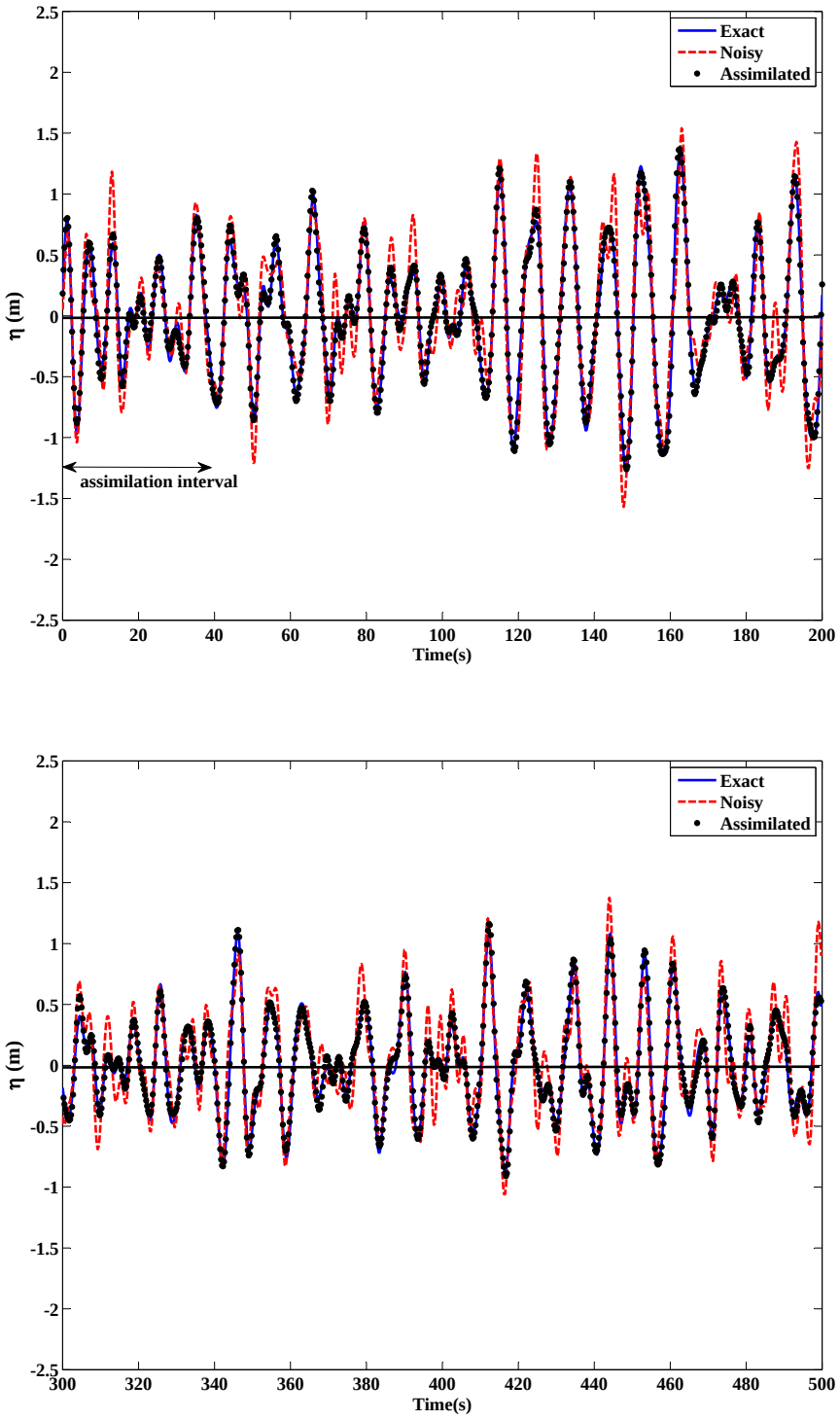

Figure 5.8: Comparison of the surface elevation time history of the middle-point ($x = Lx/2$) obtained form optimal initial condition (circles), with those obtained from exact (solid) and corrupted initial conditions (dashed). top: $t \in [0, 200]$, bottom: $t \in [300, 500]$.

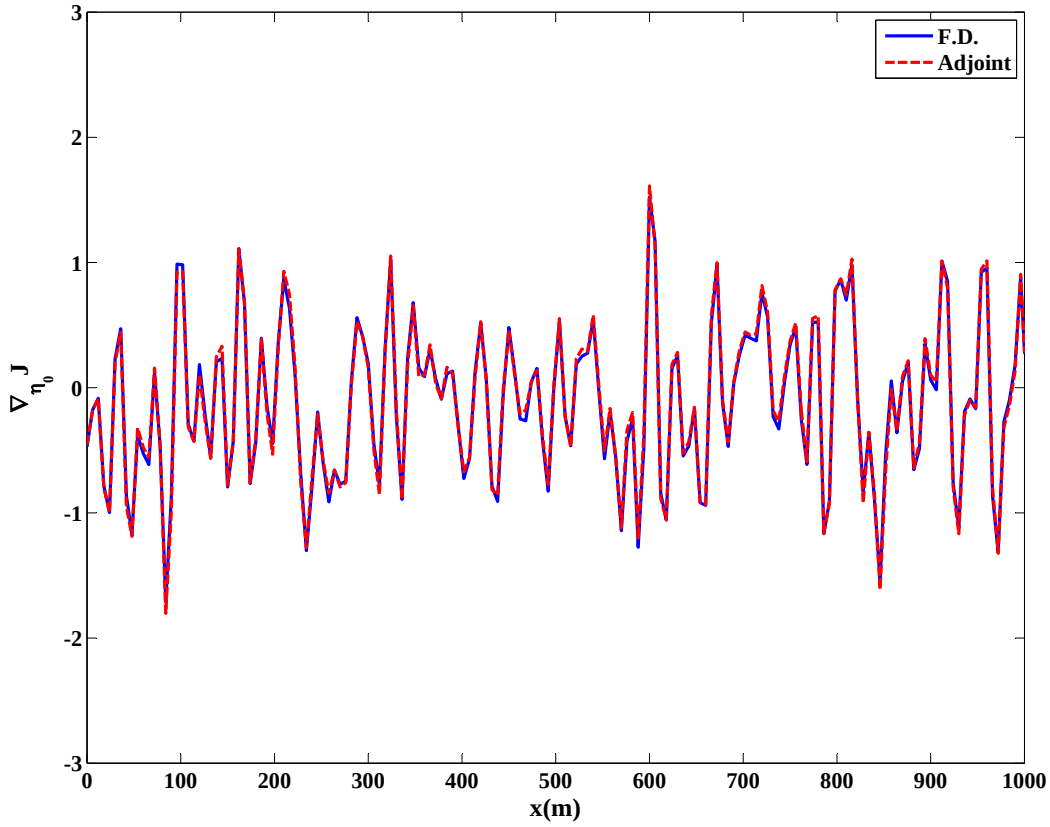

Figure 5.9: Comparison of the gradient of the cost function with respect to initial conditions calculated from adjoint and FD methods for the third-order model. The maximum absolute error = $O(\alpha)$.

frames with $2.5s$ intervals. The convergence criterion:

$$||\mathbf{g}_{k+1}|| \leq 10^{-4}||\mathbf{g}_0||, \tag{5.69}$$

was used to stop the minimization algorithm. The variation of the cost function scaled by its initial value (J/J_0) as well as those of the norm of the gradient also scaled by its initial value ($||\mathbf{g}_0||/||\mathbf{g}_0||$) as functions of the number of iterations are displayed in Figure 5.10 (top), which indicates that the convergence has been reached after 14 iterations, compared to the almost 6 iterations needed for the first-order model with the same stopping criteria (see Figure 5.6). The quality of the retrieved initial condition in physical and Fourier space are also displayed in Figure 5.10(bottom).

The RMS error between the retrieved (assimilated) initial condition and the perfect

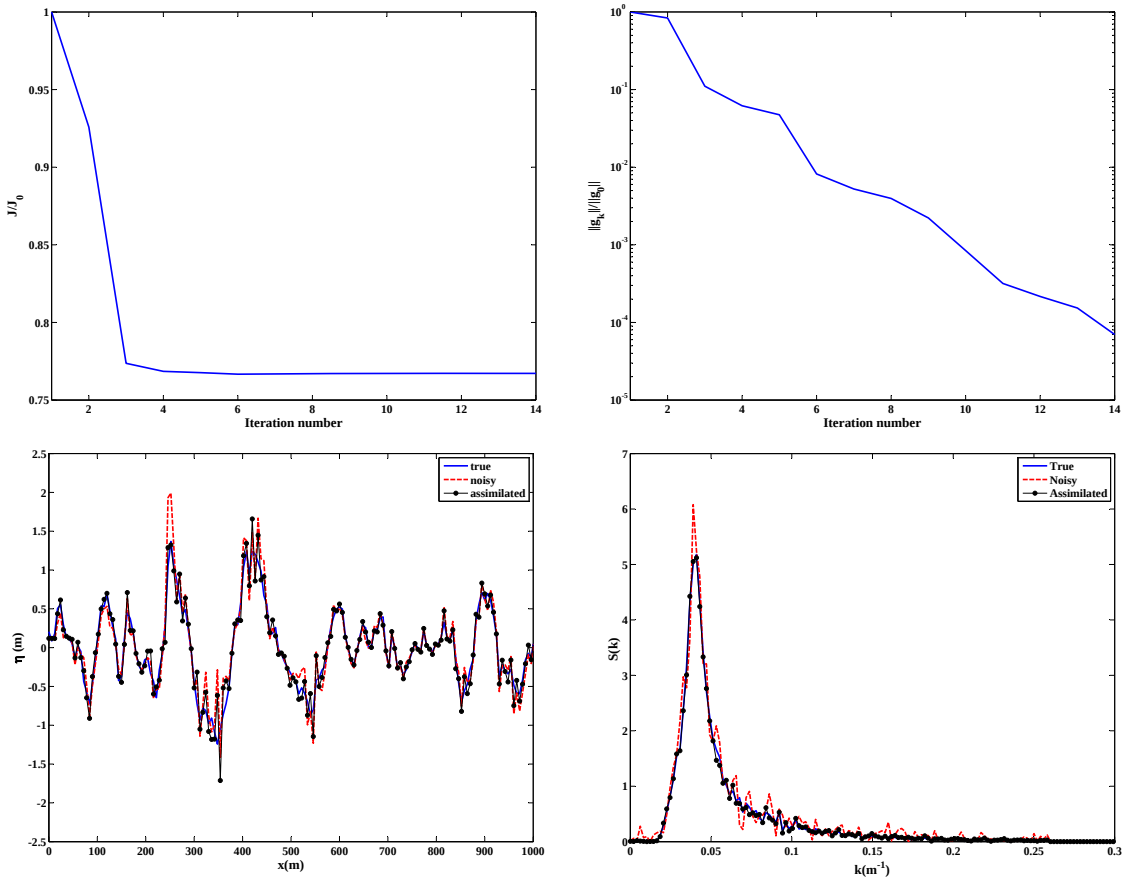

Figure 5.10: Top left: Variation of the scaled cost function (J_k/J_0) with the number of iterations; Top right: Variation of the scaled gradient norm ($||\mathbf{g}_k||/||\mathbf{g}_0||$) with the number of iterations; Bottom left: Comparison of retrieved surface profiles (circles) at $t = 0$ with the exact reference solution (solid) and noisy solution (dashed); Bottom right: Comparison of the wavenumber spectra at $t = 0$.

initial condition is $0.067m$, comparing to that ($0.183m$) between the the perfect initial surface and the first noisy observation. In order to investigate the quality of the assimilation, the retrieved surface profile was evolved using the third-order forward model. The time history of the mid-point ($x = 1533m$) obtained from the retrieved initial condition was compared with those obtained form the perfect and noisy initial conditions.

It is apparent from Figure 5.11 that this third-order data assimilation scheme is capable of improving the surface elevation forecasts.

To quantify the difference that the third-order adjoint system makes in the assimilation process, a simple experiment was done in which both first-and third-order adjoint models were used to assimilate 16 noisy observational frames which were generated using the

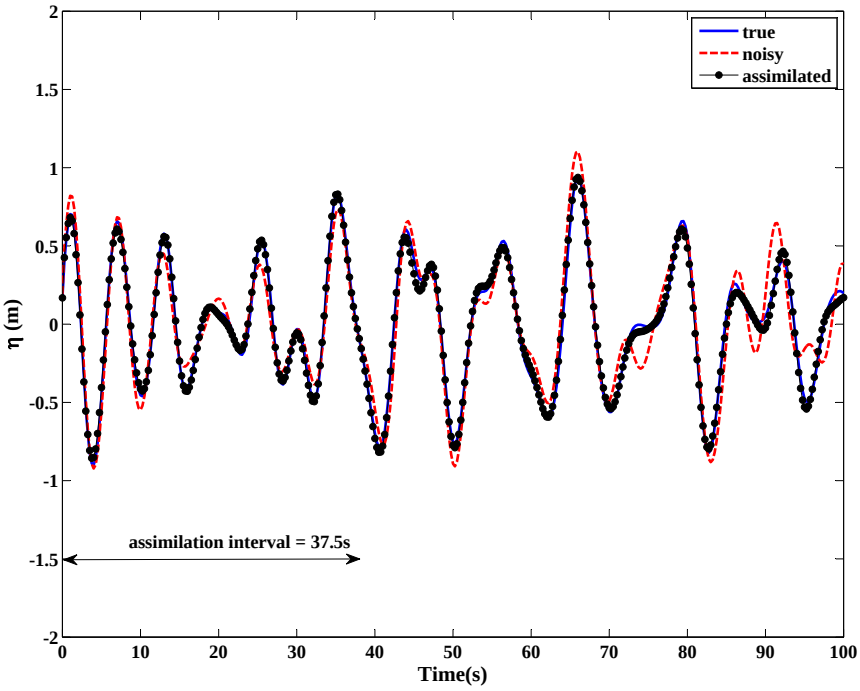

Figure 5.11: Comparison of the time histories of the mid-point, obtained from the exact initial condition(solid), noisy initial condition(dashed), and assimilated initial condition(circles). Third-order forward and adjoint models were used.

outputs of the third-order model. The retrieved optimal initial condition from both assimilation tests was then allowed to evolve using the third-order model. Figure 5.12 displays part of the time history of the mid-point ($x = L/2$) obtained by the first and third-order assimilation schemes.

The RMS error between the third-order-assimilated profile and the true surface was $0.0336m$ compared to that ($0.0736m$) between the first-order-assimilated profile and the true one. The phase error associated with the linear assimilation is clearly observed around the time $t = 182s$. As the assimilation interval gets longer and the nonlinear wave-wave interaction effects become more important, the difference becomes more pronounced.

In all numerical experiments carried out so far in this chapter, it has been assumed that the free surface elevation η is the only observed variable, which leaves it to us to approximate the tangential velocity u_s and adjoint variable u_s^* from the values of η and η^*. In the experiments carried out so far with the third-order model, the linear theory was used

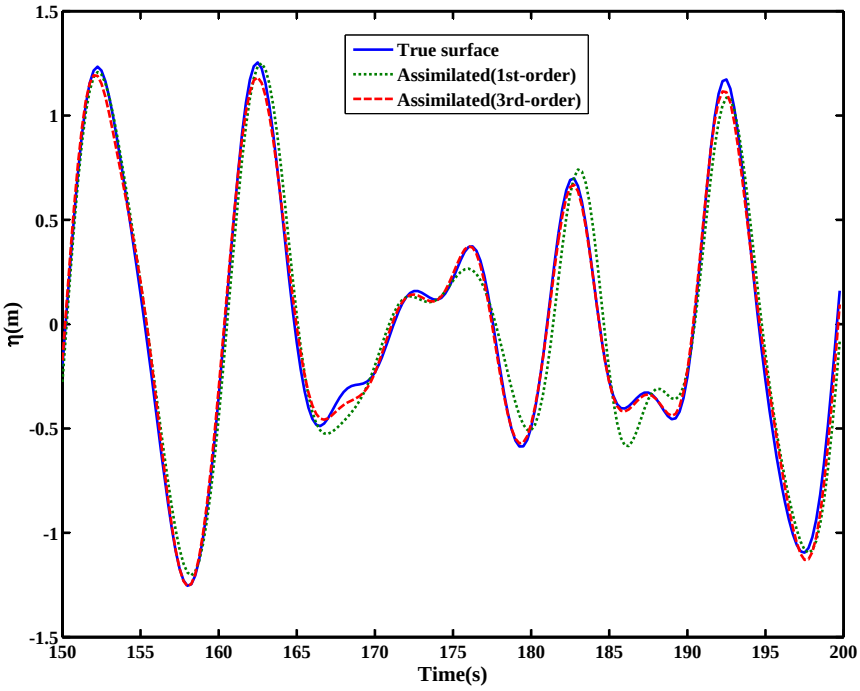

Figure 5.12: Comparison of the time histories of the free surface at the mid-point ($x = L/2$) obtained by first-order (dotted) and third-order (dashed) assimilation schemes; Solid line indicates the true surface profile.

to obtain u_s and u_s^* from η and η^*, respectively, i.e.

$$b_n(0) = \sqrt{g|k|}a_n(0),$$
$$b_n^*(t) = \frac{\tanh kh_0}{\omega}a_n^*(t), \tag{5.70}$$

where a_n^* and b_n^* are the Fourier coefficients of the adjoint variables η^* and u_s^*, respectively. In an attempt to evaluate the errors associated with these approximations, the values of u_s and u_s^* were instead calculated from the third-order forward and adjoint models (4.5) and (5.60), respectively, using a nonlinear Newton-type iterative scheme which uses the linear solution (5.70) as an initial guess. Figure 5.13 shows the time histories of the surface elevation at the point located at $x = L/4$, resulting from the third-order assimilation scheme with linear (dashed) and nonlinear iterative update (dotted) of the variables u_s and u_s^*. As shown in Figure 5.13, the difference was not significant for this example (less than 0.1%).

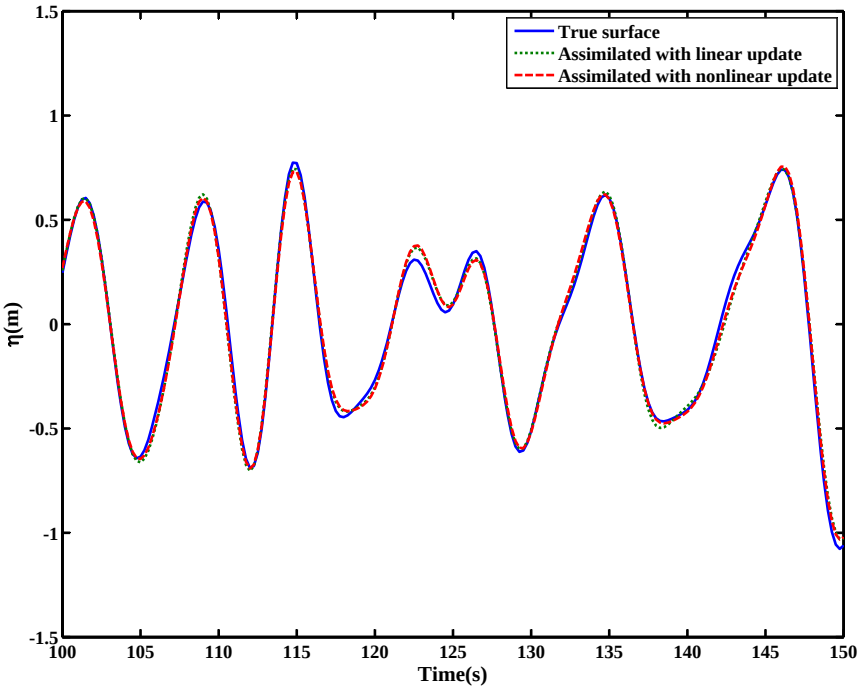

Figure 5.13: Comparison of the time histories of the free surface elevation $\eta\left(\frac{L}{4}, t\right)$ resulting from the third-order assimilation with linear (dashed) and nonlinear iterative updates (dotted) of the forward and adjoint variables u_s and u_s^*; Solid line is the true surface profile.

Uniqueness of the solution

An important issue in variational data assimilation is to determine whether the retrieved solution is unique. If more than one local minimum exists, then the solution of the minimization process may possibly change depending on different initial guesses. If at a point the gradient vanishes and the Hessian is positive definite, that point is a relative (local) minimum point. This characterization has a natural extension to the global approach where convexity ensures that if the gradient vanishes at a point, that point is a global minimum. The Hessian matrix is the generalization to the concept of the curvature of a function, and correspondingly, positive definiteness of the Hessian is the generalization of positive curvature.

In order to find out about the uniqueness of the cost function with respect to the initial conditions, the shifted power method was used to obtain the largest and smallest eigenvalues of the Hessian at each iteration during the minimization and the condition number of the

Hessian matrix was carefully monitored. The smallest and largest eigenvalues were positive at all iterations. They started off with large variations at the initial iterations and tended to remain constant at the last iterations. Most changes in the condition number also occurred during the early stage of the assimilation. The positiveness of the smallest eigenvalues during the assimilation implies the positive definiteness of the Hessian, which in turn proves the uniqueness of the optimal solution.

In order to determine whether or not the retrieved solution was the global solution, the assimilation was restarted with several slightly different initial guesses and the final value of the cost function was found to remain almost constant.

Effect of the length of assimilation interval

In order to investigate the impact of increasing the length of the assimilation interval on the outcome of the assimilation, a simple numerical experiment was carried out with 8, 16, 32, and 64 observations incorporated within the assimilation interval. Observations were model-generated with 20% of uncorrelated Gaussian noise added to the model solutions every $2.5s$. Third-order forward and adjoint models were used for assimilation and all other model parameters remained unchanged. The retrieved initial condition was evolved up to $t = 400s$. Table 5.1 summarizes the results of this experiment.

	Number of observations			
	8	16	32	64
Assimilation interval(s)	17.5	37.5	77.5	157.5
Number of iterations	7	8	8	9
J_{min}	74.280	142.41	314.25	637.52
RMS error(m)	0.0310	0.0184	0.0133	0.0097

Table 5.1: Error and iteration information for the cases where 8, 16, 32, and 64 observations were used in the assimilation.

where the root mean square errors were calculated for the point in the middle of the computational domain:

$$\text{RMS Error } = \frac{||\eta\,(L/2,t) - \eta_{true}\,(L/2,t)\,||}{\sqrt{NT}} \tag{5.71}$$

where $NT = 1600$ in this simulation. If no assimilation was used and the first observation was taken as initial condition, the RMS error would have been $0.077m$. Table 5.1 clearly shows that including more observations within the assimilation interval will certainly improve the assimilation results, however the number of iterations taken for convergence and the needed CPU time will also increase. For all cases the convergence criterion was defined as $||\mathbf{g}|| \leq 10^{-4}||\mathbf{g}_0||$. The number of iterations to the minimum ranged from 7 to 9 in all cases. Table 5.1 reveals that RMS errors decrease almost linearly by incorporating more observation within the assimilation interval.

Impact of the observational errors

If the numerical model and the observations are assumed to be perfect, the minimum value of the cost function J should converge to zero. In order to investigate this and take an assessment of the rate of convergence, a numerical experiment is carried out with the noiseless observations with a randomly perturbed initial guess. All other model parameters are kept unchanged. A table is constructed of the values $\xi_k = J_{k-1} - J_k$ from successive iterations (see table (5.2)). J_k is the value of the cost function at the kth iteration scaled by its initial value J_0. Fast linear convergence is indicated if $\xi_{k+1} \approx \xi_k/M$, where $M > 2$.

k	J_k	$\|\|\mathbf{g}_k\|\|$	ξ_k	$\xi_k/\xi_{k+1} = M$
1	0.0096	0.1020	0.9904	295.65
2	0.0062	0.0803	0.0033	0.9322
3	0.0026	0.0496	0.0036	1.7838
4	0.0006	0.0213	0.0020	4.8349
5	0.0002	0.0082	0.0004	11.610
6	0.00016	0.0057	3.59×10^{-5}	3.0447
7	0.00015	0.0044	1.18×10^{-5}	0.8855
8	0.00014	0.0023	1.33×10^{-5}	3.2010
9	0.00013	0.00087	4.16×10^{-6}	6.8439
10	0.00013	0.00031	6.08×10^{-7}	11.533
11	0.00013	0.00023	5.27×10^{-8}	1.5
12	0.00013	0.00017	3.51×10^{-8}	0.9091
13	0.00013	8.5×10^{-5}	3.86×10^{-8}	

Table 5.2: Convergence analysis information for the quasi-Newton algorithm for the case of perfect model/observations.

After 13 iterations, the cost function decreased 4 orders of magnitude. This table shows that the quasi-Newton algorithm has a fast linear convergence rate for most iterations, with an average of $M = 4.27$ while its convergence rate slows down for the last three iterations with the average $M = 1.2$. The quasi-Newton algorithm has a theoretical quadratic convergence rate. However, its numerical convergence rate in this example was only fast linear. This is due to the fact that because of the third-order nonlinearity, the gradient information obtained by integrating the adjoint equations is not exact. Therefore the error associated with calculating the gradient will make the minimization results less accurate.

In order to investigate the impact of observational errors on the variational assimilation another assimilation experiment was carried out with 16 model-generated observations having 10 to 50% uncorrelated noise. The information about the iteration and RMS errors associated with the assimilated and non-assimilated cases are summarized in table 5.3.

	Error in the observations				
	10%	20%	30%	40%	50%
Number of iterations	6	8	11	13	12
Minimized cost function	38.58	152.55	339.56	613.21	895.14
Error(without assimilation)	0.0298	0.0530	0.1006	0.1280	0.1440
Error(with assimilation)	0.0086	0.0145	0.025	0.0357	0.0426

Table 5.3: Error and iteration information for 10-50% observational errors.

RMS errors have been again calculated for the time history of the point in the middle of the computational domain ($x = L/2$), with the same definition as (5.71). Table 5.3 clearly shows that the assimilation errors (or without assimilation)increase almost linearly with increasing the observational errors. The quadratic variation of the value of the cost function at the minimum with the observational errors can be also inferred from this table. Figure 5.14 displays the variation of the norm of the gradient, scaled with its initial value, with the number of iterations for 10, 20, 30, and 40% observational errors.

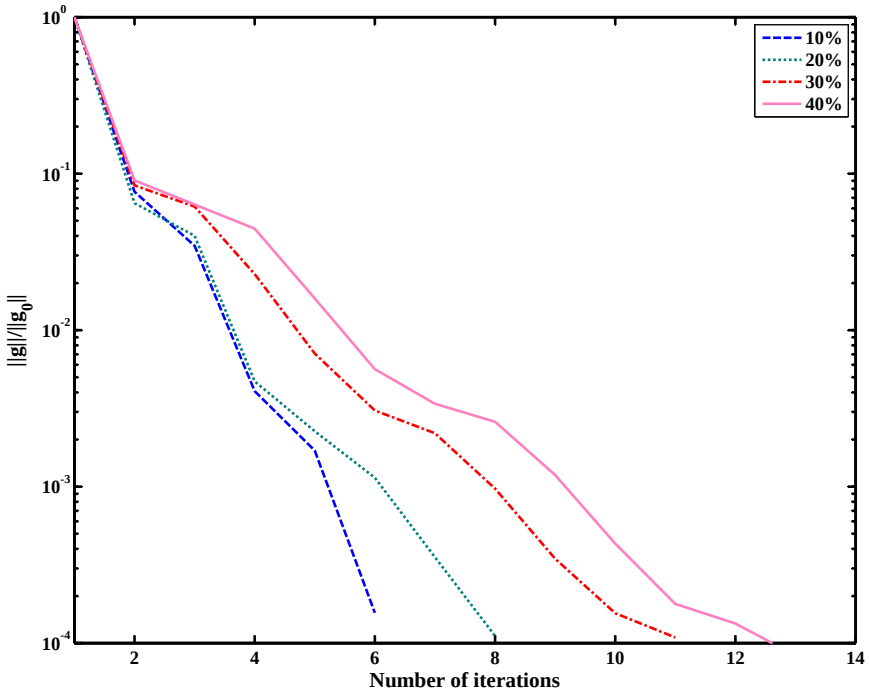

Figure 5.14: Variation of the norm of the cost function scaled by its initial value, $||\mathbf{g}||/||\mathbf{g}_0||$, for different observational errors.

Comparison with dispersion filters

In absence of surface currents, physical wave components propagate with the phase speed obtained from the dispersion relation:

$$\omega = \sqrt{gk \tanh kh}, \tag{5.72}$$

However, the propagation speed of non-physical components (noise) is not consistent with the dispersion relation. One alternative to remove the noisy components in observations is to fit the theoretical linear dispersion relation (5.72) to the two-dimensional Fourier transform of the observational frames in wavenumber-frequency domain. Thereby, the dispersion function is broadened in k and ω to also capture components of the wave spectrum that do not lie exactly on this function. To suppress those Fourier coefficients with small wavenumbers and those with noise, a band-pass filter is applied as follows:

$$\hat{\eta}_F(k,\omega) = \hat{\Omega}(k,\omega)\hat{\eta}(k,\omega) \tag{5.73}$$

where $\hat{\eta}_F(k,\omega)$ is the filtered surface profile in wavenumber-frequency domain, $\hat{\eta}(k,\omega)$ is the two-dimensional Fourier transform of the original noisy record, and the Gaussian band-pass filter function $\hat{\Omega}(k,\omega)$ is defined as (see Figure 5.15):

$$\hat{\Omega}(k,\omega) = e^{-0.25\left(\frac{\omega-\omega_0}{f_\omega}\right)^2}, \tag{5.74}$$

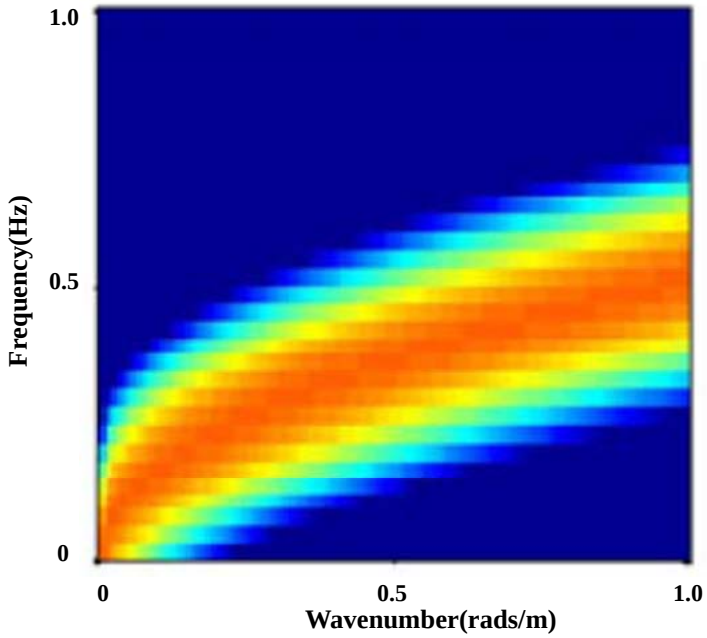

Figure 5.15: Band-pass filter in $k-\omega$ domain, applied to the original noisy profiles.

where ω_0 is obtained from the linear dispersion relation (5.72). The parameter f_ω determines the band width of the filter which is usually chosen as a fraction of the maximum frequency ω_{max} (In this example, $f_\omega = \omega_{max}/6$). To retrieve the wave field $\eta(x,t)$, the complex 2-D wave spectrum $\hat{\eta}_F(k,\omega)$ was transformed into the spatial-temporal domain by an inverse 2-D FFT. A simple experiment was carried out to evaluate the performance of the filter and compare its outcome with the assimilated results.

The initial condition obtained from the JONSWAP spectrum (with $H_s = 2m$ and $T_p = 10s$) was evolved using the third-order model and the observations were generated by adding 40% of independent Gaussian noise to the model outputs at 2.5 second intervals. Totally 128 observations were generated (up to $t = 317.5s$). The left plot in Figure 5.16 displays the generated observations in spatial-temporal domain, while the right plot shows the retrieved

profiles obtained by the application of the band-pass filter (5.74) to all 128 observational frames.

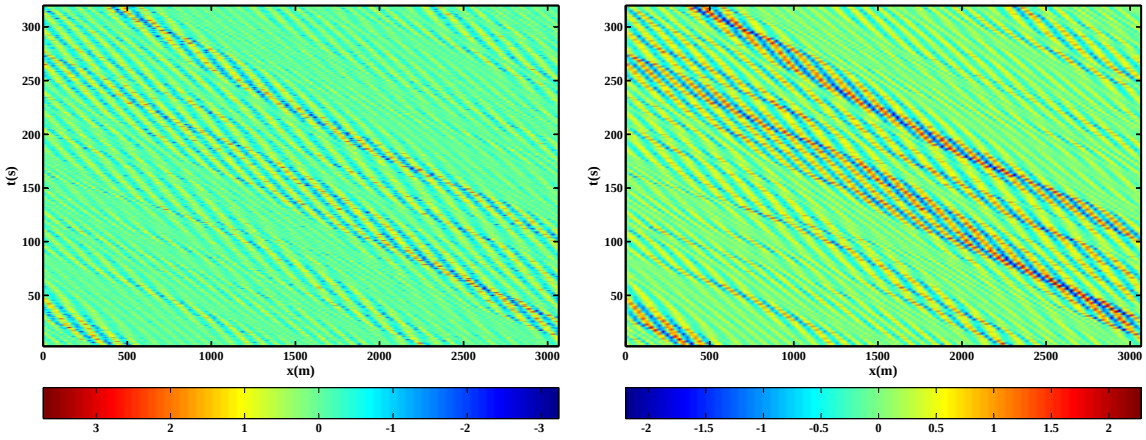

Figure 5.16: Left: Original noisy observations in spatial-temporal $(x-t)$ domain; Right: Retrieved profiles in $(x-t)$ domain obtained using the band-pass filter (5.74).

The first 16 observations were used in the assimilation, and the retrieved initial condition was allowed to evolve up to time $t = 317.5s$. Figure 5.17 shows the time histories of the point in the middle of the computational domain obtained by data assimilation and filtering. Results are compared with the true profiles and the original noisy observations.

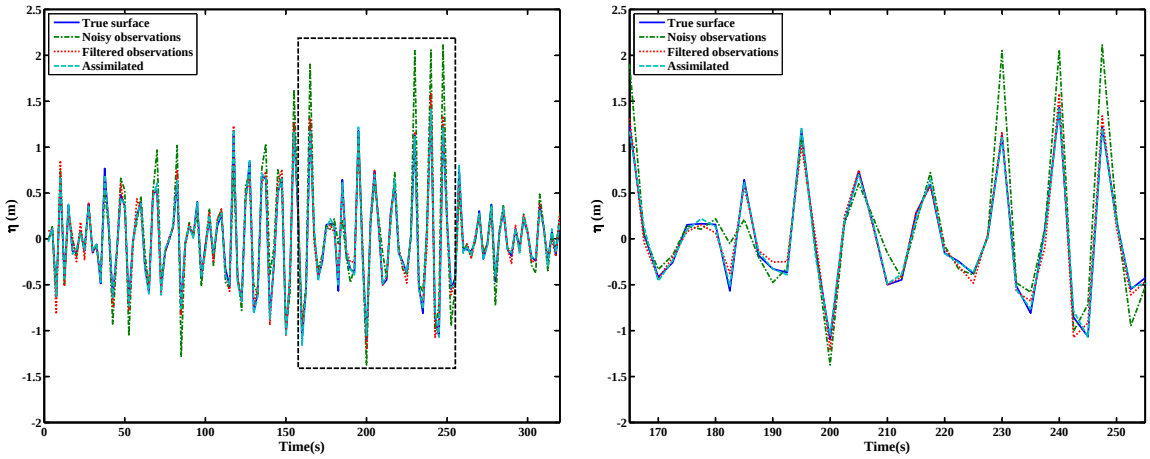

Figure 5.17: Left: Time history at the mid-point $x = L/2$, obtained by data assimilation (dashed) and band-pass filter (dotted), compared with the perfect (true) results (solid) and original noisy observations (dash-dot). Right: A zoomed view.

Referring to Figure 5.17, The RMS error in the mid-point time history, associated with the filtered profiles was $0.0061m$, while the error associated with the assimilated profiles

was $0.0029m$. The RMS error associated with the original noisy observations was $0.0177m$. Since the temporal resolution of the observations ($\Delta t_{obs} = 2.5s$) is not fine enough, and the filter does not capture the nonlinear effects, the quality of the post-filter results is not as good as those obtained by assimilation, however, the variational assimilation algorithm only uses the first few observations. The best strategy would be to apply the linear dispersion filter to the observations first, and then assimilate the first few post-filter frames into the numerical model. Numerous tests have showed that doing this would reduce the RMS errors an additional $30 - 40\%$.

5.5.3 Test with synthetic radar data

Generating observations artificially by adding Gaussian noise to the model-generated solutions does not build a realistic scenario in which the assimilation scheme can be truly examined. Even with a large amount of Gaussian noise added to the model solutions, the generated observations would still keep some level of consistency with the model. Radar images are inherently mixed with errors associated with the retrieval process. These errors exist in both phase and amplitude. In an attempt to investigate a more realistic scenario, synthetic one-dimensional radar data were considered.

Synthetic radar data from electromagnetic (EM) simulation for low-grazing angles were provided by Joel Johnson of Ohio State University ([37]). The true surface profiles were generated from Pierson-Moskowitz spectra solely parameterized by the wind speed, passed through the transformation of Creamer et al. [16]. This weakly nonlinear transformation approximates both nonlinear long wave effects, and long-short wave interactions.

Sea surfaces were modeled using an impedance boundary condition. Surface profiles were about $1200m$ long and scattering was computed at 512 frequencies ranging from 2975 to 3026.1 MHz. The transmitter was located $14m$ above the mean surface and $520m$ from the left-surface edge. The scattered power information from points within $50m$ from the edges of the domain were discarded to reduce the edge scattering. In ship applications the radar incidence angle is so low that the composite surface model approach [36] will not have enough accuracy. Given the uncertainties and the strong impact of shadowing

for ship-based radar systems, a statistical approach was adopted by Johnson et al. [37] to interpret the relationship between NRCS (Normalized Radar Cross Section) values and surface height/slope.

At very low grazing angles and for one-dimensional surfaces of small roughness, the NRCS is essentially proportional to the grazing angle raised to some power, equal to the third power in the limit of very small roughness [60]. For rougher surfaces and at grazing angles that are not negligibly small, the NRCS versus grazing angle appears to be proportional to an exponential function of the grazing angle, so that the NRCS in dB is linearly dependent on the grazing angle.

Statistical tests were performed by Johnson et al. correlating the range-resolved NRCS (linear units) raised to an arbitrary power with the corresponding surface slopes/heights (variations in the local grazing angles). Such tests showed poor correlations between the NRCS and the surface slopes for a wide range of selected exponents. However, using NRCS in dB greatly improved the correlation. Given the partial correlation observed to both surface height and slope, the effect of phase shifting the surface profile on observed correlations was also examined. Results showed that the maximum correlation was achieved when the surface height was shifted by $-30°$. Similar results were obtained for HH and VV polarizations. Given a statistically determined linear fit to the NRCS versus either surface height or slope, it is then possible to retrieve height or slope estimates from the measured NRCS data. Surface height profiles can be obtained by integrating the slope over the range.

Six data sets were provided covering the grazing angles of $1 - 2°$ and wind speeds of $5, 10$, and $15m/s$. Each data set included the following information:

- true surface profiles, filtered to around a 10m range resolution given at time steps of $0.25s$.
- retrieved profiles based on the approximate procedure (HH and VV polarizations) discussed before.
- filtered profiles using the linear dispersion in $\omega - k$ space.
- NRCS values in dB for HH and VV polarizations.

Retrieval accuracies were almost similar for HH and VV polarizations, although HH retrievals were more degraded in the shadow regions than VV. The retrievals were generally more degraded in the shadow regions. Six data sets were studied to evaluate the overall performance of the data assimilation scheme for two-dimensional problems. HH polarization retrievals were used for the assimilation.

Since the wave evolution model used in the assimilation process (leading order pseudo-spectral) was different from the one used to retrieve the surface profiles (Creamer's model [16]), the first step was to compare these models. The maximum absolute error between the mid-point time histories were about 0.29, 0.34, and 0.65, for wind speeds of $5, 10$, and $15m/s$, respectively (the errors have been scaled with the standard deviation of the time record in the mid-point). In the current study, the model errors have been assumed negligibly small, however for a more thorough investigation, the model error analysis also needs to be included.

For the numerical computations with the pseudo-spectral model, the provided data were first interpolated to $512 = 2^9$ grid points, giving a spatial resolution of $\Delta x \approx 2.15m$, and the evolution equations were integrated using the RK4 scheme with step size $\Delta t = 0.125s$ which was half the size of the interval at which the data were provided. The total length of the computational domain was about $1100m$. In order to retain the periodicity of the solution a window function was used to taper the initial surface profile at both ends to reduce the effect of non-periodicity. This window function is 1 every where with a linear transition to zero at the edges of the domain. After numerous tests, the optimal width of this transition zone was found to be about half a wavelength of the dominant wave in the computational domain.

For each data set the adjoint gradient was first compared with the finite difference approximation. The data assimilation scheme was then started with 48 frames of filtered profiles with $0.25s$ intervals used as observations, and the cost function was defined similar to (5.1) with the weighting function equal to unity. The convergence criterion for the quasi-Newton minimization method was chosen as $||\mathbf{g}_k|| \leq 10^{-4}$. In most cases $6 - 8$ iterations were needed for convergence. The converged initial state was then allowed to evolve up to the final time ($31.75s$). Figures 5.18- 5.23 present the comparison of the retrieved, filtered,

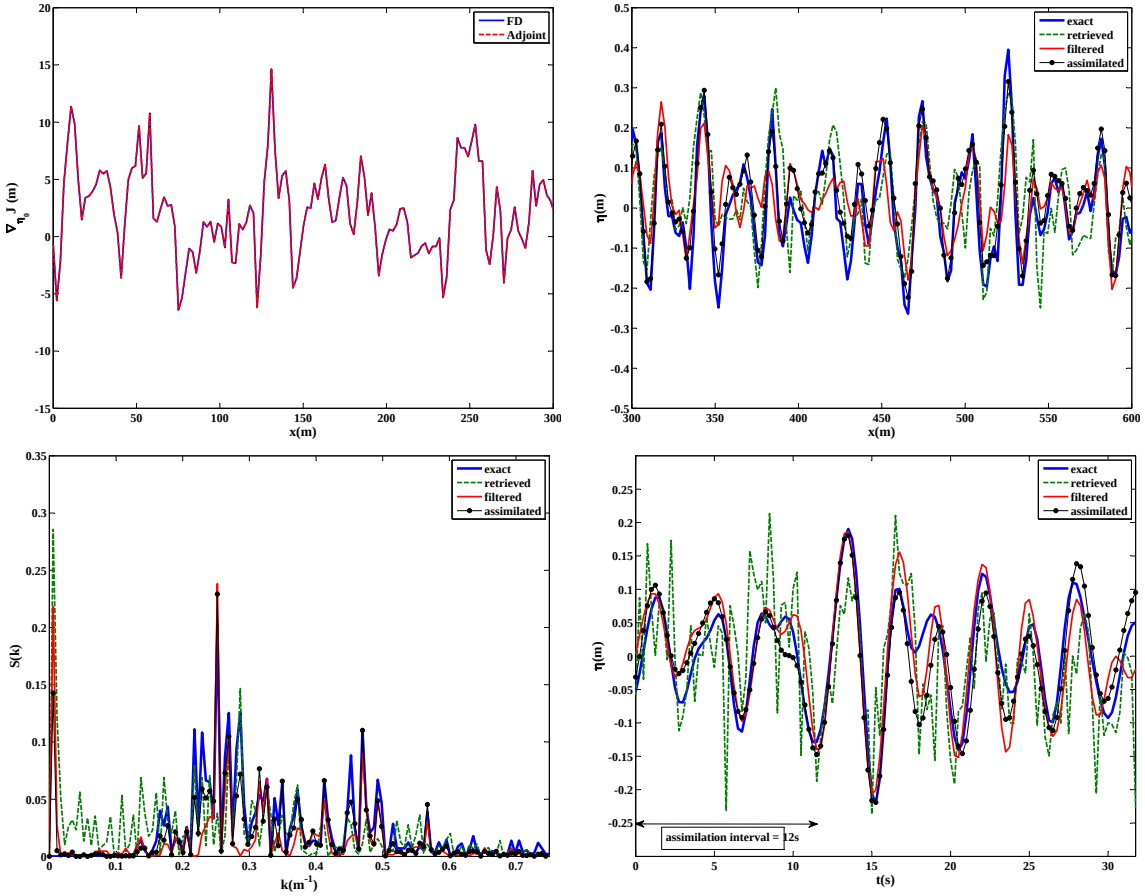

Figure 5.18: Comparison of the retrieved, filtered, and assimilated surface profiles with the true surface profiles for the case: Wind speed = $5m/s$, and grazing angle = 1°. Top left: Comparison of adjoint gradient with the FD approximation. Top right: Comparison of the profiles at $t = 0$. Bottom left: Comparison of wavenumber spectra at $t = 0$. Bottom right: Comparison of mid-point ($x \approx 550m$) time histories.

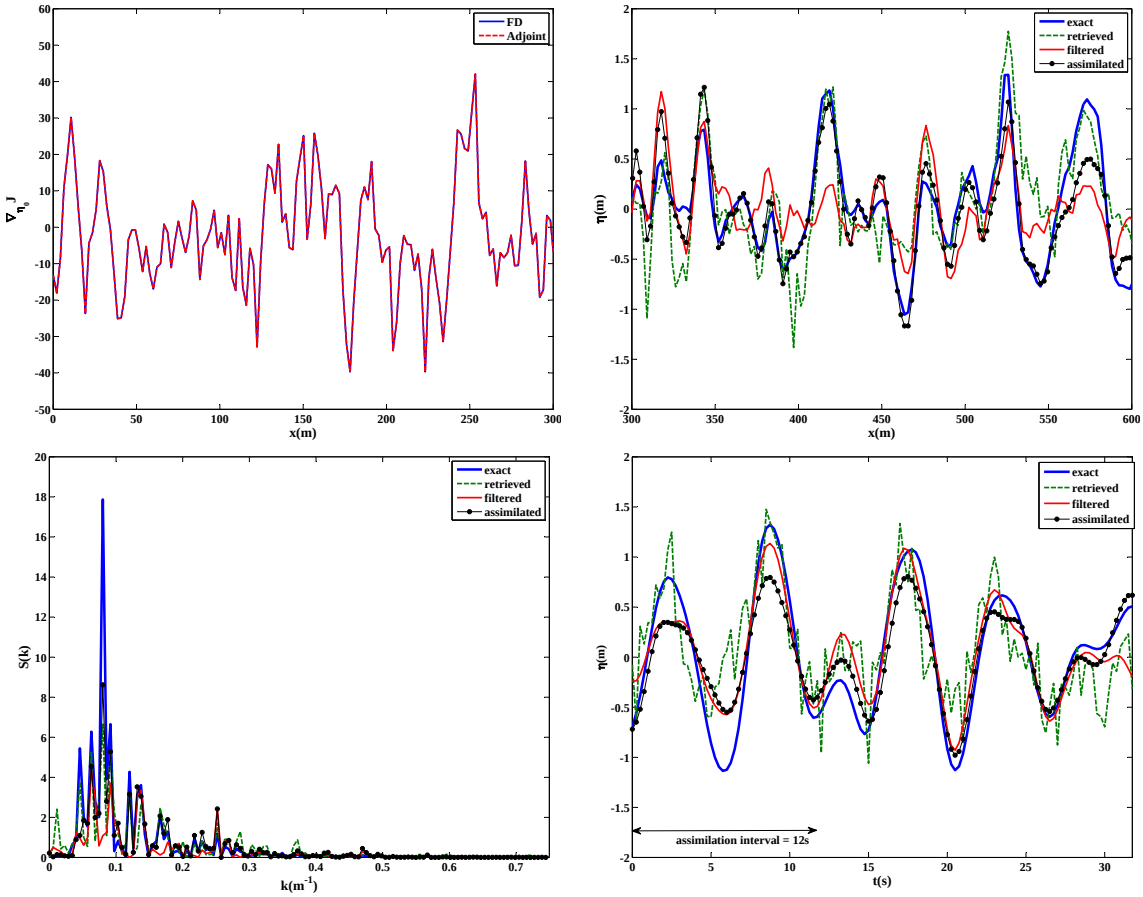

Figure 5.19: Comparison of the retrieved, filtered, and assimilated surface profiles with the true surface profiles for the case: Wind speed = $10m/s$, and grazing angle = $1°$. Top left: Comparison of adjoint gradient with the FD approximation. Top right: Comparison of the profiles at $t = 0$. Bottom left: Comparison of wavenumber spectra at $t = 0$. Bottom right: Comparison of mid-point ($x \approx 550m$) time histories.

and assimilated surface profiles with the true surfaces for different incidence angle/wind speed scenarios.

In all cases the adjoint and finite difference gradients matched to the order of the perturbations parameter which was 10^{-6} in these tests. However, the FD took $101.7s$ to calculate the gradient which is considerably larger than the time taken by the adjoint method (about $0.25s$). Figures 5.18 and 5.21 clearly show that the assimilation scheme works better for lower wind speeds (milder wave conditions), as the assimilated state works well in capturing the peaks of the spectrum. The assimilated surface profiles also did quite well in capturing the crests and troughs in the shadow regions. However, for higher wind speeds, while the assimilation improves the wave profiles within the shadowed zones behind the larger waves,

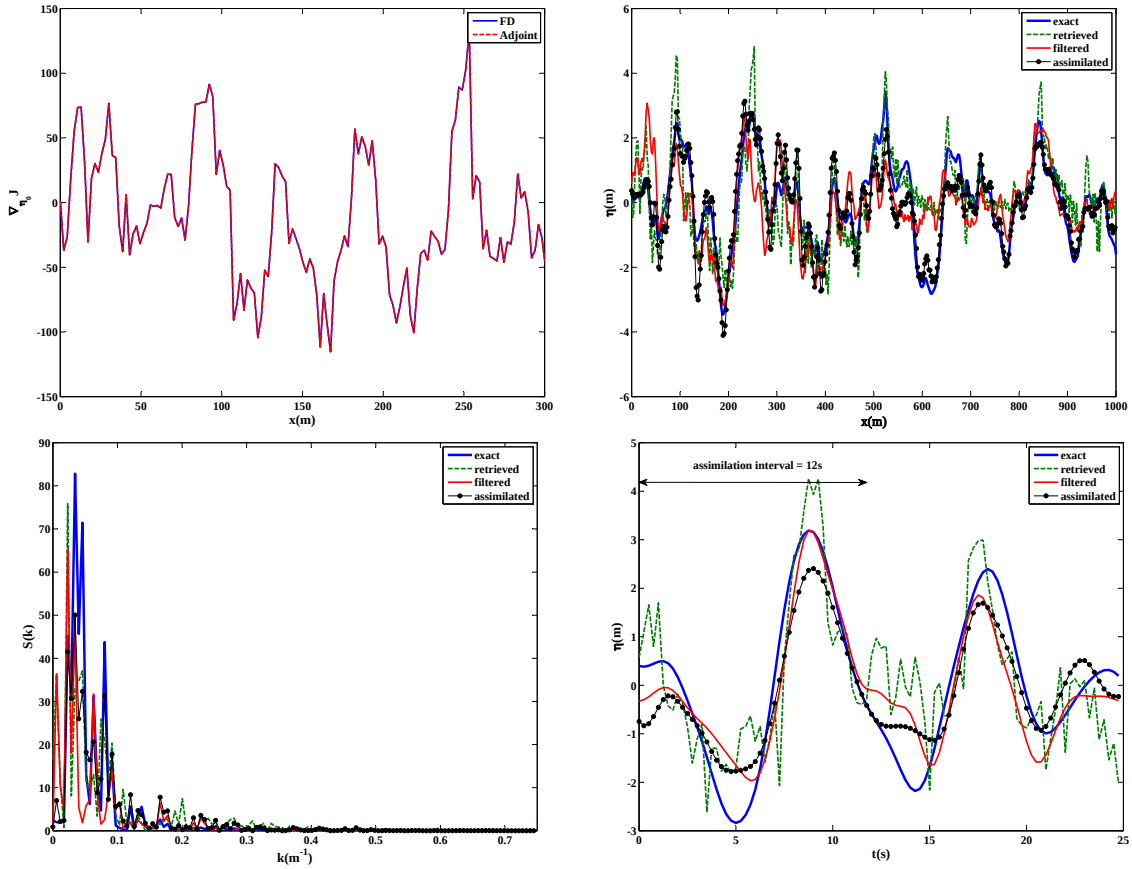

Figure 5.20: Comparison of the retrieved, filtered, and assimilated surface profiles with the true surface profiles for the case: Wind speed = $15m/s$, and grazing angle = $1°$. Top left: Comparison of adjoint gradient with the FD approximation. Top right: Comparison of the profiles at $t = 0$. Bottom left: Comparison of wavenumber spectra at $t = 0$. Bottom right: Comparison of mid-point ($x \approx 550m$) time histories.

the improvements in the spectral amplitudes and time history are less significant.

The error statistics is summarized in tables 5.4, 5.5, and 5.6. Table 5.4 presents the relative errors in the initial condition, associated with the retrieved, filtered, and assimilated surface profiles, while table 5.5 presents the relative errors at the final time ($t = 31.75s$). The columns 2-9 correspond to the errors associated with the assimilated surface profiles that used retrieved (columns 2-5), and filtered (columns 6-9) profiles as observations. ϵ_1 represents the error associated with the retrieved profiles without assimilation, and ϵ_2 corresponds to the error associated with dispersion-filtered profiles without assimilation.

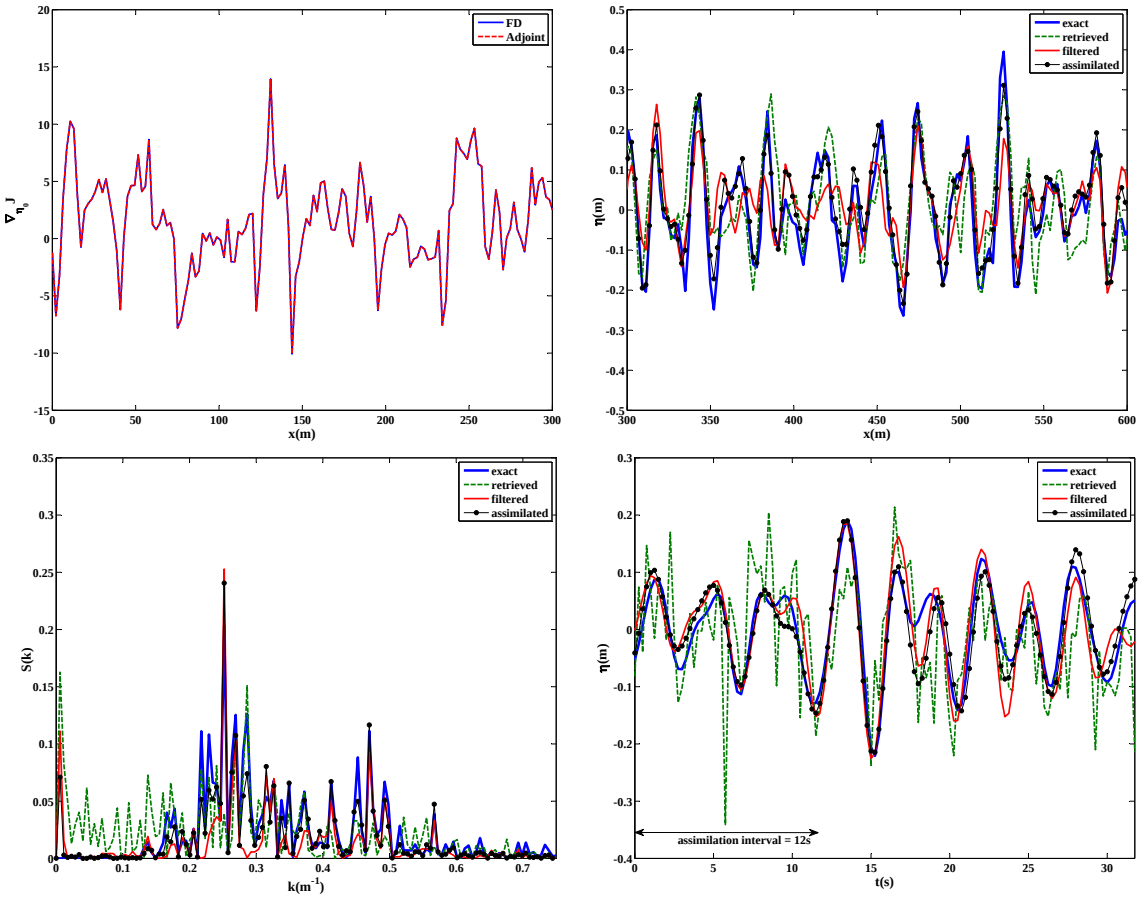

Figure 5.21: Comparison of the retrieved, filtered, and assimilated surface profiles with the true surface profiles for the case: Wind speed = $5m/s$, and grazing angle = 2°. Top left: Comparison of adjoint gradient with the FD approximation. Top right: Comparison of the profiles at $t = 0$. Bottom left: Comparison of wavenumber spectra at $t = 0$. Bottom right: Comparison of mid-point ($x \approx 550m$) time histories.

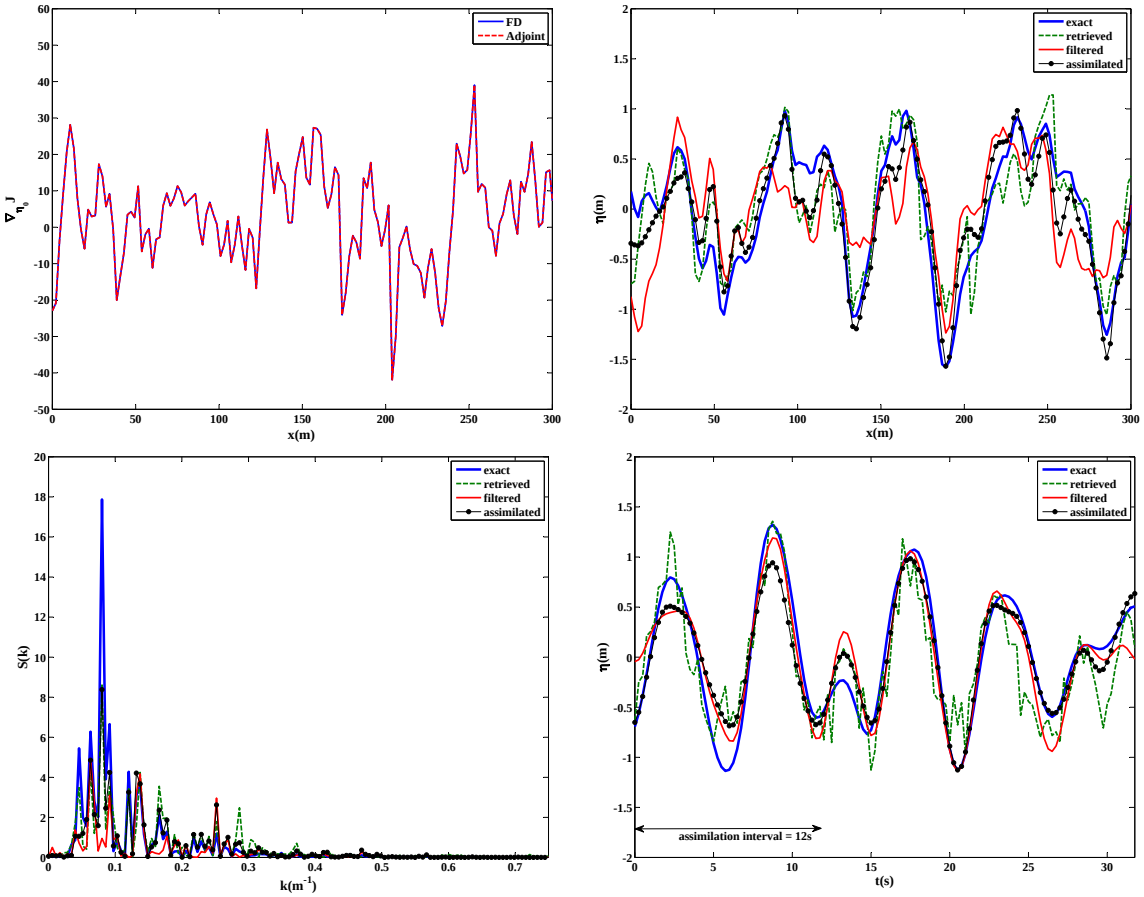

Figure 5.22: Comparison of the retrieved, filtered, and assimilated surface profiles with the true surface profiles for the case: Wind speed = $10m/s$, and grazing angle = $2°$. Top left: Comparison of adjoint gradient with the FD approximation. Top right: Comparison of the profiles at $t = 0$. Bottom left: Comparison of wavenumber spectra at $t = 0$. Bottom right: Comparison of mid-point ($x \approx 550m$) time histories.

The relative error values presented in tables 5.4, 5.5, and 5.6 are defined as follows:

$$Relative\ Error = \frac{||\eta - \eta_{true}||_2}{||\eta_{true}||_2}, \tag{5.75}$$

It is observed that for higher wind speeds (10 and $15m/s$), applying the linear dispersion filter even increases the relative error. Errors are generally higher for the smaller incidence angle, which is attributed to higher shadowing effects.

In most cases, increasing the assimilation interval, by incorporating more observations, reduces the relative errors. The best strategy would be to filter the retrieved surface profiles using the linear dispersion filter, and then assimilate the filtered profiles into the numerical

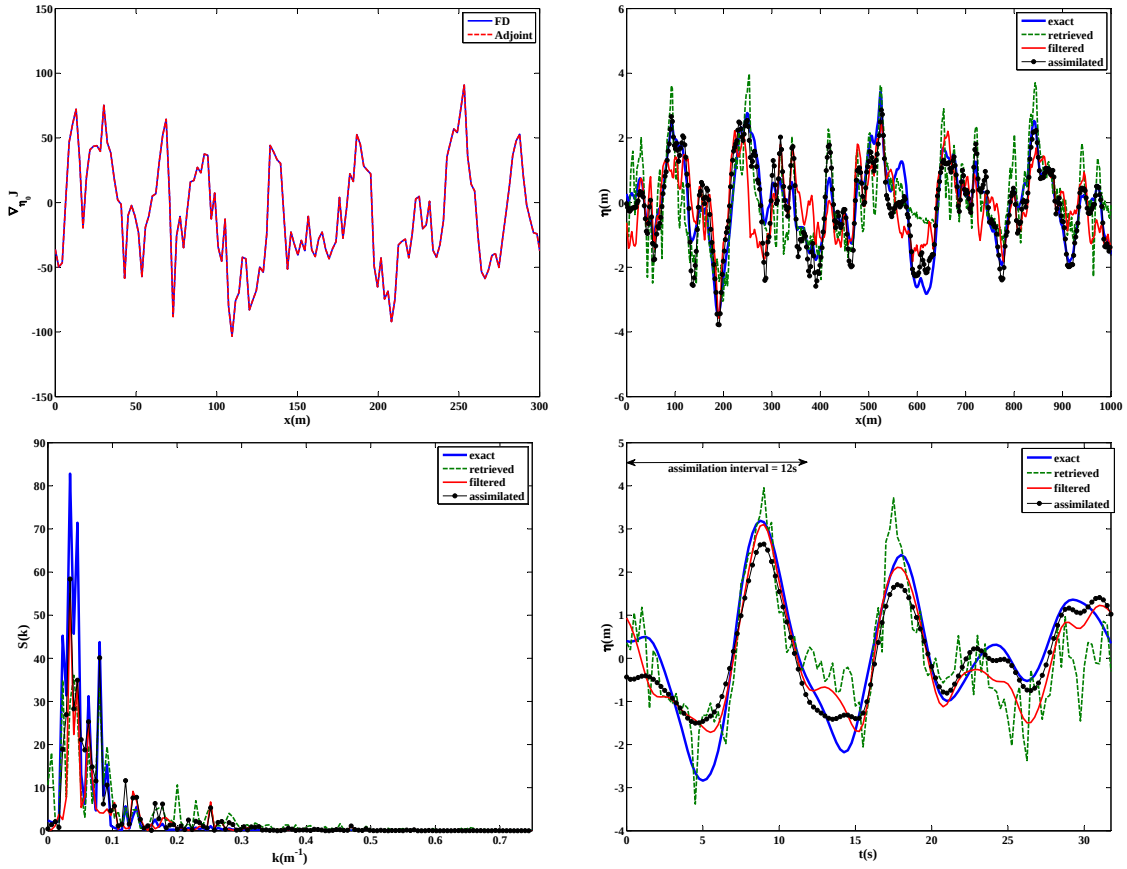

Figure 5.23: Comparison of the retrieved, filtered, and assimilated surface profiles with the true surface profiles for the case: Wind speed = $15m/s$, and grazing angle = $2°$. Top left: Comparison of adjoint gradient with the FD approximation. Top right: Comparison of the profiles at $t = 0$. Bottom left: Comparison of wavenumber spectra at $t = 0$. Bottom right: Comparison of mid-point ($x \approx 550m$) time histories.

model. This technique lead to a reduction of 30-70% in the retrieval errors.

Table 5.6 presents the error statistics for the case where the VV retrievals are used as observations. This table apparently shows that the VV retrievals have a slightly better quality than the HH ones, and the assimilated profiles obtained by VV retrievals are in some cases 5 to 10% better than those obtained by HH retrievals.

Scenario	Retrieved (as observation)				Filtered (as observation)				without assimilation	
	12	24	48	96	12	24	48	96	ϵ_1	ϵ_2
$1°, 5m/s$	0.72	0.6	0.54	0.51	0.65	0.54	0.41	0.34	0.95	0.78
$1°, 10m/s$	0.48	0.40	0.38	0.39	0.58	0.46	0.38	0.36	0.63	0.78
$1°, 15m/s$	0.57	0.52	0.45	0.45	0.60	0.52	0.44	0.43	0.73	0.82
$2°, 5m/s$	0.68	0.55	0.51	0.49	0.62	0.50	0.37	0.33	0.92	0.76
$2°, 10m/s$	0.44	0.37	0.35	0.35	0.58	0.46	0.37	0.35	0.58	0.79
$2°, 15m/s$	0.51	0.46	0.40	0.44	0.54	0.46	0.40	0.44	0.66	0.72

Table 5.4: Error statistics at time $t = 0$, associated with the assimilation using retrieved and filtered data as observations. Assimilation carried out with 12, 24, 48, and 96 observations. (HH retrievals were used).

Scenario	Retrieved (as observation)				Filtered (as observation)				without assimilation	
	12	24	48	96	12	24	48	96	ϵ_1	ϵ_2
$1°, 5m/s$	0.79	0.67	0.60	0.55	0.74	0.62	0.50	0.40	1.05	0.86
$1°, 10m/s$	0.58	0.50	0.46	0.44	0.64	0.53	0.45	0.40	0.78	0.90
$1°, 15m/s$	0.79	0.75	0.71	0.60	0.83	0.79	0.74	0.61	0.73	0.88
$2°, 5m/s$	0.74	0.63	0.57	0.53	0.71	0.59	0.47	0.39	1.02	0.83
$2°, 10m/s$	0.55	0.46	0.41	0.39	0.62	0.51	0.41	0.38	0.69	0.86
$2°, 15m/s$	0.87	0.82	0.78	0.66	0.81	0.78	0.77	0.67	0.78	0.90

Table 5.5: Error statistics at the final time $t = 31.75s$, associated with the assimilation using retrieved and filtered data as observations. Assimilation carried out with 12, 24, 48, and 96 observations. (HH retrievals were used).

Scenario	Retrieved (as observation)				Filtered (as observation)				without assimilation	
	12	24	48	96	12	24	48	96	ϵ_1	ϵ_2
$1°, 5m/s$	0.67	0.60	0.55	0.49	0.65	0.54	0.41	0.31	0.9	0.79
$1°, 10m/s$	0.40	0.35	0.32	0.34	0.56	0.44	0.35	0.33	0.57	0.78
$1°, 15m/s$	0.52	0.48	0.42	0.42	0.59	0.51	0.42	0.42	0.67	0.81
$2°, 5m/s$	0.59	0.52	0.48	0.46	0.59	0.47	0.34	0.28	0.88	0.75
$2°, 10m/s$	0.40	0.35	0.34	0.34	0.58	0.46	0.37	0.35	0.54	0.80
$2°, 15m/s$	0.46	0.42	0.39	0.43	0.53	0.45	0.39	0.44	0.64	0.71

Table 5.6: Error statistics at $t = 0$, associated with the assimilation using retrieved and filtered data as observations. Assimilation carried out with 12, 24, 48, and 96 observations. (VV retrievals were used).

5.6 Data Assimilation For Three-dimensional Flows

For the typical three-dimensional flows in the present application the number of free surface variables is of the order 10^5. For such a large-scale minimization problem, storing the Hessian matrix at each iteration would be impractical. Instead, an algorithm is sought that does not require the explicit calculation of the Hessian matrix during the course of minimization.

5.6.1 Minimization Algorithm for thee-dimensional flows

Following the work of Wang et. al. [78], for three-dimensional flows, a Newton-type algorithm is used which allows us to obtain the Newton search direction $\mathbf{d}_k$ (see equation (5.62)) by integrating the tangent linear equations (5.51) backwards in time, starting with an appropriate initial condition $\mathbf{u}_0'$. This algorithm is referred to as "Adjoint-Newton Algorithm (ANA)". The error present in approximating the Hessian in quasi-Newton type algorithms is thus completely eliminated, while the prohibitive storage issues related to the Hessian matrix no longer exist. An algorithmic presentation of ANA is presented as follows:

- Choose an initial guess for the free surface elevation η_0 and set iteration number $k = 0$.
- Calculate the gradient of the cost function with respect to the initial conditions as:

$$\mathbf{g}_k = \mathbf{g}(\eta_k) = \nabla_{\eta_k} J, \tag{5.76}$$

  by integrating the adjoint model equations (5.54) backwards in time.

- Obtain a Newton line search direction:

$$\mathbf{d}_k = -\eta'(t_1), \tag{5.77}$$

  by integrating the tangent linear model equations (5.51) backwards in time, starting

from the following initial condition at $t = t_N$:

$$\eta'(t_N) = \eta(t_N) - \eta_{obs}(t_N), \tag{5.78}$$

- Update the initial condition

$$\eta_{k+1} = \eta_k + \alpha_k \mathbf{d}_k, \tag{5.79}$$

where α_k is an appropriate step size taken by conducting a line search:

$$J(\eta_k + \alpha_k \mathbf{d}_k) = min_\alpha J(\eta_k + \alpha \mathbf{d}_k), \tag{5.80}$$

using Davidon's cubic interpolation method, which satisfies the following Wolfe conditions:

$$J(\eta_k + \alpha_k \mathbf{d}_k) \leq J(\eta_k) + \beta_1 \alpha_k \mathbf{g}_k^T \mathbf{d}_k,$$

and (5.81)

$$\frac{\mathbf{g}_k (\eta_k + \alpha_k \mathbf{d}_k)^T \mathbf{d}_k}{\mathbf{g}_k^T \mathbf{d}_k} \leq \beta_2,$$

where $\beta_1 = 0.0001$ and $\beta_2 = 0.9$.

- Check for the convergence. Given a tolerance ϵ, and if

$$||\mathbf{g}_{k+1}|| \leq \epsilon ||\mathbf{g}_0||, \tag{5.82}$$

stop. Otherwise, set $k = k + 1$ and repeat the steps 2 through 5.

The numerical cost of integrating the tangent linear model is similar to that required for the adjoint model. In this case the gradient information is only needed for the convergence check. This algorithm was shown to be more efficient than many common large-scale unconstrained minimization methods such as LBFGS, truncated Newton and conjugate gradients [78]. However care should be taken in applying this algorithm to irreversible physical

processes, where the tangent linear model cannot be integrated backwards. A schematic illustration of the adjoint Newton algorithm is displayed in Figure 5.24.

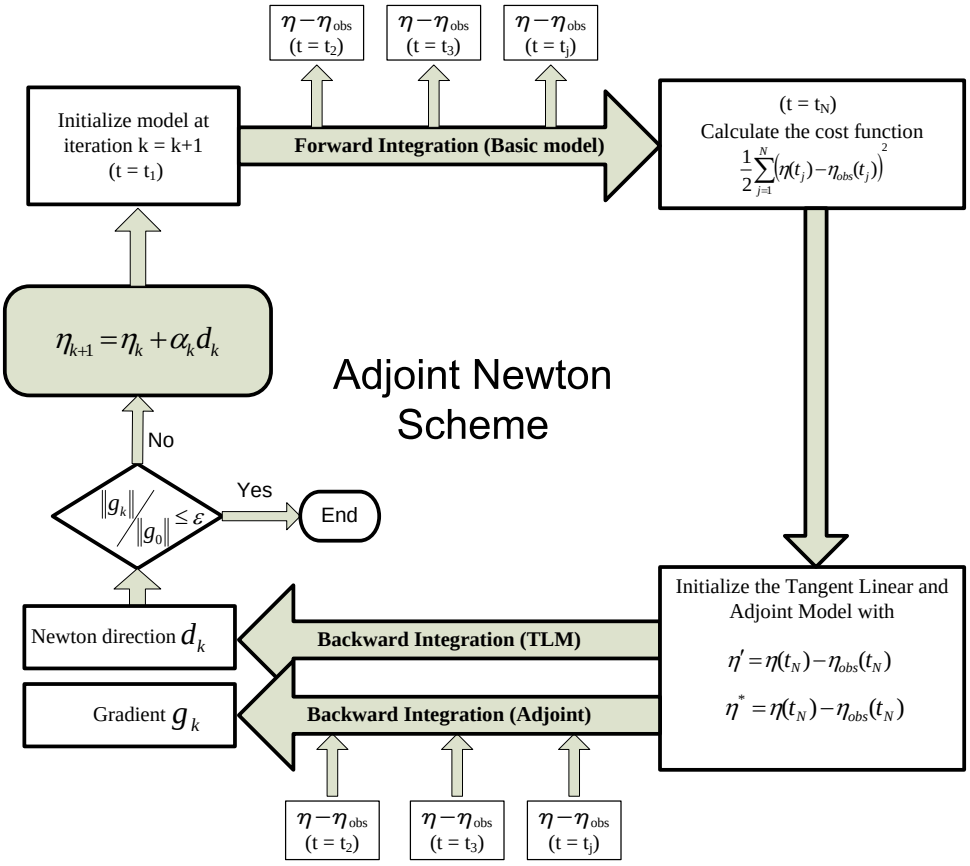

Figure 5.24: Schematic illustration of adjoint Newton minimization scheme used for three-dimensional flows.

5.6.2 Test with synthetically generated sea surface

In order to validate the three-dimensional data assimilation scheme a synthetic two-dimensional sea surface was generated from the two-dimensional JONSWAP wave number spectrum, with the observations generated from model solutions. In order to prepare the initial wave field a directional frequency spectrum was considered as:

$$S(f,\theta) = P(f)G(\theta), \tag{5.83}$$

where $P(f)$ is the original JONSWAP spectrum, which is converted into the associated wave number spectrum $S(k_x, k_y)$. The directional spreading function used here is defined as:

$$G(\theta) = \begin{cases} \frac{1}{\phi_0} \cos^2\left(\frac{\pi}{2\phi_0}\theta\right) & \text{if } \theta \leq \phi_0, \\ 0 & \text{otherwise.} \end{cases} \tag{5.84}$$

where ϕ_0 is a parameter that determines the directional spreading of the wave field. Using the linear dispersion relation for the deep water, $\omega = \sqrt{g|\mathbf{k}|}$, the wave number spectrum is derived as:

$$S(k_x, k_y) = \frac{\alpha}{2|\mathbf{k}|^4} \exp\left(-1.5\left(\frac{k_0}{|\mathbf{k}|}\right)^2\right) \gamma^{\exp\left(-\frac{\left(\sqrt{|\mathbf{k}|}-\sqrt{k_0}\right)^2}{2\sigma_0^2 k_0^2}\right)} G(\theta), \tag{5.85}$$

where $|\mathbf{k}| = \sqrt{k_x^2 + k_y^2}$, $\theta = \tan^{-1}\left(\frac{k_y}{k_x}\right)$, and σ_0 is a simple function of the wavenumber defined as:

$$\sigma_0 = \begin{cases} 0.07 & \text{for } |\mathbf{k}| \leq k_0, \\ 0.09 & \text{for } |\mathbf{k}| > k_0, \end{cases} \tag{5.86}$$

γ and α are constants that determine the shape of the spectrum and k_0 is the dominant wavenumber in the spectrum. From equation (5.85), the two-dimensional surface elevation is computed in the following way:

$$\eta(x, y) = \sum_{i=1}^{Nx} \sum_{j=1}^{Ny} C_{ij} \cos\left(k_i x + k_j y + \varphi_{ij}\right), \tag{5.87}$$

where φ_{ij}'s are uniformly distributed random phases in interval $[0, 2\pi]$, and

$$C_{ij} = \sqrt{4S\left(k_i, k_j\right) k_1 k_2}, \tag{5.88}$$

where $k_1 = \frac{2\pi}{L_1}$ and $k_2 = \frac{2\pi}{L_2}$, with L_1 and L_2 being the length of the computational domain in x and y directions, respectively. In this example, $Nx = Ny = 256$ and $L_1 = L_2 = 2550m$, which gives a spatial resolution of $10m$ in both directions. A synthetic sea surface with significant wave height $H_s = 3.25m$, peak period $T_p = 9.53s$, and directional spreading $\phi_0 = 30^\circ$ was generated from the two-dimensional wavenumber spectrum (5.85). Principal wave's direction was 30° with respect to the x-axis. After constructing the initial sea surface $\eta(x, y)$, the Fourier coefficients of the free surface tangential velocities at $t = 0$ are obtained using the linear model (3.47).

$$\begin{aligned} b_{nm}(0) &= \left(\sqrt{g|\mathbf{k}|}\cos\theta_{nm}\right) a_{nm}(0), \\ c_{nm}(0) &= \left(\sqrt{g|\mathbf{k}|}\sin\theta_{nm}\right) a_{nm}(0), \end{aligned} \tag{5.89}$$

Other physical parameters involved, were $\alpha = 0.0063$, $\gamma = 3.3$, and $k_0 = 0.0443m^{-1}$. Using the first-order model given by (3.46)- (3.47), a simulation was carried out, and the initial wave field obtained from (5.87) and (5.89) was allowed to evolve for $80s$ using a time step $\Delta t = 0.25s$ (about 40 time steps per wave period of the peak wave). Imperfect observations were generated by adding 40% of random Gaussian noise to the first few surface profiles. A total of 8 observations were provided at every $2.5s$ (close to the revolution period of typical marine radars). Therefore, the assimilation interval was $17.5s$ (about twice the peak wave period). The cost function was defined as the squared 2-norm of the error between observations and model solutions accumulated over the assimilation interval, and the Adjoint Newton Algorithm (ANA) was used to minimize the cost function.

First observation was used as an initial guess. At each iteration k, the current initial condition η_k is passed to an external function which calculates the cost function J_k, by integrating the basic model equations (3.46)- (3.47) forward, gradient $\mathbf{g}_k$, by integrating

the adjoint equations (5.52) backward in time, and Newton search direction $\mathbf{d}_k$, by integrating the tangent linear model equations (5.49) backward in time. Figure 5.25 shows the comparison of the gradient of the cost function, $\nabla_{\eta_0} J$, with respect to the initial condition, calculated using FD and adjoint methods. It also compares the calculated Newton descent direction from solving the TLM with the negative gradient from solving the adjoint equations.

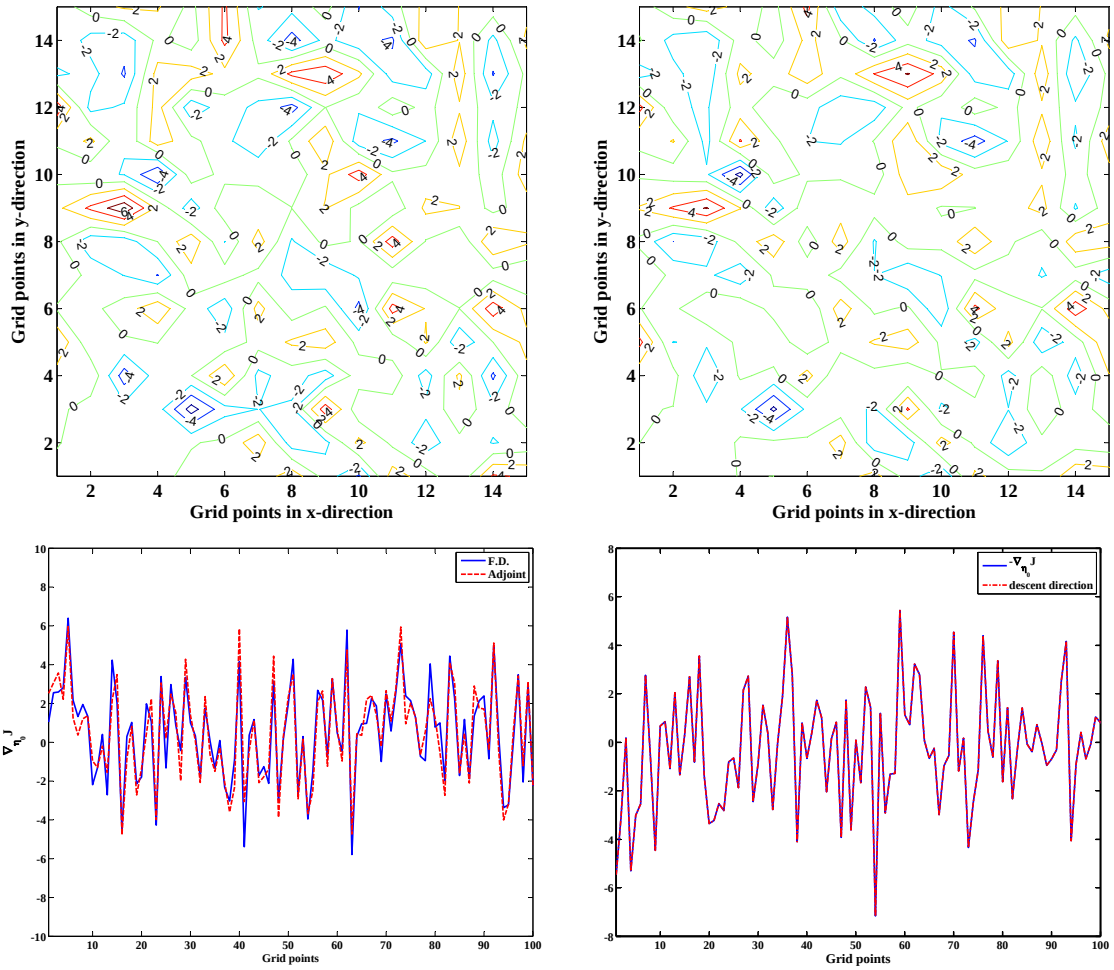

Figure 5.25: Top left: Contour lines of the gradient of the cost function with respect to the initial condition, calculated from finite differences. Results shown for a 15×15 area in the middle of the domain. Top right: Same as the left plot, calculated using adjoint method. Bottom left: Comparison of adjoint-calculated and FD-calculated gradient of the cost function with respect to the initial condition. (Results shown for a line along the x-axis). Bottom right: Comparison of the Newton search direction $\mathbf{d}_k$ with the negative gradient, $-\mathbf{g}_k$.

The perturbation parameter used in FD approximation was 10^{-6}. The RMS error

between the FD and adjoint gradients was less than $0.36m$. The RMS error between the negative gradient $-\mathbf{g}_k$ and the Newton search direction $\mathbf{d}_k$ as shown in Figure 5.25, was $0.0028m$ which confirms the proportionality of these two quantities inferred from (5.62). As an indication of the efficiency and robustness of the adjoint technique in this particular example, the CPU time needed for the calculation of the gradient using adjoint method was about one minute which is $O(10^4)$ times faster than the differencing method that could take more than one month in a single PC!

The first observation was used as an initial guess. Each step of ANA included the calculation of cost function, gradient, and the search direction. At each iteration the search direction was scaled with its 2-norm which helped improve the performance of the minimization. The initial step size α_k was 10 and Davidon's cubic interpolation scheme was used to determine the step size at later iterations.

The variation of the cost function scaled by its initial value (J/J_0) as well as that of the norm of the gradient also scaled by its initial value ($||\mathbf{g}||/||\mathbf{g}_0||$) as a function of the number of iterations is displayed in Figure 5.26. This figure shows that after 10 iterations the value of the cost function and the norm of the gradient were reduced almost 40% and 90%, respectively. At that stage, the prescribed convergence criterion with $\epsilon = 0.1$ was satisfied.

The RMS error $||\eta_{opt}(x, y, 0) - \eta_{exact}(x, y, 0)||/\sqrt{N}$, between the optimized (retrieved) initial condition after 10 iterations, and the exact initial condition was $0.029m$ which is more than 40% smaller than that ($0.05m$) between the exact initial condition and the noisy initial guess, where N is the number of variables which in this case is $256^2 = 65536$. A small portion of the noisy initial surface profile and the retrieved profile after 10 iterations are shown in Figure 5.27. This figure also shows the comparison of the spectral amplitudes of the noisy and optimized profiles at $t = 0$ with the exact spectrum.

The RMS error $||S_{opt}(k_x, k_y, 0) - S_{exact}(k_x, k_y, 0)||/\sqrt{N}$, between the retrieved spectrum and the exact one was 0.056, which is almost one-third of that (0.17) between the exact spectrum and the noisy one. In order to compare the time histories, the noisy initial guess and the retrieved optimal initial condition were allowed to evolve in time up to $t = 80s$, and their time histories were compared with the noiseless perfect solution. Comparison of

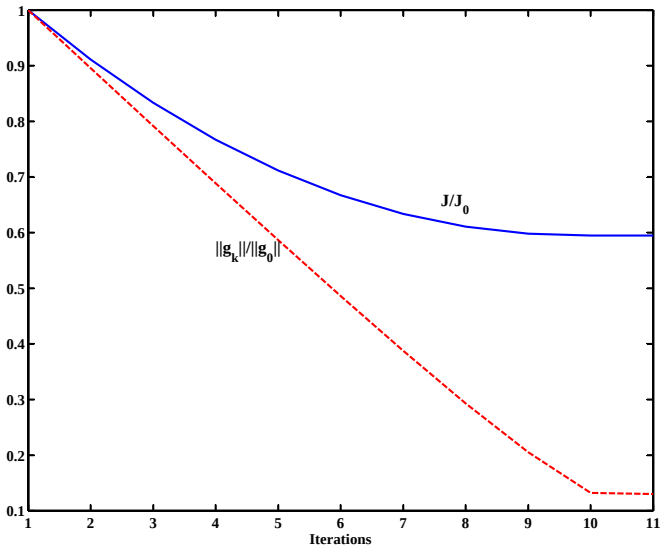

Figure 5.26: Variations of the scaled cost function (J/J_0) and scaled gradient norm ($||\mathbf{g}||/||\mathbf{g}_0||$) with the number of iterations, using the adjoint Newton algorithm, as the observations are model-generated.

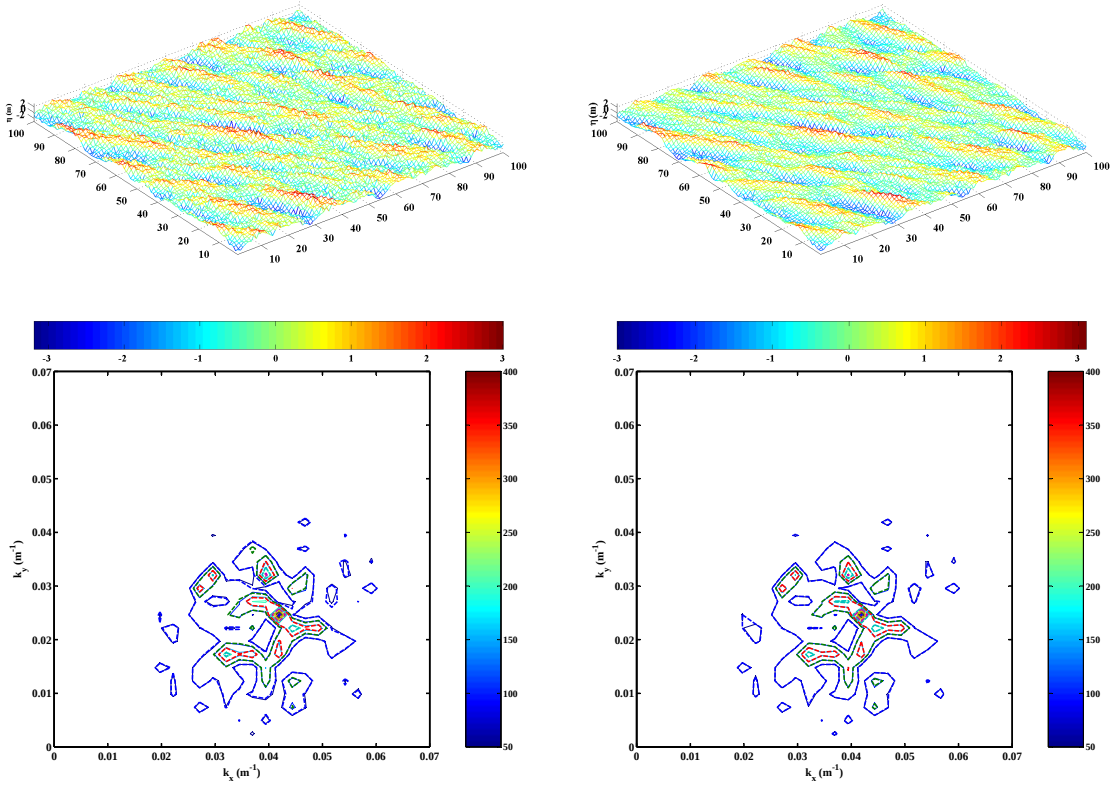

Figure 5.27: Top left: Part of the noisy initial guess (first observation); Top right: Retrieved (optimal) initial condition after 10 iterations; Bottom left: Comparison of the spectrum of the noisy initial condition (dashed) at $t = 0$ with the exact spectrum (solid); Bottom right: Comparison of the spectrum of the retrieved initial condition (dashed) with the exact spectrum (solid) at $t = 0$.

the time histories at a point located at $(L_1/4, 3L_2/4)$ is presented in Figure 5.28.

The RMS error between the retrieved (assimilated) time history and the perfect solution was $0.012m$, which is more than 60% smaller than that $(0.033m)$ between the perfect solution and the the one obtained from the noisy initial guess.

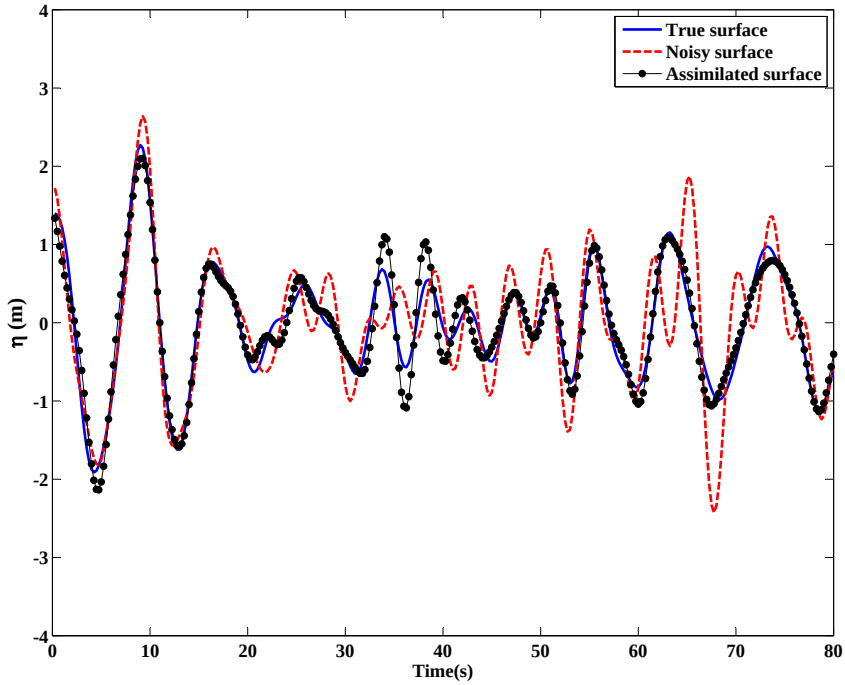

Figure 5.28: Comparison of surface elevation time histories at the point $(L_1/4, 3L_2/4)$.

Effect of nonlinearity

In order to investigate the effect of model nonlinearity on the assimilation outcome the third-order model given by (3.50) was used to evolve the same initial condition that was used in the previous simulation, with all simulation parameters kept unchanged. ANA was used to iteratively find the optimal initial surface profile that fitted best with a series of model-generated observations. These observations were generated by adding 50% uncorrelated Gaussian noise to the first 8 frames of third-order model outputs picked out at 2.5s intervals. Therefore length of the assimilation interval was 17.5s. Gradient vector $\mathbf{g}$ was calculated by integrating third-order adjoint equations (5.54) backward in time, while the Newton descent direction $\mathbf{d}_k$ was obtained by integrating the corresponding tangent linear equations (5.51)

backwards.

The forward model solutions η and (u_s, v_s) are used as the coefficients of the tangent linear and adjoint equations. Storing these variables over the assimilation interval is the only major concern in such nonlinear problems. Figure 5.29 displays 100 components of the gradient of the cost function with respect to the initial condition $\nabla_{\eta_0} J$, along the x and y-axis, calculated using the adjoint method, compared with that calculated using a finite difference.

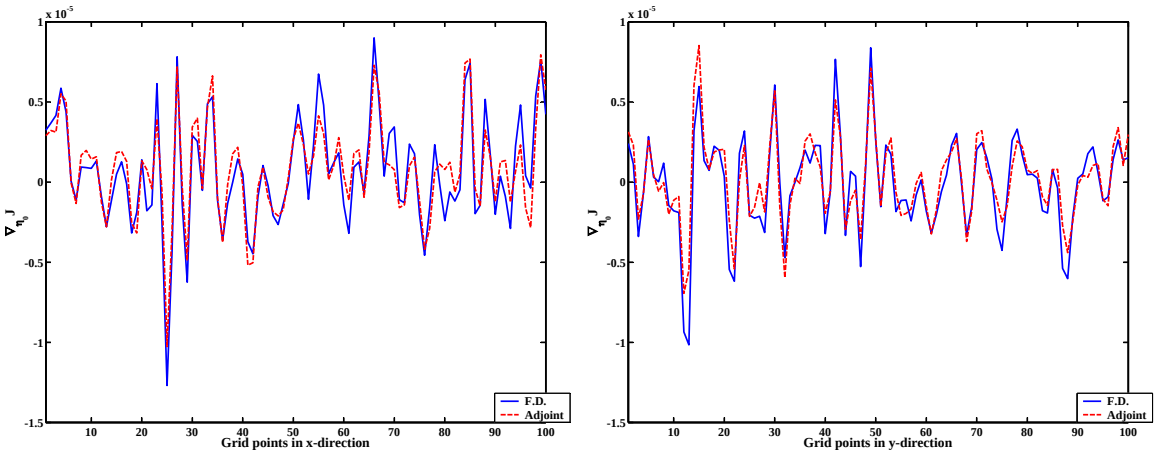

Figure 5.29: Left: Comparison of the first 100 components of the adjoint-calculated and FD-calculated gradient of the cost function with respect to the initial condition along x-axis; Right: The same as the left figure, along the y-axis; The third-order model has been used.

The perturbation parameter for FD was 10^{-8}. The RMS errors between the adjoint and finite difference results were 1.26×10^{-6} and 1.19×10^{-6} along the x and y-axis, respectively. In the present simulation the cost function was scaled by the total number of variables $Nx \times Ny$ over the assimilation interval, i.e.

$$J = \sum_{i=1}^{Nx} \sum_{j=1}^{Ny} \sum_{k=1}^{NT} \frac{1}{(NxNyNT)} \left[\eta\left(x_i, y_j, t_k\right) - \eta_{obs}\left(x_i, y_j, t_k\right)\right]^2 . \tag{5.90}$$

The RMS error between the adjoint and FD methods, for the third-order model was almost twice as large as that reported for the linear model, if it is re-scaled similar to the previous experiment. Figure 5.30 shows the comparison of the negative gradient **-g**$_k$, and Newton descent direction **d** along the x and y-axis, calculated by integrating the adjoint and tangent linear equations, respectively.

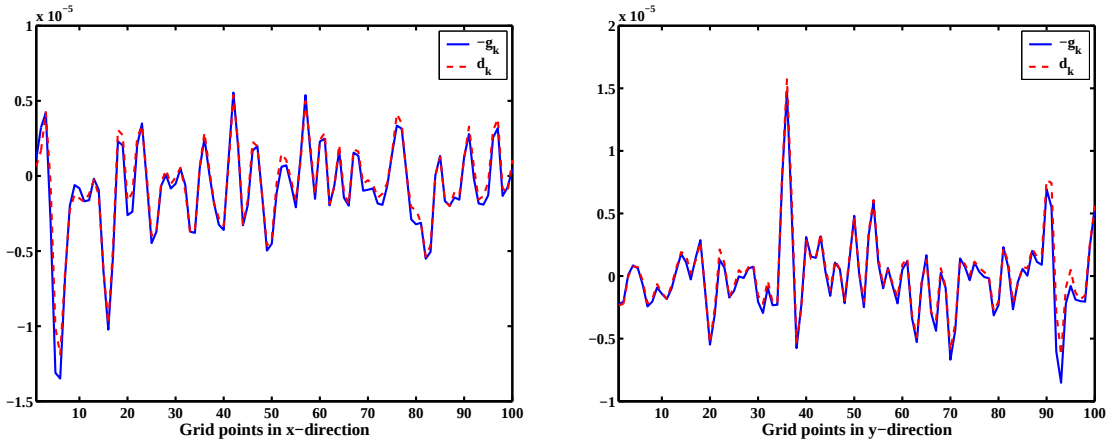

Figure 5.30: Comparison of the Newton search direction $\mathbf{d}_k$ with the negative gradient, $-\mathbf{g}_k$ along the x (Left) and y-axis (Right); The third-order model has been used.

The RMS error between the two mentioned quantities was 7.02×10^{-7} and 5.34×10^{-7} in x and y directions, respectively, which verifies the correctness of the calculated Newton direction based on (5.62). The assimilation was carried out using the first 8 observations. Figure 5.31 shows the variation of the cost function and the norm of the gradient, both scaled with their initial values, with the number of iterations.

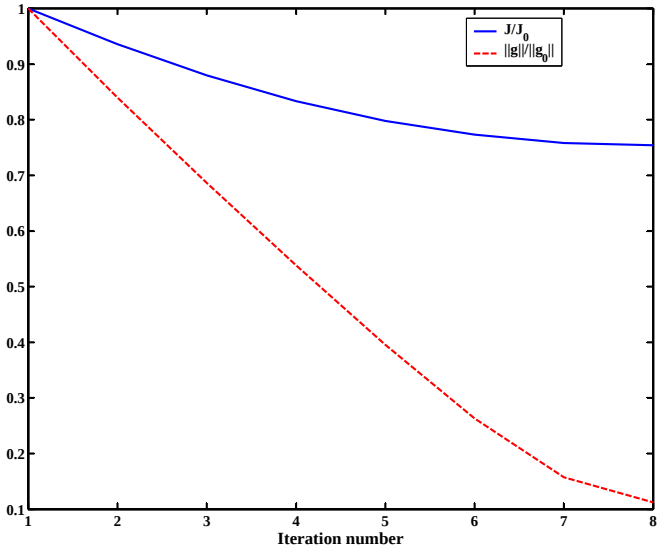

Figure 5.31: Variations of the scaled cost function (J/J_0) and scaled gradient norm ($||\mathbf{g}||/||\mathbf{g}_0||$) with the number of iterations, using the adjoint Newton algorithm, as the observations are model-generated, and the third-order model is used.

After 8 iterations the norm of the gradient has been dropped to about 10% of its initial value. The convergence rate was fast linear similar to the previous first-order case. In the present simulation, the initial values for the tangential velocities on the free surface $(u_s(x, y, 0), v_s(x, y, 0))$ were obtained from the initial surface profile $\eta(x, 0)$ using the linear approximation (5.89), while the adjoint variables (u_s^*, v_s^*) were obtained from η^* using the first-order adjoint equation (5.52), i.e.

$$b_{nm}^*(t) = \frac{\tanh kh_0 \cos\theta_{nm}}{\omega} a_{nm}^*(t),$$
$$c_{nm}^*(t) = \frac{\tanh kh_0 \sin\theta_{nm}}{\omega} a_{nm}^*(t), \tag{5.91}$$

where $b_{nm}^*(t)$ and $c_{nm}^*(t)$ are the Fourier coefficients for the adjoint variables u_s^* and v_s^*,

respectively, and $a^*_{nm}(t)$ are the Fourier coefficients for the adjoint variable η^*. Figure 5.32 shows the comparison between the noisy and retrieved spectra of the initial condition with the true spectrum.

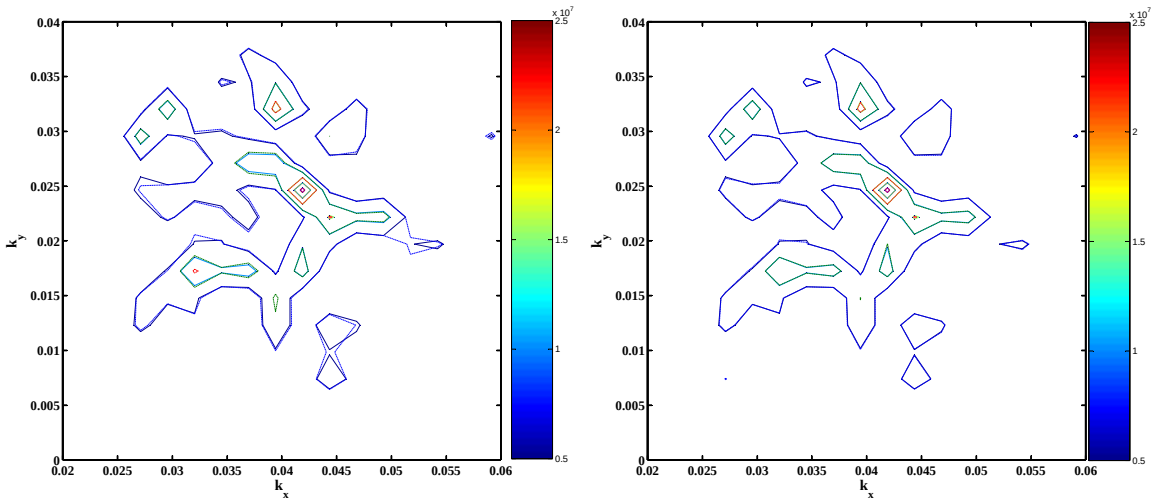

Figure 5.32: Left: Comparison of the spectrum of the noisy initial condition (dashed) at $t = 0$ with the true spectrum (solid); Right: Comparison of the spectrum of the retrieved initial condition (dashed) with the true spectrum (solid) at $t = 0$; Third-order model has been used.

Figure 5.32 apparently shows that the spectrum of the retrieved surface profile better fits the true spectrum. Note that the spectral amplitudes in Figure 5.32 have not been scaled with the total number of variables ($Nx \times Ny$). To evaluate the ability of the assimilated profile in fitting the model dynamics the third-order model was initialized with the retrieved surface profile and was allowed to evolve for 80 seconds. The left box in Figure 5.33 displays the time history of the point located at $(x = L_1/2, y = L_2/2)$, while the right box shows that for the point located at $(x = L_1/4, y = 3L_2/4)$.

The RMS error between the original noisy forecast and the true time history was $0.286m$, which was reduced to $0.085m$ using the nonlinear assimilation. Using a nonlinear update for the forward model variables (u_s, v_s) and adjoint variables (u^*_s, v^*_s) would further reduce the error. Incorporating more observations within the assimilation interval, or primarily filtering the observations using the linear dispersion relation would furhter improve the quality of the retrieved profile and that of the forecast.

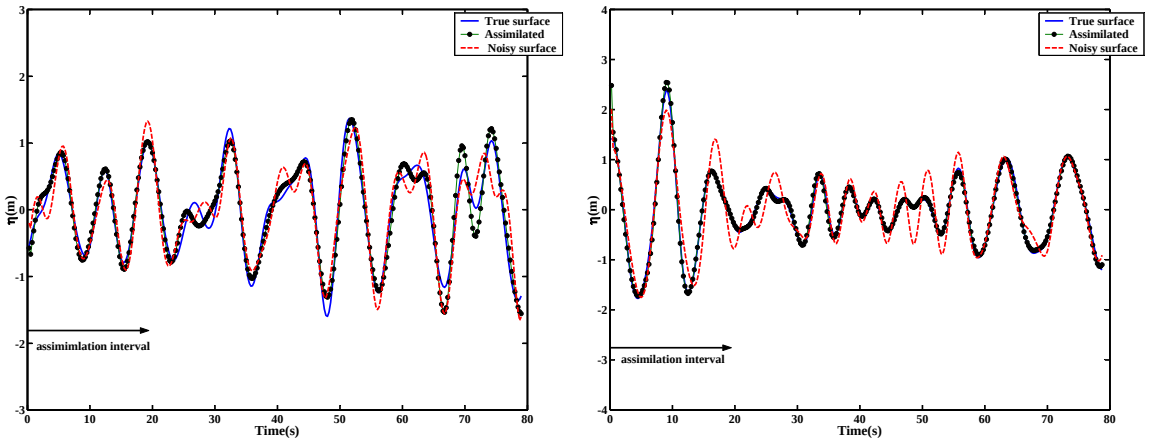

Figure 5.33: Left: Comparison of surface elevation time histories at the point $(L_1/2, L_2/2)$; Right: The same as the left one at the point $(L_1/4, 3L_2/4)$

.

Comparison with dispersion filter

As discussed in section 5.5.2, other than variational assimilation, one alternative to remove the noise from the observations is to fit the theoretical dispersion relation (5.72) to the three-dimensional Fourier transform of the observational frames in wavenumber-frequency $(\mathbf{k} - \omega)$ space. For three-dimensional flows the dispersion function is similarly broadened so that it even captures those components from the spectrum that do not lie exactly on this function. A simple Gaussian band-pass filter was used for this purpose (see (5.73) and (5.74)).

A total number of 32 model-generated observational frames, with 50% Gaussian noise in $2.5s$ intervals were selected. The filtered results were sensitive to the value of the band-width parameter f_ω. Figure 5.34 shows the time history of the point $(x = L_1/4, y = 3L_2/4)$ obtained by the described filter. The result is compared with the noiseless profile. Results have been plotted for two values $f_\omega = 6$ and $f_\omega = 2$.

Since the temporal resolution of the observations was much lower than the model resolution, the first filtered frame was picked and allowed to evolve up to $t = 77.5s$. The RMS error between the filtered profile, with $f_\omega = 2$, and the noiseless profile was $0.21m$ comparing to that $(0.29m)$ for the case $f_\omega = 6$. Figure 5.35 displays the time history of the same point, obtained by assimilating the first 8 observations (circles), and compares it with

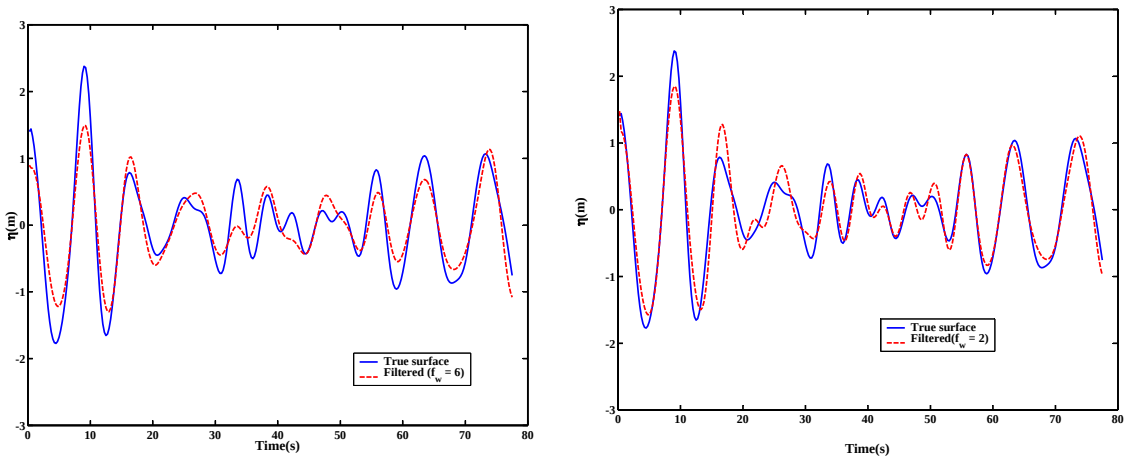

Figure 5.34: Left: Time history of the point $(x = L_1/4, y = 3L_2/4)$ obtained by the dispersion filter with $f_\omega = 6$(dashed), vs. noiseless surface profile (solid); Right: The same as the left plot with $f_\omega = 2$.

the noiseless(solid), noisy(dotted), and filtered(dashed) profiles.

The RMS error between the assimilated profile and the true one was $0.085m$ which is significantly lower than that associated with the filtered profile $(0.21m)$. This lower quality of the filtered profile compared to the assimilated one is partly attributed to the nonlinearity of the wave dynamics, as well as the poor temporal resolution of the observations.

5.6.3 Test with field data

Field experiments were also carried out from aboard a ship at a site located approximately 70 miles southeast of Kodiak, Alaska, in April, 2006. Figure 5.36 displays the geographical location of the experiments.

Triaxis buoy as well as GPS-based directional wave buoys were used to provide the ground-truth data on the directional wave field around the ship. An X-Band radar system was chosen for these experiments, because of the maturity of the technology, its ability to operate under a wide range of environmental conditions, and its potential for providing detailed surface profile measurements over spatial resolution commensurate with numerical modeling needs. The backscatter data from the ship-board radar (non-coherent, HH-polarized) were digitally recorded, an example of which is displayed in Figure 5.37.

Wave field retrievals were initially carried out using a "tilt modulation" approach similar

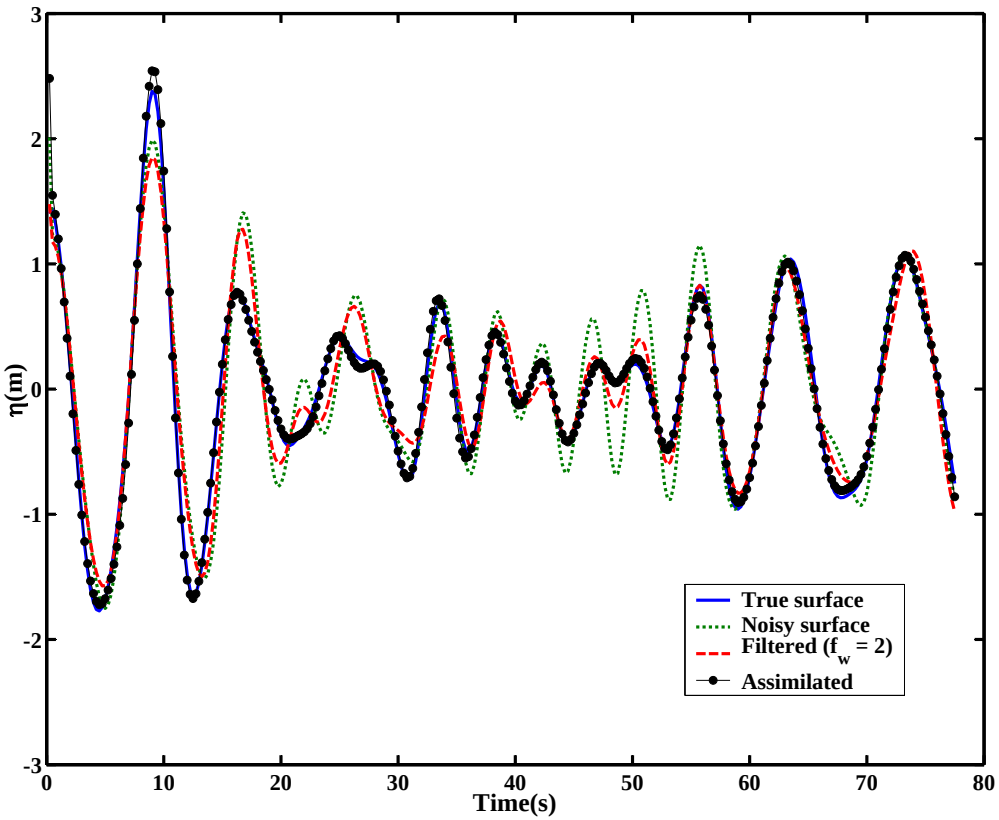

Figure 5.35: Time histories of the point $(x = L_1/4, y = 3L_2/4)$, obtained by assimilation (circles), and dispersion filter(dashed), compared with the noisy (dotted), and noiseless (solid) profiles.

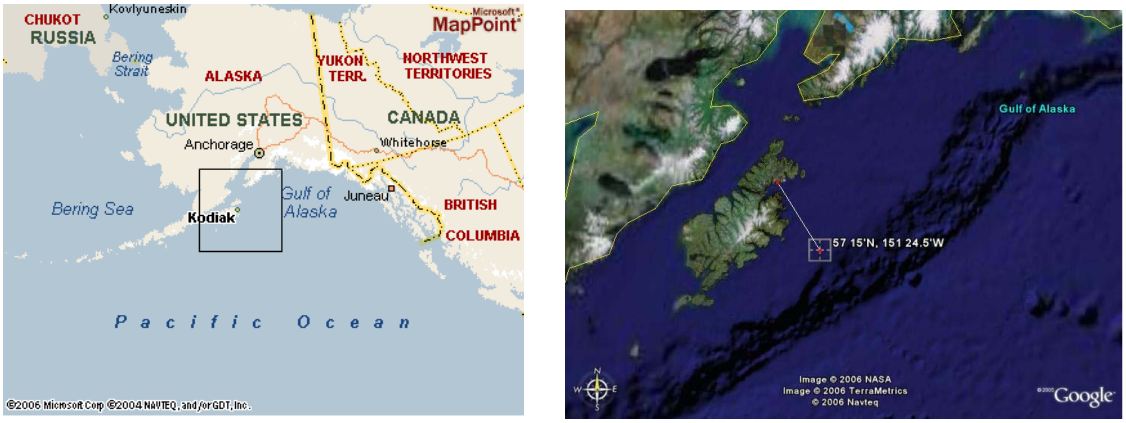

Figure 5.36: Location of the field experiments.

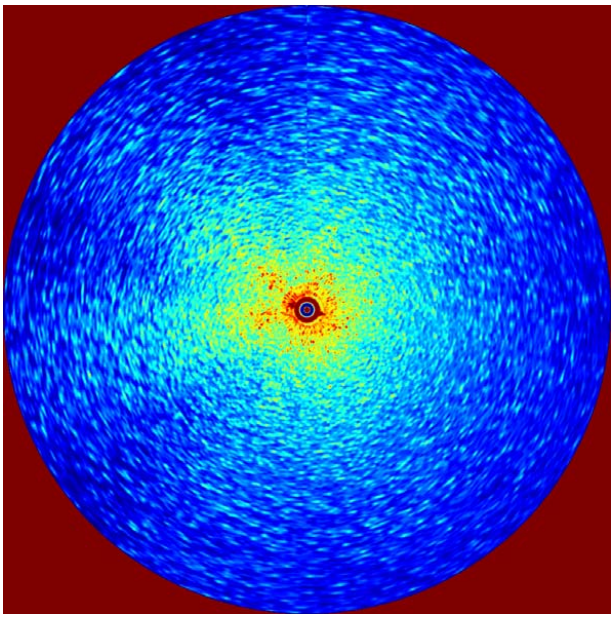

Figure 5.37: X-Band radar images collected during the field experiments in April, 2006.

to that of Dankert and Rosenthal [18]. One of the limitations of Dankert and Rosenthal approach is that the antenna must be located high enough (100m above the sea surface) to avoid shadowing effects and produce the range of grazing angles needed for determination of the tilt modulation transfer function. However, for ship-board applications involving antennas at heights of 10-30m above the sea surface and lower grazing angles, techniques still need to be developed and improved to interpret the radar backscatter signals. Preliminary comparisons of the radar and buoy-retrieved wave fields are shown in Figure 5.38.

In order to investigate the effectiveness of the proposed assimilation scheme for the field data a series of radar-retrieved surface elevation maps were assimilated into the numerical model. It was presumed that the radar images were already checked for consistency with point buoy measurements. The main objective of this section is to use the present assimilation technique to tune the numerical model such that it fits a series of radar observations better, i.e., to make the model predictions and radar measurements more consistent as an integrated system. Some preliminary assimilation results are presented here.

The computational domain was $3060m \times 3060m$ with 256 grid points in each direction. The revisiting period of the radar was about $3.06s$, and the model time increment was taken to be 1/16 of the radar revisiting period. Both linear and third-order models were tried

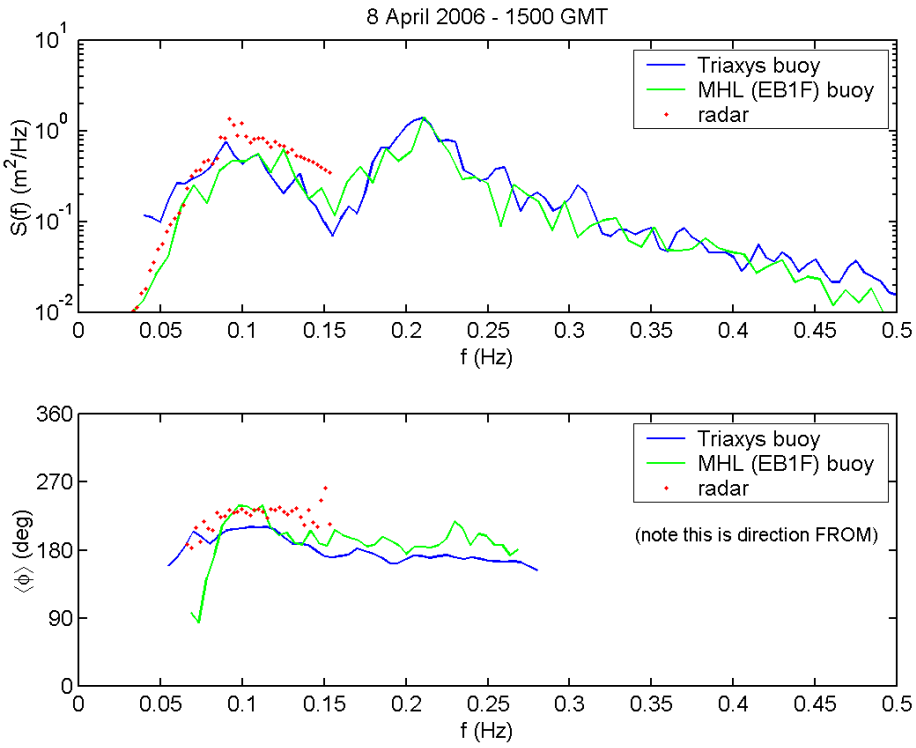

Figure 5.38: Preliminary comparison between the buoy and radar-retrieved wave fields for the data collected in April, 2006.

in the simulations; initialized with the first radar image, both models were allowed to run for 180 seconds and the time history of the point located at $(x = L_1/2, y = L_2/2)$ resulting from each model was recorded which can be seen in Figure 5.39.

Other than a slight difference in amplitudes (third-order model predictions have slightly higher amplitudes because of the nonlinear interactions), and a slight phase shift in the range $[120s, 150s]$, there is no major difference between these models, hence to keep the assimilation simple and fast, the linear model will be used in all future simulations in this section. Figure 5.40 shows the variation of the scaled cost function and norm of its gradient with the number of iterations, for the cases where 8, 16, and 32 radar images were used for the assimilation.

It is observed that the number of iterations for convergence remained almost the same (between 17 to 19 iterations) for 8, 16, and 32 observations (this behavior is different from what was observed for the synthetic data where an increase in the number of assimilated frames led to a meaningful increase in the number of iterations), with a similar relative

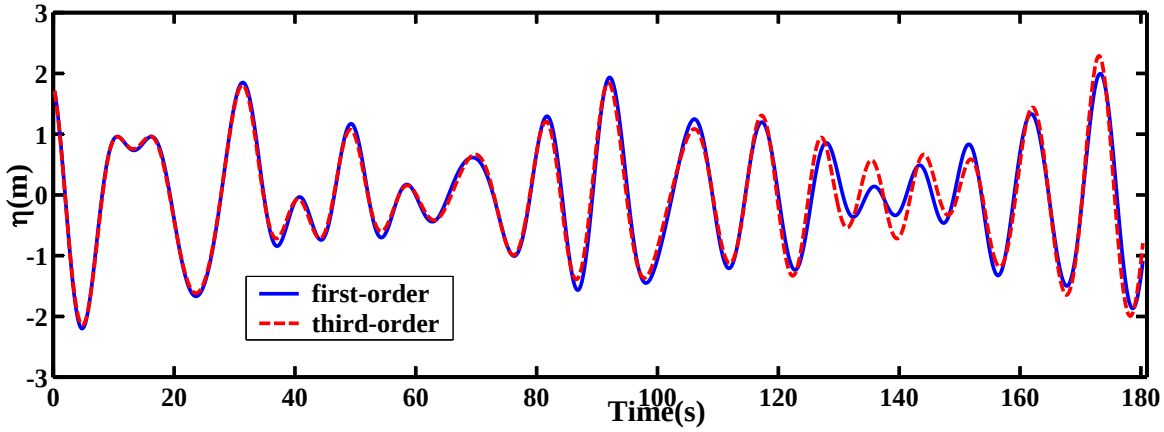

Figure 5.39: Comparison of the time history of the point $(x = L_1/2, y = L_2/2)$ obtained from linear (solid), and third-order(dashed) models; models were initialized with the first radar image.

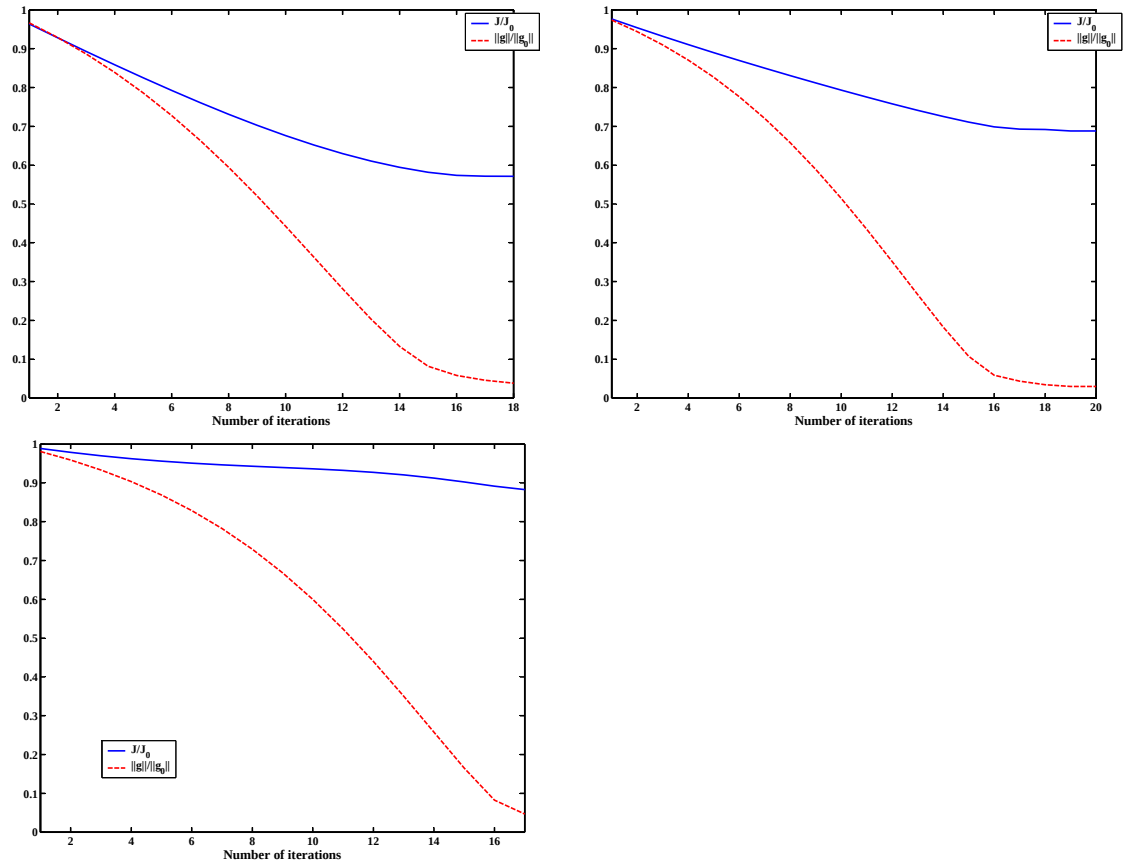

Figure 5.40: Variation of the cost function (solid) and norm of the gradient (dashed), both scaled with their initial values as a function of iterations. Top left: 8 frames used; Top right: 16 frames used; Bottom left: 32 frames used.

reduction in the gradient norm ($||\mathbf{g}||/||\mathbf{g}_0||$). However, the relative rate of reduction in the cost function (J/J_0) becomes slower by incorporating more radar images in the assimilation.

The retrieved initial conditions corresponding to each case shown in Figure 5.40 were allowed to evolve for $140s$. The resulting time histories were recorded for the following three points in the computational domain:

- $(x = L_1/4, y = 3L_2/4)$
- $(x = L_1/2, y = L_2/2)$
- $(x = 3L_1/4, y = L_2/4)$

The time histories are presented in Figures 5.41- 5.43.

A qualitative comparison of Figures 5.41- 5.43 apparently shows that the assimilation improves the forecast, however this improvement is more pronounced within the assimilation period and about $30-50$ seconds beyond that. As a general observation, for the cases where more radar images are incorporated into the model the forecast time series begins to lose accuracy in the beginning, however it makes that up at later times.

In most cases using 8 or 16 observations would be more efficient for practical applications. More improvements are expected if the cost function is scaled appropriately. Another strategy would be to add some penalty terms in the cost function in order to capture larger/steeper waves in a better way.

Figure 5.43 shows that incorporating 8 observations improves the first 40 seconds of the time record, while incorporating 16 observations extends this range to about 70 seconds and using 32 observations under-predicts the first 25 seconds, and instead improves the forecast up to around $t = 130s$.

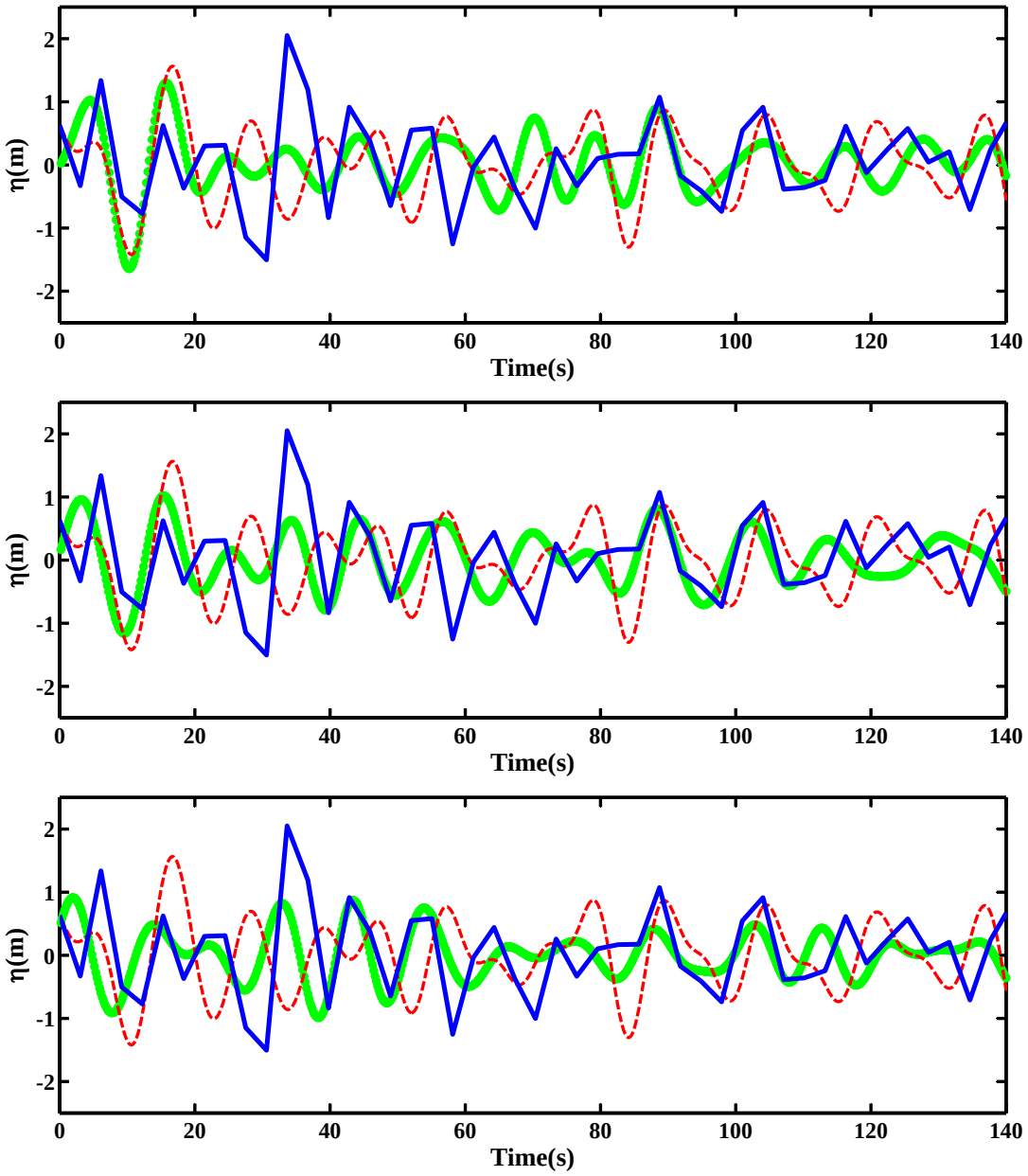

Figure 5.41: Comparisons of the time history at the point ($x = L_1/4, y = 3L_2/4$); red dashed lines were obtained by initializing the model with the first radar image without assimilation, while the green circles obtained by assimilating 8(top plot), 16(middle plot), and 32(bottom plot) radar images into the model, and the blue solid lines are the raw radar retrievals.

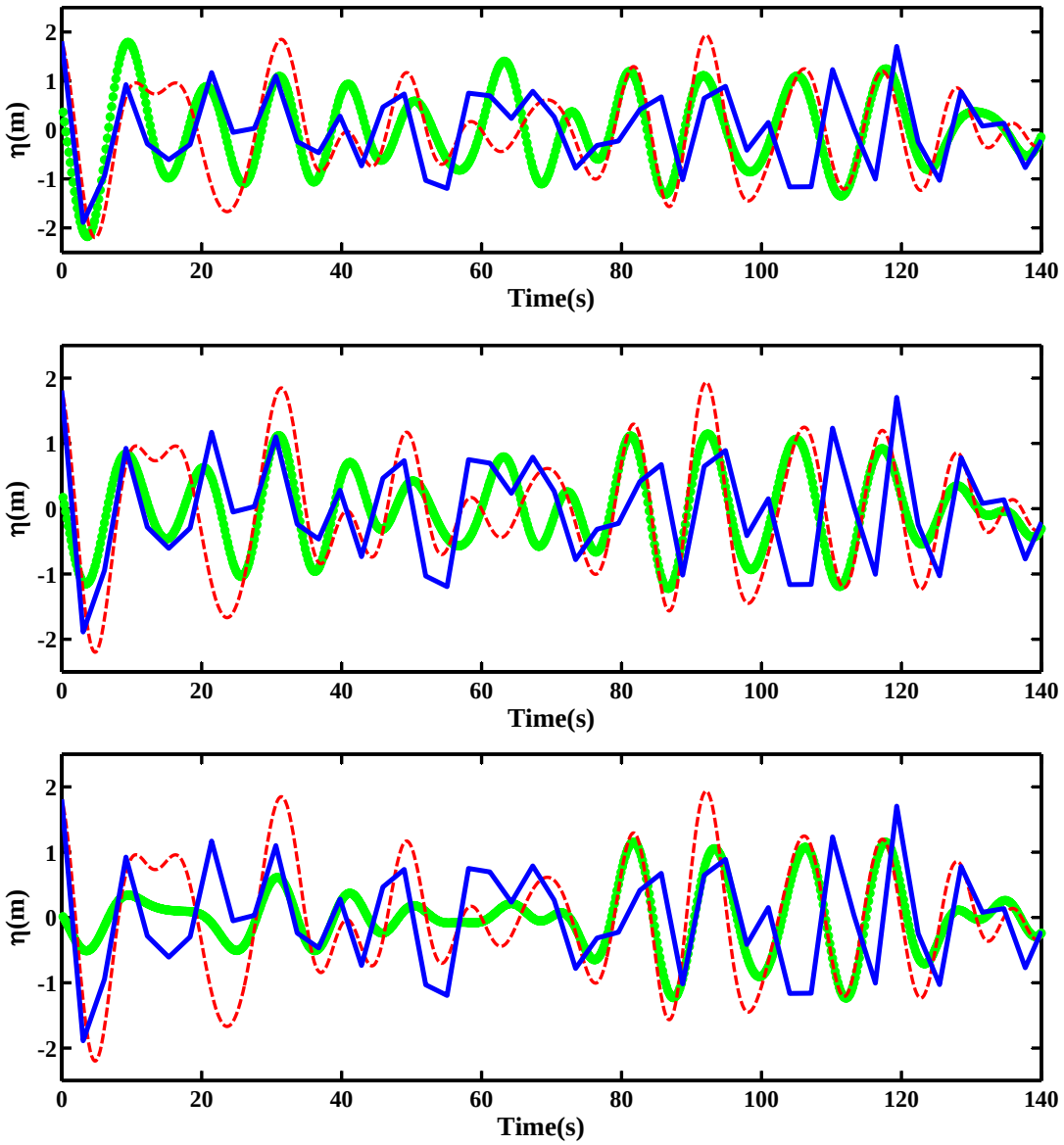

Figure 5.42: Same as Figure 5.41 for the point $(x = L_1/2, y = L_2/2)$.

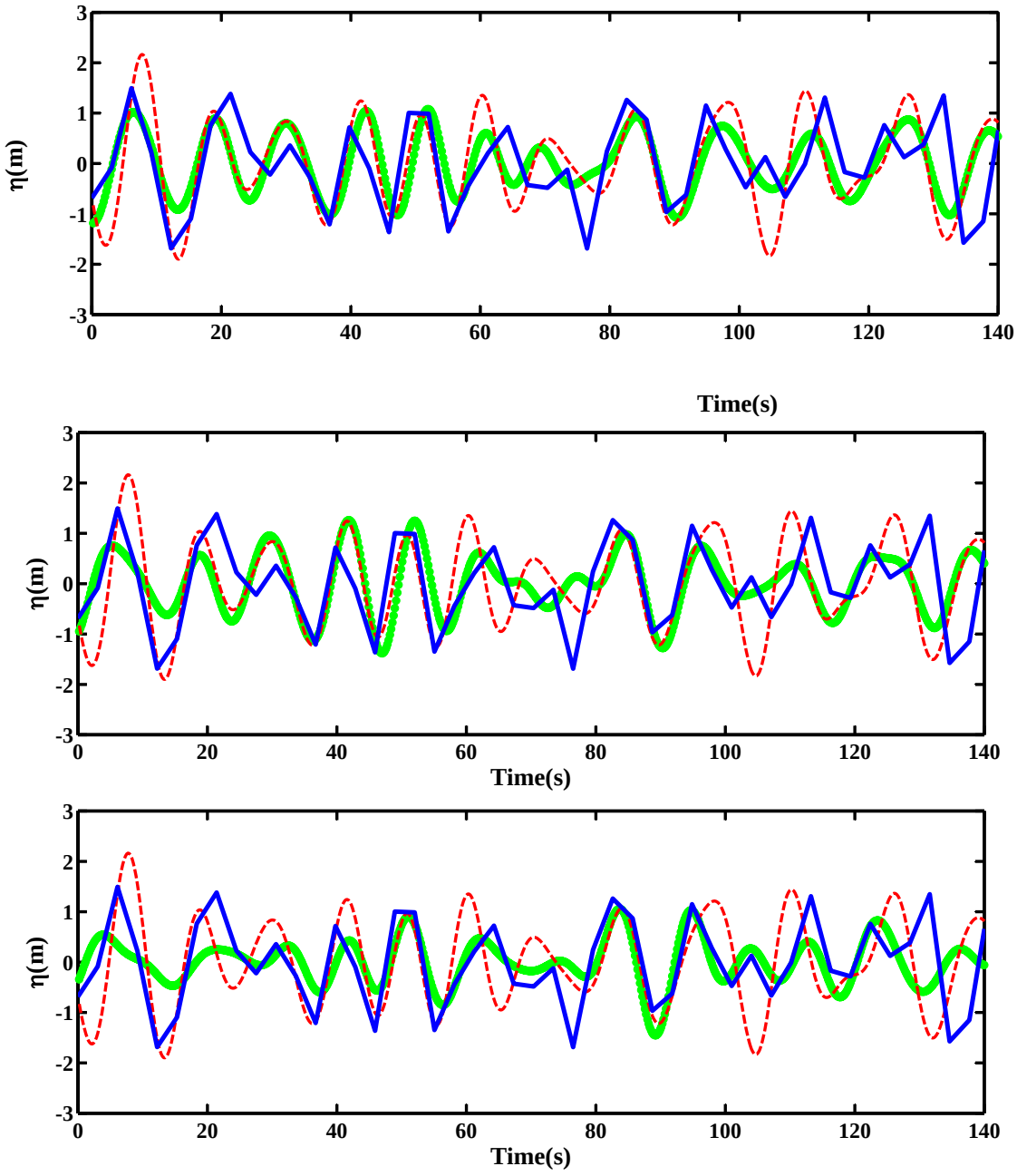

Figure 5.43: Same as Figure 5.41 for the point $(x = 3L_1/4, y = L_2/4)$.

5.7 Other applications

5.7.1 Surface current estimation

Most of wave evolution models involve unknown parameters, e.g., friction coefficients, eddy viscosities, surface/shear currents, and wind drag coefficients besides initial/boundary conditions. Obtaining optimal initial condition has been the main subject of this dissertation and the proposed assimilation scheme was validated through extensive numerical experiments with synthetic and field data. The objective of this section is to develop an efficient scheme to estimate the slowly varying surface currents from the observations of the free surface elevation which are distributed over a time interval.

Consider a one-dimensional horizontal surface current, $U = U(x)$, which is assumed to vary slowly so that $\frac{\lambda(U_x)}{|U|} = O(\mu)$, where $\mu = \lambda/L$, is a small parameter representing the slow variation of the current, with λ being the typical wavelength and L being the characteristic length of current variation. By adopting an expansion method similar to that introduced in chapter 3, it can be shown that the general evolution equations given by (4.11) for two-dimensional flows are slightly modified, with an error of $O(\epsilon^2)$, to:

$$\begin{aligned} \eta_t + (U\eta)_x &= f\left(\eta(t), u_s(t)\right), \\ u_{s,t} + (Uu_s)_x &= g\left(\eta(t), u_s(t)\right), \end{aligned} \tag{5.92}$$

It is assumed that a series of surface elevation maps from radar or any other device are available over a time interval T. In general the calculated values will be different from the measured ones. One usually attempts to minimize the following functional:

$$J = \int_t \int_x \left[\eta(x,t) - \eta^{obs}(x,t)\right]^2 \mathrm{d}x\mathrm{d}t, \tag{5.93}$$

The functional J measures the data misfit. However since some previous works in other applications [61] have reported fluctuations resulting from a minimizing criteria similar to (5.93), the following modified functional has been considered,

$$F = \frac{1}{2}\int_t\int_x W\left[\eta(x,t) - \eta^{obs}(x,t)\right]^2 \mathrm{d}x\mathrm{d}t + \frac{1}{2}T\int_x\left(\frac{\partial U}{\partial x}\right)^2 \mathrm{d}x, \tag{5.94}$$

where T is the assimilation interval or time duration of the simulation. The second term was added to reduce the variability/fluctuations in the solution for $U(x)$. The weighting factor W is used to control the influence of each term in the minimization. The second term is known as the penalty term. With the functional F suitably defined, the goal is to minimize it subject to the constraint (5.92). In order to do this, the Lagrange function formalism is used in which the first variation of (5.94) is set to zero,

$$\delta F = \int_t\int_x W\left[\eta(x,t) - \eta^{obs}(x,t)\right]\delta\eta \mathrm{d}x\mathrm{d}t + T\left(U_x\delta U|_{x=0}^{x=L} - \int_x U_{xx}\delta U \mathrm{d}x\right) = 0, \tag{5.95}$$

where integration by parts has been used for the second term. Taking the first variation of the constraints (5.92), multiplying it by the arbitrary adjoint variables η^* and u_s^* (corresponding to the Lagrange multipliers) and integrating over all x and t yields:

$$\begin{aligned}
&\int_t\int_x \eta^*\left(\delta\eta\right)_t \mathrm{d}x\mathrm{d}t + \int_t\int_x \eta^*\left(U\delta\eta\right)_x \mathrm{d}x\mathrm{d}t + \int_t\int_x \eta^*\left(\eta\delta U\right)_x \mathrm{d}x\mathrm{d}t - \int_t\int_x \eta^* f'(\delta\eta, \delta u_s)\mathrm{d}x\mathrm{d}t \\
&+ \int_t\int_x u_s^*\left(\delta u_s\right)_t \mathrm{d}x\mathrm{d}t + \int_t\int_x u_s^*\left(U\delta u_s\right)_x \mathrm{d}x\mathrm{d}t + \int_t\int_x u_s^*\left(u_s\delta U\right)_x \mathrm{d}x\mathrm{d}t \\
&- \int_t\int_x u_s^* g'(\delta\eta, \delta u_s)\mathrm{d}x\mathrm{d}t = 0,
\end{aligned} \tag{5.96}$$

Where the variables $\delta\eta$ and δu_s correspond to the tangent linear variables η' and u_s' which were introduced earlier in this chapter. The operators f' and g' correspond to the tangent linear operators which were already derived for first, second, and third-order models (see Equations (5.55)- (5.57)). Integrating by parts and transferring the derivatives and operators from $\delta\eta$ and δu_s to the adjoint variables η^* and u_s^*, one obtains:

$$\int_x [\eta^* \delta\eta]_0^T \, \mathrm{d}x - \int_t \int_x \eta_t^* \delta\eta \mathrm{d}x\mathrm{d}t + \int_t [\eta^* U \delta\eta]_0^L \, \mathrm{d}t - \int_t \int_x U \delta\eta \eta_x^* \mathrm{d}x\mathrm{d}t + \int_t [\eta^* \eta \delta U]_0^L \, \mathrm{d}t$$
$$- \int_t \int_x \eta_x^* \eta \delta U \mathrm{d}x\mathrm{d}t - \int_t \int_x \delta\eta f^* \left(\eta^*, u_s^*\right) + \int_x [u_s^* \delta u_s]_0^T \, \mathrm{d}x - \int_t \int_x u_{s,t}^* \delta u_s \mathrm{d}x\mathrm{d}t$$
$$+ \int_t [u_s^* U \delta u_s]_0^L \, \mathrm{d}t - \int_t \int_x U \delta u_s u_{s,x}^* \mathrm{d}x\mathrm{d}t + \int_t [u_s u_s^* \delta U]_0^L \, \mathrm{d}t - \int_t \int_x u_{s,x}^* u_s \delta U \mathrm{d}x\mathrm{d}t$$
$$- \int_t \int_x \delta u_s g^* \left(\eta^*, u_s^*\right) \mathrm{d}x\mathrm{d}t + b.t. = 0. \tag{5.97}$$

where f^* and g^* are the adjoint operators which have been already derived (see Equations (5.58)- (5.60)). The term $b.t.$ represents all the boundary terms which result from integration by parts. In order to simplify the analysis and obtain a more straightforward relation for the gradient, the following boundary conditions for the perturbations and adjoint variables (Lagrange multipliers) are assumed:

$$\begin{aligned} &\delta\eta(0) = \delta u_s(0) = 0, \quad \eta^*(T) = u_s^*(T) = 0, \quad \eta^*(0) = \eta^*(L), \quad u_s^*(0) = u_s^*(L), \\ &U(0) = U(L), \quad \delta\eta(0) = \delta\eta(L), \quad \delta u_s(0) = \delta u_s(L), \quad \delta U(0) = \delta U(L), \\ &U_x(0) = U_x(L), \end{aligned} \tag{5.98}$$

These assumptions will remove all of the boundary terms. Adding (5.95) and (5.97), and using the conditions (5.98) yields:

$$\begin{aligned} &- \int_t \int_x \eta_x^* \eta \delta U \mathrm{d}x\mathrm{d}t - \int_t \int_x u_{s,x}^* u_s \delta U \mathrm{d}x\mathrm{d}t - T \int_x U_{xx} \delta U \mathrm{d}x \\ &+ \int_t \int_x \left(W \left[\eta(x,t) - \eta^{obs}(x,t) \right] - \eta_t^* - U \eta_x^* - f^* \left(\eta^*, u_s^*\right) \right) \delta\eta \mathrm{d}x\mathrm{d}t \\ &+ \int_t \int_x \left(-u_{s,t}^* - U u_{s,x}^* - g^* \left(\eta^*, u_s^*\right) \right) \delta u_s \mathrm{d}x\mathrm{d}t = 0. \end{aligned} \tag{5.99}$$

The variables η^* and u_s^* can be selected in such a way that the coefficients of $\delta\eta$ and δu_s become zero. This yields:

$$\eta_t^* + U\eta_x^* + f^*\left(\eta^*, u_s^*\right) = W\left[\eta(x,t) - \eta^{obs}(x,t)\right],$$
$$u_{s,t}^* + Uu_{s,x}^* + g^*\left(\eta^*, u_s^*\right) = 0, \tag{5.100}$$

Under the constraints (5.100), $\delta F = 0$ implies that:

$$T\int_x U_{xx}\delta U \mathrm{d}x + \int_t\int_x \left(\eta\eta_x^* + u_s u_{s,x}^*\right)\delta U \mathrm{d}x\mathrm{d}t = 0, \tag{5.101}$$

which can be reformulated as:

$$U_{xx} + \frac{1}{T}\int_t \left(\eta\eta_x^* + u_s u_{s,x}^*\right)\mathrm{d}t = 0. \tag{5.102}$$

The problem of minimizing the functional (5.94) has thus resulted in new sets of equations (5.100) and (5.102). Equations (5.100) are the adjoint equations which are remarkably similar to the original model (5.92) except in two respects. First, it is forced by the data misfit $\left(\eta - \eta^{obs}\right)$ alone, when solved with the boundary conditions introduced earlier. Second, it is stable only when integrated backwards in time (i.e. from $t = T$ to $t = 0$). The same pseudo-spectral method will be used to solve the adjoint system. The (η^*, u_s^*) obtained from the adjoint model (5.100) and (η, u_s) obtained from the original model will be used to evaluate the second term of (5.102) which can be recognized as ∇J. This gradient is used to minimize J iteratively. The inclusion of the smoothing term has resulted in the first term in (5.102). Thus (5.102) represents the gradient of the functional F (rather than J), which must equal zero for F to be an extremum. The role of the smoothing term must be viewed as merely that of lending stability to the parameter estimation process.

An iterative scheme for obtaining successive estimates of $U(x)$ can now be constructed in the following steps:

- Run the forward model (5.92) with an initial estimate for the current profile; obtain $\eta(x,t)$ and $u_s(x,t)$.
- Calculate data misfit $\left(\eta(x,t) - \eta^{obs}(x,t)\right)$ at times and locations where observations are available.

- Run the adjoint model (5.100) backwards in time, forced by the data misfit $\eta - \eta^{obs}$, in conjunction with any weighting factor W; obtain $\eta^*(x,t)$ and $u_s^*(x,t)$.
- Use (η, u_s) and (η^*, u_s^*) computed in steps 1 and 3 to evaluate the second term in (5.102) and obtain new parameter estimates.
- Use a simple minimization routine to optimize the weighting factor W such that the resulting parameter estimate produces the least misfit.
- Return to step 1.
- Calculation continues until the difference in successive estimates of the parameter is less than some small parameter.

A preliminary test has been carried out to verify the gradient ∇J calculated using the developed adjoint method. A simple one-dimensional surface current was considered:

$$U(x) = U_0 + U_1 \cos^2\left(\frac{\pi\,(x - L/2)}{L}\right), \quad \text{for } 0 \le x \le L \tag{5.103}$$

Figure 5.44 displays the variation of this adverse current in the computational domain, with the following dimensional parameters: $U_0 = -1m/s$, $U_1 = 0.2m/s$, and $L = 32m$.

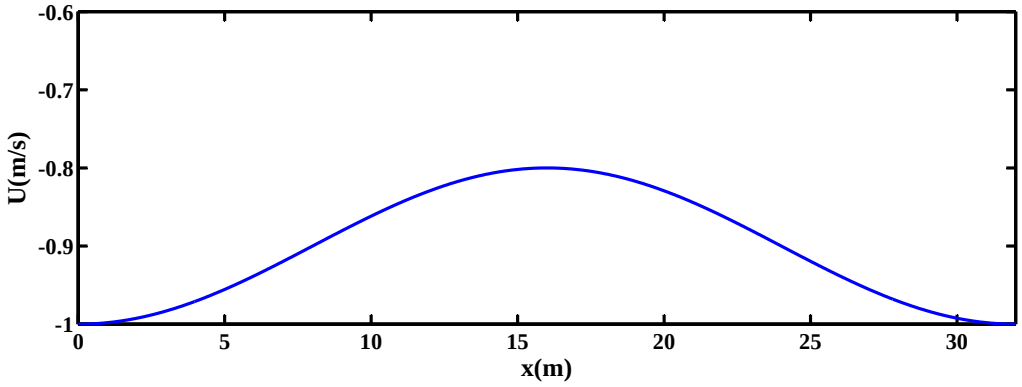

Figure 5.44: Adverse surface current profile given by (5.103).

The initial surface profile was a monochromatic wave of amplitude $1cm$ and wavelength $1m$ propagating in the positive x-direction in the absence of a surface current. The number of Fourier modes (grid points) in the computations was 1024 (with the number of grid points

per wavelength being 32), and the time step was $\Delta t = 0.02s$. The simulation was continued up to $t = 50s$ at which time the wave steepens and a singularity starts to develop (about the point $x = 10m$) due to the convergence of two wave trains with different wavenumbers at the same location (see Figure 5.45). The local wave amplitude and wavenumber increase in this case.

The observations were generated using the forward model, such that model solutions were recorded every 2 seconds (totally 26 frames were recorded). The generated observation frames are shown in Figure 5.45.

The adjoint-calculated gradient was compared with that calculated using direct finite difference approach. The latter approach needs the forward model to be integrated 1024 times, while the former will calculate the same quantity by just two integrations of the forward and adjoint models. The perturbation parameter used in the direct method was 10^{-8}. Figure 5.46 shows the comparison of the adjoint and F.D. gradients. The RMS error between these two gradients was 1.75×10^{-8} which is of the same order as the perturbation parameter (since the direct method used is first-order accurate). This verifies the correctness of the gradient value estimated by the developed adjoint method. Note that the initial estimate of the current used in calculations of the gradient was a constant profile $U_0 = -1m/s$.

Future plans would be to use this gradient to minimize the cost functional F, and check if we can retrieve the original current profile given by (5.103).

Further extension of the adjoint technique to estimate numerical model parameters besides initial/boundary conditions is under development. Some of these future challenges will be discussed in Chapter 6.

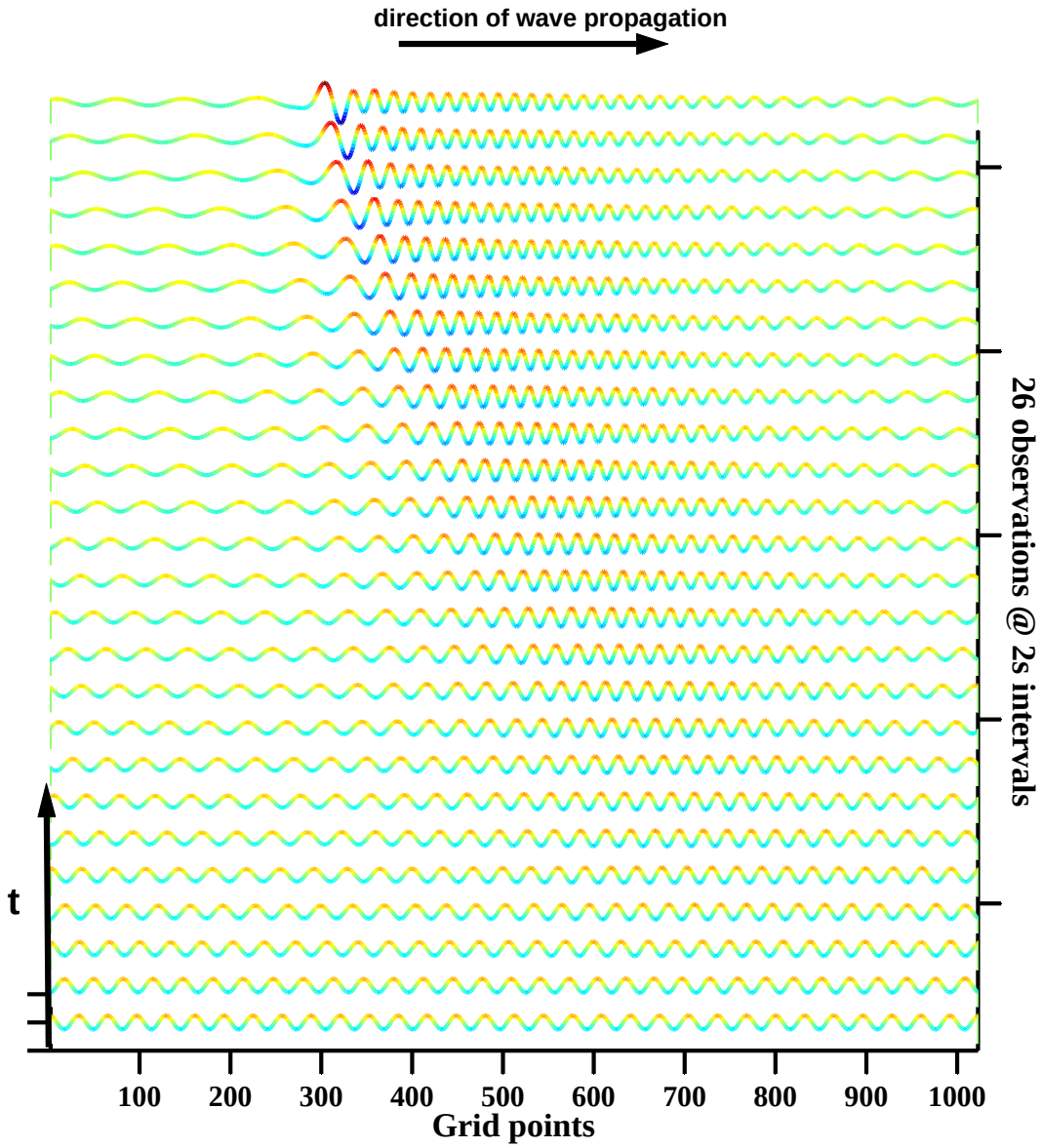

Figure 5.45: Model-generated observations of the free surface profile. The initial surface is a monochromatic wave of amplitude $1cm$ and wave length $1m$ propagating in the positive x-direction, and the surface current is given by (5.103).

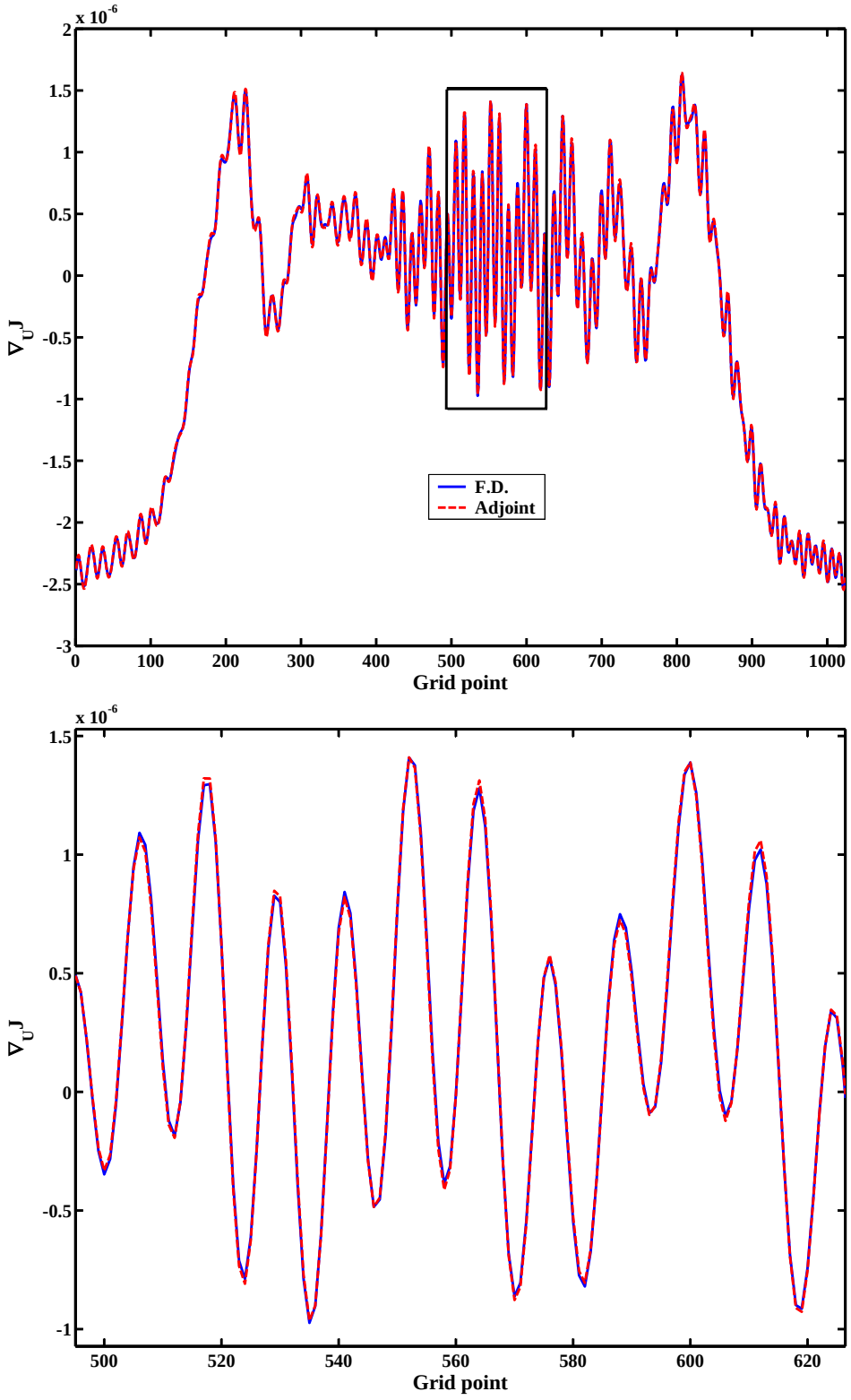

Figure 5.46: Top: Comparison of the gradient of the cost function with respect to the current profile U, calculated using adjoint (dashed) and direct(solid) methods; Bottom: A zoomed view of the left plot.

CHAPTER 6

Conclusions and Recommendations

Main objective of this thesis was to develop an efficient method to assimilate marine radar data into a numerical wave prediction model which, in turn, is used to forecast evolving nonlinear wave fields beyond the assimilation interval.

The first part of this Ph.D. research was dedicated to developing a fast and efficient numerical wave model based on slope expansion (up to third-order), which was originally developed by West *et al*[80] for deep water in Fourier space. The pair of coupled nonlinear evolution equations for surface elevation and tangential velocity were solved efficiently using a pseudo-spectral method based on the FFT, and a fourth-order Runge-Kutta integration scheme was used to evolve the free surface variables in time with a low-pass filter being used to prevent aliasing errors from occuring during the nonlinear simulations. The model was validated for the following wave problems:

- Exact steady solutions of 2-D periodic waves.
- Steady short-crested waves;
- 2-D laboratory experiments of modulation instability.
- Long-time evolution of a wavetrain with two side-bands.
- Propagation of 2-D free waves;

It was found that, as predicted by the slope expansion relations, the third-order model, compared to other approximations, was better able to capture the asymmetric features of

steep waves in two and three dimensions. For steepness parameter $\epsilon = 0.3$ (about 75% of the highest theoretical wave), the numerical phase velocity achieved by the third-order model was about 0.3% higher than the exact phase velocity, and the total energy and momentum were conserved to 0.06% and 0.05%, respectively, after a traveling time of 40 wave periods. The third-order model reasonably predicted the phases, amplitudes, and asymmetric pattern of the highly modulated waves resulting from the evolution of an incident wave with two side-bands. The model predictions also matched the measured spectrum across a broad band of frequencies.

As the numerically predicted wave field is not consistent with the radar-estimated profiles, an efficient data assimilation scheme was developed that iteratively minimizes the differences between the measured and numerically predicted values of the sea surface elevation over time. This difference was chosen as the cost (objective) function whose gradient with respect to each control variable (initial condition) was used in search for a minimum. Direct methods of calculating the gradient were ruled out, because their computational cost is so high that it makes them inefficient for real-time applications. Instead, an adjoint technique was used. This technique was shown to be very efficient, since it gives the same gradient by just one forward integration of the original(forward) model and one backward integration of the so-called adjoint model, compared to N (total number of control variables) integrations needed in direct methods. The explicit form of the evolution equations made the derivation of adjoint equations more convenient as they were derived up to the third-order approximation. These equations were also solved using a pseudo-spectral method. The continuous form of the adjoint equations derived here have significantly better stability properties than the discrete forms of the adjoint equations generated using commercial automatic differentiation codes.

For 2-D problems a quasi Newton-type minimization algorithm was used in which the Hessian matrix is updated at each iteration using the BFGS algorithm. This scheme was shown to be fast and efficient for 2-D problems where the number of variables is of order 10^3. However, for 3-D problems with much larger number of control variables (of order 10^5), the issue of storing big Hessian matrices at each iteration justified the use of so-called Adjoint Newton Algorithm (ANA). This algorithm was shown to be very efficient for highly

noisy and large-scale nonlinear problems.

The assimilation scheme was validated for the following free surface problems:

- KdV model for the propagation of solitary waves.
- 2-D synthetic sea surface generated using JONSWAP frequency spectrum.
- 2-D synthetic radar retrievals from combined electromagnetic-hydrodynamic simulations.
- 3-D synthetic sea surface generated using the JONSWAP frequency spectrum.
- Preliminary analysis of the field data.

For synthetic data, the assimilation was able to effectively remove the artificially added noise (up to 50%) with a reasonably low number of iterations and one can forecast up to an arbitrary long time, given the periodicity of the initial conditions. The number of iterations were strongly dependent on the definition of the convergence criterion. Extensive numerical simulations showed that most of the large-scale variations in the cost function occur in the first few iterations, hence, assimilation cost may be significantly reduced by defining the convergence criterion appropriately. Nonlinearity had a significant effect on the assimilation cost as the number of iterations increased by almost a factor of two. Three-dimensional large-scale problems need the forward model solutions to be stored at all time steps over the assimilation period. The storage can be a prohibitive issue when dealing with larger problems and larger numbers of observations. This can be overcome by parallelizing the code and distributing the big matrices over several machines.

More careful consideration needs to be given to the choice of the scaling factor in the cost function as it plays a significant role in the stability of the adjoint model, and overall performance of the minimization scheme. For nonlinear assimilation problems, this impact was found to be more significant. This is the reason behind using different cost function scaling factors for linear and nonlinear problems in Chapter 5. It was shown that for nonlinear assimilation experiments with synthetic data, iterating, instead of using linear theory, to obtain the tangential velocity from the surface elevation did not change the

results significantly (less than 0.1%). It was also shown that for steep sea states with higher nonlinearities, using the linear assimilation could change the retrieved results by about 40%. It was also shown that increasing the number of observations would decrease the errors associated with the assimilated profile almost linearly. Increasing the observational noise led to an almost linear increase in the errors.

Dispersion filters were also considered as an alternative approach for removing the non-physical wave components in the data. The comparisons showed that the assimilation approach is better able to fit the measurements to the dynamics by just using the first few observation frames. For the present application, temporal resolution of the measurements is not adequate (Note that the radar revisiting period is typically about 3 seconds) to resolve the wave profile in time, and all observational frames are needed for the the filtering. Instead, the numerical model's time step can be chosen fine enough in order to capture the wave dynamics appropriately. In some cases the assimilated results were about 40% better than the filtered ones.

For the synthetic radar data from EM simulations, the errors were generally found to be higher for the lower incidence angle (1°) due to the shadowing effect. In most cases incorporating more observations within the assimilation led to higher-quality retrievals. The best strategy was found to be first filtering the raw retrievals using the linear dispersion relation, and then assimilating these filtered profiles into the numerical model. This strategy was able to improve the retrievals by 30 to 70%. The wind speed was found to be a significant factor in the assimilation results as lower wind speeds ($5m/s$) led to higher-quality retrievals. The assimilated profiles based on VV-polarization had a slightly higher quality compared to those resulted from HH-polarization.

Preliminary investigations of the field data showed a strong inconsistency between the radar measurements and numerical model predictions in both phases and amplitudes. Assimilation was able to improve the initial condition such that the model predictions fitted the observations better. In most cases the improvements, defined as the reduction in RMS errors, were about 30-40%. In this work, only the initial condition was assumed as the control variable for minimization. Because of the limitations of the pseudo-spectral method, it was also assumed that the boundary information loops around in both x and y-directions.

In order to artificially impose the periodicity, the initial surface profile was tapered at both x and y-directions. Further investigations will be needed to study the effect of non-periodic boundary conditions. A good strategy would be to develop a scheme that takes both initial and boundary conditions as control variables. Another limitation associated with the field data is the time window of the forecast which strongly depends on the range of the radar.

Finally, the preliminary results of a novel assimilation scheme to estimate the slowly varying surface currents from the observations of the free surface were presented. This scheme allows one to calculate the gradient of the cost function with respect to the variation in the current profile by just one integration of the forward model and one backward integration of the adjoint model. So far, the adjoint-calculated gradient was validated for a simple current profile, however, more developments of this technique are still in progress. A similar technique may be also developed in future for retrieving the depth profile from the surface observations.

For the numerical simulations carried out in the current thesis, the typical 2-D assimilations (using 8 observations) were performed in near-real time for linear problems in 256×256 computational domains. It would be very beneficial to parallelize the code and use more efficient minimization algorithms that are to be developed in future. This will be especially useful when the nonlinear assimilation needs to be carried out for much larger computational domains and more observations.

The developed assimilation scheme has shown great promise for improving the forecasts of the sea state with great efficiency, and can be easily linked to the wave evolution model. This scheme can be used as a very useful tool to improve the consistency of measurements and model predictions.

APPENDICES

APPENDIX A

Formulation of Craig and Sulem

Craig and Sulem [15] defined a so-called Dirichlet-Neumann operator as:

$$G(\eta)\Phi = u_n = \sqrt{1+\eta_x^2}\frac{\partial\varphi}{\partial n}\bigg|_{z=\eta} \tag{A.1}$$

which maps Dirichlet data to Neumann data on the free surface, with n being the unit outward normal to the boundary. u_n is the velocity component which is normal to the free surface, and φ is the velocity potential. Using this operator they stated the one-dimensional free surface boundary conditions in terms of η and Φ:

$$\eta_t = G(\eta)\Phi \tag{A.2}$$

$$\Phi_t = \frac{-1}{2\left(1+\eta_x^2\right)}\left\{\Phi_x^2 - \left[G(\eta)\Phi\right]^2 - 2\eta_x\Phi_x G(\eta)\Phi\right\} - g\eta \tag{A.3}$$

where G is an analytic function of η and can be written in terms of a convergent Taylor expansion:

$$G(\eta) = \sum_{j=0}^{\infty} G_j(\eta) \tag{A.4}$$

where the polynomials G_j are homogeneous of degree j in η and can be found explicitly. The first three terms are given by:

$$G_0 = D\tanh(h_0 D) \tag{A.5}$$

$$G_1(\eta) = D\left(\eta - \tanh(h_0 D)\eta \tanh(h_0 D)\right) D \tag{A.6}$$

$$\begin{aligned} G_2(\eta) = -\frac{1}{2} D(D\eta^2 \tanh(h_0 D) + \tanh(h_0 D)\eta^2 D \\ - 2\tanh(h_0 D)\eta D \tanh(h_0 D)\eta \tanh(h_0 D))D \end{aligned} \tag{A.7}$$

where $D = -i\frac{\partial}{\partial x}$. In order to show that the this formulation is equivalent to the formulation derived in Chapter 3, one first finds the relationship between operator $G(\eta)$ and operator $\mathcal{T}$ introduced in (3.44). Note that in Fourier space:

$$D = -i(ik) = k, \quad hD = kh, \quad \mathcal{T} = -i\tanh(kh) \;\Rightarrow\; \tanh(hD) = i\mathcal{T} \tag{A.8}$$

If we plug these in the expression for G_0, G_1, G_2 and noting that $\frac{\partial \Phi}{\partial x} = u_s$:

$$G_0(\eta)\Phi = D\tanh(hD)\Phi = ik\mathcal{T}[\Phi] = \mathcal{T}[u_s] \tag{A.9}$$

$$\begin{aligned} G_1(\eta)\Phi &= -i\frac{\partial}{\partial x}\left(\eta - i\mathcal{T}\left(\eta\left(i\mathcal{T}\right)\right)\right)\left(-i\frac{\partial}{\partial x}\right)\Phi \\ &= -\frac{\partial}{\partial x}\left(\eta u_s\right) - \frac{\partial}{\partial x}\left(\mathcal{T}\left[\eta\mathcal{T}[u_s]\right]\right) \end{aligned} \tag{A.10}$$

$$\begin{aligned} G_2(\eta)\Phi = \frac{1}{2} i\frac{\partial}{\partial x}\Bigg\{ -i\frac{\partial}{\partial x}\left(\eta^2 i\mathcal{T}\right) + i\mathcal{T}\left[\eta^2\left(-i\frac{\partial}{\partial x}\right)\right] \\ -2i\mathcal{T}\left[\eta\left(-i\frac{\partial}{\partial x}\right)\left(i\mathcal{T}\left[i\eta\mathcal{T}\right]\right)\right]\Bigg\}\left(-i\frac{\partial}{\partial x}\right)[\Phi] \\ = \frac{1}{2}\frac{\partial^2}{\partial x^2}\left(\eta^2\mathcal{T}[u_s]\right) + \frac{1}{2}\frac{\partial}{\partial x}\left(\mathcal{T}\left[\eta^2\frac{\partial u_s}{\partial x}\right]\right) \\ + \frac{\partial}{\partial x}\left(\mathcal{T}\left[\eta\frac{\partial}{\partial x}\left(\mathcal{T}\left[\eta\mathcal{T}[u_s]\right]\right)\right]\right) \end{aligned} \tag{A.11}$$

Now if we add up all terms up to third-order:

$$
\begin{aligned}
G = G_0 + G_1 + G_2 = \mathcal{T}[u_s] - \frac{\partial}{\partial x}\left(\eta u_s\right) - \frac{\partial}{\partial x}\left(\mathcal{T}\left[\eta \mathcal{T}[u_s]\right]\right) \\
+ \frac{1}{2}\frac{\partial^2}{\partial x^2}\left(\eta^2 \mathcal{T}[u_s]\right) + \frac{1}{2}\frac{\partial}{\partial x}\left(\mathcal{T}\left[\eta^2 \frac{\partial u_s}{\partial x}\right]\right) \\
+ \frac{\partial}{\partial x}\left(\mathcal{T}\left[\eta \frac{\partial}{\partial x}\left(\mathcal{T}\left[\eta \mathcal{T}[u_s]\right]\right)\right]\right)
\end{aligned}
\tag{A.12}
$$

which is exactly the same as the right-hand side of the mass equation in (4.5) for the one-dimensional waves.

APPENDIX B

Formulation of West et al.

As indicated in Chapter 3, for deep water condition, the present pseudo-spectral model will reduce to the original formulation of West et al. [80] in Fourier space.

The procedure proposed by Watson and West (1975) to find a closure, starts from the formal relationship:

$$\Phi(\mathbf{x},\eta) = \sum_n \frac{\eta^n}{n!}\frac{\partial^n}{\partial z^n}\phi_0(\mathbf{x}) \tag{B.1}$$

They expressed the derivative of Φ in terms of the formal operator $\frac{\partial}{\partial z} \equiv \kappa$, which multiplies any one- or two-dimensional Fourier coefficient of Φ by the magnitude of the wave number vector $\mathbf{k}$. The vertical velocity on the free surface can be expressed as:

$$W = \left.\frac{\partial\phi}{\partial z}\right|_{z=\eta} = \sum_n \frac{\eta^n \kappa^{n+1}}{n!}\phi_0(\mathbf{x}) \tag{B.2}$$

Given Φ, they found the reference function ϕ_0 by formally inverting the series (C.1), and finally, calculated W from the series (C.2).

Formal expansion of the free surface variables Φ and W gives:

$$W = \sum_{n=0}^{\infty} W_n \tag{B.3}$$

$$\Phi = \sum_{n=0}^{\infty} \Phi_n \tag{B.4}$$

From expansion (C.1):

$$\begin{aligned}
\Phi &= \Phi_0 \\
0 &= \kappa\eta\Phi_0 + \Phi_1 \\
0 &= \frac{1}{2}\eta^2\kappa^2\Phi_0 + \eta\kappa\Phi_1 + \Phi_2 \\
0 &= \sum_{m=0}^{n} \frac{(\eta)^{n-m}(\kappa)^{n-m}}{(n-m)!}\Phi_m
\end{aligned} \tag{B.5}$$

which can be directly inverted to give:

$$\begin{aligned}
\Phi_0 &= \Phi \\
\Phi_1 &= -\kappa\eta\Phi_0 \\
\Phi_2 &= -\kappa\eta\Phi_1 - \frac{1}{2}\kappa^2\eta^2\Phi_0 \\
\Phi_3 &= -\kappa\eta\Phi_2 - \frac{1}{2}\kappa^2\eta^2\Phi_1 - \frac{1}{6}\kappa^3\eta^3\Phi_0 \\
\Phi_n &= -\sum_{m=1}^{n} \frac{\eta^m\kappa^m}{m!}\Phi_{n-m}
\end{aligned} \tag{B.6}$$

From the series (C.1), one can then find:

$$\begin{aligned}
W_0 &= \kappa\Phi_0 \\
W_1 &= \kappa\Phi_1 + \eta\kappa^2\Phi_0 \\
W_2 &= \kappa\Phi_2 + \eta\kappa^2\Phi_2 + \frac{1}{2}\eta^2\kappa^3\Phi_0 \\
W_3 &= \kappa\Phi_3 + \eta\kappa^2\Phi_2 + \frac{1}{2}\eta^2\kappa^3\Phi_1 + \frac{1}{6}\eta^3\kappa^4\Phi_0 \\
W_n &= \sum_{m=0}^{n} \frac{(\eta)^m(\kappa)^m}{m!}\Phi_{n-m}
\end{aligned} \tag{B.7}$$

In this approach, expressions (C.6) are solved in sequence giving the Φ of each order in terms of the Φ of lower orders and η. From the calculated Φ, W is then obtained in sequential form of (C.7). However, in the formulation presented in Chapter 3, for each order of approximation, a coupled set of evolution equations is solved and there is no requirement to obtain ϕ and W in sequential form during the simulation.

Going back to the equations derived in Chapter 3, in order to write the vertical velocity

on the free surface in a form similar to (C.7), One first writes the expansion for ϕ_0 given in (3.32) in a sequential form up to third-order:

$$\begin{aligned}
\Phi_0 &= \Phi \\
\Phi_1 &= \eta\mathcal{L}[\Phi_0] \\
\Phi_2 &= \eta\mathcal{L}[\Phi_1] + \frac{1}{2}\eta^2\nabla^2\Phi_0 \\
\Phi_3 &= \eta\mathcal{L}[\Phi_2] + \frac{\eta^2}{2}\nabla^2\Phi_1 - \frac{\eta^3}{6}\nabla^2(\mathcal{L}[\Phi_0])
\end{aligned} \tag{B.8}$$

Note that in Fourier space, $\nabla f = i\mathbf{k}f$ and $\mathcal{L}[f] = -kf$, where $k = |\mathbf{k}|$, and deep water condition has been assumed. Now, the series (C.8) is written in Fourier space as:

$$\begin{aligned}
\Phi_0 &= \Phi \\
\Phi_1 &= -\eta k\Phi_0 \\
\Phi_2 &= -\eta k\Phi_1 - \frac{1}{2}\eta^2 k^2\Phi_0 \\
\Phi_3 &= -\eta k\Phi_2 - \frac{1}{2}\eta^2 k^2\Phi_1 - \frac{1}{6}\eta^3 k^3\Phi_0
\end{aligned} \tag{B.9}$$

which is exactly the same as (C.6), since $k = \kappa$. The expression for W given in (3.33) can be similarly written in a sequential form and then transformed into Fourier space to give:

$$\begin{aligned}
W_0 &= -\mathcal{L}[\Phi_0] \equiv k\Phi_0 \\
W_1 &= -\mathcal{L}[\Phi_1] - \eta\nabla^2\Phi_0 \equiv k\Phi_1 + \eta k^2\Phi_0 \\
W_2 &= -\mathcal{L}[\Phi_2] - \eta\nabla^2\Phi_1 + \frac{1}{2}\eta^2\nabla^2(\mathcal{L}[\Phi_0]) \equiv k\Phi_2 + \eta k^2\Phi_1 + \frac{1}{2}\eta^2 k^3\Phi_0 \\
W_3 &= -\mathcal{L}[\Phi_3] - \eta\nabla^2\Phi_2 + \frac{1}{2}\eta^2\nabla^2(\mathcal{L}[\Phi_1]) + \frac{1}{6}\eta^3\nabla^4\Phi_0 \\
&\equiv k\Phi_3 + \eta k^2\Phi_2 + \frac{1}{2}\eta^2 k^3\Phi_1 + \frac{1}{6}\eta^3 k^4\Phi_0
\end{aligned} \tag{B.10}$$

which is exactly the same as (C.7).

It has been shown that the presented pseudo-spectral model for the special case of deep water, reduces to the original West's formulation in Fourier domain at different orders.

BIBLIOGRAPHY

BIBLIOGRAPHY

[1] Alpers, W., Hasselmann, K., "The two frequency microwave technique for measuring ocean wave spectra from an airplane or satellite", *Boundary Layer Meteorol.*, 13, 215-230(1978).

[2] Alpers, W. R., Ross, D. B., and Rufenach, C. L., "On the detectability of ocean surface waves by real and synthetic aperture radar.", *J. Geophys. Res.*, 86, 64816498(1981).

[3] Atanassov, V., Rosenthal, W., and Ziemer, F., "Removal of ambiguity of two-dimensional power spectra obtained by processing ship radar images of ocean waves", *J. Geophys. Res.*, Vol. 90, Issue C1, 1061-1068(1985).

[4] Beal, R. C., "Space-borne imaging radar: Monitoring of ocean waves.", *Science*, 208, 1373-1375(1980).

[5] Benjamin, T. B., "Instability of periodic wavetrains in nonlinear dispersive systems", *Proc. Roy. Soc.*, A, 299, 59-75(1967).

[6] Bennet, W., "The Kalman smoother for a linear quasi-geostrophic model of ocean circulation", *Dynamics of Atm. Oceans*, 13, 219-267(1989).

[7] Bergthorsson, P. and Doos, B., "Numerical weather map analysis", *Tellus* 7()3, 329-340(1955).

[8] Bewley, T. R., "Flow control: new challenges for a new renaissance", *Prog. Aero. Sci.*, 37, 21-58(2001).

[9] Borge, J. N. et al., "Estimation of the significant wave height with X-Band nautical radars", *Proc. 18th Int. Conf. Offshore Mech. Arctic Eng.(OMAE)*, St. John's, Newfoundland, CA(1999).

[10] Borge, J. N. et al., "Inversion of marine radar images for surface wave analysis", *J. Atmos. Oceanic Tech.*, Vol. 21, No. 8 1291-1300(2004).

[11] Cacuci, D. G., "The forward and the adjoint methods of sensitivity analysis, in uncertainty analysis", Y. Ronen, Ed., CRC Press, Inc., Boca Raton, Florida, Chap. 3(1988).

[12] Chappelear, J. E., "Direct numerical calculation of wave properties", *J. Geophys. Res.*, 66, 501-508(1961).

[13] Choi, W., "Nonlinear evolution equations for two-dimensional waves in a fluid of finite depth", *J. Fluid Mech.*, 295, 381-394(1995).

[14] Clamond, D. and Grue, J., "A fast method for fully nonlinear water wave computations", *J. Fluid Mech.*, 447, 337-355(2001).

[15] Craig, W. and Sulem, C., "Numerical simulation of gravity waves", *J. Compt. Phys.*, 108, 73(1993).

[16] Creamer, D., Henyey, F., Schult, R., and Wright, J., "Improved linear representation of ocean surface waves", *J. Fluid Mech.*, 205, 135161(1989).

[17] Daley, R., "Atmospheric data analysis", *Cambridge University Press*(1991).

[18] Dankert, H. and Rosenthal, W., "Ocean surface determination from X-Band radar-image sequences", *J. Geophys. Res.*, Vol. 109, (2004).

[19] Dankert, H., Horstmann, J., and Rosenthal, W., "Wind and wave field measurements using marine X-Band radar image sequences", *IEEE J. Ocean Eng.*, Vol. 30, No. 3(2005).

[20] Dean, R. G., "Stream function representation of nonlinear ocean waves", *J. Geophys. Res.*, 70, 4561-4572(1965).

[21] Dommermuth, D. G. and Yue, D. K. P., "A high-order spectral method for the study of nonlinear gravity waves", *J. Fluid Mech.*, 184, 267(1987).

[22] Dysthe, K. B., "Note on a modification to the nonlinear Schrodinger equation for application to deep water waves.", *Proc. R. Soc. Lond.*, A 369, 105-114(1979).

[23] Evmenov, V. F. et al., "Test of the radar method of defining ocean waves elements", *Fluid Mech. Sov. Res.*, 2, 5, 141-145(1973).

[24] Fornberg, B. and Whitham, G. B., "Numerical and theoretical study of certain nonlinear wave phenomena", *Phil. Trans. Royal Soc. A*, 289, 373-404(1978).

[25] Fenton, J. D. and Rienecker, M. M., "A Fourier method for solving nonlinear water-wave problems: An application to solitary-wave interactions", *J. Fluid Mech.*, 118, 411(1982).

[26] Fukumori, I. and Malanotte-Rizzioli, P., "An approximate Kalman filter for ocean data assimilation; an example with an idealized Gulf Stream", *J. Compt. Phys.*, 108, 73(1993).

[27] Gelb, A., "Applied optimal estimation", M.I.T. Press, Cambridge, MA, pp 374(1974).

[28] Ghil, M., "Meteorological data assimilation for oceanographers. Part I: Description and theoretical framework.", *Dyn. Atmos. Oceans*, 13, 171-218(1989).

[29] Guyenne, P. and Nichols, D. P., "Numerical simulation of solitary waves on plane slopes", *Math. Comput. Simul.*, 69, 269(2005).

[30] Hasselmann, K., "On the nonlinear energy transfer in a gravity wave spectrum, Part I.", *J. Fluid Mech.*, 12, 481-500(1962).

[31] Hatten, H., Ziemer, F., Seemann, J., and Nieto-Borge, J., "Correlation between the spectral background noise of a nautical radar and the wind vector.", *Proc. 17th Int. Conf. Offshore Mechanics and Arctic Engineering (OMAE)*, Lisbon, Portugal(1998).

[32] Hoke, J. E. and Anthes, R. A., "The initialization of numerical models by a dynamical initialization technique", *Mon. Wea. Rev.*, 194, 1551-1556(1976).

[33] Hoogeboom, P. and Rosenthal, W., "Directional wave spectra in radar images", *Int. Geosci. Remote Sens. Symp., IEEE*, Munich, June 1-4(1982).

[34] Ijima, T., Takahashi, T., and Sasaki, H., "Application of radars to wave observations", *Proc. Conf. Coastal Eng.*, 30(1), 10-22(1964).

[35] Johnson, J. T., "A numerical study of low-grazing-angle backscatter from ocean-like impedance surfaces with the canonical grid method", *IEEE Trans. Antennas and Prop.*, 46(1), 114-120(1998).

[36] Johnson, J. T., Shin, R. T., Kong, J. A., Tsang, L., and Pak, K., "A numerical study of the composite surface model for ocean scattering", *IEEE Trans. Geosc. Remote Sens.*, 36(1), 72-83(1998).

[37] Johnson, J. T., Burkholder, R. J., Toporkov, J. V., Lyzenga, D. R., and Plant, W. J., "A numerical study of the retrieval of sea surface height profiles from low grazing angle radar data", *IEEE Trans. Geosci. Rem. Sens.*, To be appeared in 2009.

[38] Kalney, "Atmospheric modeling: data assimilation and predictability", *Cambridge University Press*, pp 341(2003).

[39] Kent, C. P., A pseudo-spectral method for calculating wave-body interaction using an explicit free-surface formulation", *Dissertation*, University of Michigan, Ann Arbor (UMI No. 3192674), 119p(2005).

[40] Krasitskii, V. P., " On reduced equations in the Hamiltonian theory of weakly nonlinear surface waves", *J. Fluid Mech.*, 272, 1-20(1994).

[41] Lake, B. M., and Yuen, H. C., "A note on some nonlinear water-wave experiments and the comparison of data with theory.", *J. Fluid Mech.*, 83, 75-81(1977).

[42] Landrini, M., Oshri, O., Waseda, T., and Tulin, M. P., " Long time evolution of gravity wave systems", *Proc. 13th Intl Workshop on Water Waves and Floating Bodies*, 75-78(1998).

[43] Le Dimet, F. X. and Talagrand, O., "Variational algorithms for analysis and assimilation of meteorological observations.", *Tellus*, 38A, 97-110(1986).

[44] Lee, P., Barter, J., Beach K., Hindman, C., Lake B., Rungaldier, H., Shelton J., Williams A., Lee R., and Yuen, H., "X-band microwave backscattering from ocean waves.", *J. Geophys. Res.*, 100 (C2), 25912611(1995).

[45] Liu, D. C. and Nocedal, J., "On the limited memory BFGS method for large scale minimization", *Math. Prog.*, 45, 503-528(1989).

[46] Longuet-Higgins, M. S. and Stewart, R. W., "Changes in the form of short gravity waves on long waves and tidal currents", *J. Fluid Mech.*, 8, 565-583(1960).

[47] Longuet-Higgins, M. S. and Cokelet, E. D., "The deformation of steep surface waves on water. I. A numerical method of computation", *Proc. Royal Soc. London, Ser. A*, 350, 1(1976).

[48] Longuet-Higgins, M. S., "The instabilities of gravity waves of finite amplitude in deep water, Part I, Super-harmonics.", *Proc. Royal Soc.*, A 360, 471-488(1978).

[49] Lyzenga, D., Maffet, A., and Shuchman, R., "The contribution of wedge scattering to the radar cross section of the ocean surface.", *IEEE Trans. Geosci. Remote Sens.*, GE-21(4), 502505(1983).

[50] Malanotte-Rizzioli, P., Young, R. E., and Haidvogel, D. B., "Initialization and data assimilation experiments with a primitive equation model", *Dyn. Atmos. Oceans*, 13, 349-378(1989).

[51] Marchuk, G. I., "Adjoint equations and analysis of complex systems", *Kluwer Academic Publishers*(1995)

[52] Matsuno, Y., "Nonlinear evolutions of surface gravity waves on fluid of finite depth", *Phys. Rev. Lett.*, 69, 609-611(1992).

[53] Mattie, M. G. and Harris, D. L., "A system for using radar to record wave direction", *Tech. Rep.*, U.S. Army Corps Eng., Coastal Eng. Res. Ctr, Fort Belvoir, VA, pp 50(1979).

[54] Morales, J. L. and Nocedal, J., "Algorithm 809: PREQN: Fortran 77 subroutines for preconditioning the conjugate gradient method.", *ACM Trans. Math. Soft.*, Eng. Transl., 27(1), 83-91(2001).

[55] Morales, J. L. and Nocedal, J., "Enriched methods for large-scale unconstrained optimization", *Comput. Optim. Appl.*, 21, 121-154(2002).

[56] Multer, R. H., "Exact nonlinear model of wave generator", *J. Hydraulic Div. ASCE*, 99, 31-46(1973).

[57] Navon, I. M. and Legler, D. M., "Conjugate gradient methods for large scale minimization in meteorology", *Mon. Wea. Rev.*, 115, 1479-1502(1987).

[58] Orszag, S. A., "Transform Method for Calculation of Vector-coupled Sums: Application to the Spectral Form of the vorticity equation", *Journal of Atmospheric Sciences*, 27, 890-895 (1970).

[59] Oudshoorn, H. M., "The use of radar in hydrodynamic surveying", *Proc. 7th Conf. Coastal Eng.*, 59-76(1960).

[60] Pan, G., Burkholder, R. J., Johnson, J. T., Toporkov, J. V., and Sletten, M. A., "Studies of ocean surface profile retrieval from simulated LGA radar data", *Intl. Geoscience and Remote Sensing Symposium, conference proceedings*(2006).

[61] Panchang, V. G., and Richardson, J. E., "Inverse adjoint estimation of eddy viscosity for coastal flow models", *J. Hydraulic Eng.*, 119(4), 506-524(1993).

[62] Phillips, O. M., "The equilibrium range in the spectrum of wind-generated waves.", *J. Fluid Mech.*, 426-434(1958).

[63] Phillips, O. M., "On the dynamics of unsteady gravity waves of finite amplitude.", *J. Fluid Mech.*, 9, 193-217(1960).

[64] Phillips, O. M., "The dynamics of the upper ocean.", *Cambridge University Press*, 2nd edition.

[65] Phillips, O. M., "The dispersion of short waves in the presence of a dominant long wave.", *J. Fluid Mech.*, (1981).

[66] Rice, S. O., "Reflection of electromagnetic waves from slightly rough surfaces", *Commun. Pure Appl. Math.*, 4, 361378(1951).

[67] Rienecker, M. M., and Fenton, J. D., "A Fourier approximation method for steady water waves", *J. Fluid Mech.*, 104, 119-137(1981).

[68] Rino, C. L., Crystal, T. L., Koide, A. K., Ngo, H. D., and Guthart, H., "Numerical simulation of backscatter from linear and nonlinear ocean surface realizations", *Radio Sci.*, 26, 51-71(1991).

[69] Roberts, A. J., and Schwartz, L. W., "The calculation of nonlinear short-crested waves", *Phys. Fluids*, 26, 2388(1983).

[70] Romeiser, R., Schmidt, A., and Alpers, W., "A three-scale composite surface model for the ocean wave-radar modulation transfer function", *J. Geophys. Res.*, 99 9785-9801(1994).

[71] Sanders, B. F., and Katopodes, N. D., "Adjoint sensitivity analysis for shallow water wave control", *J. Eng. Mech.*, 126(9), 909-919(2000).

[72] Smagorinsky, J., "General circulation experiments with the primitive equations", *Monthly Weather Review*, 91, 91-164(1963).

[73] Smith, R. A., "An operator expansion formalism for for nonlinear surface waves over variable depth", *J. Fluid Mech.*, Vol. 363, 333-347(1998).

[74] Tanaka, M., "A method of studying nonlinear random field of surface gravity waves by direct numerical simulation", *Fluid Dynamics Research*, 28, 41-60 (2001).

[75] Trizna, D., and Carlson, D., " Studies of dual polarized low grazing angle radar sea scatter in near-shore regions.", *IEEE Trans. Geosci. Remote Sens.*, 34(3), 747757(1996).

[76] Tulin, M. P., and Waseda, T., "Laboratory observations of wave group evolution, including breaking effects", *J. Fluid Mech.*, 378, 197-232(1999).

[77] Wang, Z., Navon, I. M., Zou, X., and Le Dimet, F. X., "A truncated Newton optimization algorithm in meteorology applications with analytic Hessian/Vector products", *Comp. Opt. and App.*, Vol. 4, 241-262(1995).

[78] Wang, Z., Droegemeier, K, and White, L., "The adjoint Newton algorithm for large-scale unconstrained optimization in meteorology applications.", *Comp. Opt. App.*, 10, 283-320(1998).

[79] Wehausen, J. V., and Laitone, E. V., "Surface waves", *Handbuch der Physik*, 9(3), 446-778(1960).

[80] West, B. J., Brueckner, K. A., Janda, R. S., Milder, D. M., and Milton, R. L., "A new numerical method for surface hydrodynamics", *J. Geophysical Res.*, 92, 11803-11824(1987).

[81] Willis, T. G. and Beaumont, H., "Wave direction measurements using sea surveillance radars", *Tech. Memo. TR 118*, R. Aircraft Establishment, Farnbough, Great Britain(1971).

[82] Wright, F. F., "Wave observations by ship-board radar", *Ocean Sci. Ocean Eng.*, 1, 506-514(1965).

[83] Wright, J. W., "A new model for sea clutter", *IEEE Trans. Antennas Propagat.*, AP-16, 217223(1968).

[84] Wright, J. W., "Backscattering from capillary waves with applications to sea clutter.", *IEEE Trans. Antennas Propag.*, AP-14(6), 749754(1966).

[85] Young, I. R. and Rosenthal, W., "A three dimensional analysis of marine radar images for the determination of ocean wave directionality and surface currents", *J. Geophys. Res.*, Vol. 90, No. C1, 1049-1059(1985).

[86] Zakharov, V. E., "Stability of periodic waves of finite amplitude on the surface of a deep fluid", *J. of Appl. Mech. Tech. Phys.*, Eng. Transl., 2, 190-194(1968).

[87] Ziemer, F., and Rosenthal, W.,and Carlson, H., "Measurements of directional wave spectra by ship radar", *IAPSO Symp.* , Genral Assembly, Int. Assoc. Phys. Sci. Oceans, Hamburg, Federal Republic of Germany(1983).

[88] Ziemer, F., and Gunther, H., "A system to monitor ocean wave fields", *Proc. 2nd Int. Conf. Air-Sea Interaction*, Lisbon, Portugal(1994).

[89] Zou, X., Navon, I. M., and Le Dimet, F. X., "An optimal nudging data assimilation scheme using parameter estimation", *Q. J. R. Meteorol. Soc.*, 118, 1163-1186(1992).